Investigations On Selected Chalcogenide Glasses Towards The Realization Of Photonic Devices

Ph D Thesis submitted to

Cochin University of Science and Technology

In partial fulfilment of the requirements for the award of the Degree of

Doctor of Philosophy

Indu Sebastian,

Reg. No: 4023

International School of Photonics
Cochin University of Science and Technology
Cochin -682022, Kerala, India

August 2015

Investigations on selected chalcogenide glasses towards the realization of photonic devices

Ph D thesis in the field of Photonics

Author:

Indu Sebastian
Research Fellow
International School of Photonics
Cochin University of Science & Technology
Cochin -682022, Kerala, India
indusebastian@gmail.com

Research Advisor:

Dr. Sheenu Thomas
Asst. Professor
International School of Photonics
Cochin University of Science & Technology
Cochin -682022, Kerala, India
st@cusat.ac.in, sheenuthomas29@gmail.com

International School of Photonics
Cochin University of Science & Technology
Cochin -682022, Kerala, India
www.photonics.cusat.edu

August 2015

Cover image: *Schematic of alkane thiol molecules and their binding, on silver island structures patterned over chalcogenide glass surfaces. Silver islands are indicated as squares and chalcogenide glass surface is shown as in red colour.*

To

My Parents,

And

All Those Who Inspired Me

INTERNATIONAL SCHOOL OF PHOTONICS
COCHIN UNIVERSITY OF SCIENCE AND TECHNOLOGY
COCHIN -682022, KERALA, INDIA

Dr. Sheenu Thomas
Asst. Professor

Certificate

This is to certify that the thesis entitled "*Investigations On Selected Chalcogenide Glasses Towards The Realization Of Photonic Devices*" submitted by **Ms. Indu Sebastian**, is a bonafide record of research work carried out by her under my guidance and supervision in partial fulfilment of the requirement of the degree of Doctor of Philosophy of Cochin University of Science and Technology, under the Faculty of Technology and has not been included in any other thesis submitted previously for the award of any degree.

Kochi-682022
18 -08- 2015

Dr. Sheenu Thomas
(Supervising guide)

Phone: +91 484 2575848 Fax: 0091-484-2576714.
Email: st@cusat.ac.in, sheenuthomas29@gmail.com

INTERNATIONAL SCHOOL OF PHOTONICS
COCHIN UNIVERSITY OF SCIENCE AND TECHNOLOGY
COCHIN -682022, KERALA, INDIA

Dr. Sheenu Thomas
Asst. Professor

Certificate

This is to certify that the thesis entitled "***Investigations on selected chalcogenide glasses towards the realization of photonic devices***" submitted by **Ms. Indu Sebastian**, has incorporated all the relevant corrections and modifications suggested by the audience during the pre-synopsis seminar and recommended by the Doctoral Committee.

Kochi-682022
18- 08- 2015

Dr. Sheenu Thomas
(Supervising guide)

Phone: +91 484 2575848 Fax: 0091-484-2576714.
Email: st@cusat.ac.in, sheenuthomas29@gmail.com

Declaration

I, Indu Sebastian do hereby declare that the thesis entitled "***Investigations on selected chalcogenide glasses towards the realization of photonic devices***" is a genuine record of research work done by me under the supervision of Dr. Sheenu Thomas, Asst. Professor, International School of Photonics, Cochin University of Science and Technology, Kochi–22, India and has not been included in any other thesis submitted previously for the award of any degree.

Kochi-682022
18- 08- 2015

Indu Sebastian

Acknowledgement

First and foremost, I thank God, 'the Light' who lead me through the darkness, 'the Guide' who direct me when I am lost, and 'the truth' that save me when I am confused.

I am grateful to many individuals who have provided encouragement and support during the period of this research. I would like to express my sincere gratitude to my research guide, Dr. Sheenu Thomas, for her constant support and patience throughout my years as a doctoral student. Her encouragement and friendly attitude inspired me to explore different aspects of research that are both challenging and rewarding.

I owe special acknowledgements to Prof. V P N Nampoori who shared creative ideas, gave invaluable suggestions during the entire period of this work. His guidance and fruitful discussions has helped me to become a better researcher and prepared me for the challenges I will face in my professional career. I express my sincere thanks to Prof. P Radhakrishnan for his help and pain-staking effort in reviewing this thesis. I extend my thanks to our Director, Dr. M Kailasnath, for providing support.

I am grateful to Dr. Johney Issac, Dept. of instrumentation, CUSAT, for his constant encouragement and help. I would like to thank Dr. Girish Kunte, CENSE, IISc, Bangalore for Raman and FESEM analysis. I also thank Kasmir sir, Dept. of instrumentation, CUSAT for his help in sample preparation. I wish to acknowledge IIT Madras for HRTEM facility and SEIF-STIC for various analyses.

I would like to thank all those whom I've worked with over the years. I am blessed with a wonderful friend Divya, we together explored and enjoyed the world as Cooper's electron pair. I thank Divya for being such a nice companion. My special thanks to Dr Tintu for her guidance and help during my research period. Sincere thanks go to Mathew for helping and providing knowledge in Z-scan experiments. I am also grateful to Suneetha and Nideep for making such a lively environment in our research room. The valuable discussions with Suneetha have helped me in silver sample preparation and analysis. I would like to express my special thanks to Roopa for her help and support in the lab. I also thank Ajina, my 'successor', for her assistance and support.

I am grateful to all members of photonics family, Jaison, Jessy, Sr. Anju, Aparna, Linslal, Bejoy, Sabitha, Bony, Adrin, Retheesh sir, Bini, Pradeep, Dr. Roseleena, Musfir,

Sony, Bobby sir, Anand, Priyamvadha miss, Aleena, Manju, Dr. Sreelekha, Rejeena, Remya and Ajmal for making a vibrant environment. I am thankful to Dayal for his assistance and support.

Special gratitude goes to Deepu, Department of Physics, for his timely help and support. I extend my thanks to Ashraf, Department of Applied Chemistry, for his help in ATR measurements. I am grateful to Hasna, Deepa chechi, and Smitha chechi for making my hostel life enjoyable. I enjoyed the companionship with my delightful roommate, Divya Antony.

I would like to thank Lab, library and administrative staff of the ISP for the assistance extended during the tenure.

I would like to acknowledge UGC and KSCSTE for providing financial assistance.

I am deeply indebted to my parents, grandparents, sisters and my family as a whole for their love, and support.

Indu Sebastian

DREAM is not what you see in sleep

DREAM is something which doesn't let you sleep

Dr. APJ Abdul Kalam

Preface

Among various optical sensing schemes, infrared spectroscopy is a powerful tool for detecting and determining the composition of complex organic samples since vibrational finger prints of all biomolecules and organic species are located in this window. This spectroscopic technique is simple, reliable, fast, non-destructive, cost-effective while having low sensitivity. Use of metallic nanoparticles in association with a good IR transparent sensing substrate, is one of the promising solutions to enhance the sensitivity.

Chalcogenide glasses are promising substrate material because of their extended optical transmission window starting from the visible to the far infrared range up to 20 μm, high refractive index usually between 2 and 3 and high optical nonlinearity, which make them good candidates as IR sensors and optical ultrafast nonlinear devices. These glasses are favorable sensor materials for the infrared spectral range because of their high IR transparency to allow for low optical loss at wavelengths corresponding to the characteristic optical absorption bands of organic molecules, high refractive index for tight confinement of optical energy within the resonator structure, processibility into thin film form, chemical compatibility for adhesion of silver nano particles and thin films and resistance to the chemical environment to be sensed. Molecules adsorbed to silver island structures shows enhanced IR absorption spectra and the extent of enhancement is determined by many factors such as the size, density and morphology of silver structures, optical and dielectric properties of the substrate material etc.

In this context, the present thesis has been devoted for the preparation and detailed analysis of different compositions of germanium selenide based bulk, thermally as well as solution processed thin films of chalcogenide glasses, fabrication and characterization of silver island films and self-assembled monolayers (SAM) of anchor molecules for the realization of a prototype infrared (IR) sensor with chalcogenide glass (ChGs) as the sensor platform.

Chapter 1: This chapter starts with 'motivation' of the work done in this thesis followed by an overview about the basic properties and characteristics of chalcogenide glasses and how these properties relate to various

applications. A brief literature review on current researches in chalcogenide glasses is also included. A description of infrared based sensor technology along with the application of chalcogenide glasses in these systems are discussed. Different stages of fabrication of infrared based sensor are also described. Finally a short note on germanium based selenide glass and compositional selection criteria are specified in this chapter.

Chapter 2: An overview on the synthesis methods and procedures of the chalcogenide bulk as well as thin films and different material characterization techniques used in the present work is discussed in this chapter. Conventional melt quenching method has been employed for bulk glass preparation and for thin film preparation, thermal evaporation and spin coating of solution derived samples were used. Different characterization techniques along with their specifications and experimental methods with its theory used for analysis of the samples are also discussed.

Chapter 3: Four different compositions of germanium based selenide glasses $Ge_{20}Se_{80}$, $Ge_{27}Se_{73}$, $Ge_{27}Sb_{9}Se_{64}$ and $Ge_{27}Ga_{9}Se_{64}$ were selected for analysis and their preparation and detailed characterization form the subject matter of this chapter. Compositional dependence of bulk glass properties for the above mentioned compositions have been conducted and variations in the glass transition temperatures (Tg), optical band gap and the glass structure have been observed. Structural characterizations of bulk glasses were done using XRD which confirms their amorphous nature and Raman analysis, which predicts the bulk glass structure. Compositional analysis of all bulk samples were carried out using EDS and the presence and nature of the impurities present in the glass matrices were studied using FTIR. The variations of glass transition temperatures with composition were examined using DSC and the variations of optical bandgap with respect to the composition were predicted using UV-Visible NIR spectroscopy analysis. Detailed discussions on different composition dependent phenomena are presented in the chapter with valid arguments.

Chapter 4: 'Solution processing' of chalcogenide glasses enables novel thin film deposition techniques such as spin coating, dip coating, mold casting, ink jet printing etc. This chapter deals with the 'solution processing' of chalcogenide glasses of different compositions and structural, compositional and optical characterization of the prepared colloids using different techniques. The formation of nanoclusters and the dependence of cluster size with concentration are confirmed by different analysis. Absorption and

bandgap studies were carried out on different concentrations of all compositions which reveal a concentration dependent tunability in the bandgap and the presence of inevitable density of defect states in the forbidden gap of the nanoclusters. Fluorescence and thermal lens characterizations carried out on the nanocolloids show bandgap dependent change in their properties and confirms the predictions from absorption studies. Nonlinear optical studies reveal tunability of nonlinear absorption coefficient (β) and nonlinear refractive index (n_2) with respect to composition and concentration. Photo irradiation experiments were carried out using pulsed and continuous lasers of different wavelengths and variations in its structural and optical properties were studied using different techniques.

Chapter 5: This chapter deals with the preparation and detailed characterization of 'thermal evaporated' thin films of different compositions. 'Spin coated' thin films of $Ge_{27}Sb_9Se_{64}$ glass composition is also fabricated and analysed. As done in the case of bulk glasses, structural characterizations of thin films to examine its amorphous nature and glass structure were carried out. Compositional evaluation conducted on the thin film reveal the compositional variation of film from bulk glass. UV-Visible NIR spectra recorded on thermal evaporated and spin coated thin films predicts different linear optical coefficients. Composition dependent variations in different linear optical parameters were observed.

Chapter 6: In this chapter details of the work done on silver island films of different morphology prepared both by dry process and wet process on silica and chalcogenide glass substrate are described. The dry process includes thermal evaporation technique by Oblique Angle Deposition (OAD) and the wet process implicates the preparation of colloids of silver nanoparticles by wet chemical methods so that island films could be coated by employing different techniques such as spin coating, drop-casting etc. Analysis on the size and morphology of silver nanoparticles were carried out using different techniques. The preparation and characterization of metal films pave the way to the development of more sensitive and efficient IR based sensor.

Chapter 7: This chapter points out the fabrication and characterisation details of self-assembled monolayers (SAM) of anchor molecules on the surface of silver island films on different substrates. The SAM layer act as handle on the film surface to which biological functional molecules can be attached. Hexadecane-thiol (HDT), which is member of thiol group show good affinity to gold or silver and therefore the binding can be done easily. SAM layer has been fabricated on 'Ag island films' of different morphology. The binding of

HDT is confirmed from IR spectra. Enhancement of IR absorption of HDT molecule with the increase in Ag content is observed. Chalcogenide glass substrate is found to be a good host material for surface enhanced IR absorption. Feasibility of microcontact printing on the fabrication of silver patterns and anchor layer altogether is checked.

Chapter 8: The general conclusions drawn from the research work are consolidated in this chapter along with the points of possible future prospects.

Lists of publications

Journal publications

- Indu Sebastian, S. Divya, V. P. N. Nampoori, P. Radhakrishnan, and Sheenu Thomas, "Impact of intermediate localized states on nonlinear optical absorption of Ga-Ge-Se nanocolloidal solutions", Appl. Phys. Lett. 102, 031115 (2013); doi: 10.1063/1.4789436
- Indu Sebastian, S. Mathew, V. P. N. Nampoori, P. Radhakrishnan, and Sheenu Thomas, "Concentration tuned bandgap and corresponding nonlinear refractive index dispersion in Ga-Ge-Se nanocolloids", J. Appl. Phys. 114, 053102 (2013); doi: 10.1063/1.4817176
- Indu Sebastian, V. P. N. Nampoori, P. Radhakrishnan, and Sheenu Thomas, "Experimental verification of localized defect states in Ga-Ge-Se nano colloidal solutions", J. Mater Sci. 49, 3732–3735 (2014); doi 10.1007/s10853-014-8084-8
- Indu Sebastian, S. Divya, V. P. N. Nampoori, P. Radhakrishnan, and Sheenu Thomas, "Investigation of nonlinear opticalproperties of Ga-Ge-Se Nano-colloidal solutions", IEEE Optical Engineering, special edition.
- S. Divya , Indu Sebastian, V. P. N. Nampoori, P. Radhakrishnan, and A. Mujeeb, "Power And Composition Dependent Non Linear Optical Switching of TiO2- SiO2 Nano composites", IEEE Optical Engineering, special edition.
- S. Divya , Indu Sebastian, V. P. N. Nampoori, P. Radhakrishnan, and A. Mujeeb, " Non resonant excitonic effects on the third order nonlinear properties of TiO_2: From amorphous to rutile phase", Optics and Laser Technology 56 (2014) 207-210.
- S. Divya , Indu Sebastian, V. P. N. Nampoori, P. Radhakrishnan, and A. Mujeeb, "Tailoring optical properties of TiO_2 in silica glass for optical limiting applications", Chin. Phys. B (accepted).

Conference publications

- Indu Sebastian, S. Divya, V. P. N. Nampoori, P Radhakrishnan, and Sheenu Thomas, "Nonlinear optical characterization of Ge-Ga-Se glass solution", Poster Presented in "Frontiers in Optics and Photonics" (FOP 2011), IIT Delhi on 03 - 05 December, 2011.
- Indu Sebastian, S. Divya, V. P. N. Nampoori, P Radhakrishnan, and Sheenu Thomas."Optical characterization of solution based chalcogenide glassy films"
  Poster presented in "First International OSA Network of Students (IONS) Conference (IONS-1)" on 1-2 December, 2011
- Indu Sebastian, S. Divya, V. P. N. Nampoori, P Radhakrishnan, and Sheenu Thomas. "Measurement of nonlinear refraction in nanocolloidal solutions of chalcogenide glass" Poster presented in "National Symposium on Recent Advances in Nanoscience, Engineering & Technology (RANET 11)"
- Indu Sebastian, S. Divya, V. P. N. Nampoori, P Radhakrishnan, and Sheenu Thomas, "Investigation of nonlinear optical properties of Ga-Ge-Se Nano-colloidal solutions", International Conference on Optical Engineering (ICOE 2012), Belgaum, Karnataka, India.
- Indu Sebastian, V. P. N. Nampoori, P Radhakrishnan, and Sheenu Thomas, "Defect states assisted photoluminescence in Ga-Ge-Se nano colloidal solutions", Indian Association of Physics Teachers (IAPT) meeting
- Indu Sebastian, V. P. N. Nampoori, P Radhakrishnan, and Sheenu Thomas, "Defect State Annealing and Corresponding Variation in Optical Properties of Chalcogenide Glass Nanoclusters", 7th International Conference on Materials for Advanced Technologies (ICMAT 2013), Suntec, Singapore.

Contents

Chapter 1: Chalcogenide Glasses: Potential Mateials For Photonic Applications

Chapter 2: Material Preparation and Characterization Techniques

Chapter 3: Studies On The Effect Of Composition On The Properties Of Bulk Glass

Chapter 4: Synthesis And Characterization Of Nanocolloids Of Chalcogenide Glass

Chapter 5: Fabrication And Characterization Of Chalcogenide Glass Based Waveguide Structures

Chapter 6: Fabrication And Characterization Of Silver Island Structures

Chapter 7: Binding Of Anchor Molecules: Surface Enhanced Infrared Absorption Studies

List of Figures

List of tables

Chapter 1

Chalcogenide Glasses: Potential Materials For Photonic Applications

This chapter discusses the basic properties of chalcogenide glasses and describes how these properties relate to various applications. A brief literature review on current researches in chalcogenide glasses is also included. A description of infrared based sensor technology and application of chalcogenide glasses in these systems are discussed in this chapter. Finally a short note on germanium selenide glass and compositional selection criteria are specified.

1.1 Motivation

The work reported in the present thesis is focussed on the development and characterization of promising chalcogenide bulk glasses of different compositions and corresponding solvent casted and thermally coated thin films in association with silver island structures with self-assembled monolayers (SAM) of anchor molecules. The ultimate goal of this work is the production of a prototype infrared (IR) sensor with chalcogenide glass (ChGs) as the sensor platform. To achieve this aim, different chalcogenide glass substrates have been prepared and island structures of silver with different morphology are fabricated on the top of chalcogenide glass substrate. Investigations on the IR absorption spectra of anchor molecules attached silver-chalcogenide glass substrate were carried out.

Chalcogenide glasses are promising materials because of their extended optical transmission window starting from the visible to the far infrared range upto 20μm, high refractive index usually between 2 and 3 and high optical nonlinearity[1,2], which make them good candidates as IR sensors and ultrafast nonlinear optical devices. These glasses are favorable sensor materials for the infrared spectral range[3,4] because of its high IR transparency to allow for low optical loss at wavelengths corresponding to the characteristic

optical absorption bands of organic molecules, high refractive index for tight confinement of optical energy within the resonator structure, processibility into thin film form, chemical compatibility for adhesion of silver nanoparticles and thin films and resistance to the chemical environment to be sensed. The bulk chalcogenide glasses can be cut into disks of desired thickness, drawn into optical fibers[5,6] or fabricated as planar waveguides[7,8] in order to fulfill the requirements of sensor platform. Infrared spectroscopy is a powerful tool for detecting and determining the composition of complex organic samples. The mid-infrared range, between 4000 and 400cm^{-1}, is very useful because most of the infrared signatures or 'fingerprints' (fundamental transitions) of biomolecules and organic species are located in this window[9,10]. It is well known that this spectroscopic technique is simple, reliable, fast, non-destructive and cost-effective.

1.2 What are chalcogenide glasses?

The main constituents of chalcogenide glasses belong to 'group 16' in the periodic table which consists of elements sulphur, selenium, tellurium and polonium in association with other elements such as arsenic, germanium, gallium, or antimony. Oxygen is also a chalcogen but it is not included in the definition because oxide glasses form a large group with distinctively different properties to glasses formed from chalcogens. Researches on chalcogenide glasses mainly began after 1955, when Goryunova and Kolomiiets discovered electronic conductivity in vitreous substances obtained from mixtures of arsenic, antimony, and thallium chalcogenides during the synthesis of crystal semiconductors[11]. Chalcogenide glasses are infrared transparent, band gap semiconductors, generally less robust, weakly bonded materials than oxide glasses. They form both heteropolar (e.g., Ge-S) and homopolar (e.g., S-S; Ge-Ge) bonds. Thus glasses with a non-stoichiometric amount of chalcogen are possible and these excess chalcogen atoms can form chains. The chemical bonding of the glass matrix is usually directional and covalent and chalogens act as chain or network terminators.

1.3 Why chalcogenide glasses?

BeF_2-based glasses were one of the few halide glasses[12] widely investigated due to their low linear and nonlinear refractive indices and high Abbé number before the discovery of glasses in the ZrF_4–BaF_2–NaF–NdF_3

systems by Poulain[13] et al. However, these glasses are extremely hygroscopic and highly toxic, rendering them unfeasible for use in commercial systems while, heavy metal halide glasses like ZrF_4-based multicomponent fluoride glasses are neither hygroscopic nor toxic. The fluorozirconate glass with the composition $56ZrF_4–19BaF_2–6LaF_3–4AlF_3–15NaF$ (ZBLAN) is transparent up to 8μm, with chemical stability comparable with a sodium silicate glass. Fluorides typically have limited chemical durability, lower glass stability, and small nonlinear optical coefficients, as compared to other nonoxide materials. Chalcogenide glasses are good candidates for integrated optical devices because of their high optical nonlinearities and low linear and nonlinear loss, wide range of optical and electrical properties, their fabrication and structural flexibility, large capacity for doping, photosensitivity and, most importantly, they exhibit a broad optical transparency window stretching from the visible to the far infrared, which allows the realization of multimodal optical detection in the same material platform- a significant advantage for device processing and integration.

1.4 Fundamental characteristics and properties of chalcogenide glasses

Chalcogenide materials have some unique properties, which allow these amorphous semiconductors to have electrical and optical phenomena that are quite unlike those of crystalline semiconductors and other types of glasses. Unique properties of these glasses help to realize a range of optical functions in these glasses, such as fabrication of waveguides or channels, optical amplification and fluorescence emission at telecommunication wavelengths by rare-earth (e.g., Pr and Er) dopants, gratings (relief and phase) that can spectrally filter or modulate light etc.

Low optical bandgap

One of the major differences between oxide and chalcogenide glasses is their bandgap[14] energy. SiO_2 has optical bandgap around 10eV and for chalcogenide glasses it lies in between 1eV to 3eV. In 1960, Ioffe and Regel[15] recognized that the bandgap depends on the existence of short range order rather than the long range order of the lattice and suggested that the first coordination number (if exists) of the corresponding crystal is preserved in the amorphous structure.

High infrared transparency

Chalcogenide glasses have long wavelength transparency than silica and fluoride glasses which enables them to be utilized for several applications including thermal imaging, IR optical sensing[16], night vision, IR photonics[17,18], CO and CO_2 laser power delivery[19] and remote chemical analysis[20]. Figure 1.1 compares the transmission spectra of different types of glasses (2-3 mm thick) which shows wider optical window for chalcogenide glasses[21]. Sulphide glasses show good transparency in the long wavelength part of the visible spectrum where selenide and telluride glasses are opaque. Sulphide, selenide and telluride are transparent in the near IR and mid-IR region and the maximum transmission wavelengths in the far-IR are close to 12μm for sulphides, 15μm for selenides and 20μm for tellurides.

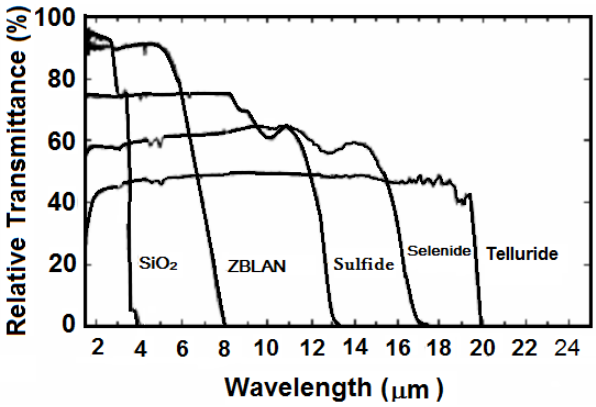

Figure 1.1: *Comparison of transmission spectra for different types of glasses, taken from reference[24].*

Good hosts for rare earth ions

Chalcogenide glasses exhibit low values of 'maximum phonon energy' resulting from the relatively large mass of their constituent atoms, which make them good hosts for rare earths. Although rare-earth solubility is often poor for these glasses, the solubility can be enhanced by adding a significant quantity[22] of 'Ga'. Certain transitions of rare earth dopants, for example, 1.3μm fluorescence from $^1G_4 \rightarrow ^3H_5$ transition of Pr^{3+} has been observed in tellurite[23] and gallium lanthanum sulphide[24] glasses whereas it is absent if silica glasses are the hosts. This is because the higher 'maximum phonon energy' of silica glass increases the probability of non-radiative decay from excited states.

High optical refractive index

Occurrence of high index of refraction is another important characteristic of chalcogenide glasses. Savage[25] has tabulated refractive indices for sulphide, selenide and telluride glasses containing As, Ge, Si and Sb measured at 20°C in the 3-5μm and 8-12μm windows and found that refractive indices are increased when sulphide is replaced by the more polarizable selenide and telluride; for example refractive index of As_2S_3 is 2.39 while that of As_2Se_3 is 2.78. Dispersion curves appear to be flatter than for oxides or fluorides and addition of Ge lowers refractive index[26]. The increase in refractive index with addition of Sn, Te, Pb, and Sb to Ge-As-Se glasses has been reported[27].

Photosensitivity

Photosensitivity is an intrinsic property of the chalcogenide glasses which leads to a variety of interesting photoinduced phenomena such as photocrystallization or amorphization, photopolymerization, photodecomposition, photocontraction or expansion, photovaporization, photodissolution of metals such as Ag into the chalcogenide glasses, and light-induced change in local atomic configuration.[28,29,30]. These changes are accompanied by changes in the optical constants of the material, in particular in the position of the optical band edge, refractive index etc.

Photosensitive effects can be classified in terms of reversibility and whether they are more structural or physico-chemical in origin[29]. Reversible effects occur in well annealed glasses while irreversible effects occur in as-deposited films condensed from the vapour state. Physicochemical effects such as metal photo-dissolution can occur in both annealed and as-deposited films. Photoinduced optical anisotropy is observed in certain chalcogenide glasses[31] when exposed to plane polarized light and can be erased by un-polarized light.

High optical nonlinearity

Chalcogenide glasses are optically high non-linear (χ^3 materials) materials and their nonlinear susceptibility 'χ' values are around two orders of magnitude higher than that of silica. This makes them a promising material for ultra-fast switching in telecommunication systems. Since the nonlinearity of silica is small (nonlinear refractive index,n_2 = 2.8×10^{-16} cm^2/W), either high power levels or long device lengths are required for switching applications. Therefore for a compact and low-threshold non-linear photonic circuit, novel non-linear materials with low losses and ultrafast Kerr nonlinearities, at least several hundred times of values of those of silica, at communication

wavelengths are required. A number of compounds like $Ge_{20}Se_{80}$[32], $Ge_{25}Se_{65}Te_{10}$[33], $Ge_{28}Se_{60}Sb_{12}$[34], As_2Se_3[35] etc. were found to have Kerr nonlinearities hundreds of times larger than that of silica. Many studies[36] reveal that a two-photon absorption (TPA) process is responsible for the optical nonlinearities observed in chalcogenide glasses; while higher order multiphoton absorption process has been suggested for the nonlinearities observed in As_2S_3, GeS_2, and TeO_2 samples glasses[37]. Tanaka[35] studied the spectral dependence of absorption using a tunable source and predicted that two-photon and two-step absorption occurs in As_2S_3, and the two-photon absorption spectrum appeared to vary exponentially with energy. Table 1.1 compares linear and nonlinear optical properties of some glasses available in literature[38].

Glass	Eg (eV)	n_0	α_0 cm^{-1}	n_2 ($x10^{-16}$ cm^2/W)
SiO_2	10	1.5	10^{-6}	2
BK-7	4	1.5		3
SF-59	3.8	2.0		30
As_2S_3	2.4	2.5	10^{-3}	200
BeF_2	10	1.3		0.8

Table 1.1: *Linear and nonlinear optical properties of some glasses; Eg is optical bandgap, n_0 is the refractive index, α_0 is the attenuation coefficient, n_2 is the nonlinear refractive index. The values are evaluated at optical communication wavelengths of 1–1.5μm and taken from reference[38]. BK-7 is borosilicate glass and SF-59 represents lead-silicate glasses with ~57 mol.% PbO.*

Compositional tunability

Another important property of chalcogenide glass is that it shows a wide 'compositional tunability' which allows the properties of chalcogenide glasses to be engineered and optimized for different applications just by changing the composition. The most commonly used glass forming units contained within the chalcogenide systems[39,40,41,42,43] are GeS_2/$GeSe_2$/$GeSe_4$ and As_2S_3/As_2Se_3 with other elements acting as intermediates like Ga, Sb, Te etc. or modifiers I, CsI, CsBr etc. An intermediate is a substance which will not form a glass on its own but will act as a glass former when combined with other materials, while a modifier is used to alter the network structure and to prevent devitrification.

Low glass transition temperature

Like all glasses, chalcogenide glasses exhibit a glass transition. Low strength and highly covalent bonding lead to comparatively low glass transition temperature (Tg) and hardness values, allowing for easy polishing and processing into thin films or fiber form. Different cooling rates, during the formation and subsequent thermal processing steps of fibers and thin films induce variation in the physical and optical properties as compared to those of the parent bulk glass[44]. Annealing, or heating of the glass to a temperature near Tg, usually helps to remove excess stress and allows many film properties to approach bulk values through structural relaxation.

1.5 Current research in chalcogenide glasses

Research is being carried out to explore the unique properties of chalcogenide glass for the realization of different optoelectronic devices. The primary optoelectronic researches on these materials are concerned with their photo-structural phase transition, photosensitivity, high optical nonlinearity and infrared transparency.

Optical recording in ChGs is well known and forms the basis of current rewritable optical disk technologies like CD/DVD–RW discs[45,46] and Numonyx memory chips. The most commonly used compositions are Ag-In-Sb-Te and Ge-Sb-Se-Te systems, that operate through laser heating and thermally-induced phase changes. Heating the glass above its glass transition temperature by applying lower pulse energies are capable of inducing rapid crystallization, while application of high pulse energies heat the film above its melting point and lead to revitrification[47]. The change in reflectivity from the crystalline and amorphous phases is used to differentiate between the '1' and '0' values needed for memory. Exploring changes in resistivity induced by crystallization, non-volatile memory systems which can be both read and written electronically are also under development[48], and Intel has reported that their next-generation memory will be based on this technology.

Various studies are conducted to explore photosensivity of chalcogenide glasses and create photo structural transformation and refractive index changes. This allow direct writing of optical waveguides into thin films[49]; production of Bragg gratings in fabricated waveguides[50]; for the production of high-Q cavities in photonic crystal membranes[51]; to tune the emission wavelengths of quantum cascade lasers[52]; and for post tuning a GaAs photonic crystal cavity to match the emission of embedded quantum dots[53]. 3-D

woodpile structures have been fabricated by laser direct writing as illustrated[54] in Figure 1.2.

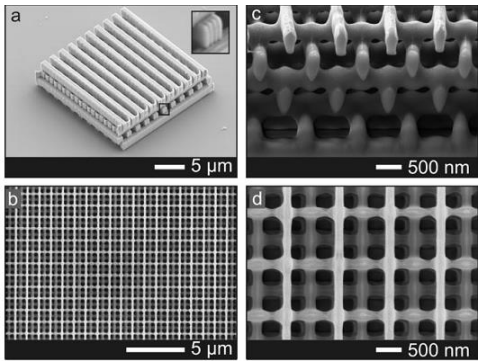

Figure 1.2: *a) Scanning electron microscopy images of As_2S_3 woodpiles fabricated by direct laser writing taken from reference[54]. b) Top view of a woodpile structure shows perfectly straight rods. c) Focused-ion-beam cross section of the woodpile in (b). d) Close up of (b).*

Nonlinear optical phenomena observed in chalcogenide glasses are the basis for fiber devices[55], such as Raman[56] amplifiers and lasers, multiplexers/demultiplexers, all-optical switches, and broadband light sources. Although the kind of nonlinearity involved with different applications are different, they all benefit from a high nonlinear refractive index, 'n_2', a small effective core area, and a large effective length[57].

1.6 Chalcogenide glasses for sensing

Among optical sensing schemes, mid-IR sensors are gaining attention because of their inherent molecular selectivity and identification of specific chemical compounds, which will allow qualitative and quantitative analysis of various chemical and biological species. As discussed above mid-IR transparent optical waveguides and fiber-optic systems offer access to fundamental vibrational fingerprint absorptions of organic molecules. The fabrication of mid-IR waveguides has helped to convert bench-top-style optical instrument such as the FT-IR spectrometer into portable, compact biological and biomedical optical sensors with higher sensitivity. Various studies[58,59,60] reveals that mid-IR approach could be used for biosensing as well as a molecular fingerprinting and thus form the basis for a comprehensive label-free detection system. As can be seen in the figure 1.3, each species has its own distinct absorption signature in infrared spectral region.

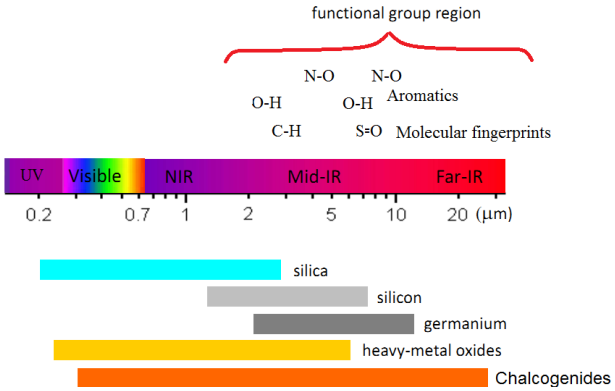

Figure 1.3: *The vibrational fingerprint of different functional groups and chemical species in IR region and the transmission window of different glass substrates.*

As was previously discussed, chalcogenide glasses are transparent in mid IR region while oxide and other glass substrates are not transparent at wavelengths higher than about 4 and 8μm respectively which make them unsuitable materials for sensing organic molecules. The ability to produce ChGs waveguides in fiber and thin film form also makes them attractive for sensing applications[61] and this gives them the flexibility to be used in different kinds of sensors. Sensors using ChG fibers have the potential to be used as a "fiber optic dipstick probe" to check the quality of engine oil or for other purposes such as detecting soil contaminants[62] or for recording the fingerprints of biomolecules in the mid infrared (MIR) range by utilizing the concept of evanescent wave spectroscopy[63].

Planar waveguide based sensors are smaller and can be integrated into 'lab-on-a-chip' type devices. All-integrated microphotonic technology leads to the miniaturization of a device such that the entire system can confine to a small chip. The basic components and principle of a 'lab-on-a-chip' sensor is demonstrated by Richardson et. al [64] which consists of an 'on chip' integrated light source, planar waveguides and resonator based on chalcogenide glasses.

1.7 Chalcogenide planar waveguides: fabrication and properties

Chalcogenide glass planar wave guides can be fabricated by cutting and polishing thin bulk glass plates or by depositing thin films by a number of techniques, including: thermal evaporation[65] (TE), chemical vapor deposition[66] (CVD), pulsed laser deposition[67] (PLD), sputtering[68], and solution based

processing[69]. In the present work, different chalcogenide glass waveguides; polished bulk glass plates, thermally as well as spin coated thin films are fabricated and characterized. Thermal evaporation technique involves heating the powdered bulk glass in an evacuated chamber until it vaporizes and then condenses on a cool substrate to form a film. For solution-based processing, glass powder is dissolved in an organic solvent and then the solution is either dip-coated or drop-casted or spun into a film onto a substrate, and then heat treated to drive off the solvent. Solution-based processing is cost effective and it is also more environmentally friendly since the harmful constituents of the glass do not need to be volatilized. In thermal evaporation method, different components volatilize at different temperatures, while in the solution-based processing the components are not volatilized and hence the composition should be easier to control. A major disadvantage of solution processed films is that it is difficult to remove all of the solvent from the film. The solvents typically have absorption in the infrared regime and hence can be a major source of loss in the film.

1.8 Objectives and methodology of present research work

This work aims at the production of a prototype infrared (IR) sensor with chalcogenide glass (ChGs) as the sensor platform. For the realization of that, different compositions of chalcogenide glass have been prepared and characterized. A schematic[70] of prototype mid-IR-based biosensor is shown in figure 1.4.

In the proposed design, an IR transparent thin film waveguide of high refractive index is coated over a cladding layer of low refractive index. The upper core layer has good IR transparency allowing strong evanescent wave absorption while target binding and produce 'absorption dips' in the detector. Silicon or silica micro-slide will act as supporting substrate.
The different stages for the realization of infrared (IR) sensor are

1. Fabrication of an IR transparent, non-reactive and chemically inert planar chalcogenide glass waveguide with high refractive index.
2. A suitable cladding layer with low refractive index than that of the core layer constructed under the signal collecting core waveguide.
3. The bio-functionalization, that means to attach and immobilize the antibodies on the chemically inert core chalcogenide glass waveguide surface, is a critical step. For that a thin layer of metal island film

(gold/silver) can be deposited on top of the core layer as shown in figure 1.4.

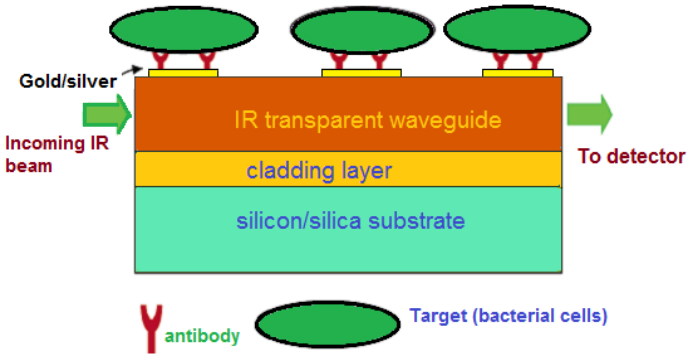

Figure 1.4: *Schematic of an IR sensor using the functionalized chalcogenide glass film.*

4. Fabrication of self-assembled monolayers (SAM) of anchor molecules on the metal island films to which biological functional molecules can be attached. Anchor molecules must firmly attach to the film and should not wash off easily. Anchor layer form a handle for biological functional molecules as shown in figure 1.5.

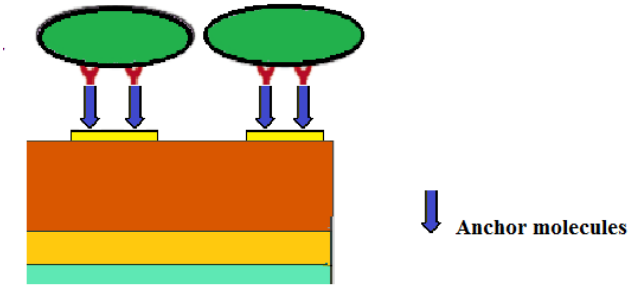

Figure 1.5: *Schematic of self-assembled monolayer of anchor molecules holding antibodies on metal island film.*

5. Binding of biological functional molecules like DNA, antibody, etc. on the top of anchor layer. Anchor molecule should be modified or should have functional groups that can react with biological functional molecules (DNA, antibody, etc.). 'Mercapto-compounds' have 'thiol' group (-SH), which readily bond with gold/silver and form SAM on the film to which proteins, DNA/RNA can be easily attached.

1.9 Surface Enhanced Infrared Absorption

Research in the micro-optical sensor mainly focus on the detection of molecules at low concentrations down to ppm or ppb level. Using metallic nanoparticles of various morphologies, thickness or inter-particle coupling, infrared absorption of organic compounds can be strongly enhanced and it is one of the promising solutions to enhance the sensitivity[71,72,73,74]. This phenomenon was first observed by Hartstein et al[75] and it is called surface enhanced infrared absorption (SEIRA). Surface plasmons of metallic nanoparticles can be excited by the electric field of appropriate light; they can consequently produce a stronger local electric field interacting with molecules by increasing their infrared absorption[76]. This phenomenon takes place for molecules very close to metallic nanoparticles or adsorbed onto them, which means- in nanometre scale[77] and decays sharply within about 5nm from the surface. Therefore deposition of thin layers of gold/silver island films on top of the chalcogenide film not only benefit for bio-functionalization of the core layer but also help to enhance the sensitivity by SEIRA

This work mainly focus on

1. The preparation of promising chalcogenide bulk glasses of different compositions and a detailed analysis of compositional dependence of bulk glass properties via structural, optical and thermal characterization.
2. A detailed study of solution processing such that the preparation of chalcogenide glass nanoclusters of different compositions based on novel solution-based approach and evaluation of structural and optical characteristics of these nanoclusters using different techniques.
3. Fabrication and characterization of chalcogenide glass thin film waveguides of various compositions via thermal evaporation as well as solvent casting technique.
4. Preparation of silver island films of different morphology by thermal evaporation as well as drop casting of silver colloids on the chalcogenide waveguide structures and their characterization.
5. Fabrication of self-assembled monolayers (SAM) of anchor molecules on silver island films and the study of the effect of silver islands on their IR spectra.

Binding of biological functional molecules on the top of anchor layer is not considered in this thesis.

1.10 Why germanium based selenide glasses?

Germanium based selenide glasses are selected for IR based sensor technology. Infrared transparency of chalcogenide glasses depicted in figure 1.1 varies as sulphide>selenide>telluride glasses. Sulphide glasses show very good transparency (near 80%) from long wavelength side of visible spectra to mid IR region while it is opaque at above 12μm where selenide glasses are transparent. The preparation of selenide glasses is easier than sulphide glasses because of the low vapour pressure at the melting temperature and it is a better glass former than that of 'S'. For example the range of glass formation in As-Se system is 0-70 at.% of 'As', which is much wider than As-S system[78]. Also selenium possesses high atomic mass and electronic polarizability which makes them to have low phonon energies, high refractive indices, and excellent nonlinear optical properties.

Most of the chalcogenide glass compositions are toxic due to the presence of elements such as arsenic and they exhibit very low thermal and mechanical robustness[79]. This makes them unsuitable for many fields like medical applications that they might otherwise be used in. Many of these glasses, especially in the As-S, As-Se, and As-S-Se systems, have a low[80] glass transition temperature (Tg) near 200°C. This limits their use in modest temperature applications. While Ge-based glasses are more rigid and have higher glass transition (Tg) and melting (Tm) temperatures than As-based glasses.

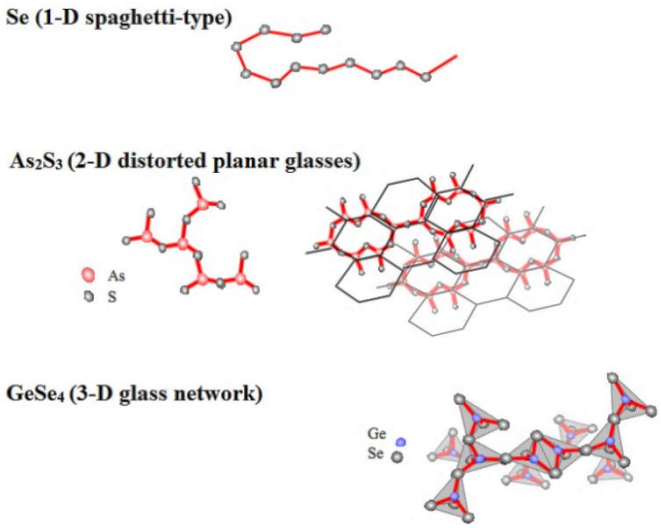

Figure 1.6: *The network structure of 'chain like Se', '2-D layer like As_2S_3', and '3-D connected $GeSe_4$' glass.*

Germanium is a four-coordinated network former, so that germanium contained glass structure becomes stronger because of its three-dimensional (3-D) connected network. In the case of 'As' whose co-ordination number is '3', it leads to a predominantly two-dimensional (2-D) layer-like network[81]. The network structure of 'Se', 'As_2S_3', and '$GeSe_4$' glass are shown in figure 1.6. Therefore replacement of 'arsenic' with 'germanium', not only remove poisonous 'As', but also increase the glass transition temperature, enhance thermal stability, tailor refractive index and to yield more stable and highly processable, thermally evaporated thin films.

1.10.1 Compositional selection criteria

The structure of chalcogenide glasses can be defined as a 'continuous random network' (CRN)[82] of covalently bonded one or more chalcogen elements, with network formers such as arsenic (As), germanium (Ge), gallium (Ga), antimony (Sb), etc. Chalcogenide glasses are a combination[83] of 'rigid' and 'floppy' regions in which 'floppy' material can be deformed easily while a 'rigid' material is not. According to M.F Thorpe[83], a glass with low average coordination number, '$\bar{r}$ ' contained a 'floppy' network with small 'rigid' regions. The size of these 'rigid' regions grows as $\bar{r}$ increases, and when $\bar{r}$ 'reaches the value 2.4, it is called 'amorphous solid' which have rigid network with small floppy regions. The four compositions that will be discussed in this thesis, $Ge_{20}Se_{80}$, $Ge_{27}Se_{73}$, $Ge_{27}Sb_9Se_{64}$, and $Ge_{27}Ga_9Se_{64}$ have $\bar{r}$ values of ≤ 2.4 which means that all of the compositions are 'amorphous solids'. The $\bar{r}$ values help to predict the variation of glass transition temperature such that 'Tg' increases for rigid glasses.

In the four different compositions investigated in this thesis $Ge_{20}Se_{80}$, $Ge_{27}Se_{73}$, $Ge_{27}Sb_9Se_{64}$, and $Ge_{27}Ga_9Se_{64}$, the first two glasses are germanium selenide glasses of different compositions and in the compositions of the last two glasses, '9' atomic percentage of Se in $Ge_{27}Se_{73}$ glass is replaced by corresponding amount of intermediates 'Sb' and 'Ga' respectively.Germanium selenide glasses represent the archetypal, binary glass composition from which many other glasses are derived, and their structural features have been studied extensively over the last two decades using a wide range of spectroscopic and diffraction techniques[84,85,86,87]. Germanium selenide glass compositions with less than 33% of germanium have the best glass forming properties.

Ge-Sb-Se and Ge-Ga-Se chalcogenide glass systems have very wide glass forming regions. Figure 1.7 (a) and (b) shows the Ternary diagrams of Ge-Sb-Se[88] and Ga-Ge-Se[89] glass systems.

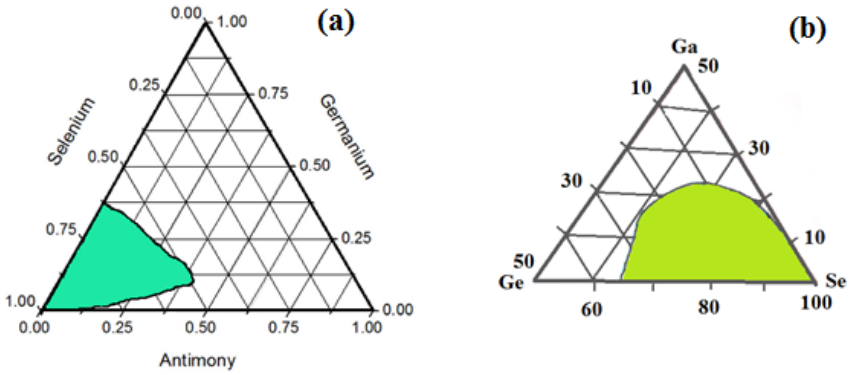

Figure 1.7: *Ternary diagram[88] of Ge-Sb-Se and (b) Ternary diagram[89] of Ga-Ge-Se glass systems.*

Ge-Sb-Se system possesses excellent thermal stability and chemical durability for fiber drawing and has low transmission loss and high transparency to infrared radiations from 2-16μm[90]. Structural and physical properties of Ge-Sb-Se glass systems are well studied[91,92,93] Ge-As-Se glass systems are well known for the fabrication of integrated optical waveguide devices[94,95,96] and compared with that, the replacement of highly toxic element As with Sb makes the glass more environmentally-compatible, and therefore searching Ge-Sb-Se glasses with stable structure and excellent optical properties is important for the application in photonics.

Glasses in the Ge-Ga-Se system are of considerable interest, because rare-earth ions of up to 1-2at% of rare earth can be introduced into their structure in appreciable concentrations, thus providing a means for creating active optical media. Photoluminescence studies on rare earth doped Ge-Ga-Se system are attaining great interest[97]. Introduction of 'Ga' into the germanium selenide glass system will vary the optical[98] and thermal[99] characteristics like optical bandgap, refractive index, glass transition temperature etc. The opportunity for the incorporation of IR emitting rare-earth ions opens the possibility of on-chip integrated light source and that will further miniaturize the size of the photonic device to all integrated photonic chip.

1.11 References

[1]Guignard Marie, Virginie Nazabal, Frédéric Smektala, J-L. Adam, Odile Bohnke, Claire Duverger, Alain Moréac et al. "Chalcogenide glasses based on germanium disulfide for second harmonic generation." *Advanced Functional Materials* 17, no. 16 (2007): 3284-3294.

[2]Monat Christelle, Marcel Spurny, Christian Grillet, Liam O'Faolain, Thomas F. Krauss, Benjamin J. Eggleton, Douglas Bulla, Steve Madden, and Barry Luther-Davies. "Third-harmonic generation in slow-light chalcogenide glass photonic crystal waveguides." *Optics letters* 36, no. 15 (2011): 2818-2820.

[3]Schmidt Markus A., Dang Yuan Lei, Lothar Wondraczek, Virginie Nazabal, and Stefan A. Maier. "Hybrid nanoparticle-microcavity-based plasmonic nanosensors with improved detection resolution and extended remote-sensing ability." *Nature communications* 3 (2012): 1108.

[4]Eggleton Benjamin J., Barry Luther-Davies, and Kathleen Richardson. "Chalcogenide photonics." *Nature photonics* 5, no. 3 (2011): 141-148.

[5]F. Charpentier, V. Nazabal, J. Troles, Q. Coulombier, L. Brilland, C. Boussard-Pledel, P. Nemec, H. Lhermite, J. Charrier F. Smektala, M. Frumar, K. Le Pierres, N. Thybaud, and B. Bureau, "Infrared optical sensor for CO_2 detection," In *SPIE Europe Optics+ Optoelectronics*, pp. 735610-735610. International Society for Optics and Photonics, 2009.

[6]Anne Marie-Laure, Julie Keirsse, Virginie Nazabal, Koji Hyodo, Satoru Inoue, Catherine Boussard-Pledel, Hervé Lhermite et al. "Chalcogenide glass optical waveguides for infrared biosensing." *Sensors* 9, no. 9 (2009): 7398-7411.

[7]Charrier Joël, Marie-Laure Brandily, Hervé Lhermite, Karine Michel, Bruno Bureau, Fréderic Verger, and Virginie Nazabal. "Evanescent wave optical micro-sensor based on chalcogenide glass." *Sensors and Actuators B: Chemical* 173 (2012): 468-476.

[8]J. J. Hu, V. Tarasov, A. Agarwal, L. Kimerling, N. Carlie, L. Petit, and K. Richardson, "Fabrication and testing of planar chalcogenide waveguide integrated microfluidic sensor," *Optics Express* 15, no. 5 (2007): 2307-2314.

[9]Brehm Markus, Thomas Taubner, Rainer Hillenbrand, and Fritz Keilmann. "Infrared spectroscopic mapping of single nanoparticles and viruses at nanoscale resolution." *Nano letters* 6, no. 7 (2006): 1307-1310.

[10]Grasso Elizabeth M., Ahmed E. Yousef, Silvia de Lamo Castellvi, and Luis E. Rodriguez-Saona. "Rapid detection and differentiation of Alicyclobacillus species in fruit juice using hydrophobic grid membranes and attenuated total reflectance infrared microspectroscopy." *Journal of agricultural and food chemistry* 57, no. 22 (2009): 10670-10674.

[11]Goryunova N. A., and B. T. Kolomiets. "New vitreous semiconductors." *Zhurn Techn Fiz* 25 (1955): 984-1015.

[12]Baldwin, C. M., R. M. Almeida, and John D. Mackenzie. "Halide glasses." *Journal of Non-Crystalline Solids* 43, no. 3 (1981): 309-344.

[13]Lucas Jacques, Maydom Chanthanasinh, Marcel Poulain, Michel Poulain, Pierre Brun, and Marvin J. Weber. "Preparation and optical properties of neodymium fluorozirconate glasses." *Journal of Non-Crystalline Solids* 27, no. 2 (1978): 273-283.

[14]Elliott Stephen R. "Chalcogenide glasses." *Materials science and technology* 9 (1991): 375.

[15]Ioffe A. F., and A. R. Regel. "Non-crystalline, amorphous and liquid electronic semiconductors." *Prog. Semicond* 4 (1960): 237-291.

[16]Hocdé Sandrine, Catherine Boussard-Plédel, Gilles Fonteneau, and Jacques Lucas. "Chalcogens based glasses for IR fiber chemical sensors." *Solid state sciences* 3, no. 3 (2001): 279-284.

[17]Aliev A. E., A. A. Zakhidov, R. H. Baughman, and E. Yablonovitch. "Chalcogenide inverted opal photonic crystal as infrared pigments."*International Journal of Nanoscience* 5, no. 01 (2006): 157-172.

[18]Kondakci H. Esat, Mecit Yaman, Ozlem Koylu, Aykutlu Dana, and Mehmet Bayindir. "All-chalcogenide glass omnidirectional photonic band gap variable infrared filters." *Applied Physics Letters* 94, no. 11 (2009): 111110.

[19]Arai Tsunenori, and Makoto Kikuchi. "Carbon monoxide laser power delivery with an As 2 S 3 infrared glass fiber." *Applied optics* 23, no. 17 (1984): 3017-3019.

[20]Adam, Jean-Luc. "Non-oxide glasses and their applications in optics." *Journal of non-crystalline solids* 287, no. 1 (2001): 401-404.

[21]Sanghera Jas S., L. Brandon Shaw, and Ishwar D. Aggarwal. "Applications of chalcogenide glass optical fibers." *Comptes Rendus Chimie* 5, no. 12 (2002): 873-883.

[22]Kasap S. O., K. Koughia, M. Munzar, D. Tonchev, D. Saitou, and T. Aoki. "Recent photoluminescence research on chalcogenide glasses for photonics applications." *Journal of non-crystalline solids* 353, no. 13 (2007): 1364-1371.

[23]Wang J. S., E. M. Vogel, E. Snitzer, J. L. Jackel, V. L. Da Silva, and Y. Silberberg."1.3μm emission of neodymium and praseodymium in tellurite-based glasses." *Journal of non-crystalline solids* 178 (1994): 109-113.

[24]Kasap S. O., K. Koughia, M. Munzar, D. Tonchev, D. Saitou, and T. Aoki. "Recent photoluminescence research on chalcogenide glasses for photonics applications." *Journal of non-crystalline solids* 353, no. 13 (2007): 1364-1371.

[25]Savage J. A. "Infrared optical materials and their antireflection coatings."*Bristol: Hilger, 1985* 1 (1985).

[26]Seddon A. B. "Chalcogenide glasses: a review of their preparation, properties and applications." *Journal of Non-Crystalline Solids* 184 (1995): 44-50.

[27]L.G. Aio, A.M. Efimov and V.F. Kokorina, "Refractive index of chalcogenide glasses over a wide range of compositions." *Journal of Non-Crystalline Solids*27, no. 3 (1978): 299-307.

[28]A.E. Owen, A.P. Firth, P.J.S. Ewen, Philos. Mag. B 52 (1985) 347.

[29]Ewen P. J. S., A. E. Owen, M. Cable, and J. M. Parker. "High Performance Glasses." *Blackie, London* (1992): 287.

[30]Zakery A., and S. R. Elliott. "Optical properties and applications of chalcogenide glasses: a review." *Journal of Non-Crystalline Solids* 330, no. 1 (2003): 1-12.

[31]Fairman Robert, and Boris Ushkov, eds. *Semiconducting Chalcogenide Glass I: Glass Formation, Structure, and Simulated Transformations in Chalcogenide Glasses*. Vol. 78. Academic Press, 2004.

[32]Smektala F., C. Quemard, L. Leneindre, J. Lucas, A. Barthelemy, and C. De Angelis. "Chalcogenide glasses with large non-linear refractive indices." *Journal of non-crystalline solids* 239, no. 1 (1998): 139-142.

[33]Lenz G., J. Zimmermann, T. Katsufuji, M. E. Lines, H. Y. Hwang, S. Spälter, R. E. Slusher, S-W. Cheong, J. S. Sanghera, and IDon Aggarwal. "Large Kerr effect in bulk Se-based chalcogenide glasses." *Optics Letters* 25, no. 4 (2000): 254-256.

[34]Harbold J. M., F. Ö. Ilday, F. W. Wise, J. S. Sanghera, V. Q. Nguyen, L. B. Shaw, and I. D. Aggarwal. "Highly nonlinear As-S-Se glasses for all-optical switching." *Optics Letters* 27, no. 2 (2002): 119-121.

[35]Tanaka Keiji. "Two-photon absorption spectroscopy of As_2S_3 glass." *Applied physics letters* 80, no. 2 (2002): 177-179.

[36]Troles J., F. Smektala, G. Boudebs, A. Monteil, B. Bureau, and J. Lucas. "Chalcogenide glasses as solid state optical limiters at 1.064μm." *Optical materials* 25, no. 2 (2004): 231-237.

[37]K.S. Bindra, H.T. Bookey, A.K. Kar, B.S. Wherrett, "Nonlinear optical properties of chalcogenide glasses: Observation of multiphoton absorption." *Applied Physics Letters* 79, no. 13 (2001): 1939-1941.

[38]Tanaka Keiji. "Optical nonlinearity in photonic glasses." *Journal of Materials Science: Materials in Electronics* 16, no. 10 (2005): 633-643.

[39]Vigreux-Bercovici C., L. Labadie, J. E. Broquin, P. Kern, and A. Pradel. "Selenide and telluride thick films for mid and thermal infrared applications." *J. Optoelectron. Adv. Mater* 7 (2005): 2625-2634.

[40]Pamukchieva V., A. Szekeres, K. Todorova, M. Fabian, E. Svab, Zs Revay, and L. Szentmiklosi. "Evaluation of basic physical parameters of quaternary Ge-Sb-(S, Te) chalcogenide glasses." *Journal of Non-Crystalline Solids* 355, no. 50 (2009): 2485-2490.

[41]Tanaka K., T. Gotoh, N. Yoshida, and S. Nonomura. "Photothermal deflection spectroscopy of chalcogenide glasses." *Journal of applied physics* 91, no. 1 (2002): 125-128.

[42]Lezal D., J. Pedlikova, and J. Zavadil. "Chalcogenide glasses for optical and photonics applications." *J. Optoelectron. Adv. Mater* 6, no. 1 (2004): 133-137.

[43]Heo Jong. "Emission and local structure of rare-earth ions in chalcogenide glasses." *Journal of non-crystalline solids* 353, no. 13 (2007): 1358-1363.

[44]Nathan A. Carlie, PhD thesis, "A solution-based approach to the fabrication of novel chalcogenide glass materials and structures".

[45]Kolobov A. V., and J. Tominaga. "Chalcogenide glasses in optical recording: recent progress." *J.Optoelectron. Adv. Mater* 4 (2002): 679-686.

[46]Mikla V. I., I. P. Mikhalko, and V. V. Mikla. "Laser-induced amorphous-to-crystalline phase transition in Sb_xSe_{1-x} alloys." *Materials Science and Engineering: B* 83, no. 1 (2001): 74-78.

[47]S.R. Ovshinsky and W. Czubatyj,"New developments in optical phase-change memory" Proc. SPIE, 4085 15-22 (2001).

[48]Nakayama Kazuya, Kazuhiko Kojima, Yutaka Imai, Toshihiko Kasai, Sanae Fukushima, Akio Kitagawa, Minoru Kumeda, Yoshio Kakimoto, and Masakuni Suzuki. "Nonvolatile memory based on phase change in Se–Sb–Te glass."*Japanese journal of applied physics* 42, no. 2R (2003): 404.

[49]Viens Jean-Francois, Chiara Meneghini, Alain Villeneuve, Tigran V. Galstian, Emile J. Knystautas, M. A. Duguay, K. A. Richardson, and T. Cardinal.

"Fabrication and characterization of integrated optical waveguides in sulfide chalcogenide glasses." *Journal of Lightwave Technology* 17, no. 7 (1999): 1184.

[50]Saliminia Ali, Alain Villeneuve, Tigran V. Galstyan, Sophie LaRochelle, and Kathleen Richardson. "First-and second-order Bragg gratings in single-mode planar waveguides of chalcogenide glasses." *Lightwave Technology, Journal of* 17, no. 5 (1999): 837-842.

[51]Lee Michael W., Christian Grillet, Snjezana Tomljenovic-Hanic, Eric C. Mägi, David J. Moss, Benjamin J. Eggleton, Xin Gai et al. "Photowritten high-Q cavities in two-dimensional chalcogenide glass photonic crystals." *Optics letters* 34, no. 23 (2009): 3671-3673.

[52]Song Shanshan, Scott S. Howard, Zhijun Liu, Afusat O. Dirisu, Claire F. Gmachl, and Craig B. Arnold. "Mode tuning of quantum cascade lasers through optical processing of chalcogenide glass claddings." *Applied physics letters* 89, no. 4 (2006): 041115.

[53]Faraon Andrei, Dirk Englund, Douglas Bulla, Barry Luther-Davies, Benjamin J. Eggleton, Nick Stoltz, Pierre Petroff, and Jelena Vučković. "Local tuning of photonic crystal cavities using chalcogenide glasses." *Applied Physics Letters*92, no. 4 (2008): 043123.

[54]Wong Sean, Markus Deubel, Fabian Pérez-Willard, Sajeev John, Geoffrey A. Ozin, Martin Wegener, and Georg von Freymann. "Direct Laser Writing of Three-Dimensional Photonic Crystals with a Complete Photonic Bandgap in Chalcogenide Glasses." *Advanced materials* 18, no. 3 (2006): 265-269.

[55]Nishii J., S. Morimoto, I. Inagawa, R. Iizuka, T. Yamashita, and T. Yamagishi. "Recent advances and trends in chalcogenide glass fiber technology: a review."*Journal of non-crystalline solids* 140 (1992): 199-208.

[56]Stegeman Robert, George Stegeman, Peter Delfyett, Laeticia Petit, Nathan Carlie, Kathleen Richardson, and Michel Couzi. "Raman gain measurements and photo-induced transmission effects of germanium-and arsenic-based chalcogenide glasses." *Optics express* 14, no. 24 (2006): 11702-11708.

[57]Richardson Kathleen, Denise Krol, and Kazuyuki Hirao. "Glasses for photonic applications." *International journal of applied glass science* 1, no. 1 (2010): 74-86.

[58]Bruch Reinhard F., Natalia I. Afanasyeva, Sydney Sukuta, Angelique L. Brooks, Volodymyr Makhine, and Sergei F. Kolyakov. "Various new applications of fiber optic infrared Fourier transform spectroscopy for dermatology." In *BiOS Europe'98*, pp. 42-51. International Society for Optics and Photonics, 1999.

[59]Afanasyeva Natalia I., Sergei F. Kolyakov, Vjacheslav G. Artioushenko, Victor V. Sokolov, and George A. Frank. "Minimally invasive and ex-vivo diagnostics of

breast cancer tissues by fiber optic evanescent-wave Fourier transform IR (FEW-FTIR) spectroscopy." In *BiOS'98 International Biomedical Optics Symposium*, pp. 140-147. International Society for Optics and Photonics, 1998.

[60]Yu Chenxu, and Joseph Irudayaraj. "Spectroscopic characterization of microorganisms by Fourier transform infrared microspectroscopy." *Biopolymers*77, no. 6 (2005): 368-377.

[61]Eggleton Benjamin J., Barry Luther-Davies, and Kathleen Richardson. "Chalcogenide photonics." *Nature photonics* 5, no. 3 (2011): 141-148.

[62]Sanghera Jas S., L. Brandon Shaw, and Ishwar D. Aggarwal. "Applications of chalcogenide glass optical fibers." *Comptes Rendus Chimie* 5, no. 12 (2002): 873-883.

[63]Keirsse Julie, Catherine Boussard-Plédel, Olivier Loreal, Olivier Sire, Bruno Bureau, Bruno Turlin, Patricia Leroyer, and Jacques Lucas. "Chalcogenide glass fibers used as biosensors." *Journal of non-crystalline solids* 326 (2003): 430-433.

[64]Richardson Kathleen, Laeticia Petit, Nathan Carlie, Bodgan Zdyrko, Igor Luzinov, Juejun Hu, Anu Agarwal, Lionel Kimerling, Troy Anderson, and Martin Richardson. "Progress on the fabrication of on-chip, integrated chalcogenide glass (ChG)-based sensors." *Journal of Nonlinear Optical Physics & Materials*19, no. 01 (2010): 75-99.

[65]Marquez E., A. M. Bernal-Oliva, J. M. Gonzalez-Leal, R. Prieto-Alcon, and T. Wagner. "Optical properties and structure of amorphous $(As_{0.33}S_{0.67})_{100-x}Te_x$ and $Ge_xSb_{40-x}S_{60}$ chalcogenide semiconducting alloy films deposited by vacuum thermal evaporation." *Journal of Physics D: Applied Physics* 39, no. 9 (2006): 1793.

[66]Huang C. C., C. C. Wu, K. Knight, and D. W. Hewak. "Optical properties of CVD grown amorphous Ge-Sb-S thin films." *Journal of Non-Crystalline Solids*356, no. 4 (2010): 281-285.

[67]Musgraves J. D., N. Carlie, J. Hu, L. Petit, A. Agarwal, L. C. Kimerling, and K. A. Richardson. "Comparison of the optical, thermal and structural properties of Ge-Sb-S thin films deposited using thermal evaporation and pulsed laser deposition techniques." *Acta Materialia* 59, no. 12 (2011): 5032-5039.

[68]Wasa Kiyotaka, Makoto Kitabatake, and Hideaki Adachi. *Thin film materials technology: sputtering of control compound materials*. Springer Science & Business Media, 2004.

[69]Chern Geeng-Chuan, and I. Lauks. "Spin-coated amorphous chalcogenide films." *Journal of Applied Physics* 53, no. 10 (1982): 6979-6982.

[70]Yu Chenxu, Ashtosh Ganjoo, H. Jain, C. G. Pantano, and Joseph Irudayaraj. "Mid-IR biosensor: detection and fingerprinting of pathogens on gold island functionalized chalcogenide films." *Analytical chemistry* 78, no. 8 (2006): 2500-2506.

[71]Osawa Masatoshi, and Masahiko Ikeda. "Surface-enhanced infrared absorption of p-nitrobenzoic acid deposited on silver island films: contributions of electromagnetic and chemical mechanisms." *The Journal of Physical Chemistry* 95, no. 24 (1991): 9914-9919.

[72]Delgado José Manuel, José Manuel Orts, and Antonio Rodes. "A comparison between chemical and sputtering methods for preparing thin-film silver electrodes for in situ ATR-SEIRAS studies." *Electrochimica acta* 52, no. 14 (2007): 4605-4613.

[73]Pucci A., F. Neubrech, D. Weber, S. Hong, T. Toury, and M. Lamy De La Chapelle. "Surface enhanced infrared spectroscopy using gold nanoantennas."*physica status solidi (b)* 247, no. 8 (2010): 2071-2074.

[74]Neubrech Frank, Annemarie Pucci, Thomas Walter Cornelius, Shafqat Karim, Aitzol García-Etxarri, and Javier Aizpurua. "Resonant plasmonic and vibrational coupling in a tailored nanoantenna for infrared detection." *Physical review letters* 101, no. 15 (2008): 157403.

[75]Hartstein A., J. R. Kirtley, and J. C. Tsang. "Enhancement of the infrared absorption from molecular monolayers with thin metal overlayers." *Physical Review Letters* 45, no. 3 (1980): 201.

[76]Osawa Masatoshi. "Dynamic Processes in Electrochemical Reactions Studied by Surface-Enhanced Infrared Absorption Spectroscopy (SEIRAS)." *Bulletin of the Chemical Society of Japan* 70, no. 12 (1997): 2861-2880.

[77]Kamata Toshihide, Akira Kato, Junzo Umemura, and Toru Takenaka. "Intensity enhancement of infrared attenuated total reflection spectra of stearic acid Langmuir-Blodgett monolayers with evaporated silver island films."*Langmuir* 3, no. 6 (1987): 1150-1154.

[78]Myers M. B., and E. J. Felty. "Structural characterizations of vitreous inorganic polymers by thermal studies." *Materials Research Bulletin* 2, no. 7 (1967): 535-546.

[79]Wilkinson Jacklyn. "Characterization and optimization of solution-derived chalcogenide glass thin films." *MS Thesis*, (2012).

[80]Richardson Kathleen, Laeticia Petit, Nathan Carlie, Bodgan Zdyrko, Igor Luzinov, Juejun Hu, Anu Agarwal, Lionel Kimerling, Troy Anderson, and Martin Richardson. "Progress on the fabrication of on-chip, integrated chalcogenide glass

(ChG)-based sensors." *Journal of Nonlinear Optical Physics & Materials*19, no. 01 (2010): 75-99.

[81]Zallen Richard. *Front Matter*. Wiley-VCH Verlag GmbH & Co. KGaA, 1983.

[82]Rao K. J. *Structural chemistry of glasses*. Elsevier, 2002.

[83]Thorpe M_F. "Continuous deformations in random networks." *Journal of Non-Crystalline Solids* 57, no. 3 (1983): 355-370.

[84]Bychkov E., C. J. Benmore, and David L. Price. "Compositional changes of the first sharp diffraction peak in binary selenide glasses." *Physical Review B*72, no. 17 (2005): 172107.

[85]Petri Ingrid, Philip S. Salmon, and Henry E. Fischer. "Defects in a disordered world: The structure of glassy $GeSe_2$." *Physical review letters* 84, no. 11 (2000): 2413.

[86]Salmon Philip S. "Structure of liquids and glasses in the Ge-Se binary system." *Journal of Non-Crystalline Solids* 353, no. 32 (2007): 2959-2974.

[87]Lucas Pierre, Ellyn A. King, Ozgur Gulbiten, Jeffery L. Yarger, Emmanuel Soignard, and Bruno Bureau. "Bimodal phase percolation model for the structure of Ge-Se glasses and the existence of the intermediate phase." *Physical Review B* 80, no. 21 (2009): 214114.

[88]Olivier Mélinda, J. C. Tchahame, P. Němec, Mathieu Chauvet, V. Besse, C. Cassagne, G. Boudebs et al. "Structure, nonlinear properties, and photosensitivity of $(GeSe_2)_{100-x}(Sb_2Se_3)_x$ glasses." *Optical Materials Express* 4, no. 3 (2014): 525-540.

[89]Tintu. R, PhD thesis, "Fabrication and characterization of chalcogenide nano composite based materials for photonic device applications."

[90]Hilton A. R., D. J. Hayes, and M. D. Rechtin. "Infrared absorption of some high-purity chalcogenide glasses." *Journal of Non-Crystalline Solids* 17, no. 3 (1975): 319-338.

[91]Wei Wen-Hou, Rong-Ping Wang, Xiang Shen, Liang Fang, and Barry Luther-Davies. "Correlation between structural and physical properties in Ge-Sb-Se glasses." *The Journal of Physical Chemistry C* 117, no. 32 (2013): 16571-16576.

[92]Wei Wen-Hou, Liang Fang, Xiang Shen, and Rong-Ping Wang. "Crystallization kinetics and thermal stability in Ge-Sb-Se glasses." *physica status solidi (b)* 250, no. 1 (2013): 59-64.

[93]Ko Jun Bin, and Tea-Sik Myung. "Structural and thermal properties of Ge-Sb-Se chalcogenide glasses for an appli-cation in infrared optical product design and manufacture." *Journal of Ceramic Processing Research* 12, no. 2 (2011): 132-134.

[94]Gai Xin, Ting Han, Amrita Prasad, Steve Madden, Duk-Yong Choi, Rongping Wang, Douglas Bulla, and Barry Luther-Davies. "Progress in optical waveguides fabricated from chalcogenide glasses." *Optics express* 18, no. 25 (2010): 26635-26646.

[95]Bulla D. A. P., R. P. Wang, A. Prasad, A. V. Rode, S. J. Madden, and B. Luther-Davies. "On the properties and stability of thermally evaporated Ge-As-Se thin films." *Applied Physics A* 96, no. 3 (2009): 615-625.

[96]Gai X., R. P. Wang, C. Xiong, M. J. Steel, B. J. Eggleton, and B. Luther-Davies. "Near-zero anomalous dispersion $Ge_{11.5}As_{24}Se_{64.5}$ glass nanowires for correlated photon pair generation: design and analysis." *Optics express* 20, no. 2 (2012): 776-786.

[97]Yan Kunlun, Khu Vu, Zhiyong Yang, Rongping Wang, Sukanta Debbarma, Barry Luther-Davies, and Steve Madden. "Emission properties of erbium-doped Ge-Ga-Se glasses, thin films and waveguides for laser amplifiers." *Optical Materials Express* 4, no. 3 (2014): 464-475.

[98]Nedeva Y., T. Petkovaa, E. Mytilineoub, and P. Petkov. "Compositional dependence of the optical properties of Ge-Se-Ga glass." *Journal of Optoelectronics and Advanced materials* 3, no. 2 (2001): 433-436.

[99]Maeda K., T. Sakai, K. Sakai, T. Ikari, M. Munzar, D. Tonchev, S. O. Kasap, and G. Lucovsky. "Effect of Ga on the structure of Ge-Se-Ga glasses from thermal analysis, Raman and XPS measurements." *Journal of Materials Science: Materials in Electronics* 18, no. 1 (2007): 367-370.

Chapter 2

Material Preparation and Characterization Techniques

This chapter gives an overview of the synthesis methods and procedures of the chalcogenide bulk as well as thin films and different material characterization techniques used in the present work. Description on conventional melt quenching method employed for bulk glass preparation and different thin film fabrication techniques are presented. Different characterization techniques along with their specifications and experimental methods with its theory used for analysis of the samples are also discussed.

2.1 Preparation techniques and methods

This section deals with the preparation techniques and methods of all the materials examined in this work.

2.1.1 Chalcogenide bulk glass preparation: melt quenching method

Chalcogenide bulk glasses were prepared by using conventional melt quenching method. During melt quenching of molten material, the glass forming ability depends on the viscosity of the melt as the amorphous solid is formed by continuous hardening of the liquid to a state which does not provide the atomic mobility necessary for forming crystallites. In order to achieve high transparency at infrared wavelengths, chalcogenide glasses should ideally be free of lighter elements, like oxygen and hydrogen, which lead to absorption bands in the mid-IR region. Therefore it is necessary to prepare all materials in a low humidity anaerobic environment. The constituent elements were weighed in proportion to their atomic weight percentages to a quartz ampoule

which is then evacuated at a pressure of 10^{-3}mbar and sealed at this vacuum using an oxygen- indane flame torch. Prior to batching and melting, quartz ampoules were cleaned and etched using hydrofluoric acid followed by thorough washing with doubly distilled water and heat treated for eight hours in order to remove adsorbed water and other contaminants.

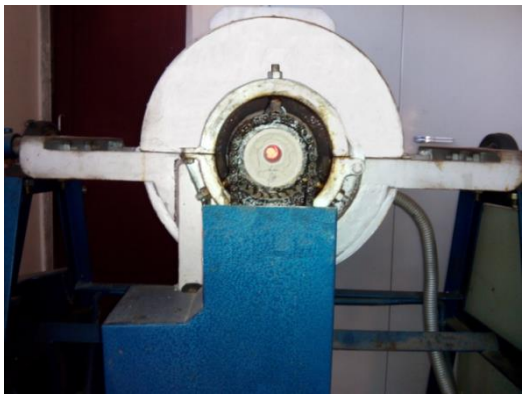

Figure 2.1: *Rocking and rotating furnace used for the preparation of chalcogenide bulk glass.*

The sealed ampoule is then transferred in a rocking and rotating furnace and is heated gradually in steps to 1000°C. The melting temperature was maintained for 24 hours to make the melt homogeneous and the melt is agitated for homogenization by rocking and rotating the quartz ampoule. After 24 hours the ampoule is quenched to ice cold water. The advantage of melt quenching technique over other techniques is the large flexibility of composition and geometry. Since quenching method does not require stoichiometry among constituents, glasses can be prepared with wide variety of compositions consisting of large number of constituents at various ratios.

The furnace can attain a maximum temperature of 1100°C and it has a C961 Blind Temperature Controller with single thermocouple or RTD input one relay output with user specific control action and relay logic. The quenched samples are extracted from the ampoule by etching out the ampoule using hydrofluoric acid.

2.1.2 Thin film preparation techniques

Thermal evaporation technique

The melt quenched bulk glasses were coated to thin films by using thermal evaporation technique. It involves the heating of the reservoir

containing the material to be evaporated and the melt so produced evaporates and condenses on to the substrate which is placed perpendicular to the vapour. The deposition technique of thin films using thermal evaporation requires a high degree of vacuum to retain the required composition and purity. The process of deposition starts by creating vacuum in the deposition chamber, usually of the order of 10^{-5}mbar or less. The general description of vacuum evaporation apparatus working along with the basic plant layouts and design features, reviews of the common types of vacuum hardware and established operating techniques have been extensively reported in various books[1,2,3].

The instrument used for deposition is Indian High vacuum pump (12A4-D). Firstly, required bulk glass sample to be coated is loaded in a Molybdenum boat in the system. High vacuum is maintained inside the system using INDVAC diffusion pump (model 114D) backed by IVP rotary vacuum pump. Before coating, the substrate is subjected to plasma cleaning. The heating element in the system has a power rating of 500W, 120V to 140V. The evaporation rate as well as the film thickness can be controlled using a quartz crystal in digital thickness monitor (Model-CTM-200). When the desired thickness is reached, the shutter is closed.

Spin coating and drop casting

Thin films of nanocolloidal solutions were prepared by using a programmable spin coating unit (SPIN 150). It involves the acceleration of a liquid puddle on a rotating surface. In this technique the coating material is loaded at the centre of the substrate and given an optimum 'rotation per minute' (rpm). The time of spinning depends on the viscosity of the liquid to be coated. Spin coated nanocolloidal solutions were heat treated to remove the residual solvent from the film.

The drop casting is a simple technique to deliver drops of liquids in micro-molar to milli-molar range by using micro-pipettes. The required volume of the sample solutions were taken in a micro-pipette and placed on the cleaned substrate surface. The films were then allowed to dry at ambient conditions.

2.2 Characterization techniques

The physical, thermal, optical, structural and morphological properties of the fabricated bulk glass, nanocolloids and thin films of chalcogenide glasses and silver colloids and thin films were characterized using a series of

techniques including, differential scanning calorimetry (DSC), X-ray diffraction technique (XRD), UV-Visible, Fourier-transform infrared spectroscopy (FTIR), Scanning electron microscopy, Raman spectroscopy etc.

2.2.1 Structural characterizations

X-ray diffraction technique

X-ray diffraction technique (XRD) is the most widely used technique to characterize the amorphous nature of bulk glasses and their thin films. The powder method (P-XRD) was used to check the amorphous nature of the samples. The bulk samples were crushed into fine powder using mortar and pestle before analysis. Bruker AXS D8 Advance X-ray Diffractometer with Cu-Kα line of wavelength λ=1.5406 Å was employed for the analysis. Data acquisition was made in 2θ range from 5° to 80°. Thin films coated on the microscopic glass slides were also analysed to check its amorphous nature.

Micro-Raman spectroscopy

Micro-Raman spectroscopy is used to characterize the structure of the glasses. Inelastic scattering of photons by optical-mode phonons is known as Raman scattering. The scattered photon will have lost or gained energy, equivalent to that of the vibrational modes of the lattice and therefore it is of a different wavelength than the incident photon. The wavelength shift is unique for a material and it indicates the vibrational energies of chemical bonds within the glass.

The molecular structures of the bulk glass and thin films were characterized with the help of Raman spectroscopy, using LabRAM HR system at 785nm. This spectroscopic system offers both great flexibility and high performance because of its high spectroscopic resolution and a unique wavelength range capability. LabRAM HR allows the collection of large area Raman images, using the X, Y and Z mapping features in seconds/minutes using UV, Visible, NIR Raman with 325nm, 514nm and 785nm LASER and CCD detector.

Fourier-transform infrared spectroscopy

The presence of impurities within the glass matrix is analyzed using FTIR spectroscopy. This spectroscopic technique is also utilized to analyze the binding of anchor molecules with silver surfaces. The instruments used in this study are Thermo Nicolet, Avatar 370 for transmission studies and JASCO

FT-IR-5300 Spectrometer for attenuated total internal reflection (ATR). The FTIR instrument consists of a broad band infrared source with Michelson interferometer, with a movable mirror in one arm. The mirror is translated at a constant rate while intensity of the light passing through the interferometer is recorded. The pattern generated by this process contains information on the temporal coherence of the light which is modulated in the presence of the sample in the beam path. The transmittance of the sample can be extracted by applying the well-known Fourier transform.

Schematic of attenuated total reflection is shown in figure 2.2. The sample is mounted in contact with an IR transparent prism of high refractive index. The infrared rays incident on this sample at an angle larger than the critical angle induces total reflection and the light which is totally reflected by the interface between the sample and the prism is measured to obtain an infrared spectrum.

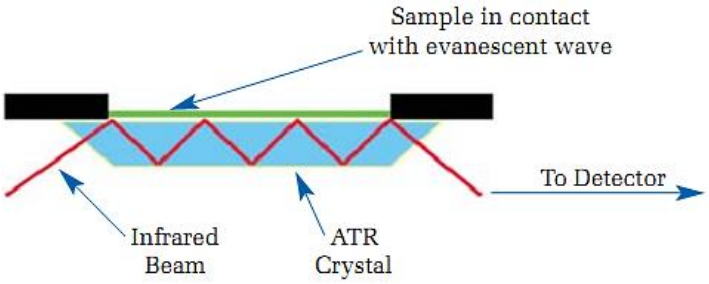

Figure 2.2: *Schematic of a multiple reflection ATR system*

2.2.2 Composition, Morphology and Size analysis

Scanning electron microscopy

Surface imaging of the chalcogenide nanoclusters in the spin coated thin films, obliquely deposited silver films and compositional analysis of bulk and thin film samples were done using Scanning electron microscope (JEOL Model JSM-6390LV) equipped with JEOL Model JED-2300 energy dispersive X-ray spectroscopy (EDS).

High Resolution Transmission Electron Microscopy

Morphology and size of the silver nanoparticles prepared were analysed by using high resolution transmission electron microscopy (HRTEM). The instrument used is JEOL 3010. It is equipped with a UHR pole-piece which gives a lattice resolution of 0.14nm and a point to point resolution of

0.12nm. It consists of a standard probe and a variable temperature probe (100 to 500 K) and a Gatan digital camera.

Dynamic light scattering

Dynamic light scattering from Horiba Scientific (SZ-100) is used to measure the size distribution of particles dispersed in a liquid medium. Particle size can be determined by measuring the random changes in the intensity of light scattered from a suspension or solution[4]. Small particles in liquid suspension undergo random thermal motion known as Brownian motion and this random motion is measured to calculate particle size. A schematic of the optical setup for particle size measurements in the SZ-100 is shown in figure 2.3 (a).

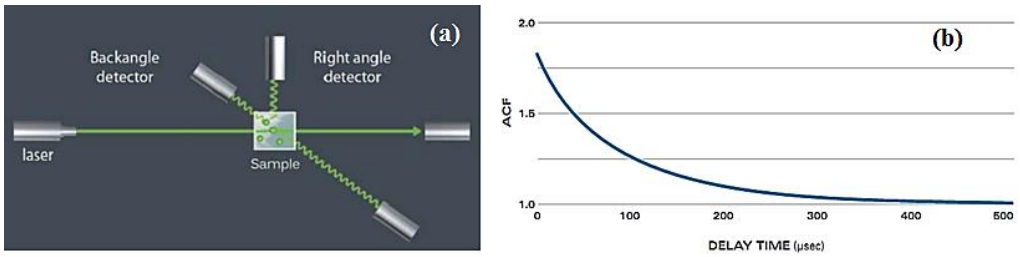

Figure 2.3: *(a) Dynamic light scattering layout[5] for the SZ-100 system. (b) Autocorrelation function from dynamic light scattering for a mono-dispersed sample.*

The liquid sample is taken in cell and the light from the laser light source is allowed to illuminate the sample in the cell. Two detectors are arranged, one at 90° (right angle) and other at 173° (back angle) scattering angle and the scattered light signal is collected with one of two detectors. The optical signal detected shows random changes due to the randomly changing relative position due to Brownian motion of the particles and the obtained signal can be interpreted using an autocorrelation function. Incoming data is processed in real time with a digital signal processing device known as a correlator and the autocorrelation function (ACF) as a function of delay time 'T' is extracted. The autocorrelation function from dynamic light scattering for a sample, where all of the particles are the same size is shown in figure 2.3 (b) which is simply an exponential decay of the following form

$$ACF = e^{-2\Gamma} \tag{2.1}$$

Γ is derived from experimental data by a curve fit. The diffusion coefficient (D_t) can be obtained from the relation, $\Gamma = D_t q^2$, where q is the scattering vector, $q = \left(\frac{4\pi n}{\lambda}\right)\sin(\theta/2)$, where n is the refractive index of the liquid; λ is the wavelength of the laser light; and θ is the scattering angle. Substituting D_t in Stokes-Einstein equation given below gives particle size (hydrodynamic diameter) D_h.

$$D_h = \frac{k_B T}{3\pi\eta D_t} \tag{2.2}$$

Where D_h is hydrodynamic diameter, D_t is translational diffusion coefficient, k_B is Boltzmann's constant, T is temperature and η is dynamic viscosity.

2.2.3 Thermal characterizations

Differential Scanning Calorimeter

In this study, glass transition temperature (Tg) of bulk glasses was determined using a Mettler Toledo (model 822e)[5] differential scanning calorimeter (DSC). The instrument is equipped with a ceramic sensor FRS5 (heat-flux sensor with 56 thermocouples). Using indium and zinc standards, the instrument was calibrated for temperature and pressure. The equipment is designed to measure the amount of heat required to rise the temperature of the sample by a fixed amount, with respect to a reference. 10mg of samples were weighed and sealed in an aluminum crucible and heated under nitrogen flow with a heating rate of 10°C. The heat flow was then recorded with respect to temperature. The glass transition temperature (Tg) was assigned as the inflection point of this endotherm, and is taken as the minimum of the first derivative curve of heat flow versus temperature curve.

Thermal lens technique

The heat diffusivity studies in nanocolloids were conducted using Dual mode matched thermal lens method at 532 nm. The method[6] is based on the optical measurement of the thermal energy released by a sample due to light absorption corresponding to non-radiative relaxation of the excited species. In this method, sample is illuminated using a Gaussian beam (pump beam). A part of the incident radiation is absorbed by the sample and subsequent non-radiative decay of excited state population leads to the local heating of the medium. The temperature distribution in the medium mimics the beam profile of the pump beam and hence a refractive index gradient is created in the

medium. Due to this refractive index modification, the medium acts as a lens and it is called thermal lens (TL). The thermal lens usually has a negative focal length since most materials expand upon heating and hence have negative temperature coefficient of refractive index. The formation of the thermal lens causes the probe beam to expand and is detected as a time dependent decrease in power at the centre of the beam at far field. Most of the current techniques for thermal parameter evaluation are mainly depending upon the heat exchange mechanism or on temperature gradients. However, the thermal lens technique depends upon change in refractive index due to nonradiative transition in the sample following the optical excitation which can offer accurate results.

A schematic of experimental set up is shown in Figure 2.4. Laser radiation at 532 nm wavelength from a Diode Pumped Nd: YVO4 laser (Micro DPSS model[7] BWT-50 at 50mW) is used as the pump beam to generate the thermal lens in the medium. Radiation of wavelength 632.8 nm from a 4mW, intensity stabilized He-Ne laser source is used as the probe beam. The pump beam is intensity modulated using a mechanical chopper and the probe beam is made to pass collinearly through the sample using a dichroic mirror. An optical fibre mounted on a XYZ translator serves as the finite aperture. The chopper used in this study is HMS/ITHACO model 230 light beam chopper[8]. The other end of the fiber is coupled to a fast photodetector and the signal output from detector is processed using a digital storage oscilloscope.

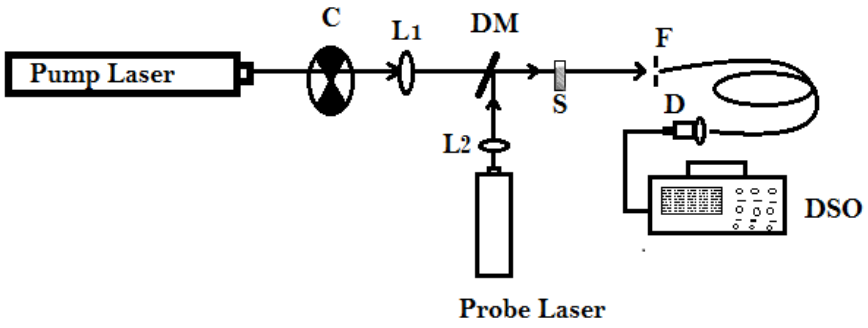

Figure 2.4: *Schematic diagram of the Thermal lens set up. C-Chopper, L1, L2-lens, DM-Dichroic Mirror, S-Sample, F-Filter, D-Detector, DSO-Digital Storage Oscilloscope.*

Mechanically chopped optical radiation from pump laser is focused using lens L1 to the sample in a cuvette of 1cm length, placed in a micrometer translational stage. When the chopper allows impinging of pump beam on the sample, it creates a thermal lens within the sample. The probe beam from the

He-Ne laser which travel collinearly with pump beam experience a diverging lens and therefore the beam shape expands in the presence of thermal lens. The change in intensity of the probe beam is measured using a fast photodetector using fiber which is fixed on the optic axis of the experimental set up. The TL signal is recorded from which the relative change in intensity and initial slope is measured. The value of probe beam phase shift induced by the thermal lens (θ) and TL characteristic response time (t_c) are determined. From these values, the thermal diffusivity (D) of the sample under investigation is evaluated.

Theory

The magnitude of the effective thermal lens produced by propagation of a continuous wave Gaussian laser beam of spot size 'ω' is governed by the steady state balance between laser heating and solvent or matrix heat dissipation. If the beam is suddenly turned on at time t=0, the lens approaches to a steady state governed by[9,10]

$$f(t) = f_\infty \left(1 + \frac{t_c}{2t}\right) \tag{2.3}$$

and the steady state focal length f_∞ of such a lens is derived as

$$f_\infty = \frac{\pi k \omega^2}{PA\left(\frac{dn}{dt}\right)} \tag{2.4}$$

where k is the thermal conductivity ($Wcm^{-1}K^{-1}$), P is the laser power (W), A is the sample absorbance, $\frac{dn}{dt}$ is the refractive index change with temperature and t_c is the time response to attain the steady state focal length given by

$$t_c = \frac{\omega^2}{4D} \tag{2.5}$$

from which thermal diffusivity 'D' can be calculated. The thermal diffusivity in the sample is detected by its effect on the propagation of the probe laser beam aligned with the centre of the lens. The expression relating the intensity as a function of time is given as

$$I(t) = I_0 \left(1 - \frac{\theta}{1+\frac{t_c}{2t}} + \frac{\theta^2}{2\left(1+\frac{t_c}{2t}\right)^2}\right) \tag{2.6}$$

The modified equation for continuous wave laser source is,

$$I(t) = I_0\left(1 - \frac{\theta}{1+\frac{t_c}{2(t-t_0)}} + \frac{\theta^2}{2\left(1+\frac{t_c}{2(t-t_0)}\right)^2}\right) \quad (2.7)$$

where t_0 is the time at t=0; θ is directly proportional to the laser power degraded to heat (P_{th}) by the relation

$$\theta = \frac{P_{th}\left(\frac{dn}{dT}\right)}{\lambda k} \quad (2.8)$$

where λ is the laser wavelength. For a given solvent or matrix the experimental parameter of interest is θ, which may be obtained from the initial intensity I_0 and the intensity after the steady state has been established, I_∞ ,so that

$$\theta = 1 - (1 + 2I)^{1/2} \quad (2.9)$$

$$I = \frac{I_0 - I_\infty}{I_\infty} \quad (2.10)$$

The initial slope of the decay curve

$$m = \frac{2\theta}{I_0 t_c} \quad (2.11)$$

from which the value of t_c and hence D is calculated.

2.2.4 Optical characterizations

UV-Vis-NIR Spectroscopy

JASCO V-570 UV-Vis-NIR spectrophotometer was used to examine the optical absorption, reflection, and transmission studies over the wave length of 200 to 2500nm. This equipment measures the ratio of optical intensity transmitted over a reference path and through the sample to give the transmittance of the sample.

The general sources for the loss of optical power transmitted through the sample are: reflection, scattering, and absorption. The first source of optical loss is reflection, resulting from the difference of refractive index (n) as the light passes from air to glass. According to Fresnel equation[11]

$$r = \frac{(n_1 - n_2)^2}{(n_1 + n_2)^2} \quad (2.12)$$

where r is the reflection coefficient for normal incidence at the interface between two media with refractive indices n_1 and n_2. The combined reflection coefficient (R) by including material's Frenel reflections (reflections at both glass surfaces) as well as multiple reflections is given by

$$R = \frac{2r}{(1+r)} \tag{2.13}$$

The second source of optical loss is due to Rayleigh scattering, and it is caused by surface roughness or inhomogeneities within the sample which possesses a refractive index differing from that of the surrounding medium, such as bubbles or striae, and is dependent both on the refractive index difference and on the size of the scattering center.

The third source of optical loss is absorption which may be either intrinsic, where the electronic transitions are due to the material itself, such as valence band to conduction band transition or extrinsic, where the transitions are due to impurities or dopants within the sample, respectively. After correcting for the Fresnel reflective losses and neglecting scattering loss, the absorbance (A) of the sample can be calculated from Beers's law[12] as

$$A = -log\left(\frac{1}{T}\right) \tag{2.14}$$

And the absorption coefficient (α), or equivalently the absorptivity, is calculated from the absorbance of the sample (A) and the path length of the light (sample thickness (d)) as

$$\alpha = \frac{2.303 \times A}{d} \tag{2.15}$$

a) Calculation of optical bandgap

A typical energy-dependent optical absorption spectrum for a chalcogenide glass is divided into three regions[13] as shown in figure 2.5. Region I (where absorption coefficient, $\alpha < 10^2 cm^{-1}$) is believed to arise from transitions involving defect-states as the absorption in this region has been found to depend strongly upon the material preparation and thermal history[14,15]. In most of the chalcogenide systems investigated, region II (where $\alpha = 10^2 - 10^4\ cm^{-1}$) is characterized by exponential behavior, termed the 'Urbach edge'. In general, absorption in region III deviates from exponential behavior and the value of absorption coefficient (α) attains a value $\geq 10^4 cm^{-1}$. This region is termed as Tauc region and can be written as

$$\alpha h\upsilon = B(h\upsilon - Eg)^{s} \qquad (2.16)$$

where s=1/2 for direct allowed transition, 3/2 for direct forbidden transition, 2 for an indirect allowed transition and 3 for indirect forbidden transition.

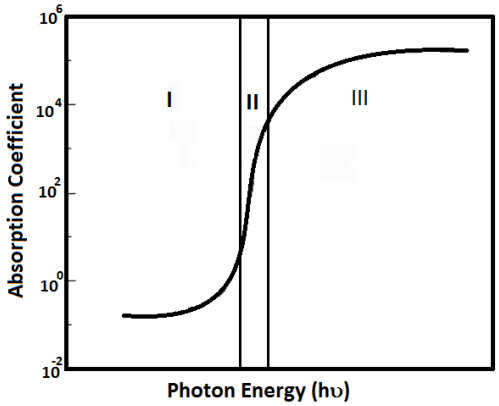

Figure 2.5: *Schematic representation of absorption spectrum in chalcogenide glasses.*

Chalcogenide glass are known to have an indirect-type band gap transition, indicative of a change of momentum of the electron as it is promoted from the valence to the conduction band[16].

b) Calculation of refractive index and film thickness

A first approximation of the refractive index (n_1) in the region of weak and medium absorption has been put forward by Swanepoel[17] based on the idea of Manifacier et al[18] of creating upper and lower envelops of interference maxima and minima. The practical situation of multiple reflection and interference for normal incidence in a thin film, with thickness 'd' and complex refractive index $n^* = n - ik$ on a transparent substrate is shown in figure 2.6 Where n is the refractive index, s is substrate refractive index and k the extinction coefficient. If the thickness 'd' is uniform, interference effects give rise to spectrum as shown in figure 2.7. The transmission T is a complex function, T = T (λ, n, A), where $A(\lambda)$ is the absorbance. In the transparent region (α = 0), refractive index 'n' has been derived[17] by considering extremes of interference fringes T_M and T_m.

$$n = \left[M + (M^2 - s^2)^{1/2}\right]^{1/2} \qquad (2.17)$$

where

$$M = \frac{2s}{T_m} - \frac{s^2+1}{2} \tag{2.18}$$

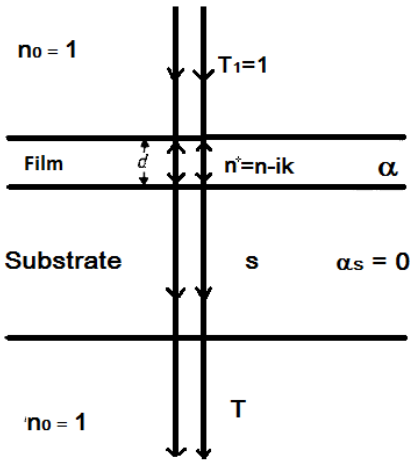

Figure 2.6: *Schematic representation of light passing with multiple reflection through a thin film on a thick finite transparent substrate.*

In the region of weak and medium absorption ($\alpha \neq 0$), n has been derived as

$$n = \left[N + (N^2 - s^2)^{1/2}\right]^{1/2} \tag{2.19}$$

where

$$N = \frac{2s(T_M - T_m)}{T_M T_m} + \frac{s^2+1}{2} \tag{2.20}$$

The substrate refractive index 's' can be obtained from the transmission spectra (T_s) of substrate, using the relation.

$$s = \frac{1}{T_s} + \left(\frac{1}{T_s} - 1\right)^{1/2} \tag{2.21}$$

If n_1 and n_2 are refractive indices of two adjacent maxima or minima at λ_1 and λ_2 wavelengths then the thickness of the thin film can be derived as

$$d = \frac{\lambda_1 \lambda_2}{2(\lambda_1 n_2 - \lambda_2 n_1)} \tag{2.22}$$

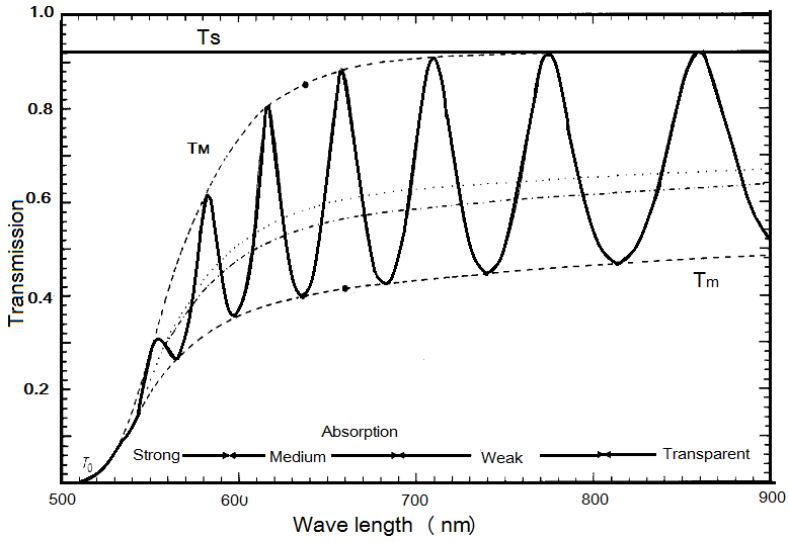

Figure 2.7: *Transmission spectra showing interference fringes.*

c) Dispersive analysis of refractive index using Wemple-DiDomenico mode

Refractive index and its spectral dependence has been analyzed using Wemple-DiDomenico (WDD) model[19,20], based on the single effective oscillator approach. According to this model the relation between the refractive index (n) and the single oscillator strength ($f = E_0E_d$) can be written as

$$(n^2 - 1) = \frac{E_dE_0}{{E_0}^2 - (h\upsilon)^2} \tag{2.23}$$

where E_d is the dispersion energy which measures the average strength of interband optical transitions and is associated with the changes in the structural order of the material i.e., it is related to the ionicity, anion valency and coordination number of the material. E_0 is the effective oscillator energy. As the oscillator energy E_0 scales with the Tauc gap, Eg, i.e. $E_0 \approx 2Eg$, as was verified by several chalcogenide films[21,22,23]. The static refractive index (n_0) and static dielectric constant (ε_∞) has been calculated from E_0 and E_d as,

$$n_0 = \left(1 + \frac{E_d}{E_0}\right)^{1/2} \tag{2.24}$$

$$\varepsilon_\infty = (n_0)^2 \tag{2.25}$$

n_0 can be calculated by extrapolating the WDD dispersion equation with $h\upsilon \rightarrow 0$.

d) Extinction coefficient, dielectric constants and optical conductivity

The values of extinction coefficient (k) and refractive index (n) are calculated from the absorption coefficient (α) using the relation[24]

$$k = \frac{\alpha\lambda}{4\pi} \tag{2.26}$$

The complex dielectric constant;

$$\varepsilon = \varepsilon_r + i\varepsilon_i \tag{2.27}$$

where ε_r is the real part of the dielectric constant and is a measure of polarizability of a material. The imaginary part (ε_i) of the dielectric constant indicates the energy loss, i.e. the energy lost in aligning the dipoles. The loss tangent ($\tan\delta = \frac{\varepsilon_i}{\varepsilon_r}$) measures the intrinsic dissipation of energy of a dielectric material. The real and imaginary part of the dielectric constant have been determined from

$$\varepsilon_r = n^2 - k^2 \tag{2.28}$$

$$\varepsilon_i = 2nk \tag{2.29}$$

To get a better idea on the electric loss, the optical conductivity (σ) has been calculated using the relation

$$\sigma = \frac{\alpha nc}{2\pi} \tag{2.30}$$

where c is the velocity of the light. σ is directly related to the imaginary part of dielectric constant 'ε_i' $\left(\varepsilon_i = \frac{\sigma(\omega)}{\omega\varepsilon_0}\right)$ and tells about the electronic structure of the system[25].

Photoluminescence spectroscopy

Photoluminescence studies on nanocolloidal solutions were done using Cary Eclipse fluorimeter (Varian[26]). It has a single cell holder for liquid sample analysis and another holder accessory with rotational and translational adjustments for solid samples and thin films. The angle of incidence of the source excitation can be varied from 20° to 35° for solid samples. The excitation source used is xenon lamp.

2.2.5 Nonlinear optical characterization

Z-scan Technique

Z-scan is a single beam technique developed by Sheik Bahae[27,28] which allows a direct measurement of the nonlinear absorption coefficient as well as the sign and magnitude of nonlinear refraction. The technique is based on the principle of spatial beam distortion, and offers simplicity as well as high sensitivity comparable to interferometric methods. When a high intensity laser beam propagates through any nonlinear material ensuing self-refraction can be studied using the z-scan technique. Using a single Gaussian laser beam in a tight focus geometry, as depicted in figure 2.8, the transmittance of a nonlinear medium through a finite aperture in the 'far field' as a function of the sample position 'z' can be measured with respect to the focal plane and it is closed aperture Z-scan. On the other hand, if the transmitted light is measured without an aperture, it is open aperture Z-scan and the output is sensitive only to nonlinear absorption. In a z-scan measurement, the sample thickness should be much less than Rayleigh's range z_0 (diffraction length of the beam), defined as $z_0 = \frac{k\omega_0{}^2}{2}$, where k is the wave vector and ω_0 is the beam waist radius ($\omega_0 = \frac{f\lambda}{D}$) , where f is the focal length of the lens used, λ is the wavelength of the source and D is the beam radius at the lens. Z-scan technique is highly sensitive to the profile of the beam as well as the thickness of the sample. Deviation from Gaussian profile of the beam and also from thin sample approximation will give rise to erroneous results.

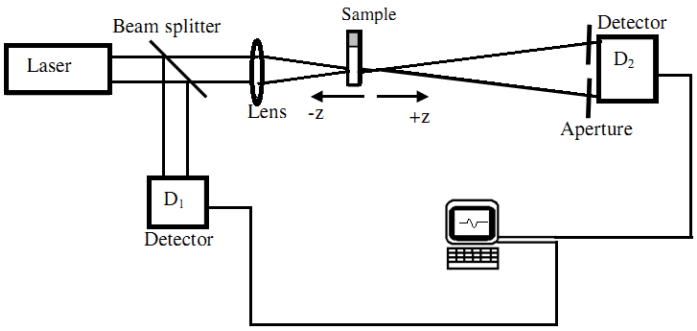

Figure 2.8: *Schematic diagram of the Z-scan set up.*

Closed aperture Z-scan technique

The basis of closed aperture z-scan is the self-refraction and self-phase modulation effects. Starting the scan far away from the focus (negative z), the

beam irradiance is low and negligible nonlinear refraction occurs; hence, the transmittance (D_2/D_1 in Figure 2.8) remains relatively constant. As the sample is brought closer to focus, the beam irradiance increases, and it leads to self-lensing in the sample. A negative self-lensing prior to focus will tend to collimate the beam, causing a beam narrowing at the aperture and it increases in the measured transmittance. As the scan continues and the sample passes the focal plane to the right (positive z), the same self-defocusing increases the beam divergence, leading to beam broadening at the aperture, and therefore a decrease in transmittance. This suggests that there is a null effect as the sample crosses the focal plane. This is analogous to placing a thin lens at or near the focus, which results in changing the far-field pattern of the beam. The scan is completed as the sample is moved away from focus (positive z) such that the transmittance becomes linear since the irradiance is again low.

A pre-focal transmittance maximum (peak) followed by a post-focal transmittance minimum (valley) is, signature of a negative refractive nonlinearity. Positive nonlinear refraction, following the same analogy, gives rise to an opposite valley-peak configuration.

Theory

In a cubic nonlinear medium the index of refraction (n) is expressed in terms of nonlinear indices n_2 (m^2/W) through

$$n = n_0 + n_2|E|^2 = n_0 + n_2 I \tag{2.31}$$

where n_0 is the linear index of refraction, E is the peak electric field, n_2 the intensity dependent refractive index and I denotes the irradiance of the laser beam within the sample. Assume a TEM_{00} beam of waist radius ω_0 travelling in the +z direction. E can be written as

$$E(z,r,t) = E_0(t)\frac{\omega_0}{\omega(z)} exp\left[-\frac{r^2}{\omega^2(z)} - \frac{ikr^2}{2R(z)} e^{i\varphi(z,t)}\right] \tag{2.32}$$

where $\omega^2(z) = {\omega_0}^2(1 + \frac{z^2}{{z_0}^2})$ is the beam radius, $R(z) = z(1 + \frac{z^2}{{z_0}^2})$ is the radius of curvature of the wave front at z, $z_0 = \frac{k{\omega_0}^2}{2}$ is the diffraction length of the beam and $k = \frac{2\pi}{\lambda}$ is the wave vector. $E_0(t)$ denotes the radiation electric field at the focus and contains the temporal envelope of the laser pulse. The term $e^{i\varphi(z,t)}$contains all the radially uniform phase variations. For calculating the radial phase variations $\Delta\varphi(r)$, the slowly varying envelope approximation (SVEA) is used and all other phase changes that are uniform in radius 'r' are

ignored. $L << z_0/\Delta\varphi(0)$, where L is the sample length, the amplitude I and the phase φ of the electric field as a function of z are now governed in the SVEA by

$$\frac{d\Delta\varphi}{dz'} = \Delta n(I)k \tag{2.33}$$

And

$$\frac{dI}{dz'} = -\alpha(I)I \tag{2.34}$$

where z is the propagation depth in the sample and $\alpha(I)$ in general includes linear and nonlinear absorption terms. In the case of cubic nonlinearity and negligible nonlinear absorption, above equations can be solved to get the phase shift $\Delta\varphi$ at the exit of the sample and is given by

$$\Delta\varphi(z,r,t) = \Delta\varphi(z.t)exp\left[-\frac{2r^2}{\omega^2(z)}\right] \tag{2.35}$$

With

$$\Delta\varphi(z,t) = \frac{\Delta\varphi_0(t)}{\left(1+\frac{z^2}{{z_0}^2}\right)} \tag{2.36}$$

where $\Delta\varphi_0(t)$ is the on axis phase shift at the focus which is defined as

$$\Delta\varphi_0(t) = k\Delta n_0(t)L_{eff} = \frac{2\pi}{\lambda}n_2 I_0(t)L_{eff} \tag{2.37}$$

where $I_0(t)$ is the on axis irradiance at focus (i.e. at $z = 0$). The complex electric field exiting the sample E_e now contains the nonlinear phase distribution

$$E_e(z,r,t) = E(z.r,t)e^{\left(\frac{-\alpha l}{2}\right)}e^{i\Delta\varphi(z,r,t)} \tag{2.38}$$

By virtue of Huygens's principle and making use of Gaussian decomposition method [GD] one can show that

$$e^{i\Delta\varphi(z,r,t)} = \sum_{m=0}^{\infty}\frac{[i\Delta\varphi_0(z,t)]^m}{m!}e^{\left(\frac{-2mr^2}{\omega^2(z)}\right)} \tag{2.39}$$

Each Gaussian beam can now be simply propagated to the aperture plane where they will be resumed to reconstruct the beam. When including the initial beam curvature for the focused beam, we derive the resultant electric field pattern at the aperture as

$$E_a(r,t) = E(z,r=0,t)e^{\left(\frac{-\alpha l}{2}\right)}\sum_{m=0}^{\infty}\frac{[i\Delta\varphi_0(z,t)]^m}{m!}\frac{\omega_{m0}}{\omega_m}exp\left[-\frac{r^2}{{\omega_m}^2}-\frac{ikr^2}{2R_m}+i\theta_m\right] \tag{2.40}$$

Defining d as the propagation distance in free space from the sample to the aperture plane and $g = 1 + \frac{d}{R(z)}$, the remaining parameters in above equation are expressed as

$$\omega_{m0}{}^2 = \frac{\omega^2(z)}{2m+1} \qquad d_m = \frac{k\omega_{m0}{}^2}{2} \qquad \theta = tan^{-1}\left[\frac{d/d_m}{g}\right]$$

$$\omega_m{}^2 = \omega_{m0}{}^2\left[g^2 + \frac{d^2}{d_{mo}{}^2}\right] \qquad \text{and} \qquad R_m = d\left[1 - \frac{g}{g^2+d^2/d_m{}^2}\right]^{-1}$$

The on-axis electric field at the aperture plane can be obtained by putting $r = 0$ in equation 2.40. In the limit of small nonlinear phase change ($\Delta\varphi << 1$) and small aperture, only two terms in the sum in equation 2.40 needs to be retained. The normalized z-scan transmittance can be written as

$$T(z, \Delta\varphi_0) = \frac{|E_a(z,r=0,\Delta\varphi_0)|^2}{|E_a(z,r=0,\Delta\varphi_0=0)|^2} = \frac{\left|\left(g+i\frac{d}{d_0}\right)^{-1} + i\Delta\varphi_0\left(g+i\frac{d}{d_1}\right)^{-1}\right|^2}{\left|\left(g+i\frac{d}{d_0}\right)^{-1}\right|^2} \tag{2.41}$$

The far field condition d >> z_0 can give a geometry-independent normalized transmittance as

$$\mathrm{T}(\mathrm{z}, \Delta\varphi_0) = 1 - \frac{4\Delta\varphi_0 \mathrm{x}}{(\mathrm{x}^2+9)(\mathrm{x}^2+1)} \qquad \text{where } x = z/z_0 \tag{2.42}$$

For a cubic nonlinearity, the peak and valley of the z-scan transmittance can be calculated by solving the equation

$$\frac{dT(z,\Delta\varphi_0)}{dz} = 0 \tag{2.43}$$

Solution to this equation 2.43 yields the peak valley separation as

$$\Delta Z_{p,v} = 1.7 z_0 \tag{2.44}$$

Then the peak valley transmittance change is for small aperture (s~0)

$$\Delta T_{p,v} = 0.406\Delta\varphi_0 \tag{2.45}$$

The value of $\Delta\varphi_0$, the phase shift, due to change in refractive index could be obtained from the theoretical fit to the equation 2.42. Then the nonlinear refractive index n_2 can be determined using equation 2.37 and is given by

$$n_2 = \frac{\lambda\Delta\varphi_0}{2\pi I_0 L_{eff}} \quad (\mathrm{m^2/W}) \tag{2.46}$$

$$n_2 = \frac{cn_0\lambda\Delta\varphi_0}{80\pi^2 I_0 L_{eff}} \quad \text{(esu)} \tag{2.47}$$

The n_2 is related to real part of the third order nonlinear susceptibility ($Re\chi^3$) by the relation,

$$Re\chi^3 = \frac{n_0 n_2}{3\pi} \qquad \text{(esu)} \tag{2.48}$$

Open aperture z-scan

Open aperture z-scan technique measure the effect of nonlinear absorption in the sample. Z-scan with a fully open aperture ($S = 1$) is insensitive to nonlinear refraction (thin sample approximation). Such Z-scan traces without aperture are symmetric with respect to the focus (z = 0) where they have a minimum transmittance (e.g., multiphoton absorption) or maximum transmittance (e.g., saturation of absorption) If nonlinear absorption such as two photon absorption is present, it is manifested in the measurements as a transmission minimum at the focal point. On the other hand, if the sample is a saturable absorber, transmission increases with increase in incident intensity and results in a transmission maximum at the focal point[29]. Brief description[28] of the theory is given below.

Theory

In the case of an open aperture z-scan, the transmitted light measured by the detector is sensitive only to intensity variations. Hence, phase variations of the beam are not taken into consideration. The intensity dependent nonlinear absorption coefficient α(I) can be written in terms of linear absorption coefficient α and TPA coefficient β as

$$\alpha(\mathrm{I}) = \alpha + \beta \mathrm{I} \tag{2.49}$$

The irradiance distribution at the exit surface of the sample can be written as

$$I_r(z,r,t) = \frac{I(z,r,t)e^{-\alpha l}}{1+q(z,r,t)} \tag{2.50}$$

where $$q(z,r,t) = \beta I(z,r,t) L_{eff} \tag{2.51}$$

L_{eff} is the effective length and is given in terms of the sample length (l) as

$$\mathrm{L_{eff}} = \frac{(1-\mathrm{e}^{-\alpha \mathrm{l}})}{\alpha} \tag{2.52}$$

The total transmitted power $P(z,t)$ is obtained by integrating equation 2.50 over z and r and is given by

$$P(z,t) = P_I(t)\mathrm{e}^{-\alpha \mathrm{l}\frac{\ln(1+q_0(z,t))}{q_0(z,t)}} \tag{2.53}$$

where $P_I(t)$ and $q_0(z,t)$ are given by

$$P_I(t) = \frac{\pi {\omega_0}^2 I_0(t)}{2} \tag{2.54}$$

$$q_0(z,t) = \frac{\beta I_0(t) \mathrm{L_{eff}} {z_0}^2}{z^2+{z_0}^2} \tag{2.55}$$

For a pulse of Gaussian temporal profile, equation 2.53 can be time integrated to give the normalized transmission for open aperture z-scan as

$$\mathrm{T(z,\ s=1)}=\frac{1}{\sqrt{\pi}\mathrm{q_0(z,0)}}\int_{-\infty}^{\infty}\ln\left[1+\mathrm{q_0(z,0)e^{-\tau^2}}\right]\mathrm{d\tau} \tag{2.56}$$

If $|q_0| < 1$, equation 2.56 can be simplified as

$$\mathrm{T(z,\ s=1)}= \sum_{m=0}^{\infty}\frac{[-q_0(z,0)]^m}{(m+1)^{3/2}} \tag{2.57}$$

where m is an integer. Once an open aperture z-scan is performed, the parameter $\mathrm{q_0}$ can be obtained by fitting the experimental results to equation 2.57. Then the nonlinear absorption coefficient β can be unambiguously deduced using equation 2.51. The imaginary part of third order susceptibility ($Im\chi^3$) determines the strength of the nonlinear absorption. The TPA coefficient is related to $Im\chi^3$ by the relation

$$Im\chi^3 = \frac{\epsilon_0 n_0^2 c^2 \beta}{\omega} \qquad (\mathrm{m^2V^{-2}}) \tag{2.58}$$

$$Im\chi^3 = \frac{n_0^2 c^2 \beta}{240\pi^2\omega} \qquad (\mathrm{esu}) \tag{2.59}$$

where λ is the excitation wavelength, n_0 is the linear refractive index, ε_0 is the permittivity of free space and c the velocity of light in vacuum.

Dependence of TPA, Raman transitions and ac Stark contributions on n_2

The bound electronic nonlinear refractive index n_2 is theoretically obtained using Kramers-Kronig transformation from nondegenerate nonlinear absorption calculated using two-band model[30]. Based on the principle of causality, Kramers-Kronig transformation states that a change in the

refractive index (Δn) at ω is associated with changes in the absorption coefficient $(\Delta\alpha)$ throughout the spectrum (ω') and vice versa. Therefore fluctuations in the absorption coefficient which originate due to different 'causes' like Two-Photon absorption, Raman transitions and Stark shift (virtual band blocking) will be accompanied with a change in the refractive index. The effects of above 'causes' on the dispersion, scaling and sign of n_2 were theoretically deduced as a function $G_2(h\upsilon/Eg)$ called universal dispersion function. The function G_2 which relates with the nonlinear refractive index n_2 is given by equation.

$$n_2(esu) = \frac{K' G_2(\mathrm{h}\upsilon/\mathrm{Eg})}{n_0 Eg^4} \tag{2.60}$$

where K' is a constant, $K' = 3.4 \times 10^{-8}$ and the bandgap Eg is in eV

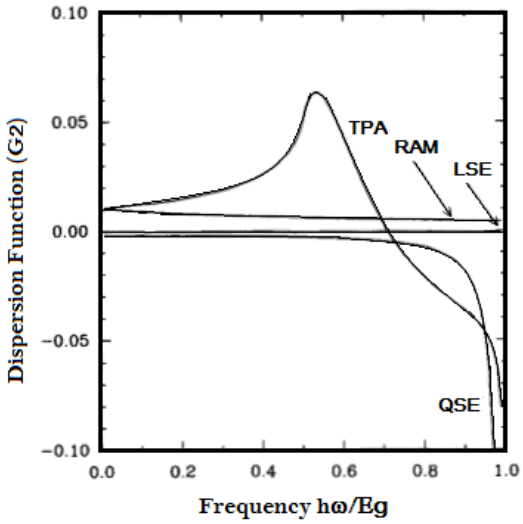

Figure 2.9: *Frequency dependence of the various contributions to the nonlinear refractive index n_2. Each contribution is derived from a Kramers-Kronig transform of the various nonlinear absorption processes: TPA, Raman transitions, and linear and quadratic Stark shifts of the band edge. (Reported by Mansoor Sheik-Bahae et. al[30])*

Studies[30] conducted on more than twenty five different materials show excellent agreement between theoretically calculated n_2 with measured values for a five order of magnitude variation in the modulus of n_2 in semiconductors and wide-gap optical solids. The individual contributions of the dispersion function $G_2(h\upsilon/Eg)$ to the nonlinear refraction are shown[30] in table 2.1 as a function of frequency. The divergence in each of each term as $\omega \to 0$ has been

subtracted for clarity. A graphical comparison of the dispersion function $G_2(h\upsilon/Eg)$ arised from TPA, Raman transitions (RAM), and linear (LSE) and quadratic Stark (QSE) effects is given in figure 2.9. It can be seen that the most significant contribution to the spectral dependence of function $G_2(h\upsilon/Eg)$ arises from the 2PA term, except close to the band edge where the quadratic Stark term becomes dominant. The linear Stark term arising from the self-coupling of the bands is insignificant when it is compared to the quadratic term.

Contribution	$G_2(x)$
TPA	$\frac{1}{(2x)^6}\left[-\frac{3}{8}x^2(1-x)^{-\frac{1}{2}}+3x(1-x)^{\frac{1}{2}}-2(1-x)^{\frac{3}{2}}+2\theta(1-2x)(1-2x)^{3/2}\right]$, θ(x) is the Heaviside step function
Raman	$\frac{1}{(2x)^6}\left[-\frac{3}{8}x^2(1+x)^{-\frac{1}{2}}-3x(1+x)^{\frac{1}{2}}-2(1+x)^{\frac{3}{2}}+2(1+2x)^{3/2}\right]$
Linear Stark	$\frac{1}{(2x)^6}\left[2-(1-x)^{\frac{3}{2}}-(1+x)^{\frac{3}{2}}\right]$
Quadratic Stark	$\frac{1}{(2^{10}x^5)}\left[(1-x)^{-\frac{1}{2}}-(1+x)^{-\frac{1}{2}}-\frac{x}{2}(1-x)^{-\frac{3}{2}}-\frac{x}{2}(1+x)^{-\frac{3}{2}}\right]$
Divergent term	$\frac{1}{(2x)^6}\left[-2-\frac{35x^2}{8}-\frac{x}{8}(3x-1)(1-x)^{-\frac{1}{2}}-3x(1-x)^{\frac{1}{2}}+(1-x)^{\frac{3}{2}}+\frac{x}{8}(3x+1)(1+x)^{-\frac{1}{2}}+3x(1+x)^{\frac{1}{2}}+(1+x)^{\frac{3}{2}}\right]$

Table 2.1: *Dispersion of $G_2(x)$, $x= h\upsilon/Eg$.*

2.3 Reference

[1]Kern, Werner. *Thin film processes II*. Vol. 2. Academic press, 2012.

[2]Mattox, Donald M., and Vivienne Harwood Mattox. *Vacuum coating technology*. William Andrew Publishing, New York, 2003.

[3]Holland, Leslie. "Vacuum deposition of thin films." *London: Chapman & Hall, 1970* 1 (1970).

[4]Horiba scientific, “A guidebook to particle size analysis”, manual.

[5]Mettler-Toledo DSC model 822e, Switzerland, manual.

[6]Kurian, Achamma, Rajesh B. Kumar, and Sajan D. George. "Thermal characterization of nanofluids using laser induced thermal lens technique." In*SPIE NanoScience+ Engineering*, pp. 73930U-73930U. International Society for Optics and Photonics, 2009.

[7]Instruction manual, Diode pumped solid state lasers. BWH/BWT-xx series.

[8]HMS light beam chopper instruction manual ITHACO model 230, New York (1985).

[9]Magde, Douglas, James H. Brannon, Teresa L. Cremers, and John Olmsted. "Absolute luminescence yield of cresyl violet. A standard for the red." *Journal of Physical Chemistry* 83, no. 6 (1979): 696-699.

[10]Bindhu, C. V., S. S. Harilal, Geetha K. Varier, Riju C. Issac, V. P. N. Nampoori, and C. P. G. Vallabhan. "Measurement of the absolute fluorescence quantum yield of rhodamine B solution using a dual-beam thermal lens technique." *Journal of Physics D: Applied Physics* 29, no. 4 (1996): 1074.

[11]Hecht, E. "Optics 4ed." (2002).

[12]Ball, David W. *Field guide to spectroscopy*. Vol. 8. Spie Press, 2006.

[13]Brodsky, Marc Herbert, ed. *Amorphous semiconductors*. Vol. 36. Springer, 1979.

[14]Vaško, A., D. Ležal, and I. Srb. "Oxygen impurities and defects in chalcogenide glasses." *Journal of Non-Crystalline Solids* 4 (1970): 311-321.

[15]Urbach, Franz. "The long-wavelength edge of photographic sensitivity and of the electronic absorption of solids." *Physical Review* 92, no. 5 (1953): 1324.

[16]Tauc, Jan, ed. *Amorphous and liquid semiconductors*. Springer Science & Business Media, 2012.

[17]R. Swanepoel,“Determination of the thickness and optical constants of amorphous silicon”, *Journal of Physics E: Scientific Instruments* 16 (1983): 1214-1222.

[18]Manifacier, J. C., J. Gasiot, and J. P. Fillard. "A simple method for the determination of the optical constants n, k and the thickness of a weakly absorbing thin film." *Journal of Physics E: Scientific Instruments* 9, no. 11 (1976): 1002.

[19]Wemple, S. H., and M. DiDomenico Jr. "Behavior of the electronic dielectric constant in covalent and ionic materials." *Physical Review B* 3, no. 4 (1971): 1338.

[20]Wemple, S. H. "Refractive-index behavior of amorphous semiconductors and glasses." *Physical Review B* 7, no. 8 (1973): 3767.

[21]Tanaka, Keiji. "Optical properties and photoinduced changes in amorphous As-S films." *Thin Solid Films* 66, no. 3 (1980): 271-279.

[22]Bernal-Oliva, A. M., E. Marquez, J. M. Gonzalez-Leal, A. J. Gamez, R. Prieto-Alcon, and R. Jimenez-Garay. "Spectral dependence of the complex refractive index of GeS2 chalcogenide glass thin films." *Journal of materials science letters* 16, no. 8 (1997): 665-668.

[23]Ruiz-Pérez, J., E. Márquez, D. Minkov, J. Reyes, J. B. Ramirez-Malo, P. Villares, and R. Jiménez-Garay. "Computation of the optical constants of thermally-evaporated thin films of GeSe2 chalcogenide glass from their reflection spectra." *Physica Scripta* 53, no. 1 (1996): 76.

[24]Tintu, R., K. Saurav, K. Sulakshna, V. P. N. Nampoori, P. Radhakrishnan, and Sheenu Thomas. "Ge28Se60Sb12/PVA composite films for photonic applications." *Journal of Non-Oxide Glasses* 2, no. 4 (2010): 167-174.

[25]Pankove, Jacques I. *Optical processes in semiconductors*. Courier Corporation, 2012.

[26]Cary Eclipse Hardware operational manual. Varian. Australia (2000).

[27]Sheik-Bahae, Mansoor, Ali Said and E W van Stryland. "*High-sensitivity, single-beam n_2 measurements*", Optics Letters 14, (1989): 955-957.

[28]Sheik-Bahae, Mansoor, Ali Said, Tai-Huei Wei, David J. Hagan, and Eric W. Van Stryland. "Sensitive measurement of optical nonlinearities using a single beam." *Quantum Electronics, IEEE Journal of* 26, no. 4 (1990): 760-769.

[29]Wei, Tai-Huei, Tzer-Hsiang Huang, Huang-Der Lin, and Sheng-Hsien Lin. "Lifetime determination for high-lying excited states using Z scan." *Applied physics letters* 67, no. 16 (1995): 2266-2268.

---

[30]Sheik-Bahae, Mansoor, David Crichton Hutchings, David J. Hagan, and Eric W. Van Stryland. "Dispersion of bound electron nonlinear refraction in solids."*Quantum Electronics, IEEE Journal of* 27, no. 6 (1991): 1296-1309.

Chapter 3

Studies on the effect of composition on the properties of bulk glass

The preparation and detailed characterization of four different compositions of germanium based selenide glasses $Ge_{20}Se_{80}$, $Ge_{27}Se_{73}$, $Ge_{27}Sb_9Se_{64}$ and $Ge_{27}Ga_9Se_{64}$are are described in this chapter with the aim of understanding the role of chemical composition in determining their structural and physical properties. Compositional dependence of bulk glass properties for the above mentioned compositions have been conducted and variations in the glass transition temperatures, glass structure and optical band gap have been observed. Detailed discussions on different composition dependent phenomena are presented in the chapter with valid arguments.

3.1 Introduction

Chalcogenide glasses are promising materials[1,2] for a variety of photonic applications such as ultrafast all-optical switches, frequency converters and optical amplifiers due to their low phonon energy, extended infrared transparency, high refractive index, good photosensitivity, ease of fabrication and processing, good chemical durability and special property of second/third-order optical non-linearity[3,4,5].

Selenium exhibits unique property of reversible phase transformation and also has device applications like photocells, xerography, memory switching etc. Since the pure selenium has disadvantage like short life time and low photo-sensitivity, impurity atoms like Ge, In, Bi, Te, Ga, Sb, Ag, etc. can be used to make alloys with Se, which may enhance sensitivity, crystallization temperature and reduce ageing effects[6,7]. In this work we have prepared and analysed four different compositions of selenide glasses $Ge_{20}Se_{80}$,

$Ge_{27}Se_{73}$, $Ge_{27}Sb_9Se_{64}$, and $Ge_{27}Ga_9Se_{64}$. The first two glasses are germanium selenide glasses of different compositions and in the compositions of the last two glasses, '9' atomic percentage of Se in $Ge_{27}Se_{73}$ glass is replaced by corresponding amount of intermediates Sb and Ga respectively.

In the present chapter compositional dependence of bulk glass properties for above mentioned compositions have been carried out. Composition dependent variations in the glass transition temperatures (Tg), optical band gap and the glass structure have been studied.

The chapter is divided into four sections as structural characterization by XRD, Raman and FTIR; compositional analysis using using EDS; thermal characterization using DSC and optical characterization using UV-VIS-NIR spectroscopy.

3.2 Scope of the chapter

Different passive and active applications of chalcogenide glasses in the area of optoelectronics require different forms (bulk, thin film nanostructures, fibers etc.) and compositions of chalcogenide glasses. Research on special glasses includes preparation procedure of high purity bulk glasses, diagnostic of their physical, chemical and optical properties and their implementation in active or passive devices. Here, the preparation and analysis of bulk glass is of great importance since it is the first step towards the realization of IR based sensor.

3.3 Preparation and characterization of bulk $Ge_{20}Se_{80}$, $Ge_{27}Se_{73}$, $Ge_{27}Ga_9Se_{64}$ and $Ge_{27}Sb_9Se_{64}$ glass

Bulk chalcogenide glasses were prepared by conventional melt quenching method. High purity materials were used for the glass preparation. The elemental form of Se, Ge (Sigma Aldrich, 5N purity) were taken in appropriate weight percentage and sealed in an evacuated fused quartz ampoule at about 10^{-3} mbar pressure. The sealed ampoule was then loaded to a rocking and rotating furnace at 1000°C. It was held in the furnace for 24 hours with continuous rocking and rotation for thorough mixing and homogenization of the melt and then rapidly quenched in ice cold water. The bulk glass is extracted from the ampoule by etching out the ampoule using hydro fluoric acid. Figure 3.1shows different stages of bulk glass preparation (a) shows the photograph quartz ampule (b) evacuated sealed ampoule

containing glass constituents before loading to rocking and rotating furnace and (c) photograph of ice water quenched ampoule (d) the prepared bulk $Ge_{20}Se_{80}$ sample after etching out the ampoule.

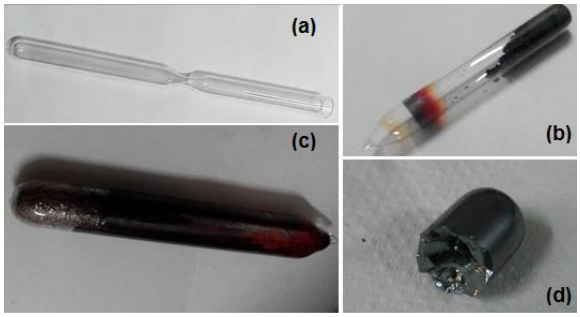

Figure 3.1: *(a) Photograph of quartz ampoule, (b) evacuated sealed ampoule with sample before loading to Rocking and Rotating furnace, (c) sealed ampoule after quenching, (d) bulk $Ge_{20}Se_{80}$ sample after removing the ampoule.*

3.3.1 Structural characterizations

X-ray diffraction studies

X-ray diffraction (Powder XRD) (Bruker AXS D8 Advance X-ray Diffractometer) studies were conducted on the powdered samples and the diffractograms obtained are shown in the figure 3.2.

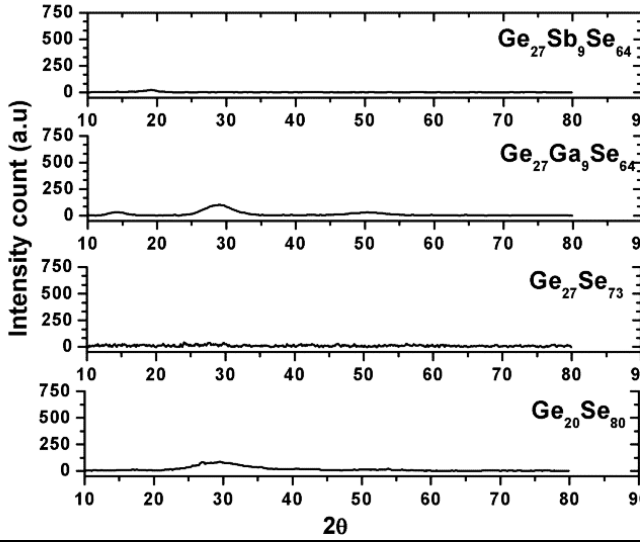

Figure 3.2: *XRD spectra of all compositions of bulk glasses show no prominent sharp peaks which reveal the amorphous nature of the samples.*

No prominent peaks were observed in the X-ray diffraction spectrum which reveals the amorphous nature of the samples. The occurrence of broad peaks in the XRD pattern of $Ge_{27}Ga_9Se_{64}$ and $Ge_{20}Se_{80}$ at 30° reveals the presence of Se chains which show the polymeric nature of the glass[8]. The absence of hump in the XRD pattern of $Ge_{27}Sb_9Se_{64}$ glass indicates the formation of a glass matrix with no excess 'Se' rings or chains.

FTIR Analysis

Chalcogenide glasses are well-known for infrared transparency due to its low phonon energy. Therefore infrared spectroscopy cannot be used to study its structural property analysis. However it can be used for the detection of different impurity elements. The major impurities present in chalcogenide glass materials are carbon, oxygen, and hydrogen. Figure 3.3 shows Fourier transform infrared spectra (FTIR) of all bulk glasses and it displays good infrared transparency.

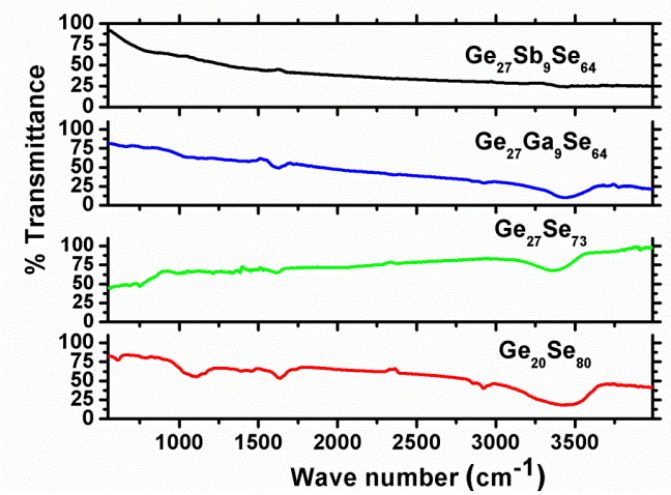

Figure 3.3: *FTIR spectra of $Ge_{27}Sb_9Se_{64}$ (black), $Ge_{27}Ga_9Se_{64}$ (blue), $Ge_{27}Se_{73}$ (green) and $Ge_{20}Se_{80}$ (red) bulk glass shows good transparency in IR region except the presence of some impurity peaks.*

FTIR spectrum of $Ge_{27}Sb_9Se_{64}$ glass shows no remarkable impurity absorption and it has almost constant IR transmittance throughout the region. A dip in the FTIR spectrum around 3400cm^{-1} observed for $Ge_{27}Ga_9Se_{64}$, $Ge_{27}Se_{73}$ and $Ge_{20}Se_{80}$ is corresponding to -OH stretching which is either connected to the glass network as Ge-OH or free as in interstitial H_2O[9]. The small absorption observed at 1630cm^{-1} is for H-O-H scissor bending vibration which is attributed to H_2O[10], indicating the presence of traces of impurity

water content in the sample. From the figure it is clear that other impurity bonds like Ge-O-Ge and Ga-O-Ga etc. bridges are absent, such that the presence of former would have caused absorption at 850cm^{-1} and 558cm^{-1} (stretching of -Ge-O and bending of Ge-O-Ge)[11] and the latter[12] at 510cm^{-1}. The small absorption dip observed at 2800cm^{-1} for $Ge_{20}Se_{80}$ glass is the signature of Se-H bond[13].

Raman analysis

In order to evaluate the bonding structure of the bulk glasses Raman spectroscopy has been employed. Micro-Raman analysis carried out on each bulk sample is shown in figure 3.4. The decomposed Gaussian which gives the relative contribution of each structural unit is also plotted in Figure 3.4. The Raman studies were conducted at near infrared wavelength, 785nm to avoid the possibility of photoinduced structural change with the irradiation[14,15,16]of visible wavelength during the time of analysis.

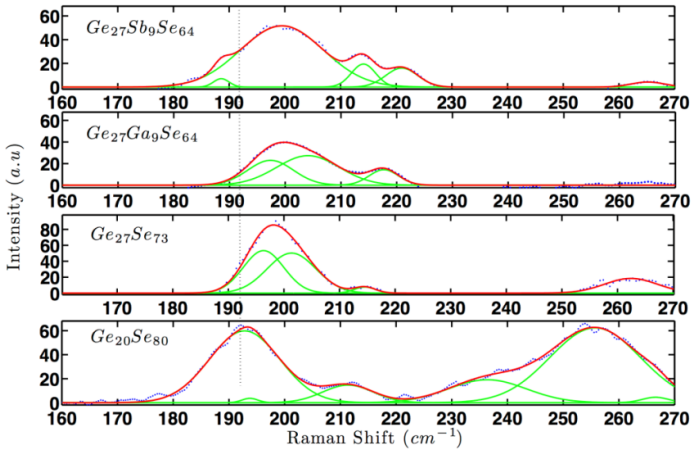

Figure 3.4: *Raman spectra of bulk glasses (red line) with 785nm excitation. Corner-Shared (CS) $GeSe_4$ vibrational frequency is found to be blue shifted from 193cm^{-1} to 198cm^{-1} with the increase of 'Ge' content. Here the green line represents the decomposed Gaussian.*

The main regions in these spectra are : (a) a broad, low-intensity band between 50 and 175cm^{-1}, (b) a relatively sharp high-intensity band around 198cm^{-1} except for $Ge_{20}Se_{80}$ (for which it is at 193cm^{-1}) along with a shoulder around 214cm^{-1}, and (c) a broad, high-intensity band spanning from 240 to 300cm^{-1}. Region (a) is associated with low-frequency bending and rocking modes of Se atoms in the structure. The 198cm^{-1} band in region (b) corresponds to the symmetric stretching of -Se- atoms in Ge-Se-Ge linkages

that are corner-shared (CS) between $GeSe_4$ tetrahedra (A_1^c mode) while the shoulder 214cm^{-1} band corresponds to the breathing mode of a pair of Se atoms (A_1 mode) that are edge-shared (ES) between two neighboring $GeSe_4$ tetrahedra[17,18,19,20]. The highest frequency band observed in region (c) is characteristic of that in the Raman spectrum of pure Se and is related to Se-Se stretching in Se chains and rings[21,22]. The shoulder at 190cm^{-1} in $Ge_{27}Sb_9Se_{64}$ has been attributed to heteropolar Sb-Se bond vibrations in the Sb_2Se_3 units[23,24].

Sample	Raman shift (cm^{-1})	Assignment
$Ge_{20}Se_{80}$	193	A1 breathing motion of CS $GeSe_4$.
$Ge_{27}Sb_9Se_{64}$, $Ge_{27}Ga_9Se_{64}$, $Ge_{27}Se_{73}$	198	A1 breathing motion of CS $GeSe_4$.
$Ge_{27}Sb_9Se_{64}$, $Ge_{27}Ga_9Se_{64}$, $Ge_{27}Se_{73}$, $Ge_{20}Se_{80}$	From 50 to 175	Bending and rocking modes of Se atoms in the structure
	214	Breathing mode of edge shared 'Se' between $GeSe_4$ tetrahedra
	260	Se-Se stretching in Se chains and rings.
$Ge_{27}Sb_9Se_{64}$	190	Sb–Se bond vibrations in the $SbSe_{3/2}$ pyramids

Table 3.1: *Raman band assignments for all compositions of chalcogenide glasses.*

Raman band assignments for all compositions are summarized in Table 3.1 and the Figure 3.5 represents the schematic of corner shared and edge shared tetrahedra.

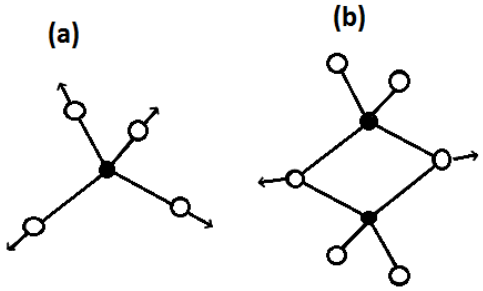

Figure 3.5: *The A1 modes (a) in the corner-sharing tetrahedron and (b) in the edge-sharing tetrahedron.*

In the $Ge_{20}Se_{80}$ glass the CS vibrational frequency (υ_{cs}) is observed at 193cm^{-1} and it is blue shifted with the increase of the 'Ge' content. For $Ge_{27}Se_{73}$, $Ge_{27}Sb_9Se_{64}$, and $Ge_{27}Ga_9Se_{64}$ samples (All of which have same atomic percentage of 'Ge') the CS vibrational frequency (υ_{cs}) is observed at 198cm^{-1}. With the increase of 'Ge' content, the intensity of the highest frequency band centered at ~260cm^{-1} decreases while that of the CS and ES vibrational bands increase monotonically, consistent with the progressive replacement of Se-Se-Se chains with CS and ES tetrahedral species in the glass structure. The bonding arrangement of the germanium selenide glasses from Raman analysis are (i) predominantly corner-connected $GeSe_{4/2}$ tetrahedra, (ii) a smaller fraction, edge-connected $GeSe_{4/2}$ tetrahedra, (iii) a comparable concentration of Se-Se bonds which interconnect the groups in (i) and (ii). In $Ge_{20}Se_{80}$ glass '40'out of '80' atomic percentage of 'Se' are bonded with 'Ge' and forms $GeSe_{4/2}$ CS as well as a small percentage of ES tetrahedral units and the remaining 'Se' connects these units by -Se-Se- chains. Similar is the case for $Ge_{27}Se_{73}$, such that out of '73' atomic percentage '54' are bonded with 'Ge' and forms $GeSe_{4/2}$ CS as well as a comparatively larger (than $Ge_{20}Se_{80}$) number of ES tetrahedral units and the remaining '19' atomic percentage of 'Se' which inter connects these units with -Se-Se- chains.

The composition $Ge_{27}X_9Se_{64}$ (where 'X' is Sb/Ga) is such that '9' atomic percentage of 'Se' is replaced by equivalent amount of 'Sb/Ga' and it results in a substantial reduction of the band around 260cm^{-1} arising from Se-Se stretching in Se chains and rings. That is CS and ES $GeSe_{4/2}$ tetrahedra are connected with a fraction of X_2Se_3 units[25,26]. K. Maeda[27] et.al have conducted a study on the effect of 'Ga' content on the structure of Ge-Se-Ga glasses and has observed that the 216cm^{-1} Raman band intensity (I_{216}) decreases with addition of Ga content up to 12 atomic percentage of Ga. Gallium forms dative bonds with 'Se' due to its high electropositive nature. The bonding model for Ga_2Se_3 can be represented symbolically as follows[27]

$$2Ga_2Se_3 = 3GaSe_{4/2}^{-} + Ga^{3+} \qquad (3.1)$$

In this bonding model, all of the Se-atoms are 3-fold coordinated, making two partially ionic, covalent bonds with Ga in the tetrahedrally-coordinated network component, and one forms donor-acceptor dative bond with the Ga^{3+} ions. So the dominant bonding arrangements in 'GeGaSe glass' are neutral $GeSe_{4/2}$ groups, negatively charged $GaSe_{4/2}^{-}$ (or equivalently $Se_3GaSe_1^{-}$) groups, and Ga^{3+} ions. Three $Se_3GaSe_1^{-}$ groups are required to neutralize each 6-fold coordinated Ga^{3+} ion, with additional screening by three network Se atoms.

From the XRD and Raman analysis, it is confirmed that $Ge_{27}Sb_9Se_{64}$ glass composition consists of structural units of the type $GeSe_2$ and Sb_2Se_3 with very little amount of Se-Se bonds leading to a completely cross linked three dimensional network consisting of $GeSe_2$ and Sb_2Se_3 unit and hence the resulting structure is highly rigid for this composition[28].

3.3.2 Compositional and density evaluation

EDS analysis

EDS spectrum have been taken to confirm the composition of all bulk glasses. Table 3.2 compares the atomic percentage of components obtained from EDS analysis with respect to the nominal composition. Figure 3.6 shows EDS spectrum of $Ge_{27}Ga_9Se_{64}$ glass.

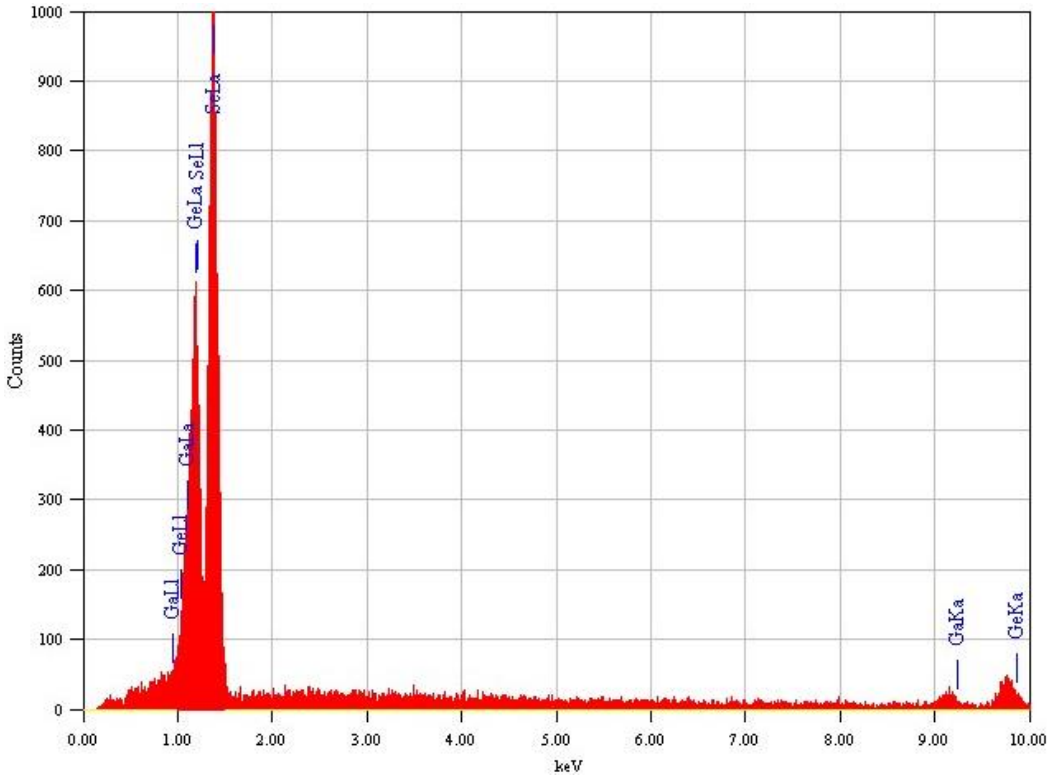

Figure 3.6: *EDS spectrum of $Ge_{27}Ga_9Se_{64}$ glass shows peaks corresponding to Ge, Ga, and Se.*

Nominal Composition	Element	Atomic %
$Ge_{20}Se_{80}$	Ge	11.31
	Se	88.69
$Ge_{27}Se_{73}$	Ge	30.78
	Se	69.22
$Ge_{27}Sb_9Se_{64,}$	Ge	27.32
	Sb	9.37
	Se	63.31
$Ge_{27}Ga_9Se_{64,}$	Ge	27.05
	Ga	9.36
	Se	63.59

Table 3.2: *Variation of atomic percentage of components obtained from EDS analysis with respect to the nominal composition.*

Density evaluation using Archimedes' principle

Densities of the bulk glasses were directly measured using Archimedes' principle. The samples were first weighed in air and then suspended in a liquid of known density. According to Archimedes' principle the weight of the sample when suspended may be expected to be reduced by the mass of the liquid displaced, which was equal to sample volume multiplied by the density of the liquid. The density of the sample can then be calculated to within ±0.02 g/cm^3 as follows[29,30]

$$\rho_s = \frac{m\rho_l}{\Delta w} \tag{3.2}$$

where ρ_s is the density of the sample, ρ_l is density of the liquid, m is the mass of the sample in air, and Δw is the change in weight of the sample upon submersion.

Densities of all compositions of bulk glasses have been determined by immersing specific mass of bulk glass pieces in de-mineralised water.

Composition	Density g/cm^3
$Ge_{20}Se_{80}$	4.35
$Ge_{27}Se_{73}$	4.21
$Ge_{27}Ga_9Se_{64}$	4.36
$Ge_{27}Sb_9Se_{64}$	4.6

Table 3.3: *The variation of density with respect to the composition*

The variation of density with respect to the composition is tabulated and is shown in table 3.3. $Ge_{27}Sb_9Se_{64}$ shows the highest density.

3.3.3 Thermal characterization

DSC Analysis

Glass transition temperature (Tg) of bulk glasses was determined by Differential scanning calorimetry (DSC). 'Tg' is assigned as the inflection point of DSC thermogram or it can be predicted as the minimum of the first derivative of heat flow versus temperature curve. Figure 3.7 shows DSC thermogram with 10°C/min heating rate as well as its first derivative for $Ge_{20}Se_{80}$ glass. Table.3.4 depicts the variation of 'Tg' with respect to the composition. The lowest value of Tg is observed for $Ge_{20}Se_{80}$ glass composition and the highest is for $Ge_{27}Ga_9Se_{64}$. The average coordination number ($\bar{r}$) for all glass compositions was calculated using the standard method[31] and is presented in the table.3.4. For example, for the composition $Ge_aGa_bSe_c$ system

$$\bar{r} = \frac{aN_{Ge}+bN_{Ga}+cN_{Se}}{a+b+c} \qquad (3.3)$$

where a, b and c are the atomic % of Ge, Ga and Se respectively and N_{Ge}, N_{Ga}, N_{Se}, are their respective coordination numbers.

In binary Ge_xSe_{100-x} glasses, at low x (< 20) or at an average coordination number $\bar{r}$ (< 2.4), the glass is at a floppy phase and the 'Ge' atoms randomly cross-link polymeric chains of Se_n. Under these situations, variations in T_g with x can be computed exactly using Stochastic Agglomeration Theory (SAT)[32,33], and one finds the slope to be given by a parameter-free relation,

$$\frac{dTg}{dx} = {T_0(x=0)}\Big/{\ln(\frac{r_{Ge}}{r_{Se}})} \tag{3.4}$$

where r_{Ge} (=4) and r_{Se} (=2) denote the coordination numbers of Ge and Se respectively. T_0 denotes the glass transition temperature for amorphous 'Se'.

Sample	Glass transition Temperature, Tg (°C)	Coordination Number ($\bar{r}$)	Average bond energy $< E >$ eV/atom
$Ge_{20}Se_{80}$	212	2.4	2.35
$Ge_{27}Se_{73}$	250	2.54	2.46
$Ge_{27}Sb_9Se_{64}$	262	2.63	2.77
$Ge_{27}Ga_9Se_{64}$	343	2.63	3.07

Table 3.4: *Variation of Tg, $\bar{r}$ and $< E >$ with respect to the composition.*

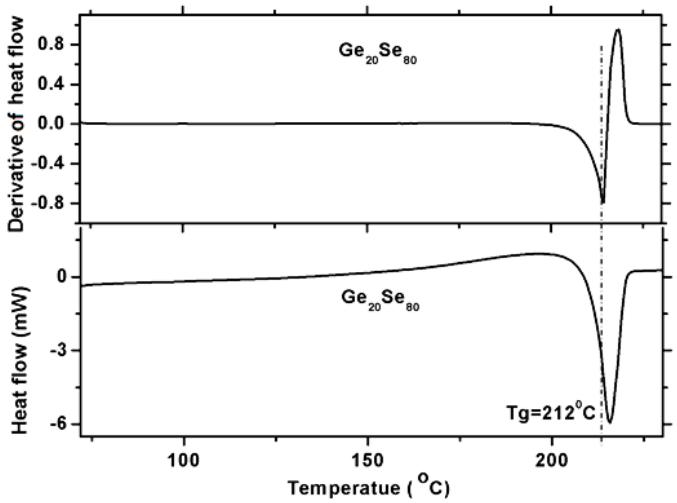

Figure 3.7: *DSC Thermogram and its first derivative of $Ge_{20}Se_{80}$ acquired at a rate of 10°C/min.*

The addition of Ge atoms, (which is higher coordinated) to the base network of selenium chains steadily increases T_g in an almost linear fashion. Variation of T_g values with respect to the composition in Ge_xSe_{1-x} glasses has been presented by P. Boolchand et.al[15] showing a linear increase at low x, and a maximum near x = 34. The linear increase in T_g at low x is excellent in accordance with the predictions of slope equation (eqn 3.4) corresponding to

the straight line drawn. At higher x (≥20) or at $\bar{r}$ (≥2.4), the stochastic agglomeration process ceases to be stochastic as isostatically rigid local structures form and self-organize. At this stage a nonlinear increase in T_g is observed. At still higher x (>27), the glass is over coordinated and stressed–rigid corner-sharing $GeSe_{4/2}$ tetrahedra and homopolar Ge–Ge bonds form, and one does not expect SAT to really work. A comparison of theory with experiment reported by P. Boolchand et.al clearly supports the general picture and is shown in figure 3.8.

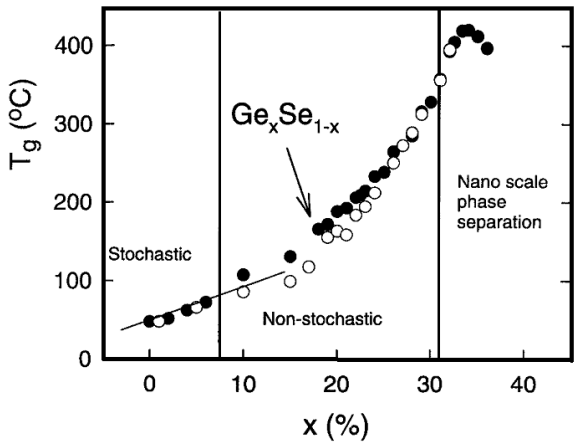

Figure 3.8: *Variation of T_g with respect to 'Ge' concentration in binary Ge_xSe_{100-x} glasses reported by Boolchand et.al*[15]

In the case of $Ge_{27}X_9Se_{64}$ (which has a common $\bar{r}$ = 2.63) glass samples $Ge_{27}Ga_9Se_{64}$ shows highest value of Tg even though both have same 'coordination number'. Substitution of Ga for Sb leads an increase in T_g about 81°C which is close to literature value 80°C, reported by L. Calvez. Et al[34]. This phenomenon can be explained by the fourfold coordination of the gallium (formation of additional dative bond with 'Se' lone pairs), which increases the glass reticulation and thereby 'Tg'. According to Tichy[35] et. al, the value of glass transition temperature should not only be related to connectedness of the network which is related to $\bar{r}$, but should also be related to the quality of connections, i.e., the mean bond energy between the atoms of the glass network. The overall mean bond energy for the glass system is given by

$$< E >= \bar{E}_c + \bar{E}_{rm} \tag{3.5}$$

where $\bar{E}_c$ is the mean bond energy of the average cross-linking/atom (heteropolar bond energy) and $\bar{E}_{rm}$ is the average bond energy per atom of

the "remaining" matrix (homopolar bond energy) after the strong bonds have been maximized. For 'Se' rich glasses, for example consider $Ge_xSe_yGa_z$ system, where (x + y + z) = 1

$$E_c = 4xE_{Ge-Se} + 3zE_{Se-Ga} \tag{3.6}$$

$$E_{rm} = \left[\frac{2y-4x-3z}{\bar{r}}\right] E_{Se-Se} \tag{3.7}$$

Variation of average bond energy with respect to the composition is depicted in table 3.4 and it is clear that glass transition temperature increases with the increase of average bond energy.

3.3.4 Optical Characterization

UV-VIS-NIR Spectroscopy

Variation of optical bandgap for different compositions of bulk glass is shown in figure 3.9. From the figure it is observed that the bulk samples are not transparent in visible region. Absorption spectra of all samples are featured with an extended band tail upto IR region. Variation of bandgap with respect to the composition is shown in Table 3.5. The lowest bandgap is observed for $Ge_{20}Se_{80}$ and the highest for $Ge_{27}Ga_9Se_{64}$.

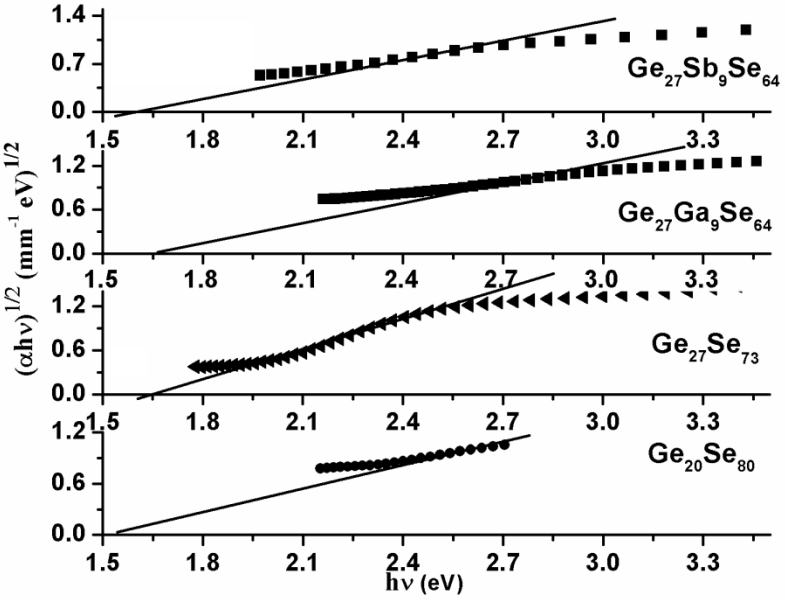

Figure 3.9: *Tauc plot of all samples featured with an extended band tail upto IR region and it shows a variation in optical bandgap with respect to composition.*

The bonding and the resulting variation in the bandgap in chalcogen contained amorphous materials have been explained by Marc Kastner[36]. According to Kastner, the electronic states of a solid may be considered to be a broadened superposition of the molecular orbital states of the constituent bonds. 'Ge' atom in fourfold coordination, hybridized to sp^3 orbitals, are split into bonding (σ) and antibonding (σ*) states. In solids, these molecular states are broadened into bands. Thus, in tetrahedral semiconductors, the bonding band forms the valence band and the antibonding band forms the conduction band as shown in figure 3.10(A). In Se, on the other hand, the s states lie well below the p states and need not be considered. Since Se has two-fold coordination, only 'two' of the 'three P states' are utilized for bonding, which spits into bonding and antibonding states. This leaves one nonbonding (lone pair) electron pair and the situation is sketched in figure 3.10 (B).

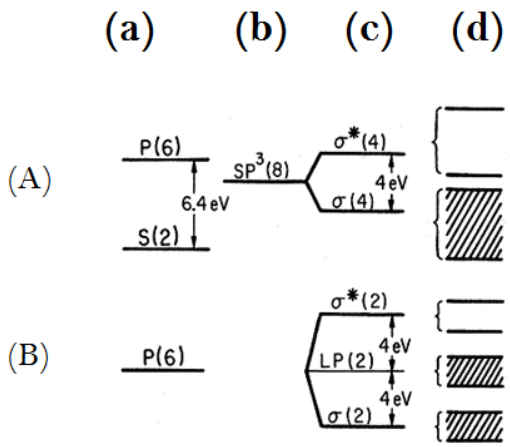

Figure 3.10: *Bonding in (A) Ge and (B) Se; (a) atomic states, (b) hybridized states, (c) molecular states, (d) broadening of states into bands in the solid.*

If we alloy these two to a vitreous compound, the coordination environment will be adjusted to satisfy valance requirement of each atom and results in the formation of an inorganic Se-Se, Ge-Se network. The LP band of Se fall near the gap of Ge, therefore, the presence of excessive Se concentration leads to the delocalization of LP band, and the resultant bandgap in chalcogenide glass becomes narrower, which is clear from bulk glass absorption spectrum. This situation is demonstrated[36] in figure 3.11, and it is clear from the table 3.5 that the replacement of Se with Ge shows an increase in the bandgap, i.e. the composition $Ge_{27}Se_{73}$ has a bandgap of 1.64eV whereas for $Ge_{20}Se_{80}$, it is 1.55eV.

The molecular state energy of Antimony (Sb) which is also sketched in figure 3.11 shows its bonding and antibonding states fall in the gap region of Se which reduces the bandgap. Therefore in a particular Ge_xSe_{1-x} composition substitution of Se with Sb with fixed Ge content will lead to the decrease in the bandgap of the resultant glass. $Ge_{27}Se_{73}$ glass has an optical bandgap of 1.64eV whereas for $Ge_{27}Sb_9Se_{64}$ it is 1.59eV.

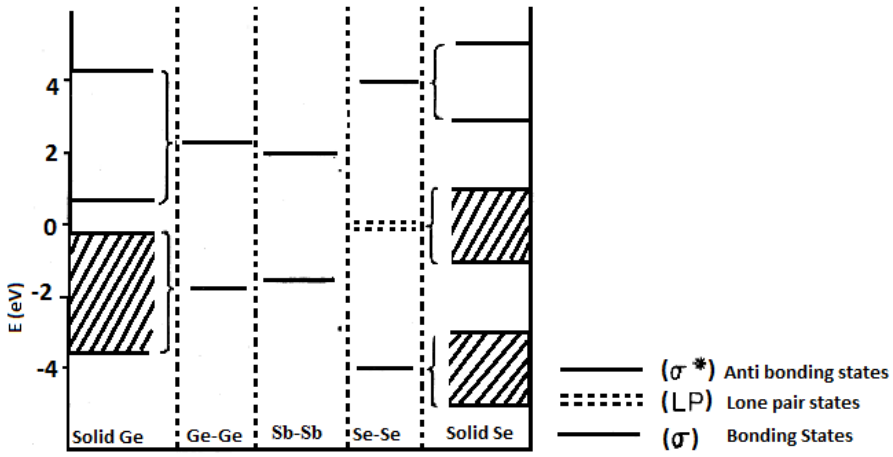

Figure 3.11: *Molecular states of Ge-Ge, Sb-Sb, and Se-Se bonds. Energy bands of solid Ge and Se are sketched for comparison.*

As discussed earlier substitution with Ga will widen the bandgap of the resulting glass since Ga has a tendency to increase its coordination number from 3 to 4 by forming dative bonds with the Se atom lone pairs (LP). These bonds lower the LP electronic states and widen the LP-σ* transition, thus increasing the bandgap. From the table 3.5 it is clear that the $Ge_{27}Ga_9Se_{64}$ glass shows the highest bandgap. The number of LP electrons is calculated using the relation[37]

$$L = V - Z \tag{3.8}$$

where L is the number of lone pair electrons, V is the valance electron and Z is the average coordination number. Variation of number of LP electrons for different compositions is shown in table. According to Pauling[38], increasing in the number of lone-pair electrons decreases the strain energy in a system and structures with large numbers of lone-pair electrons favours glass formation.

Composition	Lone-pair electrons L=V-Z	Bandgap eV
$Ge_{20}Se_{80}$	3.2	1.55
$Ge_{27}Se_{73}$	2.92	1.64
$Ge_{27}Ga_9Se_{64}$	2.56	1.66
$Ge_{27}Sb_9Se_{64}$	2.74	1.59

Table 3.5: *Variation of bandgap and lone-pair electrons with respect to composition*

3.4 Summary of findings

- Chalcogenide glasses of compositions $Ge_{20}Se_{80}$, $Ge_{27}Se_{73}$, $Ge_{27}Sb_9Se_{64}$ and $Ge_{27}Ga_9Se_{64}$ have been prepared and its physical, structural, thermal and optical characterization were conducted.
- X-ray diffraction (Powder XRD) studies were conducted on the powdered samples and no prominent peaks were observed in spectrum which reveals the amorphous nature of the samples
- Compositional analysis of all samples was carried out using EDS which reveals a slight variation compared to the expected composition.
- Structural characterization using Raman analysis predicts the bonding arrangement in the glasses as (i) predominantly CS tetrahedra, (ii) a smaller fraction ES units, and (iii) a comparable concentration of Se-Se bonds which interconnect the groups in (i) and (ii). In the case of $Ge_{27}X_9Se_{64}$ (where 'X' is Sb/Ga) analysis predicts CS and ES $GeSe_{4/2}$ tetrahedra interconnected with a fraction of X_2Se_3 units as well as -Se-Se- bonds.
- Thermal characterization reveals that Tg values increases with the increase in the mean coordination number and average bond energy.
- Optical characterization carried out using UV-Vis-NIR spectroscopy shows highest bandgap for $Ge_{27}Ga_9Se_{64}$ and the lowest for Se rich $Ge_{20}Se_{80}$. LP band of Se which is located in the gap region of Ge make the bandgap narrower with the increase of Se content. Addition of Ga leads to the widening of the bandgap due to the formation of dative bonds with LP electrons which widen the LP-σ* transition. The molecular state energy level of Sb is narrower than that of Se and Ge which results in decrease of the bandgap.

3.5 References

[1]Vogel E. M., M. J. Weber, and DMon Krol. "Nonlinear optical phenomena in glass." *Physics and chemistry of glasses* 32, no. 6 (1991): 231-254.

[2]Zakery A., and S. R. Elliott. "Optical properties and applications of chalcogenide glasses: a review." *Journal of Non-Crystalline Solids* 330, no. 1 (2003): 1-12.

[3]Liu Q. M., X. J. Zhao, and F. X. Gan. "Second harmonic generation in the system Ge-As-S and analysis of the poling mechanism." *Acta Physica Sinica* 49, no. 9 (2000): 1726-1730.

[4]Liu Qiming, Fuxi Gan, Xiujian Zhao, Katsuhisa Tanaka, Aiko Narazaki, and Kazuyuki Hirao. "Second-harmonic generation in $Ge_{20}As_{25}S_{55}$ glass irradiated by an electron beam." *Optics letters* 26, no. 17 (2001): 1347-1349.

[5]Quémard C., F. Smektala, V. Couderc, A. Barthelemy, and J. Lucas. "Chalcogenide glasses with high nonlinear optical properties for telecommunications." *Journal of Physics and Chemistry of Solids* 62, no. 8 (2001): 1435-1440.

[6]M. Saxena, J. Physics D: Applied Phyics, "A crystallization study of amorphous $Te_x(Bi_2Se_3)_{1-x}$ alloys with variation of the Se content", 2005, 38, 460–463.

[7]Tanaka Keiji. "Structural phase transitions in chalcogenide glasses." *Physical Review B* 39, no. 2 (1989): 1270-1279.

[8]Anant Vidya Nidhi, Vivek Modgil, V. S. Rangra, "The Effect of Compositional Variation on Physical Properties of $Te_9Se_{72}Ge_{19-x}Sbx$ (X = 8, 9, 10, 11, 12) Glassy Material", *New Journal of Glass and Ceramics*, no. 3, (2013), 91-98

[9]Ma D. S., P. S. Danielson, and Cornelius T. Moynihan. "Bulk and impurity infrared absorption in $0.5As_2Se_3$-$0.5GeSe_2$ glass." *Journal of Non-Crystalline Solids* 37, no. 2 (1980): 181-190.

[10]Ma D.S., Dong Sung, P. S. Danielson, and C. T. Moynihan. "Multiphonon absorption in XAs_2S_3-$(1-X)GeS_2$ glasses." *Journal of non-crystalline solids* 81, no. 1 (1986): 61-70

[11]Sharma Shiv K., and Dean W. Matson. "Raman spectra and structure of sodium aluminogermanate glasses." *Journal of non-crystalline solids* 69, no. 1 (1984): 81-96.

[12]Ruller Jacqueline A., and John M. Jewell. "Raman and infrared spectra of lead gallosilicate glasses." *Journal of non-crystalline solids* 175, no. 1 (1994): 91-97.

[13]Moynihan C. T., P. B. Macedo, M. S. Maklad, R. K. Mohr, and R. E. Howard. "Intrinsic and impurity infrared absorption in As 2 Se 3 glass." *Journal of Non-Crystalline Solids* 17, no. 3 (1975): 369-385.

[14]Boolchand P., and W. J. Bresser. "The structural origin of broken chemical order in GeSe2 glass." *Philosophical Magazine B* 80, no. 10 (2000): 1757-1772.

[15]Boolchand P., X. Feng, and W. J. Bresser. "Rigidity transitions in binary Ge–Se glasses and the intermediate phase." *Journal of Non-Crystalline Solids* 293 (2001): 348-356.

[16]Wang Fei, Sergey Mamedov, P. Boolchand, B. Goodman, and Meera Chandrasekhar. "Pressure Raman effects and internal stress in network glasses." *Physical Review B* 71, no. 17 (2005): 174201.

[17]Jackson Koblar, Arlin Briley, Shau Grossman, Dirk V. Porezag, and Mark R. Pederson. "Raman-active modes of a-GeSe 2 and a-GeS 2: A first-principles study." *Physical Review B* 60, no. 22 (1999): R14985.

[18]Sugai S. "Stochastic random network model in Ge and Si chalcogenide glasses." *Physical Review B* 35, no. 3 (1987): 1345.

[19]Wang Yong, Osamu Matsuda, Koichi Inoue, Osamu Yamamuro, Takasuke Matsuo, and Kazuo Murase. "A Raman scattering investigation of the structure of glassy and liquid Ge_xSe_{1-x}." *Journal of non-crystalline solids* 232 (1998): 702-707.

[20]Wang Yong, and K. Murase. "Floppy modes and relaxation in Ge_xSe_{1-x} glasses." *Journal of non-crystalline solids* 326 (2003): 379-384.

[21]Lucovsky G., A. Mooradian, W. Taylor, G. B. Wright, and R. C. Keezer. "Identification of the fundamental vibrational modes of trigonal, α-monoclinic and amorphous selenium." *Solid State Communications* 5, no. 2 (1967): 113-117.

[22]Carroll P. J., and J. S. Lannin. "Raman Scattering of amorphous selenium films." *Solid State Communications* 40, no. 1 (1981): 81-84.

[23]Ivanova Z. G., V. Pamukchieva, and M. Vlček. "On the structural phase transformations in Ge x Sb 40− x Se 60 glasses." *Journal of non-crystalline solids* 293 (2001): 580-585.

[24]Petit L., N. Carlie, H. Chen, S. Gaylord, J. Massera, G. Boudebs, J. Hu, A. Agarwal, L. Kimerling, and K. Richardson. "Compositional dependence of the nonlinear refractive index of new germanium-based chalcogenide glasses."*Journal of Solid State Chemistry* 182, no. 10 (2009): 2756-2761.

[25]Gopal E. S. R., T. S. Mukundan, J. Philip, and S. Sathish. "Low temperature elastic behaviour of As-Sb-Se and Ge-Sb-Se glasses." *Pramana-Journal of Physics* 28, no. 5 (1987): 471-482.

[26]Calvez, Laurent, Pierre Lucas, Mathieu Rozé, H. L. Ma, Jacques Lucas, and X. H. Zhang. "Influence of gallium and alkali halide addition on the optical and thermo–mechanical properties of $GeSe_2$-Ga_2Se_3 glass." *Applied Physics A* 89, no. 1 (2007): 183-188.

[27]Maeda K., T. Sakai, K. Sakai, T. Ikari, M. Munzar, D. Tonchev, S. O. Kasap, and G. Lucovsky. "Effect of Ga on the structure of Ge–Se–Ga glasses from thermal analysis, Raman and XPS measurements." *Journal of Materials Science: Materials in Electronics* 18, no. 1 (2007): 367-370.

[28]Giridhar A., P. S. L. Narasimham, and Sudha Mahadevan. "Electrical properties of Ge-Sb-Se glasses." *Journal of Non-crystalline solids* 37, no. 2 (1980): 165-179.

[29]Hughes Stephen W. "Archimedes revisited: a faster, better, cheaper method of accurately measuring the volume of small objects." *Physics education* 40, no. 5 (2005): 468.

[30]Nathan A. Carlie, PhD thesis, "A solution-based approach to the fabrication of novel chalcogenide glass materials and structures".

[31]Sharma Pankaj, and S. C. Katyal. "Effect of tellurium addition on the physical properties of germanium selenide glassy semiconductors." *Physica B: Condensed Matter* 403, no. 19 (2008): 3667-3671.

[32]Kerner Richard, and Matthieu Micoulaut. "A theoretical model of formation of covalent binary glasses. I. General setting." *Journal of non-crystalline solids*176, no. 2 (1994): 271-279.

[33]Micoulaut Matthieu. "The slope equations: A universal relationship between local structure and glass transition temperature." *The European Physical Journal B-Condensed Matter and Complex Systems* 1, no. 3 (1998): 277-294.

[34]L. Calvez, H.L. Ma, J. Lucas, X.H. Zhang," Preparation and properties of glasses and glass-ceramics based on $GeSe_2$-Sb_2Se_3 and halides,", Phys. Chem. Glasses: Eur. J. Glass Sci. Technol. B 47, 142 (2006).

[35]Tichý L., and H. Ticha. "On the chemical threshold in chalcogenide glasses." *Materials Letters* 21, no. 3 (1994): 313-319.

[36]Kastner Marc. "Bonding bands, lone-pair bands, and impurity states in chalcogenide semiconductors." *Physical Review Letters* 28, no. 6 (1972): 355.

[37]Zhenhua Liang. "Chemical bond approach to the chalcogenide glass forming tendency." *Journal of non-crystalline solids* 127, no. 3 (1991): 298-305.

[38]Pauling Linus. *The nature of the chemical bond and the structure of molecules and crystals: an introduction to modern structural chemistry*. Vol. 18. Cornell University Press, 1960.

Chapter 4

Synthesis and characterization of nanocolloids of chalcogenide glass

---

Journal publications

- *Indu Sebastian, S. Divya, V. P. N. Nampoori, P. Radhakrishnan, and Sheenu Thomas, "Impact of intermediate localized states on nonlinear optical absorption of Ga-Ge-Se nanocolloidal solutions", Appl. Phys. Lett. 102, 031115 (2013); doi: 10.1063/1.4789436*
- *Indu Sebastian, S. Mathew, V. P. N. Nampoori, P. Radhakrishnan, and Sheenu Thomas, "Concentration tuned bandgap and corresponding nonlinear refractive index dispersion in Ga-Ge-Se nanocolloids", J. Appl. Phys. 114, 053102 (2013); doi: 10.1063/1.4817176*
- *Indu Sebastian, V. P. N. Nampoori, P. Radhakrishnan, and Sheenu Thomas, "Experimental verification of localized defect states in Ga-Ge-Se nanocolloidal solutions", J. Mater Sci. 49, 3732–3735 (2014); doi 10.1007/s10853-014-8084-8*
- *Indu Sebastian, S. Divya, V. P. N. Nampoori, P. Radhakrishnan, and Sheenu Thomas, "Investigation of nonlinear opticalproperties of Ga-Ge-Se nanocolloidal solutions", IEEE Optical Engineering, special edition.*

This chapter deals with the solution processing of chalcogenide glasses of different compositions and their structural, compositional and optical characterization using different techniques. The formation of nanoclusters and the dependence of cluster size with concentration are confirmed by different analysis. Various characterizations carried out on nanocolloids confirms a concentration dependent variation in linear and nonlinear optical properties of all compositions of nanocolloids. Photo irradiation experiments were carried out using pulsed and continuous lasers of different wavelengths and variations in the structural and optical properties of the nanoclusters were studied by employing various methods.

4.1 Introduction

Chalcogenide glasses when dissolved in organic solvents allow new and simple deposition routes. The solution processing and thin film deposition of chalcogenide glasses were first reported by Chern and Lauks[1]. Dissolution of chalcogenide glasses is a low cost process and it results in the formation of clusters[2] with dimensions of several nanometers. Studies on structural[3], optical[4] and thermal[5] properties of solvent processed films reveal that it retains the bulk glass stoichiometry.

The main advantages of solution processing are 1) it enables spin-coating of the solution onto a substrate which permits large area or thick film deposition, both of which are difficult to obtain through the techniques such as thermal evaporation, sputtering, or pulsed laser deposition, 2) the solutions can be adopted for other deposition techniques such as mold casting[6,7] and ink jet printing[8], 3) the resulting film could be made substantially micro-structure free so as to be potentially useful for high resolution pattern replication and 4) most of the chalcogenide materials dissolved in amines lead to homogeneous thin films that retain the optical, physical and chemical properties of the solute[9,10]. The elimination of high vacuum during the deposition also allows for higher production rates and simpler processing. Also, the solution based deposition opens up the opportunity for the fabrication of composite films by incorporating other materials[11] like carbon, noble metal or semiconductor nanoparticles, or polymers such that these materials may be dissolved or dispersed into the same solution.

4.2 Scope of the chapter

This chapter deals with the preparation of chalcogenide glass nanocolloids based on novel solution-based approach and evaluation of their structural and optical characteristics using different techniques. Different analysis conducted on these colloids reveal that they are promising materials and the studies carried out on all four compositions of nanocolloids help to understand compositional dependent variations of different optical and structural properties of the nanoclusters. This will open an opportunity to engineer solution derived, chalcogenide glass based IR transparent substrates.

4.3 Synthesis of chalcogenide glass nanocolloids

Chalcogenide glass nanocolloids can be prepared by dissolving it in various alkali[12,13] and amine[14,15,16] solutions. Studies reveal that dissolution in amine retains the bulk glass stoichiometry than that in alkaline solutions. In general, there are three basic forms of organic amines: primary ($R\text{-}NH_2$), secondary ($R_2{=}NH$) and tertiary ($R_3{\equiv}N$), with R being some form of carbon chain. All of these are considered as bases because of their ability to donate their electron lone pair. During the reaction of amines containing N-H bonds it is possible to cleave the bonds in the bulk glass network which results in the formation of nano-sized fragments.

Nanocolloidal chalcogenide glasses of four different compositions $Ge_{27}Ga_9Se_{64}$, $Ge_{27}Sb_9Se_{64}$, $Ge_{27}Se_{73}$, and $Ge_{20}Se_{80}$ and with varying concentrations were prepared by dissolving it in n-butyl amine as well as ethanol amine (Sigma Aldrich, 99.9%). Ethanolamine is a colourless, viscous liquid whereas n-butylamine is a less viscous, highly evaporative liquid. Both amines act as weak base and have an odour similar to that of ammonia. The dissolution was carried out inside a sealed glass container by giving 24 hours stirring. After dissolution, the solutions were filtered out using a 200nm pore size Polytetrafluoroethylene (PTFE) syringe filter to remove any undissolved particles. Initially studies were carried out with butylamine as the solvent and subsequently chalcogenide glasses dissolved in ethanolamine was also taken up for studies.

4.4 Studies on Chg/Butylamine nanocolloids

Dissolution of all compositions in solvent butyl amine is time consuming. Table 4.1 displays the concentrations of different compositions of the nanocolloidal solutions prepared and their assigned sample codes.

Composition	Sample code	Concentration mg/ml
$Ge_{27}Ga_9Se_{64}$	C0	0.54
	C1	0.30
	C2	0.25
	C3	0.20
	C4	0.11
	C5	0.096
$Ge_{27}Sb_9Se_{64}$	D0	0.54
	D1	0.30
	D2	0.25
	D3	0.20
$Ge_{27}Se_{73}$	E0	0.54
	E1	0.30
	E2	0.25
$Ge_{20}Se_{80}$	F0	0.54
	F1	0.30

Table 4.1: *Concentrations of different compositions of the nanocolloidal solutions prepared and their assigned sample codes.*

4.4.1 Analysis on cluster size and composition

0.2ml of C1 concentration were spin coated on a 1cmx1cm silica substrate at 1000rpm and its scanning electron microscope (JEOL Model JSM-6390LV) image was taken. Figure 4.1 (a) and 4.1 (b) show SEM images of unfiltered and filtered $Ge_{27}Ga_9Se_{64}$ solution in butyl amine respectively with concentration C1=0.30mg/ml. Unfiltered sample shows large pieces of clusters with the range 1-2μm and after filtration the average cluster size reduced to around 100nm. The actual cluster size of chalcogenide glass solute in the solution is much less than the grain size in the spin coated samples used for

SEM analysis as reported by Kohoutek et al[2]. The increase in the cluster size is due to the agglomeration of the solute particles as a result of solvent evaporation at the time of spin coating.

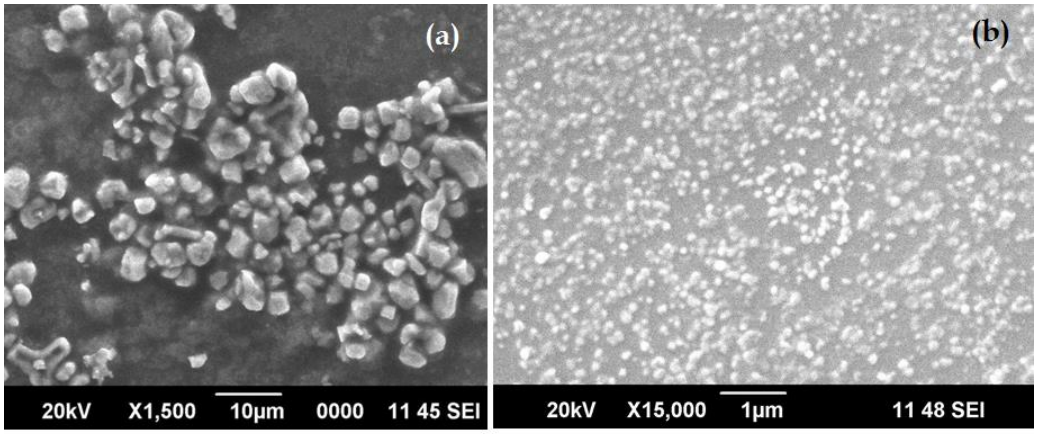

Figure 4.1: *(a) SEM image of unfiltered, spin coated $Ge_{27}Ga_9Se_{64}$ solution in butyl amine with concentration C1=0.30mg/ml showing undissolved large sized particles and clusters, (b) filtered, spin coated C1 shows small clusters after filtration.*

Figure 4.2 (a) is the SEM image of the drop casted films with concentration C1 (filtered) and it shows very large, uneven clusters or agglomerations than spin coated sample. This is because spin coating allows fast evapoation of the solvent than drop casting which slows down the agglomeration in spincoating. The EDS image of the clusters taken is presented in figure 4.2 (b) and it confirms the presence of all elements in the cluster. The peaks corresponding to 'Si' and 'O' observed in the spectrum is from the substrate. The existence of the peak corresponding to 'C' indicates the presence of unevaporated solvent in the clusters.

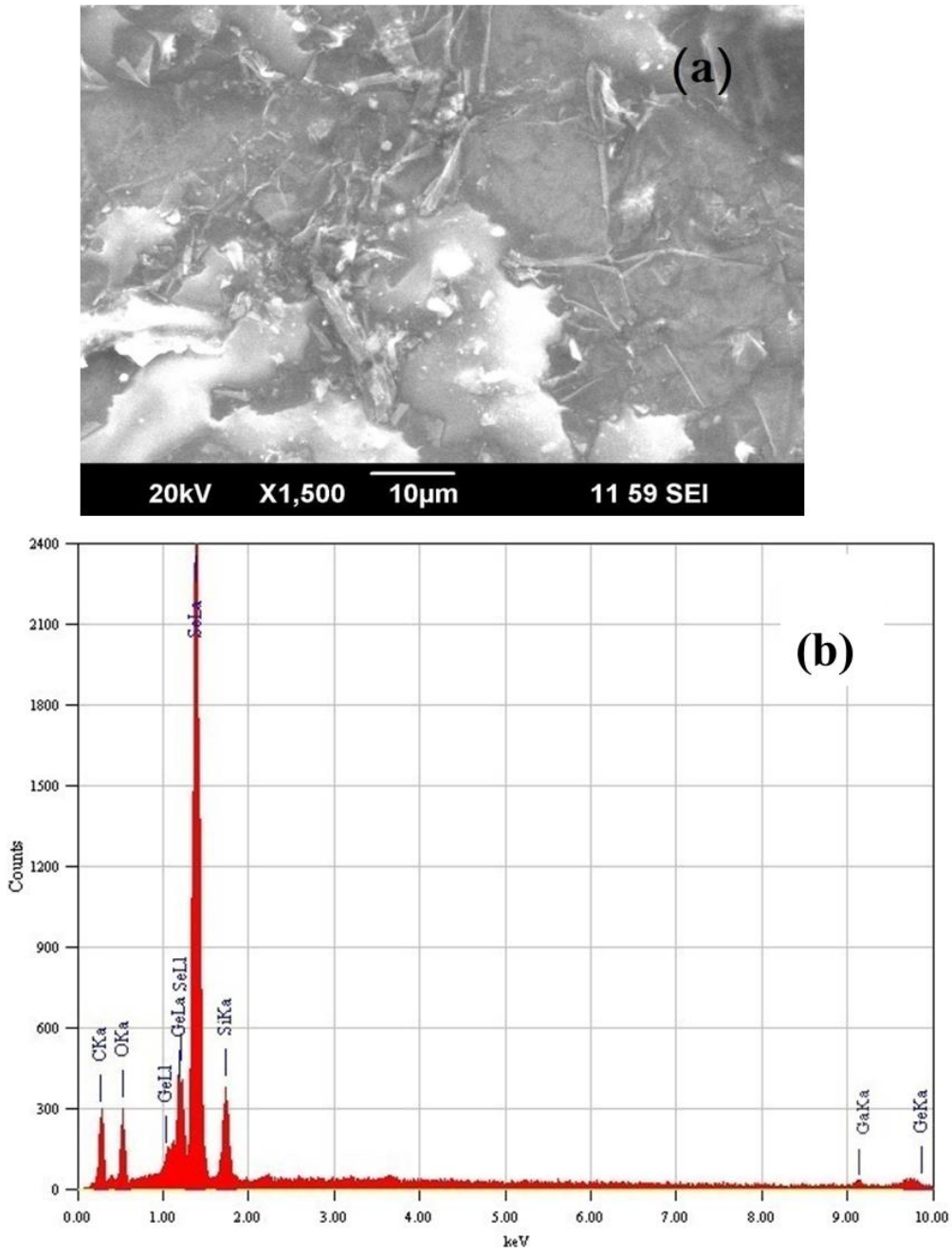

Figure 4,2: *(a) SEM image showing very large, uneven clusters or agglomerations in drop casted C1, (b)EDS image of the cluster which confirms the presence of all elements in the cluster. The excistence of the peak corresponding to 'C' indicates the presence of unevaporated solvent in the clusters.*

Cluster size of $Ge_{27}Ga_9Se_{64}$ glass solutes of concentration C1 (0.30mg/ml) in butyl amine solvent has been analyzed by dynamic light scattering (DLS) at 532nm using Horiba SZ-100 nanoparticle size analyzer.

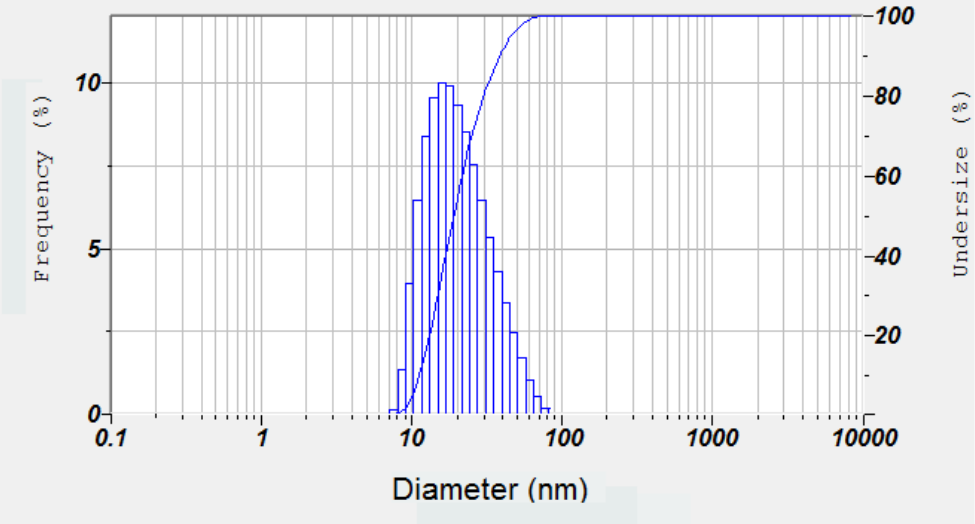

Figure 4.3: *Particle size distribution curve of C1 obtained from dynamic light scattering method. The average size of the solute found from the distribution curve is 9.5nm with a standard deviation of 13.4nm.*

Figure 4.3 depicts particle size distribution curve for C1. The average size of the solute found from the distribution curve is 9.5nm with a standard deviation of 13.4nm. From the figure, it is clear that the distribution is not Gaussian which indicates that it has got more than one size distributions.

4.4.2 Optical absorption spectroscopy

Optical absorption spectroscopy of the colloidal solutions were carried out using a JascoV-570 UV/VIS/IR spectrophotometer. Samples were taken in a fused silica square optical cell with an optical path length of 1cm. Dissolution of all compositions in solvent butyl amine is time consuming and there are negligible changes in the absorption spectra before and after filtering, probably due to the capture of some tiny "insoluble" chalcogenide clusters on the filter, which however does not practically change the sample concentration. Figure 4.4 (a) shows the variation in the absorption spectra of C1 with ageing. From the figure it is clear that the absorption edge for pure butylamine lies in UV region and it is red shifted as the time elapses. Figure 4.4 (b) displays the shift in the wavelength corresponding to absorption edge due to ageing which fits with an exponential function.

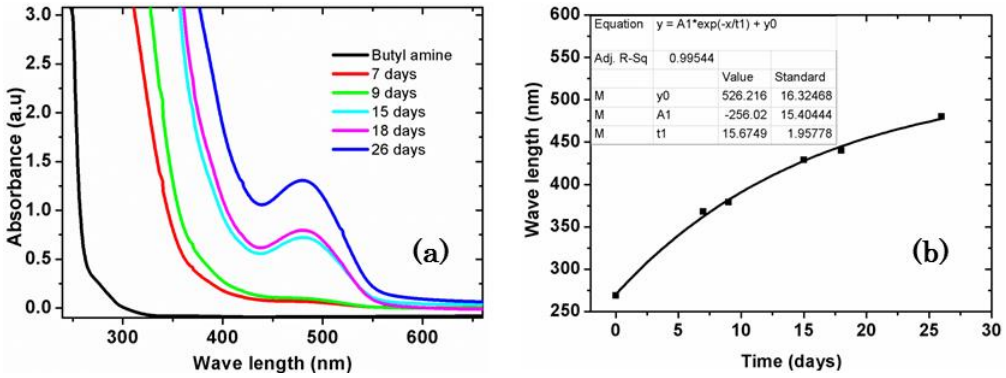

Figure 4.4: *(a) Absorption spectra of the concentration C1 at different intervals of time. Time dependent Red shift is observed due to ageing. (b) Variation in the wavelength corresponding to absorption edge with respect to the interval of time. Solid curve shows exponential fit.*

After one month the samples are filtered out using a 200nm PTFE syringe filter which prevents further dissolution and band edge shift. The dissolved samples are orange-yellow in colour and is observed as orange red in high concentrations. The dissolution process of $Ge_{20}Se_{80}$ glass is very slow and the solution is pale orange even after one month. Comparitively large amount of undissolved portion is filtered out for both $Ge_{20}Se_{80}$ and $Ge_{27}Se_{73}$. The absorption spectra of $Ge_{27}Ga_9Se_{64}$/butyl amine solutions (after one month) of varying concentrations are presented in figure 4.5(a). The absorption spectra of chalcogenide nanocolloids are located in the visible region whereas for bulk chalcogenide glass it is in near IR region. The band edge is blue shifted towards the visible region of electromagnetic spectrum with decrease in the concentration. There exists a peak, centred around 480nm in the band tail of all samples due the presence of defect states in the bandgap. These defects are responsible for various desirable (Photo induced phenomena[17], nonlinear absorption applicable for optical limiters[18] etc.) and undesirable (nonlinear two-step photon absorption[19] in optical switches etc.) optical phenomena in chalcogenide glasses. From the absorption spectra (Figure 4.5(a)) it is clear that there exists a concentration dependent blue shift and decrease in the density of defect states while varying the samples from bulk to nanocolloids with least concentration[20]. Figure 4.5(b) shows the photograph of C0, C1, C2, C3, C4 and C5 nanocolloidal solutions in decreasing order of their concentrations. A corresponding blue shifted and faded luminescence from the intermediate defect states is obvious in this photograph.

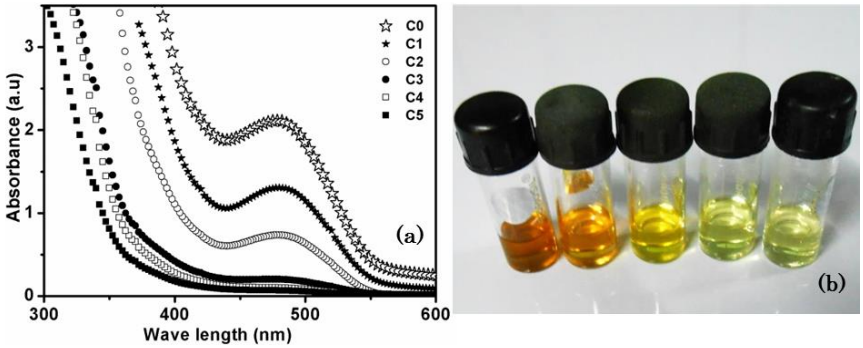

Figure 4.5: *(a) Absorption spectra of $Ge_{27}Ga_9Se_{64}$/butylamine nanocolloids of concentration C0, C1, C2, C3, C4 and C5 shows a concentration dependent blue shift and diminishment in the density of defect states (b) Photograph of C1, C2, C3, C4 and C5 nanocolloids showing quantum size effect.*

The defects in chalcogenide glasses arise due to the unique property of chalcogens such that the presence of lone pair states lies in between the bonding states (σ) and antibonding states (σ*). In solid, these atomic energy states become broad and form energy band. Since the 'σ' energy band in chalcogen lies far below, the lone pair energy band acts as valance band. In Ge atom, the fourfold coordination undergoes sp^3 hybridization and split into occupied 'bonding' and 'unoccupied antibonding' bands. If we alloy these two to a vitreous compound, the coordination environment will be adjusted to satisfy valance requirement of each atom and results in the formation of an inorganic Se-Se, Ge-Se polymer network. The lone pair band of Se fall near the gap of Ge. Therefore the presence of excessive Se-Se bonds leads to the delocalization of LP band and the resultant bandgap in chalcogenide glass becomes narrower which is clear from bulk glass absorption spectrum. The situation is demonstrated in figure 3.10 of chapter 3. When the particle size decreases, both the conduction and valence bands shifts away from each other and results in an increase in the bandgap. As the solute concentration in the solvent decreases, size of the nanoclusters also decreases as reported by Kohoutek et al[2] leading to a blue shift in the band edge. This 'size effect' affects the fluorescence emission such that the emission wavelength also is blue shifted with decrease in concentration which is clear from the photograph (figure 4.5 (b)). During dissolution, the continuous network of bulk glass solute is fragmented[2,3] and therefore the number of Se- bonds in the cluster gets decreased with the decrease in concentration. This leads to the localization of the LP band in the gap and its density diminishes with the decrease in the cluster size. This explains the reduction in defect state density with the decrease in cluster size.

Optical bandgap (Eg) of the nanoclusters in the colloidal solution can be found from linear absorption spectra or from transmission curves. Absorption edge of the glasses are not sharp and optical bandgap is taken to be the point at which the absorption curve changes from a qudratic dependence on energy to an exponential dependence[21]. Minimun of the first derivative of the transmission curve which corresponds to the inflection point and is usually considered as an accurate estimation of Eg.

The dependence of concentration on the bandgap of all compositions dissolved in butyl amine is given in the figure 4.6. It is observed for all compositions and the bandgap decreased almost linearly with the increase in the concentration. The variation of bandgap with concentration shows two regions of linear variations– strong depndence at low concentration in comparison with high concentration. Size dependence effect of nanocolloids on bandgap is predominent at low concentration samples containing small particles. Table 4.2 shows the bandgap of both bulk glasses and nanocolloids with concentration 0.30mg/ml for all compositions.

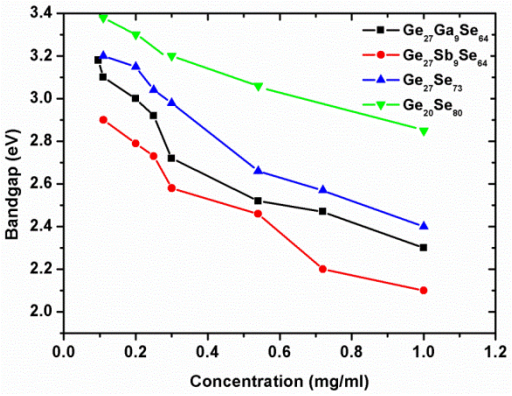

Figure 4.6: *Concentration dependant variations in the bandgap of all compositions of nanocolloids in butylamine. For all compositions, bandgap decreased almost linearly with the increase in concentration. Two regions of linearities are clearly seen (details are given in the text.)*

The variation in the bandgap with respect to the composition is not in the same way as the variations in the bulk glass bandgap. In bulk glasses the bandgap varies as $Ge_{27}Ga_9Se_{64}$ > $Ge_{27}Se_{73}$ > $Ge_{27}Sb_9Se_{64}$ > $Ge_{20}Se_{80}$ whereas in nanocolloids it varies as $Ge_{20}Se_{80}$ > $Ge_{27}Se_{73}$ > $Ge_{27}Ga_9Se_{64}$ > $Ge_{27}Sb_9Se_{64}$. The reaction of amine with the chalcogenide glass is expected to occur through nucleophilic attack of 'N lone pair' present in the amine on either electropositive Ga/Sb/Ge or at chalcogen atoms in chalcogen-chalcogen chains[22]. Chern et al. investigated the dissolution of arsenic sulphide in n-

propylamine and n-butylamine[1-5] and described the dissolution as the amine solvent breaking up the bulk, amorphous arsenic sulphide into small flat clusters. In $Ge_{27}Ga_9Se_{64}$ and $Ge_{27}Sb_9Se_{64}$ glasses, number of bonds involved by electropositive atoms is higher than the other two which helps more strong attack of the nucleophile and faster cleaving of the bonds. This may be the reason for the large undissolved remainings present in $Ge_{20}Se_{80}$ and $Ge_{27}Se_{73}$ nanocolloidal solutions.

Composition	Bulk Bandgap (eV)	Nanocolloid Concentration	Sample code	Nanocolloid Bandgap (eV)
$Ge_{27}Ga_9Se_{64}$	1.67		C1	2.72
$Ge_{27}Se_{73}$	1.64		E1	2.98
$Ge_{27}Sb_9Se_{64}$	1.59	0.30mg/ml	D1	2.58
$Ge_{20}Se_{80}$	1.55		F1	3.20

Table 4.2: *Variation of optical bandgap of nanocolloids of concentration 0.3mg/ml with respect to composition.*

4.4.3 Photoluminescence studies

The photoluminescence studies were done using Cary Eclipse fluorescence spectrophotometer (Varian). Nanocolloidal solutions of all compositions show fluorescence emission. Emission spectra of sample C1 for different excitation wavelengths are presented in Figure 4.7 (a). As the excitation wavelength shifts from shorter to longer wavelength, the fluorescence emission peak also shifts towards longer wavelength region. A maximum fluorescence emission peak is observed at 580nm with 480nm excitation. For a wavelength higher than 480nm excitation, the emission intensity decreases but the emission wavelength is around 580nm. The most intense fluorescence emission is observed at 480nm excitation. Intermediate absorption peak in the forbidden energy gap (clear from absorption spectra figure 4.5 (a)) and the corresponding fluorescence emission in C1 emphasizes the existence of localized energy band in the nanoclusters with an increase in density of states up to a level corresponding to 480nm (2.58eV). The excitation and emission spectrum of C1 shown in figure 4.7(b) consists of a broad excitation centered on 480nm and the corresponding emission peak at about 580nm.

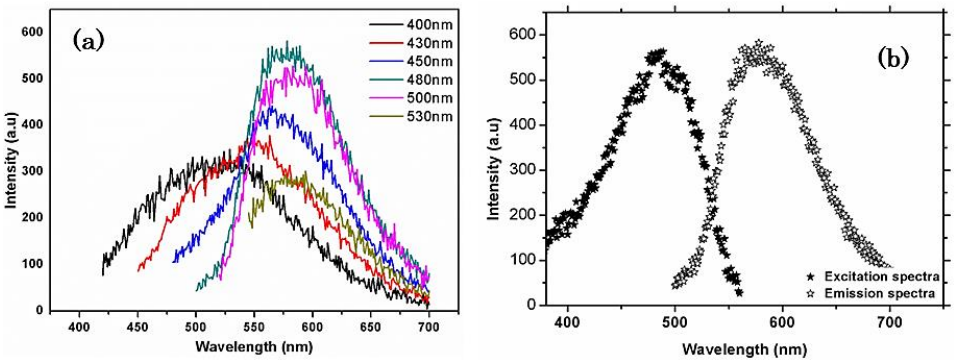

Figure 4.7: *(a) Emission spectra of C1 corresponding to different excitation wavelengths indicated as inset show a maximum emission with 480nm excitation. (b) Excitation and emission spectra of sample C1. The excitation spectrum which consists of a broad peak around 480 nm shows the presence of localized states.*

Figure 4.8 (a) shows fluorescence emission spectra of low concentration sample C5 for different wavelengths of excitation. From the absorption spectrum of C5, it is clear that the absorption by localized defect states (around 480 nm) in the band gap is very less. Fluorescence studies on C5 reveal that a comparably less intensity fluorescence emission is observed for low wave length excitation which starts from UV side. This is due to the absorption of defect states (located in the band tail leading to a spread in band tail.) originating from the lattice disorder, which is the signature of amorphous materials, which in turn depends upon the thermal history of the sample. Photo luminescence emission peak wavelength versus excitation wavelength plots with different concentrations of $Ge_{27}Ga_9Se_{64}$/butyl amine are shown in figure 4.8 (b).

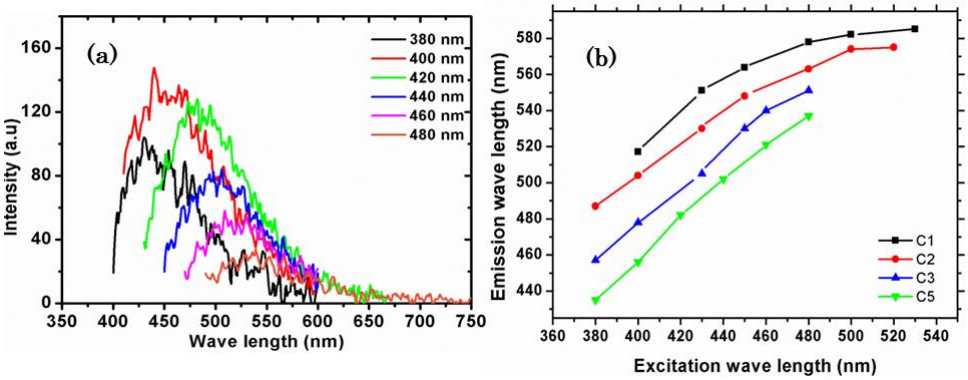

Figure 4.8: *(a) Fluorescence emissions from C5 at different excitation wave lengths show a maximum emission with 400nm excitation. (b): Photo luminescence emission peak wavelength versus excitation wavelength for C1, C2, C3, and C5.*

Fluorescence spectra for C1 are broader than C5 and it is explained[23] as follows. Absorption spectrum of bulk glass is very broad due to the delocalization[24] of defect (originating from the Se dangling bonds) states which extends upto infrared region. But in the nanocolloidal solutions the defect states are localized in the bandgap and show specific absorption peak in the absorption spectra as observed in C1. The localization of defect states occurs due to the fragmentation of solute bulk glass during dissolution[20] and the fragments have a lesser number of Se^- bonds. Obviously as the concentration of solute glass in the solvent decreases, the density of localized defect states will also decrease as observed in the absorption spectra of C5. Since C1 has a broad and well-defined defect state absorption which covers a range of wavelengths, fluorescence emission spectra is also broad for C1 and it embraces most of the visible region. For shorter wavelength excitation, the energy of excited carriers are reduced and transited to the lower lying defect states by nonradiative transitions and the corresponding emission spectra are less intense and broader. As the excitation wavelength increases to the wavelength at which maximum defect states occur (i.e around 480nm), the fluorescence width decreases and becomes almost constant. In the case of C5 the intermediate defect state absorption is comparatively less and therefore the fluorescence emission is not as broad and intense as that of C1.

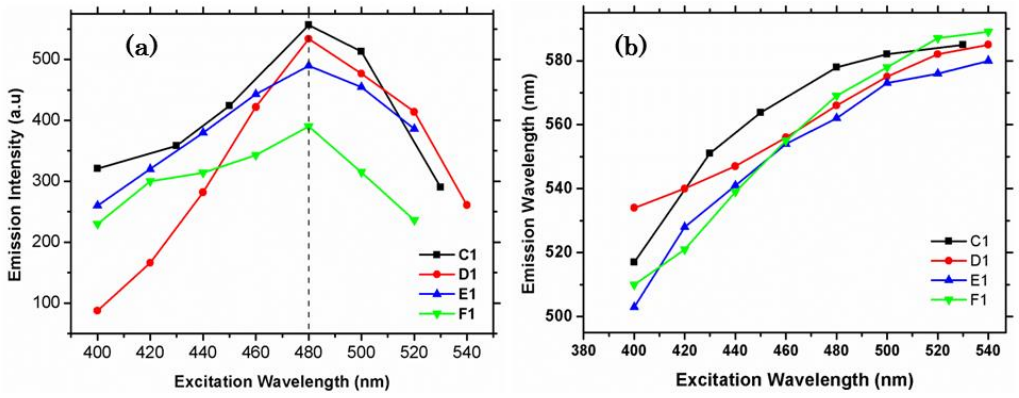

Figure 4.9: *(a) Variations in the intensity of emission peak with different excitation wave lengths for C1, D1, E1, and F1. Maximum emission intensity is observed for 480nm excitation for all compositions of nanocolloids. (b) Photoluminescence emission peak wavelength versus excitation wavelength for C1, D1, E1, and F1.*

Nanocolloidal solutions of all compositions show same behavior and solutions of higher concentration exhibit maximum emission with 480nm excitation. Figure 4.9 (a) shows the variations of emission peak intensity with various

wavelengths of excitations and figure 4.9 (b) depicts the change in emission peak wavelength with respect to the change in excitation wavelength. For all compositions the emission peak wavelength increases with the increase in the excitation wavelength up to 480 nm excitation and no further considerable shift in the emission peak wavelength is observed for higher wavelength excitation. The maximum peak intensity is observed at 480nm for all compositions.

4.4.4 Thermal diffusivity measurements of nanocolloids

Thermal diffusivity of all compositions of nanocolloids have been carried out using dual mode-matched thermal lens technique at 532 nm. Figure 4.10 represents decay curve for $Ga_9Ge_{27}Se_{64}$ nanocolloid at concentration C1. Thermal diffusivity of a material depends on its thermal conductivity which is governed by phonon mean free path which inturn depends upon the network structure. Table 4.3 shows thermal diffusivity variation of nanocolloidal solution with different concentrations of all compositions of nanocolloids. Thermal diffusivity of all compositions of nanocolloidal solutions shows same variations with concentration, i.e. thermal diffusivity decreases with increase in solute concentrations. It is clear from the absorption spectra that as the solute concentration in the solvent increases the defect density also increases. Since the presence of defect states leads to scattering of thermal waves[25], nanocolloidal solutions with large cluster size offer more resistance to thermal wave propagation and results in a lower thermal diffusivity. Thus the thermal diffusivity studies confirm the predictions based on absorption spectra analysis.

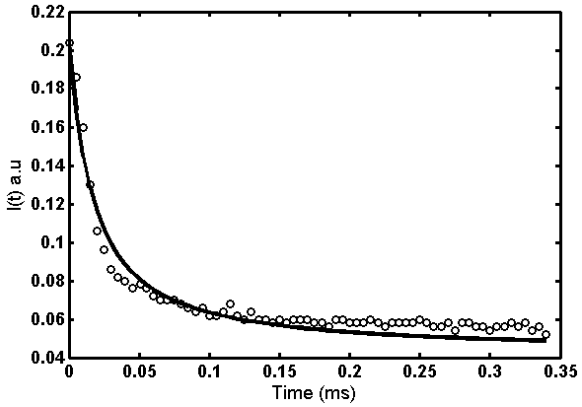

Figure 4.10: *Thermal lens response curve for $Ge_{27}Ga_9Se_{64}$ nanocolloid for concentration C1.*

Lower concentrations of $Ge_{27}Se_{73}$ and $Ge_{20}Se_{80}$ nanocolloids show less lensing effect and it is difficult to detect. This may be due to low amount of nanoclusters present in the colloids than $Ge_{27}Ga_9Se_{64}$ and $Ge_{27}Sb_9Se_6$. Nanocolloids of $Ge_{27}Sb_9Se_6$ glass shows least thermal diffusivity compared to other compositions which indicates the presence of high density of defect states. This may be due to the presence of 'Sb' which also has a lone pair state with one electron.

Composition	Sample code	Concentration	Thermal diffusivity (cm^2/s) $x10^{-4}$
$Ge_{27}Ga_9Se_{64}$	C0	0.54mg/ml	0.11
	C1	0.30mg/ml	4.5
	C2	0.25mg/ml	14.7
	C3	0.20mg/ml	19.0
	C4	0.11mg/ml	20.5
	C5	0.096mg/ml	24.9
$Ge_{27}Sb_9Se_6$	D0	0.54mg/ml	0.05
	D1	0.30mg/ml	3.6
	D2	0.25mg/ml	10.4
	D3	0.20mg/ml	17.1
$Ge_{27}Se_{73}$	E0	0.54mg/ml	5.5
	E1	0.30mg/ml	13.1
	E2	0.25mg/ml	24.5
$Ge_{20}Se_{80}$	F0	0.54mg/ml	8.1
	F1	0.30mg/ml	19.2

Table 4.3: *Thermal diffusivity variation of nanocolloidal solution with different concentrations of all compositions of nanocolloids.*

4.4.5 Nonlinear optical studies on Nanocollloids

Z-scan studies were carried out on nanocolloids by using open and closed aperture Z-scan techniques. The samples to be investigated were translated through the focal point of a lens which has a focal length 20cm. The beam waist radius ω_0 was calculated to be 35.4μm and the Rayleigh length, $z_0 = \frac{\pi {\omega_0}^2}{\lambda}$, was 7.4mm. Nanocolloidal solutions were taken in a 1mm cuvette

which is considerably less than the diffraction length '$n_0 z_0$', thereby satisfying the prerequisite for z- scan experiments[26].

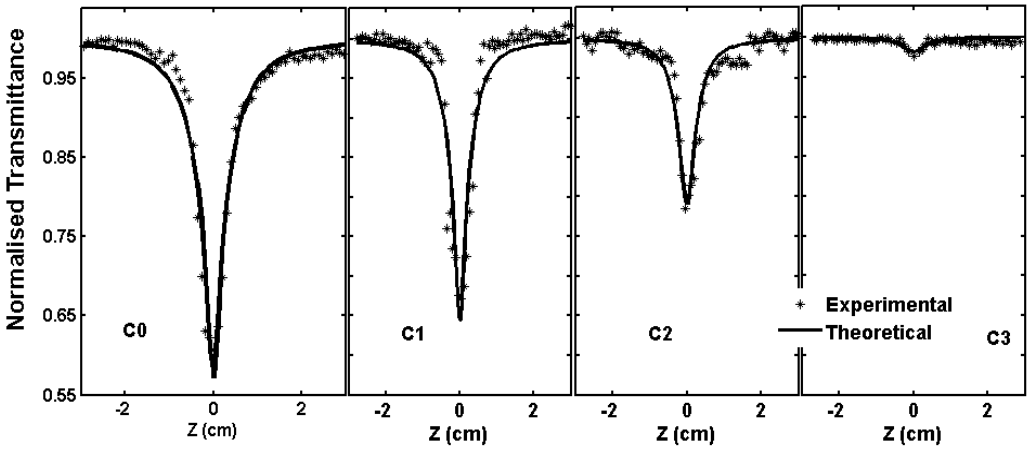

Figure 4.11: *Normalized transmittance for different concentrations in the open aperture scheme at 532nm with an input fluence of 320MW/cm². The solid line shows the theoretical fit. Nonlinear absorption decreases with the decrease in concentration and finally vanishes as the concentration decreases to C4 and C5 which is not shown in this figure.*

Open aperture Z-scan studies conducted on nanocolloidal solutions exhibit reverse saturable absorption (RSA). Figure 4.11 shows the RSA curves for different concentrations of $Ge_{27}Ga_9Se_{64}$/butyl amine at a fluence of 320MW/cm². The experimental (scatter) RSA fits with the theoretically (solid curve) simulated curve based on the Two Photon Absorption (TPA) calculations suggested by Sheik-Bahae et.al[26]. From the fit, we can confirm that the basic mechanism involved in the nonlinear absorption of nanocolloidal solutions is two-photon absorption (TPA) process. Previous studies[27,26] conducted on different semiconductors reveal that TPA is the dominant nonlinear absorption in materials with bandgap $Eg<2h\upsilon<2Eg$, where $h\upsilon$ is laser photon energy. Since the energy corresponding to 532 nm ($h\upsilon$ =2.33eV) lies in 'band tail peak', absorption of '$h\upsilon$' might have resulted in the excitation of the carriers to the localized state in the gap. From this energy level, the carriers can go to the conduction band by absorbing another photon. Instead of a virtual state, these localized energy bands may act as a resonant intermediate level which leads to a two-step cascade photon[28] absorption. Probability for resonant two photon absorption; that is simultaneous absorption of two photons is also there. Schematic representation of two step photon absorption as well as resonant two photon absorption in nanocolloidal[18] solution is given in figure 4.12. Nonlinear absorption decreases with decrease

in concentration and finally vanishes as the concentration reaches to C4 and C5. So it is not given in figure 4.11. Comparing with table 4.3, it is clear that the nonlinear absorption decreases with the increase in thermal diffusivity. The mid-gap states resulting from the localized defects, lead to a two-step photon absorption which is responsible for the high nonlinear absorption coefficient (β) at high concentrations[18]. From figure 4.5 (a) & (b) it is clear that as the concentration decreases the density of these defect states diminishes and the absorption shifted to shorter wavelength due to size effect. Therefore for very low concentrations (C4 & C5) the density of defect states are very less and they are lying above the photon energy of pump laser ($h\upsilon$ =2.33eV), so that it will not act as the intermediate step in two step photon absorption.

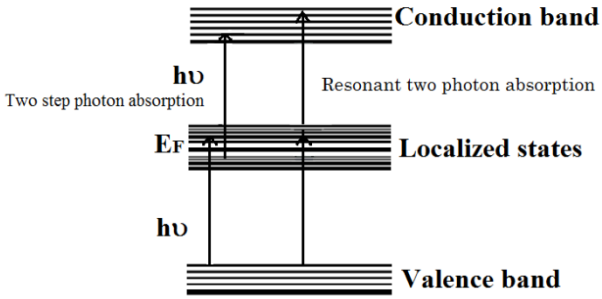

Figure 4.12: *Schematic of two step photon absorption as well as resonant two photon absorption in nanocolloids.*

The calculated nonlinear absorption coefficient (β) shows a dependence on the size and concentration of the nanoclusters. Nonlinear absorption of chalcogenide glass colloids are found to increase with decrease in optical bandgaps as reported[29]. The optical bandgap of the material could be tuned by varying the chalcogenide glass concentration in butyl amine. Therefore for greater nonlinearity, large cluster size is required. This is due to the enhancement of optical nonlinear interaction between radiation and the sample with the increase in cluster size. Thus cluster size and therefore the concentration has a significant effect on limiting performance. With a small increase in the bandgap a significant increase in the nonlinear absorption is observed. This can be explained by the fact that with the increase in solute concentration, the number of particles in the solvent increases which results in a rise in the multiple scattering from the nanoclusters, than with solutions with less solute contents. This rise in multiple scattering leads to a large effective interaction length which in turn results in an enhancement in nonlinear absorption.

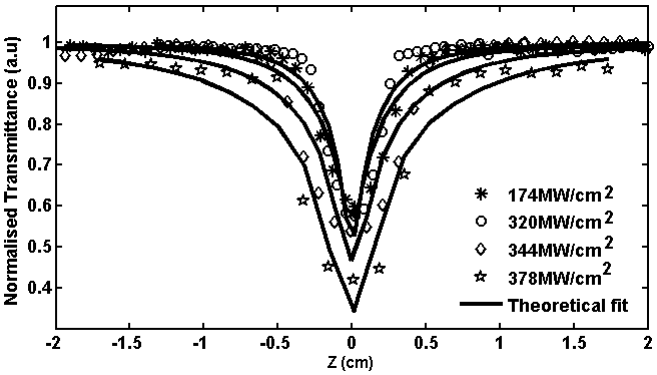

Figure 4.13: *Normalized transmittance as a function of position for C1 in the open aperture scheme at 532nm with different laser input fluence. The solid line shows the theoretical fit.*

Figure 4.13 shows the open aperture Z-scan curves for C1 at different input laser intensity (I_0). The measured value of nonlinear absorption coefficient (β) decreases with input intensity and it may be due to the removal of the appreciable fraction of photo carriers from the ground state[30].

Nanocolloidal solutions of all compositions show RSA. Figure 4.14 depicts the open aperture Z-scan curves of C1, D1, E1 and F1. $Ge_{27}Sb_9Se_{64}$/butyl amine shows the highest nonlinearity and $Ge_{20}Se_{80}$/butyl amine solution has the least nonlinear absorption. This indicates that the optical nonlinearity of different compositions of chalcogenide glass nanocolloids varies with respect to bandgap. The variation of nonlinear absorption coefficient (β) with respect to the composition in nanocolloids (for a fixed concentration) is as $Ge_{27}Sb_9Se_{64}$ > $Ge_{27}Ga_9Se_{64}$ > $Ge_{27}Se_{73}$ > $Ge_{20}Se_{80}$. This shows that nonlinear absorption coefficient (β) increases with the decrease in optical bandgap.

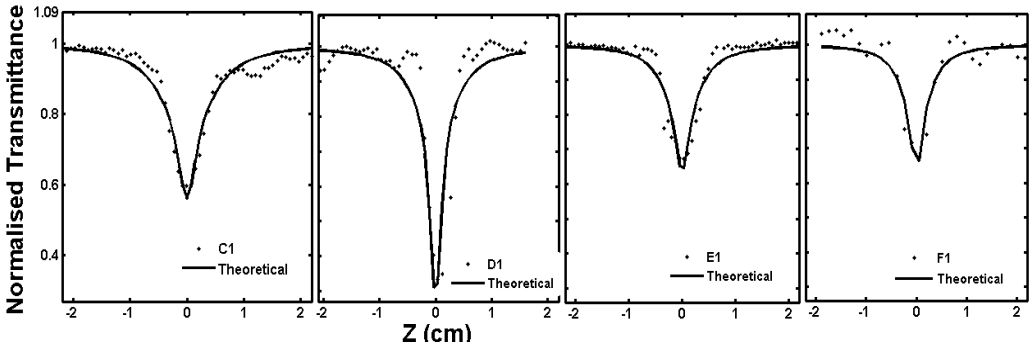

Figure 4.14: *Normalized transmittance for C1, D1, E1 and F1 in the open aperture scheme for 532nm at 320MW/cm². The solid line shows the theoretical fit. D1 shows the highest nonlinearity.*

Figure 4.15 plots the log (β) versus log (I_0) for all compositions and it indicates that the measured value of nonlinear absorption coefficient (β) decreases almost linearly with input intensity for all compositions.

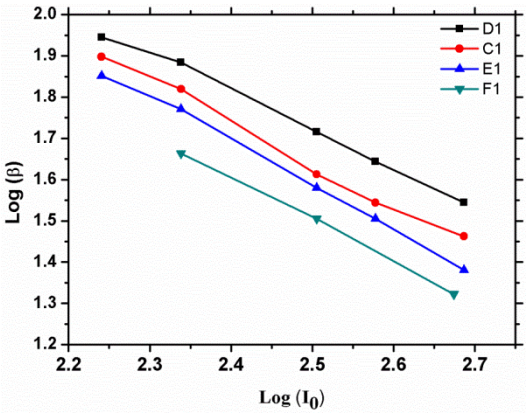

Figure 4.15: *log(β) versus log (I_0) for D1, C1, E1 and F1shows a linear decrease in β with I_0 for all compositions of nanocolloids.*

Closed aperture Z-scan studies were conducted on different nanocolloidal solutions by measuring the transmittance through a finite aperture with aperture size $s = 0.3$ in the far field, as the sample is moved along the propagation path (z) of a focused Gaussian beam. The sign and magnitude of the nonlinear refraction are deduced from the closed aperture Z-scan transmittance curve, using the procedure put forward by Sheik-Bahae et.al[26]. The analysis shows that all nanocolloidal samples have negative nonlinear index of refraction and the magnitude of nonlinear refractive index $|n_2|$ increases with the decrease in bandgap. Table 4.4 shows the variation of nonlinear absorption coefficient (β) and nonlinear refractive index (n_2) with respect to the change in bandgap and composition. Figure 4.16 gives the closed-aperture z-scan traces of $Ge_{27}Ga_9Se_{64}$ /butylamine nanocolloids of different concentrations at an input intensity of 320MW/cm^2.

For samples with refractive and absorptive nonlinearities, closed-aperture measurements contain contributions from intensity-dependent changes in the transmission[26]. By dividing the normalized closed-aperture transmittance by the corresponding normalized open-aperture data, we could get the transmittance change created due to the change in refractive index only and this result is shown in Figure 4.16. It is observed that the peak-valley of the closed-aperture z-scan satisfied the condition $\Delta z \sim 1.7 z_0$, therefore satisfying the existence of cubic nonlinearity[26]. The value of $\Delta\varphi_0$, the phase

shift, due to change in refractive index could be obtained from the theoretical fit to the equation 2.42.

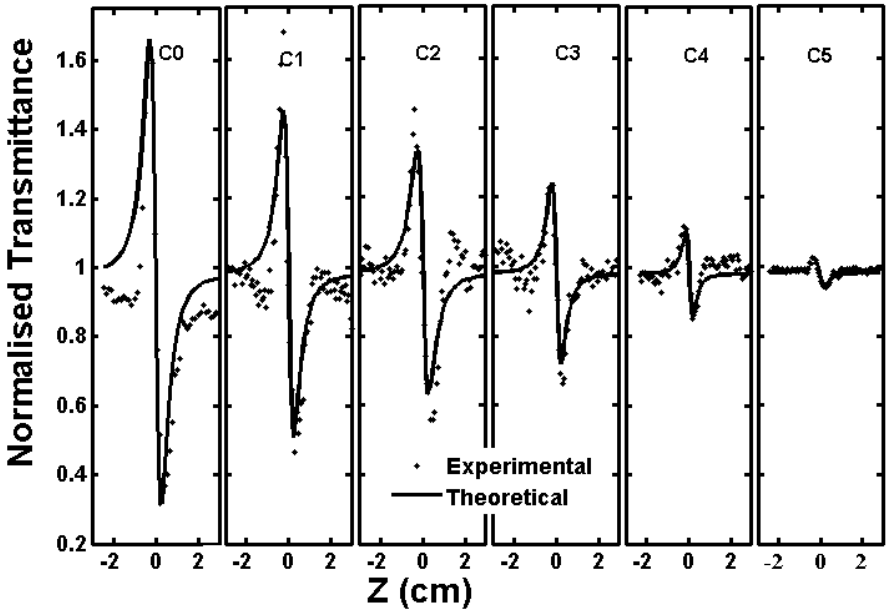

Figure4.16: *Closed aperture Z-scan traces at 320MW/cm² for $Ge_{27}Ga_9Se_{64}$ /butylamine solutions of different concentrations with an aperture size* $s = 0.3$.

Figure 4.17 demonstrates the variation of radial phase shift ($\Delta\varphi_0$) at the exit surface of the sample, after travelling a path of 1mm through the nanocolloids with respect to the change in bandgaps of $Ge_{27}Ga_9Se_{64}$ /butylamine nanocolloids of different concentrations.

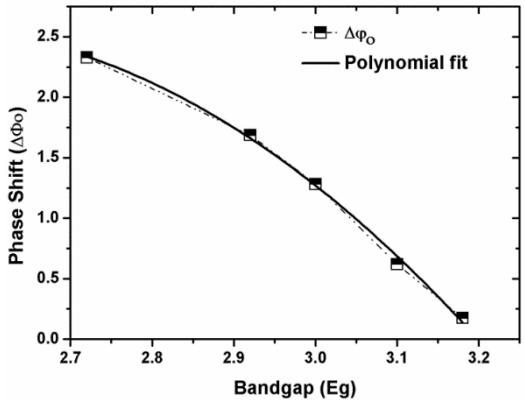

Figure 4.17: *Variation of radial phase shift ($\Delta\varphi_0$) with respect to the change in bandgaps. Solid curve shows quadratic polynomial fit.*

Table 4.4 shows the variation of nonlinear absorption coefficient ($\boldsymbol{\beta}$), and nonlinear refractive index $\boldsymbol{n_2}$ with respect to the bandgap (Eg) of different nanocolloids.

Composition	Concentration	Bandgap (eV)	Nonlinear absorption coefficient β (cm/GW)	Nonlinear refractive index, n_2 10^{-10} (esu)
$Ge_{27}Ga_9Se_{64}$	C5	3.18	-	-0.25
	C4	3.10	-	-1.2
	C3	3.0	1.7	-2.0
	C2	2.92	26	-2.9
	C1	2.72	40	-4.0
	C0	2.52	51	-4.9
$Ge_{27}Sb_9Se_{64}$	D2	2.73	41	-6.5
	D1	2.58	52	-8.6
	D0	2.46	59	-10.6
$Ge_{27}Se_{73}$	E2	3.04	1.1	-0.5
	E1	2.98	38	-1.89
	E0	2.66	40	-3.1
$Ge_{20}Se_{80}$	F1	3.2	32	-0.13
	F0	3.06	37	-0.58

Table 4.4: *Bandgap dependent variation in nonlinear optical coefficients for all compositions.*

In semiconductors, the sign and magnitude of nonlinear refraction is determined by Eg as well as the energy of laser photon ($h\upsilon$) such that by exciting optical materials at frequencies much less than Eg, a considerably smaller, but faster, positive nonlinear refractive index n_2 (magnitude of this positive n_2 increases with '$h\upsilon$' upto Two Photon Absorption edge (Eg/2) where $\frac{h\upsilon}{Eg} = 0.5$ and then it starts to decrease.) due to bound electronic effects is observed[31]. At frequencies ($\frac{h\upsilon}{Eg} \approx 0.7$) substantially above TPA edge, n_2 is negative[32], whose magnitude increases as it approaches to one photon absorption edge Eg due to TPA generated free carrier refraction and other bandgap resonant effects such as ac stark effect[33].In chalcogenide nanocolloids, at 532nm ($h\upsilon = 2.33$eV) bandgap resonant effects (since $\frac{h\upsilon}{Eg} > 0.7$ for all concentrations) in combination with defect state assisted thermal

nonlinearity, leads to self-defocusing and therefore we get negative nonlinear refractive index n_2. From the table it is clear that as the bandgap approaches to the one photon absorption edge ($h\upsilon = 2.33$eV) the negative nonlinear refractivity increases sharply as reported. The low concentration nanocolloids of all composition which have highest bandgap (given in in table.4.4) shows little nonlinear absorption since their defect states are very less and they lie above the photon energy ($h\upsilon = 2.33$eV) of laser.

Composition	Concentration	Imaginary part of nonlinear susceptibility Im χ^3 x10^{-10} (esu)	Real part of nonlinear susceptibility Reχ^3 x10^{-10} (esu)	Nonlinear Susceptibility (χ^3) x10^{-10} (esu)	Figure of merit (FOM) $\left\|\frac{\gamma}{\beta\lambda}\right\|$
$Ge_{27}Ga_9Se_{64}$	C5	-	-0.07	0.07	-
	C4	-	-0.30	0.30	-
	C3	0.017	-0.55	0.55	3.8
	C2	0.18	-0.77	0.80	0.34
	C1	0.28	-1.07	1.10	0.3
	C0	0.35	-1.31	1.35	0.29
$Ge_{27}Sb_9Se_{64}$	D2	0.29	-0.92	0.96	0.25
	D1	0.36	-1.25	1.3	0.27
	D0	0.41	-1.52	1.57	0.29
$Ge_{27}Se_{73}$	E2	0.007	-0.13	0.41	1.43
	E1	0.255	-0.50	0.56	0.15
	E0	0.268	-0.81	0.85	0.23
$Ge_{20}Se_{80}$	F1	0.214	-0.034	0.22	0.01
	F0	0.248	-0.153	.084	0.05

Table 4.5: *Variation in nonlinear susceptibility and figure of merit with respect to concentration for all compositions of nanocolloids.*

Table 4.5 shows the variation of nonlinear susceptibility (χ^3) and figure of merit (FOM = $\left|\frac{\gamma}{\beta\lambda}\right|$, where γ is nonlinear refractive index in m²/W) with respect to the change in concentration of different compositions of nanocolloids. Nonlinear susceptibility (χ^3) increases with concentration and Figure of merit (FOM) displayed in table shows very large value, for low concentration samples since nonlinear absorption (β~0) is absent or very less.

The bound electronic nonlinear refractive index n_2 is theoretically obtained for all compositions of nanocolloidal solutions using Kramers-Kronig transformation from nondegenerate nonlinear absorption calculated using two-band model[32,33]. According to Kramers-Kronig rule states that, a change in the refractive index (Δn) at ω is associated with changes in the absorption coefficient ($\Delta\beta$) throughout the spectrum (ω') and vice versa. Therefore fluctuations in the absorption coefficient which originate due to different 'causes' like Two-Photon absorption, Raman transitions and Stark shift (virtual band blocking) will be accompanied by a change in the refractive index. The effects of above 'causes' on the dispersion, scaling and sign of n_2 were theoretically deduced as a function of G_2(hυ/Eg) called universal dispersion function.

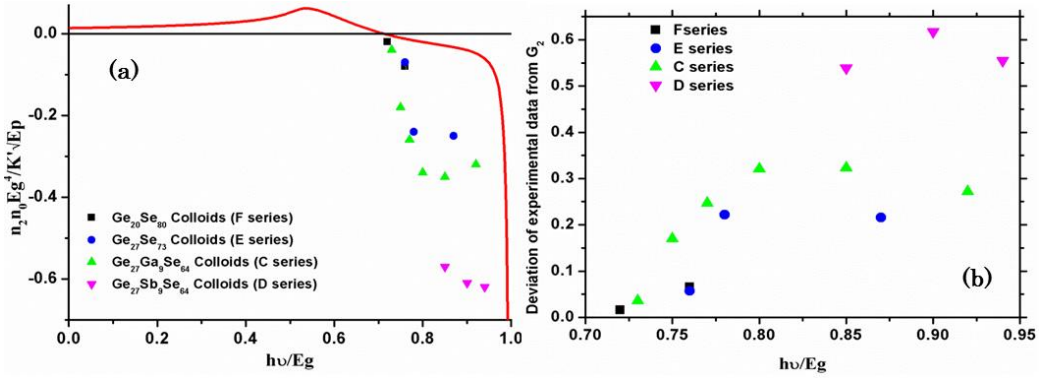

Figure 4.18: *(a) Data of n_2 scaled as $n_2n_0Eg^4/K'$ versus hυ/Eg represented by scatters. Solid curve represented in red, is the universal dispersion curve G_2(hυ/Eg) which illustrates the theoretical dispersion of n_2 with respect to frequency and bandgap. (b) The deviation of experimental $n_2n_0Eg^4/K'$ from G_2(hυ/Eg) plotted against hυ/Eg. $Ge_{27}Sb_9Se_{64}$ nanocolloids (D series) shows maximum deviation from theoretically predicted G_2.*

The function G_2 which relates to the nonlinear refractive index n_2 is given by equation[33] (4.2).

$$n_2(esu) = \frac{K'\sqrt{E_p}G_2(\text{hυ/Eg})}{n_0Eg^4} \qquad (4.2)$$

where K' is a constant, $3.4\text{x}10^{-8}$ E_p is a material independent constant and possess a value E_p~21eV and the bandgap Eg is in eV

Studies[33] conducted on more than twenty five different materials show excellent agreement with theoretically calculated n_2 with measured values for a five order of magnitude variation in the modulus of n_2 in semiconductors and wide-bandgap optical solids. We plotted the function $G_2(h\upsilon/Eg)$ which has contributions from two photon absorption and quadratic stark effect and it is shown as solid red curve in figure 4.18 (a). Figure 4.18 (a) depicts the variation of experimentally obtained n_2 multiplied by n_0Eg^4/K' with respect to universal dispersion function G_2. The solid curve represents theoretically calculated $G_2(h\upsilon/Eg)$ and the scatter denotes experimentally obtained n_2 multiplied by n_0Eg^4/K' for all compositions of nanocolloids. From the figure it is clear that the experimental (scatter) data shows a large deviation from the theoretically, simulated curve for all nanocolloids. As the bandgap approaches the one photon absorption edge (where $h\upsilon/Eg=1$) the magnitude of negative nonlinear refractive index increases sharply. Figure 4.18 (b) shows the deviation of experimental value of nonlinear optical coefficient n_2 multiplied with n_0Eg^4/K' from universal dispersion function $G_2(h\upsilon/Eg)$. From the figure it is clear that $Ge_{27}Sb_9Se_{64}$ nanocolloids (D series) show maximum deviation from theoretically predicted G_2.

As explained in section 4.4.2 all of these nanoclusters have localized defect states in the bandgap produced by lone pairs. Presence of these intermediate localized states in the bandgap is responsible for large and unusual nonlinear optical coefficients in nanocolloids and it also leads to enormous deviation of $n_2n_0Eg^4/K'$ from theoretically predicted G_2. $Ge_{27}Sb_9Se_{64}$ nanocolloids (D series) show maximum deviation and it may be due to the presence of Antimony which also has a lone pair electron and it shows good dissolution in butyl amine. The localized states serve as an intermediate resonant level for cascaded two step photon absorption and therefore nonlinear absorption coefficient (β) increases with the increase in density of localized states. Therefore as reported[28] we can write linear absorption coefficient $\alpha(h\upsilon)$ and the nonlinear absorption coefficient $\beta(h\upsilon)$ for glasses by neglecting momentum conservation, as

$$\alpha(h\upsilon) \propto \left|\langle\phi_f|H|\phi_i\rangle\right|^2 \int D_f(E+h\upsilon)D_i(E)dE \qquad (4.3)$$

$$\beta(h\upsilon) \propto \left|\sum_n \frac{\langle\phi_f|H|\phi_n\rangle\langle\phi_n|H|\phi_i\rangle}{(E_{ni}-h\upsilon)}\right|^2 \times \int D_f\,(E+2h\upsilon)D_i(E)dE \qquad (4.4)$$

where H is the perturbation Hamiltonian, ϕ is the electron wavefunction, D is the density of states and the subscripts *i*, *n*, and *f* represent

initial, intermediate, and final states respectively. The above equations show that α and β are connected to the electronic band structure, i.e. wavefunctions and density-of-states, which is determined by atom species as well as bonding nature and structures. The Kramers–Krönig transformation states that the change in the refractive index (Δn) at ω is connected with changes in the absorption coefficient ($\Delta\alpha$) throughout the spectrum and vice versa. Using nonlinear Kramers–Krönig relations one can write change in the refractive index Δn due to the perturbation caused by pump field (Ω) in connection with change in absorption coefficient $\Delta\alpha$[33].

$$\Delta n(\omega;\xi) = \left(\frac{c}{\pi}\right)\int_0^\infty \{\Delta\alpha(\omega';\xi)/(\omega'^2-\omega^2)\}d\omega' \qquad (4.5)$$

Where ω is pump field frequency and ξ is a parameter (or parameters) denoting the 'cause' of change in the 'absorption'. In the case of nanocolloidal solutions, the localized defect states acts as the major "cause" for nonlinear absorption and it was not included in the theoretical calculation of n_2 in figure 4.18(a). This results in large deviation of experimentally observed n_2 from the theoretically simulated curve.

Optical limiting

Optical limiters are devices that transmit light at low input fluences or intensities, but become opaque at high inputs. The limiting property occurs mainly due to absorptive nonlinearity. While the sample is translated through the focus of the Gaussian beam, the sample experiences variation in the incident fluence levels. It is possible to generate optical limiting curves from open aperture z-scan data. From the value of fluence at focus, the fluence values at other positions could be calculated, $I(Z) = \frac{E}{\pi\omega_0^2(z)t}$, using standard equations for Gaussian beam waist, $\omega^2(z) = {\omega_0}^2(1+\frac{z^2}{{z_0}^2})$ where the beam waist radius at focus, $\omega_0 = \frac{f\lambda}{D}$, f being the focal length of the lens, D and λ the radius and wavelength of the beam respectively, E is the energy per pulse and t is the pulse width. The plot of fluence versus transmittance represents the optical limiting curve. An important term in the optical limiting measurement is the limiting threshold. The optical limiting threshold (onset optical limiting) is the corresponding input fluence value at which the deviation from linearity in the normalized transmittance is observed. The lower the optical limiting threshold, the better the optical limiting material. Figure 4.19 illustrates the optical limiting response of C0, C1, C2, and C3 at an input fluence of 320MW/cm^2.

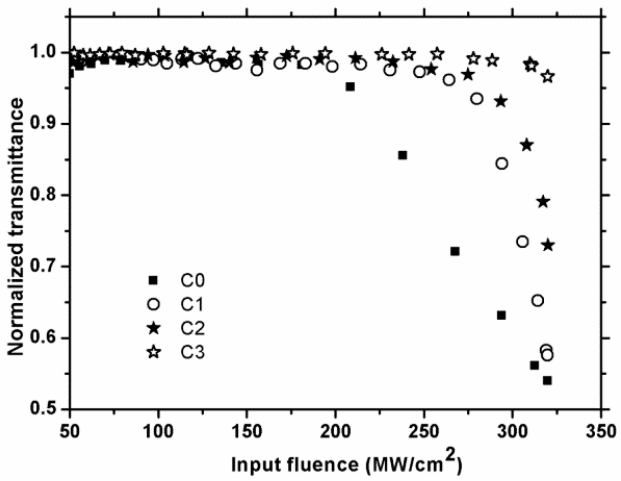

Figure 4.19: *Optical limiting response of C0, C1, C2 and C3 at 532 nm at an input fluence (I_0) of 320MW/cm^2. The optical limiting threshold is found to decrease with concentration.*

The optical limiting threshold is seen to decrease with increase in cluster size. The limiting threshold obtained from figure 4.19 is given in the table 4.6

Input laser fluence (MW/cm^2)	Optical limiting threshold MW/cm^2			
	C0	C1	C2	C3
320	199	249	275	315
344	220	279	308	340
378	261	320	343	371

Table 4.6: *Variation of optical limiting threshold at various input fluence (I_0) for different concentrations of $Ge_{27}Ga_9Se_{64}$/butylamine.*

Optical limiting threshold increases linearly with the input fluence (I_0) for all compositions of nanocolloids C1, D1, E1 and F1 and are shown in figure 4.20. From the figure it is clear that D1 shows good optical limiting property than all other concentrations. Optical limiting threshold is found to be minimum for D1 solution and it varies as D1<C1<E1<F1.

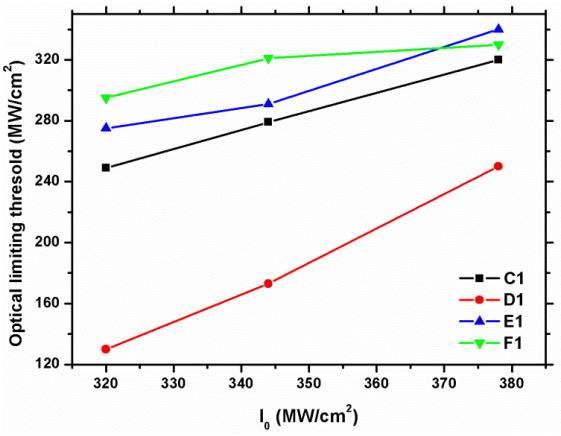

Figure 4.20: *Variation of optical limiting threshold of different compositions of nanoclusters having concentrations C1, D1, E1 and F1 at 532 nm with change in input fluence (I_0).*

Nonlinear optical characterization conducted on chalcogenide glass nanocolloids revealed that all of the nonlinear optical parameters and limiting threshold varies with bandgap and which is governed by either concentration of the solute (bulk glass) in the solvent (amine) or the composition of the solute.

4.4.6 Photo irradiation Experiments

Chalcogenide glasses are highly sensitive to electromagnetic radiation and show a variety of photoinduced effects as a result of illumination[34,35,36,37]. Photo induced increase of the refractive index as well as the film densification[38] has been observed in solution-deposited arsenic sulphide. Photodarkening and photo-induced 'Ag' diffusion in spin-coated As-S, As-Se and Sb-S films were reported[39,40,41,42] and were consistent with thermal evaporated materials.

Since nonlinear studies on nanocolloidal solution were carried out using high intensity pulsed laser, the probability for the occurrence of photoinduced changes in the nanocolloids are very high. Optical absorption spectroscopy using UV/VIS/IR spectrophotometer, fluorescence, SEM and XRD analyses were employed to evaluate the structural characterization of nanocolloidal solutions after high intensity laser exposure. 1ml of sample C0, C2 and C3 were exposed to laser radiation at 400MW/cm^2 for 45 minutes. Scanning electron microscope (SEM) (JEOL Model JSM-6390LV) images and XRD analysis of spin coated, laser exposed nanocolloids were taken to check for any structural changes after laser exposure. Figure 4.21(a) and 4.21(b)

indicates X-ray diffraction graph of spin coated C0 before and after laser exposure. Lack of any sharp peak in the XRD pattern of the sample after laser exposure shows that the tendency to crystallize, after laser exposure, is less.

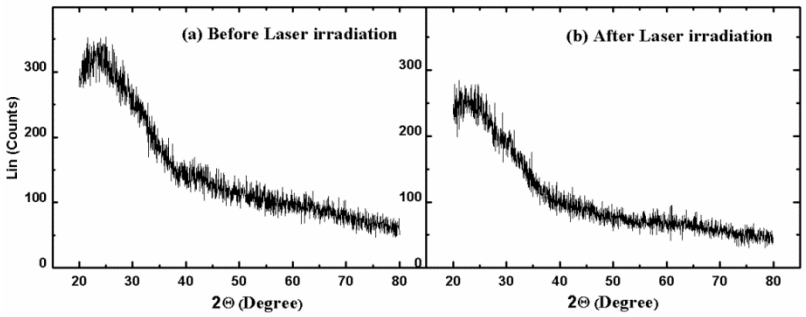

Figure 4.21: (a)*XRD of spin coated nanocolloidal solution 'C0' before laser exposure. (b) 'C0' after laser exposure.*

The SEM images of unexposed and laser exposed C0 displayed in Figure 4.22(a) and 4.22(b) respectively show some agglomeration but no structural change is observed after laser irradiation. Absorption and fluorescence spectra of irradiated nanocolloidal solution were taken and no remarkable change could be observed after laser exposure.

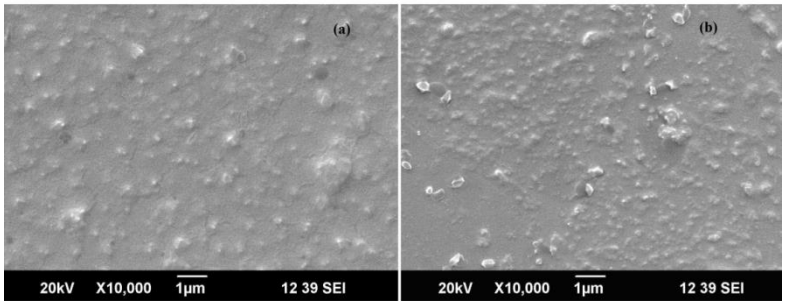

Figure 4.22: *(a) SEM image of unexposed and (b) laser exposed nanocolloid of concentration C0 spin coated on silica substrate. It shows some agglomeration but no structural change is observed after laser irradiation*

Irradiation using continuous wave laser with emission below bandgap

Irradiation experiments were carried out using semiconductor continuous wave laser with 532nm wavelength at a power of 75mW by varying time. 1ml solution of concentration C3 was taken in a 1cmx1cm cuvette and exposed to laser light. Figure 4.23 (a) shows absorption spectra of nanocolloidal solution of concentration C3 for different durations of irradiation

and figure 4.25 (b) shows the corresponding fluorescence spectra. A laser induced blue shift in the bandgap as well as a detraction in the intermediate defect state peak is observed. Fluorecence spectra after irradiation shows fluorescence quenching because of the deminishment of intermediate defect states. However, we could not observe any bandgap shift after pulsed laser irradiation.

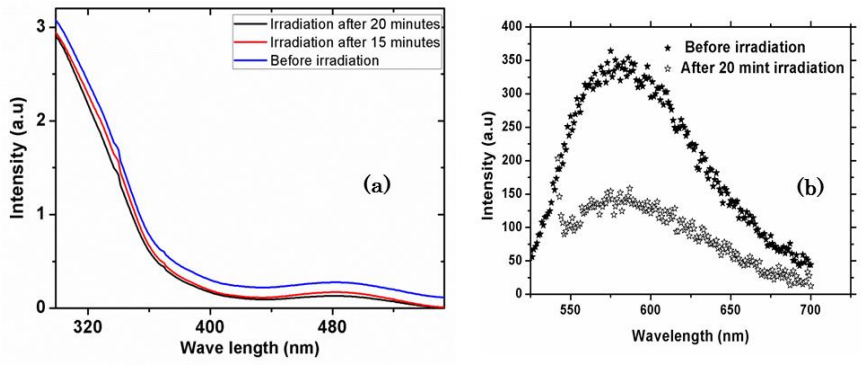

Figure 4.23: *(a) Absorption spectrum of C3 colloidal solution after 532nm continuous semiconductor laser exposure. (b) Corresponding fluorescence spectra of C3 colloidal solution after 532nm continuous semiconductor laser irradiation.*

Irradiation using continuous wave laser with emission above bandgap

Irradiation studies using 404nm continuous laser at 100mW was also carried out. Figure 4.24 shows absorption spectra of nanocolloidal solution for different durations of irradiation.

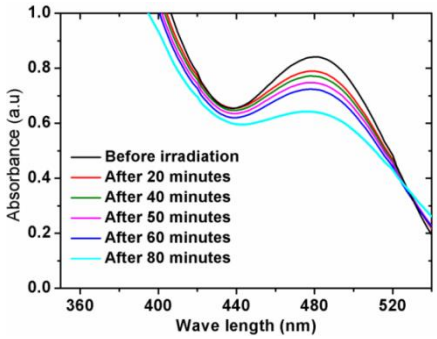

Figure 4.24: *Absorption spectra of 404nm laser irradiated nanocolloidal solution C2 for different durations of irradiation.*

As the irradiation duration is increased, absorption edge is blue shifted or photobleaching occurs. The absorption peak around 480nm corresponding to

localized defect states detracts with increase in exposure time. Figure 4.25 (a) and (b) represent variation of band edge and decrease in defect state density with respect to irradiation time. Both of these graphs show same form of variation.

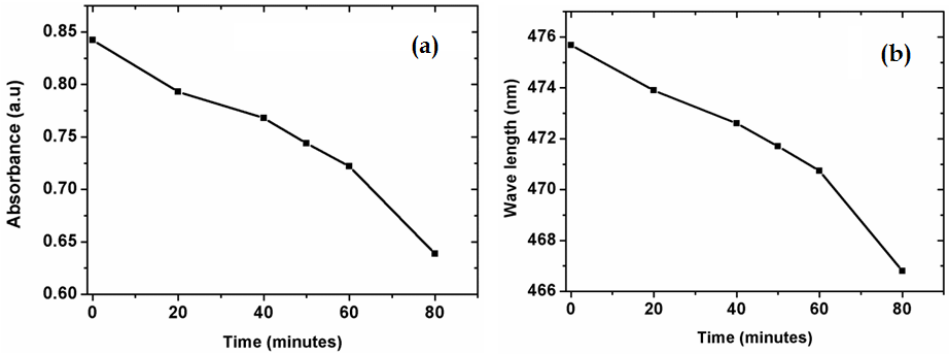

Figure 4.25: *(a) Variation of defect state absorbance with respect to irradiation time. (b) Variation of wave length corresponding to band edge with respect to irradiation time.*

With the increase in irradiation time absorption edge is blue shifted or photobleaching has occurred. The absorption peak around 480nm corresponding to localized defect states detracts with increase in exposure time. Figure 4.25 (a) and (b) represents variation of band edge and decrease in defect state density with respect to irradiation time. Both of these graphs show same form of variation.

4.5 Studies on Chg/Ethanol amine nanocolloids

Nathan A Carlie[43] investigated the variation of dissolution properties of different compositions of chalcogenide glasses in different solvents. His studies revealed that chalcogenide glass in ethanolamine shows high dissolution rate and is identified as a preferred solvent due to better solubility limits, high solution viscosity, and reduced evaporation limits. Finely ground $Ge_{27}Sb_9Se_{64}$ glass was dissolved in ethanol amine by stirring at room temperature until complete dissolution was achieved as discussed in section 4.3. Nanocolloidal solutions of two concentrations (0.05g/ml (G1) and 0.02g/ml (G2)) were prepared by dissolving it in ethanol amine (Sigma Aldrich, 99.9%). The dissolution was carried out inside a sealed glass container and the samples were readily soluble in ethanol amine. The dissolved samples G1 and G2 appeared in dark red and black colour respetively. Nanocolloidal solutions

of less concentration (as in the case of butylamine) were also prepared which shows no colour change after dissolution. In that case, the powdered samples in the solvent disappeared within few seconds. After dissolution the solutions were filtered out using a 200nm pore size Polytetrafluoroethylene (PTFE) syringe filter to remove any undissolved particles.

4.5.1 Analysis of cluster size and composition

To evaluate the composition of the nanoclusters, EDS studies were conducted. Figure 4.26 shows the EDS spectra of the spin coated G2 and it confirms the presence of all elements, germanium, selenium and antimony in the cluster. The existence of the peak coresponding to 'Carbon' and 'Oxygen' indicates the presence of unevaporated solvent in the clusters.

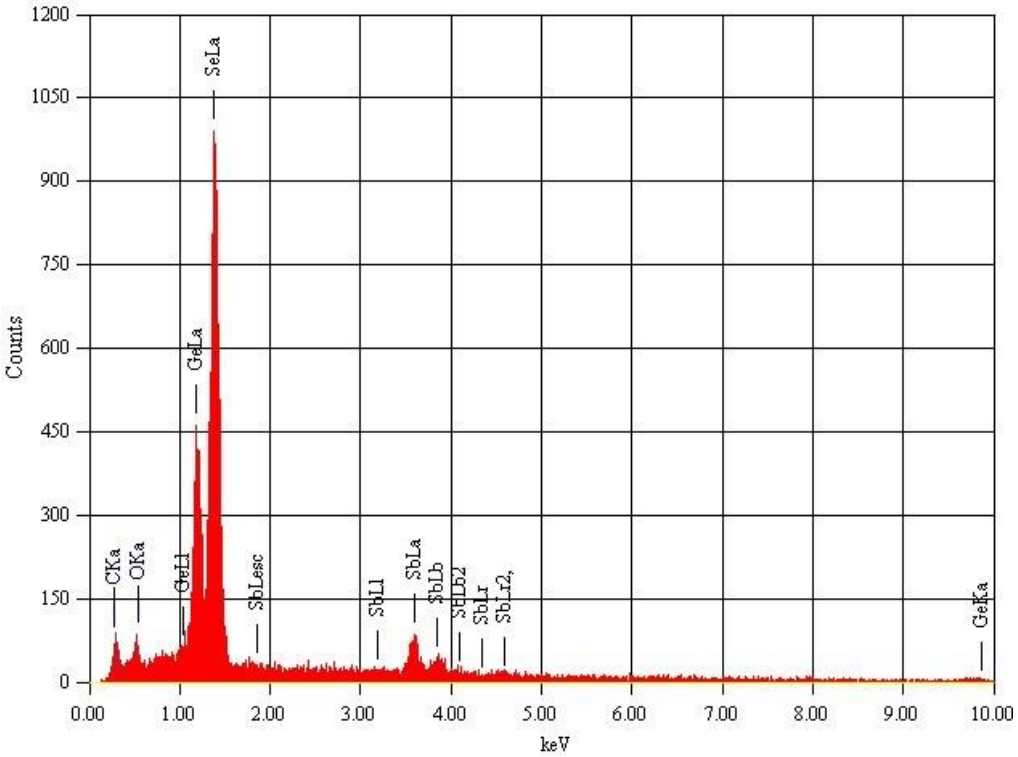

Figure 4.26: *EDS image of $Ge_{27}Sb_9Se_{64}$/ethanolamine cluster (G2) which confirms the presence of all the elements in the cluster. The existence of the peak corresponds to 'C' and 'O' indicates the presence of unevaporated solvent in the clusters.*

Cluster size of $Ge_{27}Sb_9Se_{64}$ glass solutes of concentration G1 and G2 in ethanolamine solvent was analyzed by dynamic light scattering (DLS) at

532nm using Horiba SZ-100 nanoparticle size analyzer. Figure 4.27 (a) and 4.27 (b) depicts particle size distribution for G1 and G2 respectively. The average size of the solute found from the distribution curve is 10.1nm for G1 and 6.8nm for G2. It is clear that the distribution curve is very wide with a standard deviation of 38nm and 59nm for G1 and G2 respectively. From the figure, it is clear that the distribution is not Gaussian which indicates that it has got more than one size distributions. As in the case of 'butylamine' nanocolloids a concentration dependent size reduction is observed in $Ge_{27}Sb_9Se_{64}$/ethanolamine samples also.

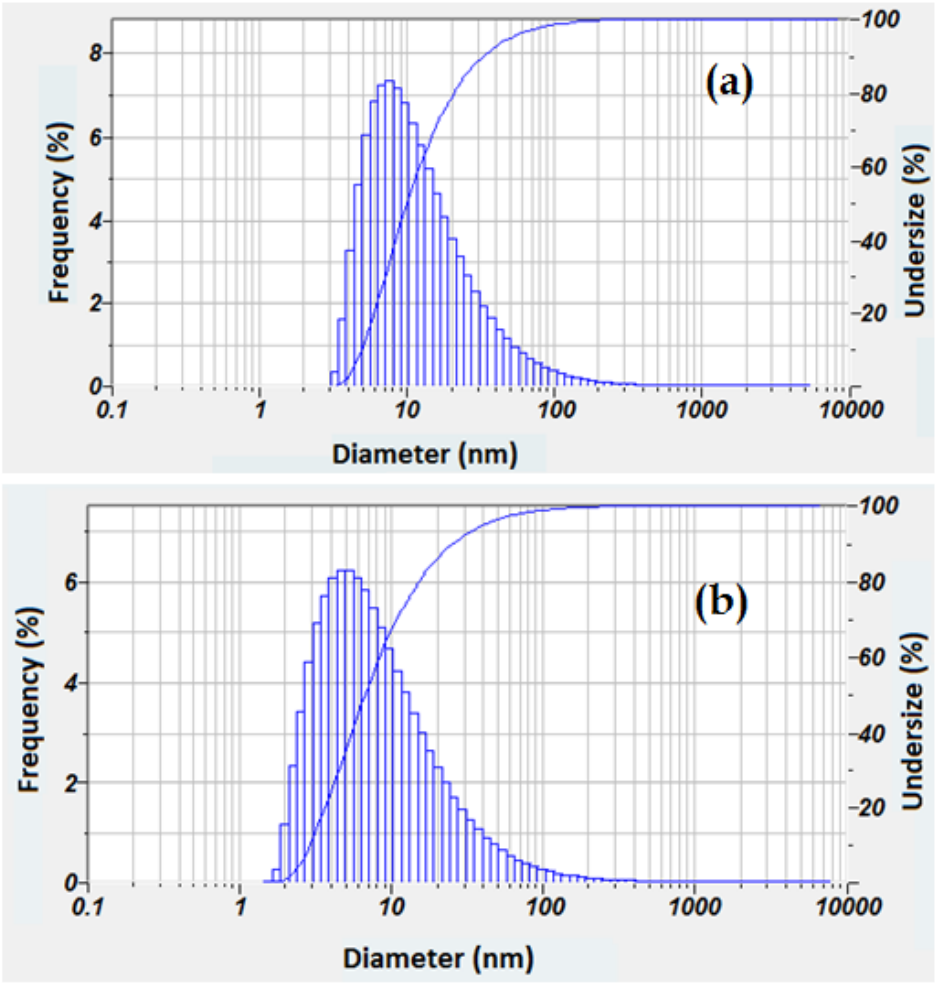

Figure 4.27 : *(a) Particle size distribution curve of G1 obtained from dynamic light scattering method. (b) Particle size distribution curve of G2.*

4.5.2 Optical absorption spectroscopy

Linear optical characterization of $Ge_{27}Sb_9Se_{64}$/ethanolamine nanocolloids were carriedout using UV-Vis NIR spectroscopy. Optical bandgap (Eg) of the nanoclusters in the colloidal solution can be found from linear absorption spectra or from transmission curves. Absorption edge of the glasses are not sharp and optical bandgap is taken to be the point at which the absorption curve changes from a qudratic dependence on energy to an exponential dependence.

The absorption spectra of $Ge_{27}Sb_9Se_{64}$/ethanolamine solutions of varying concentrations are given in figure 4.28. The absorption spectra of $Ge_{27}Sb_9Se_{64}$/ethanolamine solutions show that the absorption edge is located in the near IR region as in the case of bulk chalcogenide glasses. This is due to the presence of very high concentration of the solute in the solvent. As in the case of 'butyl amine nanocolloids', the band edge is blue shifted towards the visible region of electromagnetic spectrum with the decrease in the solute concentration.

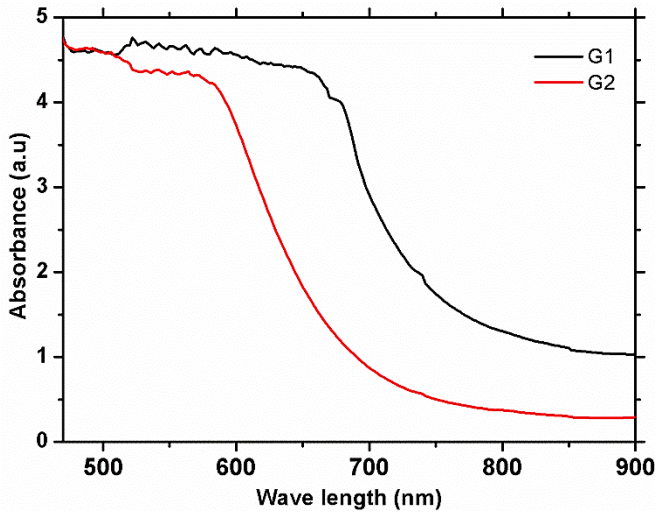

Figure 4.28: *Absorption spectra of $Ge_{27}Sb_9Se_{64}$/ethanolamine nanocolloids of concentration G1 and G2 showing a concentration dependent blue shift in the band edge*

The optical bandgap of the nanoclusters have been calculated for G1 and G2 as 1.8eV and 2.03eV respectively. It shows a concentration dependent decrease in the bandgap as in the case of butylamine nanocolloids as indicated earlier. $Ge_{27}Sb_9Se_{64}$/ethanolamine solutions of concentration G1 and G2 show no fluorescence emission as in the previous case. It is clear from the

absorption spectra that, due to very high concentration of the colloidal solution, the absorption peak due to LP band merge with the main absorption 'bonding (σ)' and 'unoccupied antibonding' (σ*) bands. Since the colloidal solutions G1 and G2 have no optical transperancy at 532nm, the nonlinear as well as thermal diffusivity measurements could not be carried out.

4.6 Summary of findings

- Nanocolloidal chalcogenide glasses of four different compositions $Ge_{27}Ga_9Se_{64}$, $Ge_{27}Sb_9Se_{64}$, $Ge_{27}Se_{73}$, and $Ge_{20}Se_{80}$ and with varying concentrations were prepared by dissolving them in n-butyl amine as well as in ethanol amine.
- Analyses on cluster size of Chg/butylamine nanoclusters were carried out using SEM as well as particle size analyzer. Compositional studies conducted on the nanoclusters confirm the presence of all elements in the cluster.
- Optical absorption spectroscopy of the colloidal solutions were carried out and it shows defect state absorption in nanoclusters which is observed as a peak around 480nm in the absorption spectra. A blue shift in the band edge and diminishment in the density of defect states is noticed with the decrease in the concentration of the chalcogenide glass in butylamine. That is, by varying solute concentration in the solvent we can tune the bandgap, density and energy of mid-gap defect states.
- The Photoluminescence studies conducted on the nanocolloids confirms the existence of intermediate defect state level. Fluorescence emission for excitation wavelengths in the band tail peak is observed, and the emission is maximum at 480nm excitation. These results emphasize the occurrence of defect states with varying density of states with a maximum energy corresponding to 480nm. As the concentration of solute glass decreases, the defect state absorption diminishes and shows a fluorescence blue shift.
- Thermal lens analysis conducted on the colloids shows a higher thermal diffusivity for samples with less defect state density, which is attributed to the low levels of scattering of thermal waves from defect centers.
- Open aperture Z-scan studies carried out on different compositions of nanocolloids using nanosecond laser show RSA arised due to the phenomenon of two photon absorption combined with two step cascade

process of photon absorption. The localized state located in the forbidden energy gap acts as an intermediate state, from where the second photon gets absorbed. For all compositions of nanocolloids, nonlinear absorption is found to be reduced and finally vanished with decrease in concentration. This is due to the detraction of defect states in the bandgap at low concentrations. $Ge_{27}Sb_9Se_{64}$/butyl amine shows the highest nonlinearity and $Ge_{20}Se_{80}$/butyl amine solution has the least nonlinear absorption.

- Nonlinear optical studies using closed aperture Z-scan technique reveal large negative nonlinear refraction near the one photon absorption edge due to bandgap resonant effects as well as due to defect state assisted thermal nonlinearity. A bandgap dependent variation in nonlinear refractive index is observed. By varying the concentration of solute in the solvent, we can tune the bandgap, density, and energy of mid-gap defect states and thereby nonlinear optical properties of nanocolloids. Nonlinear optical coefficients of various concentrations for all compositions of nanocolloids were evaluated and among them $Ge_{27}Sb_9Se_{64}$ solutions seem to be the material having highest nonlinear optical properties.
- Universal dispersion function G_2, which displays the dispersion and magnitude of n_2 with frequency, is plotted by including the effect of two photon absorption (TPA) as well as quadratic stark effect. Experimental data of nanocolloids show large deviation from the theoretical curve and it is explained as due to the presence of localized lone-pair states located in the bandgap. The localization occurs due to the network fragmentation of bulk glass which has resulted from the interaction of solvent butylamine. $Ge_{27}Sb_9Se_{64}$ solutions show maximum deviation from the theoretical curve in expansion to others.
- The optical limiting threshold calculated for each concentration reveals that the solution with a high solute concentration is a better optical limiter. Nonlinear optical characterization conducted on chalcogenide glass nanocolloids revealed that all of the nonlinear optical parameters and limiting threshold varies with bandgap which inturn is governed by either concentration of the solute (bulk glass) in the solvent (amine) or the composition of the solute.
- Structural property variations of nanocolloidal solutions after high intensity laser exposure were evaluated using optical absorption spectroscopy, fluorescence, SEM and XRD analysis. Studies conducted using 532nm, pulsed laser exposure shows no noticeable structural change in XRD and SEM except a small increase of 532nm

transmission is observed and it becomes constant after the elapse of 15 minutes.

- A laser induced blue shift in the bandgap as well as a detraction in the intermediate defect state peak were observed after exposure to below bandgap (532nm) laser radiation. Fluorecence spectra after irradiation show fluorescence quenching because of the deminishment of intermediate defect states.
- A blue shift in the absorption edge (or photobleaching) and a corresponding detraction in the absorption peak around 480nm from localized defect states is observed with increase in exposure time with continuous wave laser with emission above bandgap (404nm).
- Two different concentrations of $Ge_{27}Sb_9Se_{64}$ nanocolloids were prepared by dissolving it in ethanolamine. Compositional as well as cluster size analysis were done using energy dispersive spectroscopy (EDS) and dynamic light scattering (DLS) techniques. EDS image of $Ge_{27}Sb_9Se_{64}$/ethanolamine cluster confirms the presence of all elements in the cluster. It also shows the signature of unevaporated solvent. DLS analysis confirms the formation of nano-sized clusters after dissolution and the cluster size decreases with decrease in the solute concentration as in the case of 'butylamine' nanocolloids.
- Linear optical characterization of $Ge_{27}Sb_9Se_{64}$/ethanolamine nanocolloids were carried out using UV-Vis NIR spectroscopy and studies show that the absorption edge is located in the near IR region as in the case of bulk chalcogenide glasses. This is due to the presence of very high concentration of the solute in the solvent. As in the case of 'butyl amine nanocolloids', the band edge is blue shifted towards the visible region of electromagnetic spectrum with decrease in the solute concentration. Since $Ge_{27}Sb_9Se_{64}$/ethanolamine colloidal solutions have no optical transperancy at 532nm, it was not possible to carry out the nonlinear as well as thermal diffusivity measurements.

4.7 Reference

[1]Chern Geeng-Chuan, and I. Lauks. "Spin-coated amorphous chalcogenide films." *Journal of Applied Physics* 53, no. 10 (1982): 6979-6982.

[2]Kohoutek T., T. Wagner, M. Frumar, A. Chrissanthopoulos, O. Kostadinova, and S. N. Yannopoulos. "Effect of cluster size of chalcogenide glass nanocolloidal solutions on the surface morphology of spin-coated amorphous films." *Journal of Applied Physics* 103, no. 6 (2008): 063511.

[3]Chern G. C., and I. Lauks. "Spin coated amorphous chalcogenide films: Structural characterization." *Journal of Applied Physics* 54, no. 5 (1983): 2701-2705.

[4]Chern G. C., I. Lauks, and K. H. Norian. "Spin-coated amorphous chalcogenide films: photoinduced effects." *Thin solid films* 123, no. 4 (1985): 289-296.

[5]Chern G. C., I. Lauks, and A. R. McGhie. "Spin coated amorphous chalcogenide films: Thermal properties." *Journal of applied physics* 54, no. 8 (1983): 4596-4601.

[6]Tsay Candice, Yunlai Zha, and Craig B. Arnold. "Solution-processed chalcogenide glass for integrated single-mode mid-infrared waveguides." *Optics express* 18, no. 25 (2010): 26744-26753.

[7]Tsay Candice, Elvis Mujagić, Christi K. Madsen, Claire F. Gmachl, and Craig B. Arnold. "Mid-infrared characterization of solution-processed As_2S_3 chalcogenide glass waveguides." *Optics express* 18, no. 15 (2010): 15523-15530.

[8]Sanchez Eric A., Maike Waldmann, and Craig B. Arnold. "Chalcogenide glass microlenses by inkjet printing." *Applied optics* 50, no. 14 (2011): 1974-1978.

[9]Song Shanshan, Nathan Carlie, Julie Boudies, Laeticia Petit, Kathleen Richardson, and Craig B. Arnold. "Spin-coating of $Ge_{23}Sb_7S_{70}$ chalcogenide glass thin films." *Journal of Non-Crystalline Solids* 355, no. 45 (2009): 2272-2278.

[10]Song Shanshan, Janesha Dua, and Craig B. Arnold. "Influence of annealing conditions on the optical and structural properties of spin-coated As_2S_3 chalcogenide glass thin films." *Optics express* 18, no. 6 (2010): 5472-5480.

[11]Tintu, R., K. Saurav, K. Sulakshna, V. P. N. Nampoori, P. Radhakrishnan, and Sheenu Thomas. "$Ge_{28}Se_{60}Sb_{12}$/PVA composite films for photonic applications." *Journal of Non-Oxide Glasses* 2, no. 4 (2010): 167-174.

[12]Mamedov S. B., and M. D. Mikhailov. "Dissolution kinetics of glassy and crystalline As_2S_3 in aqueous sodium sulfide and hydroxide." *Journal of non-crystalline solids* 221, no. 2 (1997): 181-186.

[13]Michailov M. D., S. B. Mamedov, and S. V. Tsventarnyi. "Dissolution kinetics of glassy arsenic sulfide in alkali and amine solutions." *Journal of non-crystalline solids* 176, no. 2 (1994): 258-262.

[14]M.D. Mikhailov, S.B. Mamedov, and S.V. Tsventarnyi,"Kinetics of Dissolution of Glassy Arsenic Sulfide in Alkali and Amine Solutions" Journal of applied chemistry of the USSR 60, no. 4 (1987): 693-696.

[15]S.A. Zenkin, S.B. Mamedov, and M.D. Mikhailov,"Kinetics of Dissolution of Arsenic Sulfide Films in Solutions of Ammonia, Methylamine, and

Dimethylamine" Journal of applied chemistry of the USSR 61, no. 7 (1988): 1336-1340.

[16]MacColl Robert, and Stanley Windwer. "Spectroscopy of sulfur in ethylenediamine." *The Journal of Physical Chemistry* 74, no. 6 (1970): 1261-1266.

[17]Shimakawa K., A. Kolobov, and S. R. Elliott. "Photoinduced effects and metastability in amorphous semiconductors and insulators." *Advances in Physics* 44, no. 6 (1995): 475-588.

[18]Sebastian Indu, S. Divya, V. P. N. Nampoori, P. Radhakrishnan, and Sheenu Thomas. "Impact of intermediate localized states on nonlinear optical absorption of Ga-Ge-Se nanocolloidal solutions." *Applied Physics Letters* 102, no. 3 (2013): 031115.

[19]Tanaka Keiji. "Optical nonlinearity in photonic glasses." *Journal of Materials Science: Materials in Electronics* 16, no. 10 (2005): 633-643.

[20]Sebastian Indu, S. Mathew, V. P. N. Nampoori, P. Radhakrishnan, and Sheenu Thomas. "Concentration tuned bandgap and corresponding nonlinear refractive index dispersion in Ga-Ge-Se nanocolloids." *Journal of Applied Physics* 114, no. 5 (2013): 053102.

[21]Urbach Franz. "The long-wavelength edge of photographic sensitivity and of the electronic absorption of solids." *Physical Review* 92, no. 5 (1953): 1324.

[22]Daly Francis P., and Chris W. Brown. "Raman spectra of sulfur dissolved in primary amines." *The Journal of Physical Chemistry* 77, no. 15 (1973): 1859-1861.

[23]Sebastian Indu, V. P. N. Nampoori, P. Radhakrishnan, and Sheenu Thomas. "Experimental verification of localized defect states in Ga-Ge-Se nano colloidal solutions." *Journal of Materials Science* 49, no. 10 (2014): 3732-3735.

[24]Kastner Marc. "Bonding bands, lone-pair bands, and impurity states in chalcogenide semiconductors." *Physical Review Letters* 28, no. 6 (1972): 355.

[25]Manikandan N., M. Paulraj, and S. Asokan. "Thermal diffusivity measurements on As–Te–Ga glasses by photo-thermal deflection technique: Composition dependence and topological thresholds." *Journal of Non-Crystalline Solids* 355, no. 1 (2009): 58-60.

[26] Sheik-Bahae Mansoor, Ali Said, Tai-Huei Wei, David J. Hagan, and Eric W. Van Stryland. "Sensitive measurement of optical nonlinearities using a single beam." *Quantum Electronics, IEEE Journal of* 26, no. 4 (1990): 760-769.

[27]Van Stryland, Eric W., M. A. Woodall, H. Vanherzeele, and M. J. Soileau. "Energy band-gap dependence of two-photon absorption." *Optics letters* 10, no. 10 (1985): 490-492.

[28]Tanaka Keiji, and Akira Saitoh. "Optical nonlinearity in glasses: the origin and photo-excitation effects." *Journal of Materials Science: Materials in Electronics*18, no. 1 (2007): 75-79.

[29]Tintu R., V. P. N. Nampoori, P. Radhakrishnan, and Sheenu Thomas. "Nonlinear optical studies on nanocolloidal Ga–Sb–Ge–Se chalcogenide glass."*Journal of Applied Physics* 108, no. 7 (2010): 073525.

[30]Tintu R., and Thomas Sheenu. "Fabrication and Characterization of Chalcogenide nano composite based materials for Photonic device applications." PhD diss., Cochin University of Science and Technology, 2011.

[31]Adair Robert, L. L. Chase, and Stephen A. Payne. "Nonlinear refractive index of optical crystals." *Physical Review B* 39, no. 5 (1989): 3337.

[32]Sheik-Bahae, M., D. J. Hagan, and E. W. Van Stryland. "Dispersion and band-gap scaling of the electronic Kerr effect in solids associated with two-photon absorption." *Physical review letters* 65, no. 1 (1990): 96.

[33]Sheik-Bahae, Mansoor, David Crichton Hutchings, David J. Hagan, and Eric W. Van Stryland. "Dispersion of bound electron nonlinear refraction in solids."*Quantum Electronics, IEEE Journal of* 27, no. 6 (1991): 1296-1309.

[34]Zakery A., and S. R. Elliott. "Optical properties and applications of chalcogenide glasses: a review." *Journal of Non-Crystalline Solids* 330, no. 1 (2003): 1-12.

[35]Seddon A. B. "Chalcogenide glasses: a review of their preparation, properties and applications." *Journal of Non-Crystalline Solids* 184 (1995): 44-50.

[36]Owen A. E., A. P. Firth, and P. J. S. Ewen. "Photo-induced structural and physico-chemical changes in amorphous chalcogenide semiconductors."*Philosophical Magazine B* 52, no. 3 (1985): 347-362.

[37]Ewen P. J. S., A. E. Owen, M. Cable, and J. M. Parker. "High Performance Glasses." *Blackie, London* (1992): 287.

[38]Song Shanshan. *Solvent-casting of chalcogenide glasses and their applications in mid-infrared optics*. Princeton University, 2011.

[39]Shtutina S., M. Klebanov, V. Lyubin, S. Rosenwaks, and V. Volterra. "Photoinduced phenomena in spin-coated vitreous As_2S_3 and AsSe films."*Thin Solid Films* 261, no. 1 (1995): 263-265.

[40]Zha Yunlai, and Craig B. Arnold. "Solution-processing of thick chalcogenide-chalcogenide and metal-chalcogenide structures by spin-coating and multilayer lamination." *Optical Materials Express* 3, no. 2 (2013): 309-317.

[41]J. Gutwirth, T. Wagner, T. Kohoutek, M. Vlcek, S. Schroeter, V. Kovanda, M. Vlcek, and M. Frumar, "Physical properties and structure of amorphous $Ag_x(Sb_{0.33}S_{0.67})_{(100-x)}$ prepared by optically-induced diffusion and dissolution of silver into spin-coated amorphous $Sb_{33}S_{67}$ films and their application for optical recording," *Journal of Optoelectronics and Advanced Materials* 5, no. 5 (2003): 1139-1146.

[42]T. Wágner, M. Krbal, T. Kohoutek, V. Peřina, M. Vlček, M. Vlček, and M. Frumar, "Kinetics of optically- and thermally-induced diffusion and dissolution of silver in spin-coated $As_{33}S_{67}$ amorphous films; their properties and structure," *Journal of non-crystalline solids* 326 (2003): 233-237.

[43]Nathan A. Carlie, "A solution based approach to the fabrication of novel chalcogenide glass materials and structures", PhD thesis, Graduate school of Clemson university (2010)

Chapter 5

Fabrication and characterization of chalcogenide glass based waveguide structures

The present chapter deals with the structural and optical characterization of thermally evaporated as well as solvent casted thin films of different compositions of chalcogenide glasses. Detailed studies on structural, compositional and optical properties of thermal evaporated thin films are presented in the first section. Thin films of $Ge_{27}Sb_9Se_{64}$ glass were prepared by wet chemical method and the structural, compositional and optical characteristics of the prepared thin films were analyzed using different techniques. Array of ridge waveguides were fabricated on thermally evaporated $Ge_{27}Sb_9Se_{64}$ glass thin films by capillary force lithography (CFL) technique which opens up the opportunity for the fabrication of waveguide arrays in IR based sensor.

5.1 Introduction

Thin films have attracted most of the scientific interest and are more exploitable in the application sector than bulk glasses. Fabrication of an IR transparent, non-reactive and chemically inert planar chalcogenide glass waveguide with high refractive index is an essential requirement for the fabrication of IR based sensor

The capability of fabricating and tailoring in a consistent way of amorphous semiconductor thin films is important for modern electronic devices. Different methods that are typically employed[1,2,3,4,5] for thin film deposition include thermal evaporation, magnetron sputtering, pulsed laser

deposition, etc , which eventually lead to different local atomic arrangements and hence to films with different properties.

Main shortcomings are encountered with the conventional techniques ranging from poor control of materials compositions (for evaporation techniques) or high cost of film fabrication. On the other hand, wet-chemistry methods, where film deposition is achieved[6,7] through spin coating, dip coating or drop casting of material's solution, have recently gained attraction in view of their simplicity, reliability in depositing thin films and low cost of operation.

5.2 Scope of the chapter

High refractive index, low loss, IR transparent optical waveguides are required for the realization of IR based sensors. Since the properties of chalcogenide glasses are a function of its thermal history, the thin film waveguides or fibers derived from bulk glass may not have the same properties that are seen in their melt-derived bulk analogues. Therefore detailed evaluations of structural and optical properties of thin films are required. This chapter focuses on the fabrication of different compositions of chalcogenide glass waveguides by thermal evaporation as well as solution processing techniques and their analysis using different characterization techniques.

5.3 Studies on thermal evaporated thin films

Thermal evaporation technique is a conventional method, widely used for the preparation of thin films. Chalcogenide glass thin films of different compositions of bulk glass have been deposited on to glass substrate using thermal evaporation technique. The bulk samples were taken in a molybdenum boat and the coating was carried out through resistive heating by applying 8.5A current across the boat for five to ten minutes in a closed chamber at around 3×10^{-5}mbarr pressure to reduce contamination. The vaporized samples were allowed to condense on plasma cleaned silica glass substrate placed above the molybdenum boat. $Ge_{20}Se_{80}$ melts and evaporates at a low current even when the molybdenum boat gets red hot. Therefore $Ge_{20}Se_{80}$ thin film samples were coated at a low current, 7.45A.

5.3.1 Structural characterizations

X-ray diffraction studies

The prepared thin film samples are characterized using X-ray diffraction technique (XRD). Figure 5.1 (a) shows the XRD traces of $Ge_{27}Ga_9Se_{64}$ thin film and (b) displays XRD spectra of $Ge_{20}Se_{80}$ thin film. No sharp structural peaks have been observed in the XRD traces of $Ge_{27}Ga_9Se_{64}$, $Ge_{27}Sb_9Se_{64}$, and $Ge_{27}Se_{73}$ thin films and this confirms their amorphous nature. However XRD pattern of $Ge_{20}Se_{80}$ glass shows two prominent sharp peaks around 24° and 30° and a less intensity peak at 42°, which indicates the presence of crystalline nature. All the diffraction peaks in this pattern can be indexed as a trigonal phase of selenium (JCPDS, No. 6-362) with a cell constants a=4.37Å, c=4.95Å. 'Se' exists in four major allotropic forms: amorphous, trigonal (hexagonal), α and β-monoclinic allotropes; of which the trigonal selenium (consists of helical -Se- chains[8]) is the most stable crystal form. Vapour phase deposition[9] influences the structure and hence properties of the as-deposited chalcogenide films, which can be different from their melted, bulk counterparts.

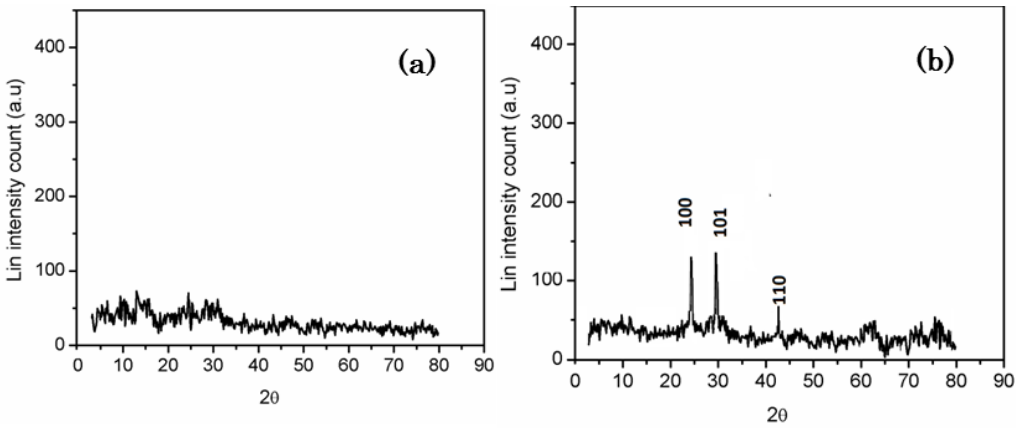

Figure 5.1: (a)*XRD spectrum of $Ge_{27}Ga_9Se_{64}$ shows no prominent sharp peaks revealing the amorphous nature of the samples. (b) XRD spectra of $Ge_{20}Se_{80}$ shows prominent sharp peaks revealing the presence of crystalline structure in the thin film.*

Raman Analysis

In order to evaluate the bonding structure of the thermally coated thin film samples, Micro-Raman analysis has been employed on each sample at near infrared wavelength, 785nm. Raman spectra of all compositions of thin

films are shown in figure 5.2. As noted in the bulk glasses, the three main regions are (a) a broad, low-intensity band between 50 and 175cm^{-1}, (b) a relatively sharp high-intensity band around 196cm^{-1} except for $Ge_{20}Se_{80}$ along with a shoulder around 214cm^{-1}, and (c) a broad, high-intensity band spanning from 240 to 300cm^{-1}. Raman band assignments for all compositions are summarized in Table 3.1 of chapter 3. The band at 196cm^{-1} corresponds to the symmetric stretching of corner-shared (CS) $GeSe_4$ tetrahedra while the shoulder at 214cm^{-1} corresponds to the breathing mode of edge-shared (ES) Se atoms connected between two neighboring $GeSe_4$ tetrahedra[10,11,12].

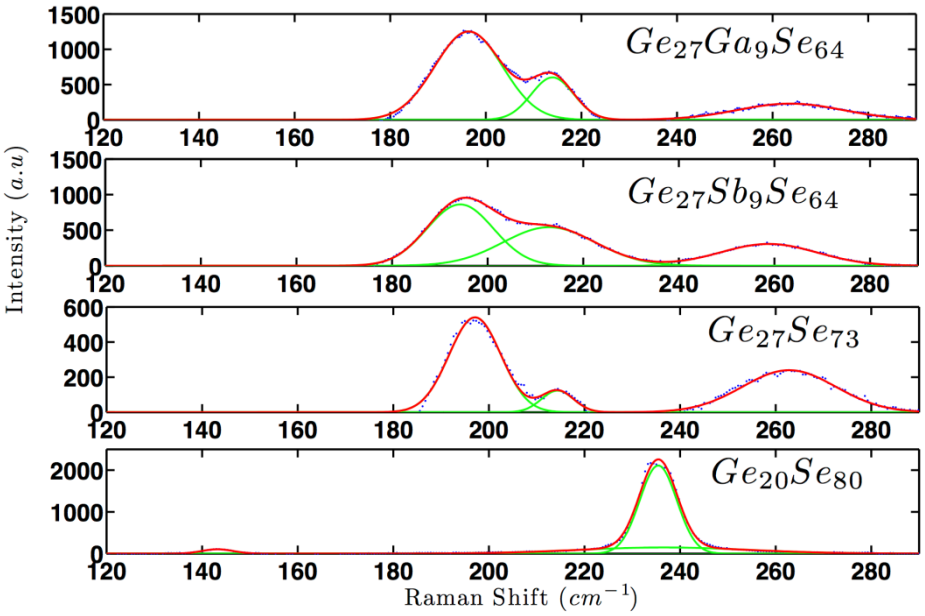

Figure 5.2: *Raman spectra of thermally coated $Ge_{27}Ga_9Se_{64}$, $Ge_{27}Sb_9Se_{64}$ and $Ge_{27}Se_{73}$ thin films with 785nm excitation shows similar bands as in the case of bulk glasses. The Raman spectrum of $Ge_{20}Se_{80}$ thin film shows stretching band of trigonal selenium. (red line experimental and green line decomposed Gaussian.)*

The Raman spectrum of $Ge_{20}Se_{80}$ thin film in figure 5.2 shows no 'CS' and 'ES' vibrational band while an intense peak at 234cm^{-1} is observed which is the characteristic stretching mode of a chain[13] like structure that exists only in trigonal[14,15] selenium and a peak around 145cm^{-1} is attributed to the transverse optical photon mode[16]. The shoulder band at 190cm^{-1} present in $Ge_{27}Sb_9Se_{64}$ bulk glass which corresponds to heteropolar Sb-Se bond vibrations in the Sb_2Se_3 units is seen to be merged with high intensity 'CS' vibration band in $Ge_{27}Sb_9Se_{64}$ glass thin film sample.

5.3.2 Compositional evaluation

EDS analysis

To confirm the composition of all thermal evaporated thin films, EDS spectra have been taken.

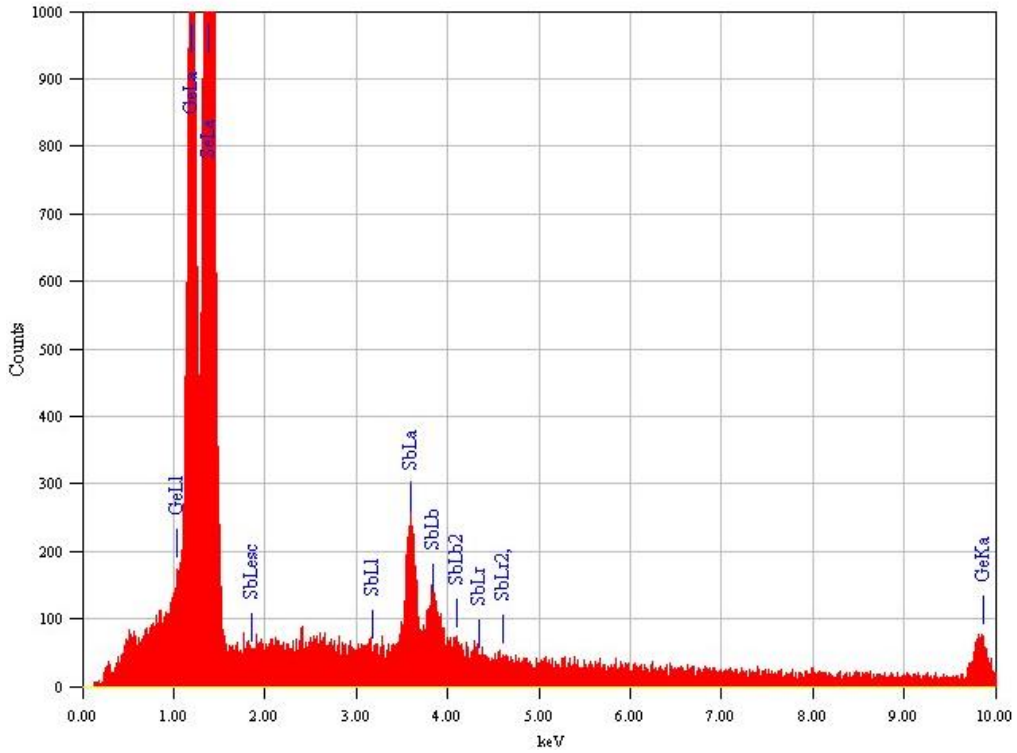

Figure 5.3: *EDS spectra of $Ge_{27}Sb_9Se_{64}$ glass thin film shows peaks corresponding to Ge, Sb, and Se.*

Table 5.1 compares the atomic percentage of components obtained from EDS analysis with respect to the nominal composition. Figure 5.3 shows EDS spectra of $Ge_{27}Sb_9Se_{64}$ thin film.

Nominal Composition	Element	Atomic %
$Ge_{20}Se_{80}$	Ge	6.31
	Se	93.69
$Ge_{27}Se_{73}$	Ge	25.70
	Se	74.30
$Ge_{27}Sb_9Se_{64,}$	Ge	29.58
	Sb	5.19
	Se	65.23
$Ge_{27}Ga_9Se_{64,}$	Ge	24.35
	Ga	8.59
	Se	67.06

Table 5.1: *Variation of atomic percentage of components obtained from EDS analysis with respect to the nominal composition in different compositions of thin films.*

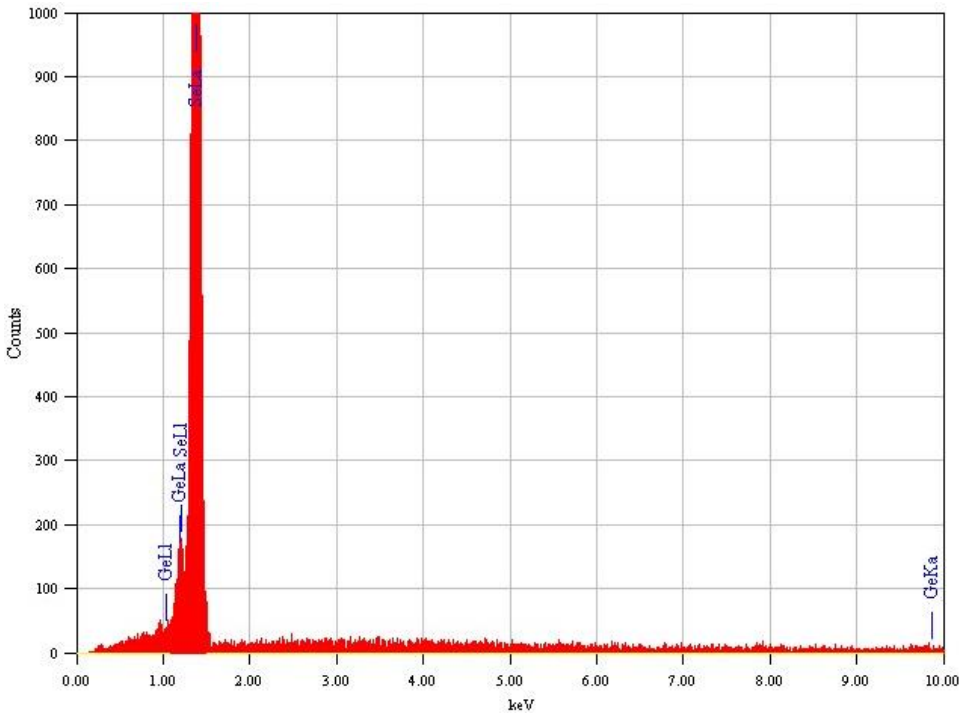

Figure 5.4: *EDS spectra of $Ge_{20}Se_{80}$ glass shows intense peak for Se and a suppressed peak corresponding to Ge indicating large compositional variation in comparison with that of the bulk glass.*

5.3.3 Optical Characterization

UV-VIS- NIR Spectroscopy

Optical characterization of thin films with different compositions was carried out using UV-Vis-NIR (JASCO V-570) spectroscopy, at normal incidence of light in a wavelength range from visible to near IR region. The transmission spectra show interference fringes as continuously oscillating maxima and minima at various wavelengths which confirm the optical homogeneity of deposited thin films. The number of interference fringes increases and are more closely spaced with the increase in thickness. Figure 5.5 shows the transmission spectra of $Ge_{27}Ga_9Se_{64}$ thin films of different thicknesses.

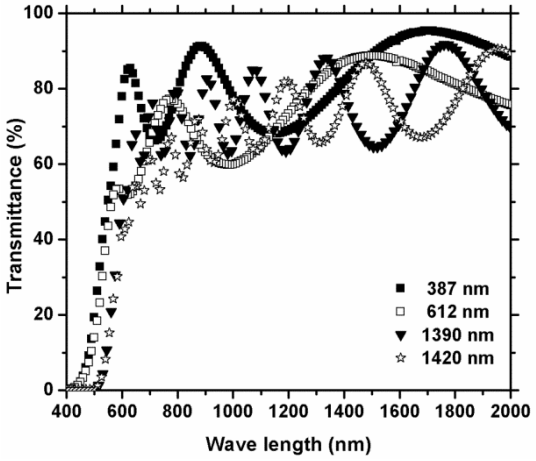

Figure 5.5: *Transmittance spectra of $Ge_{27}Ga_9Se_{64}$ thin films of varying thicknesses, deposited on silica substrates showing interference fringes.*

Various optical parameters are calculated for different compositions of thin films as given in chapter 2 (section 2.2.4) using straight forward method proposed by Swanepoel[17], which is based on the use of upper and lower envelops of the interference maxima and minima. To evaluate optical bandgaps, the variation of $(\alpha h\upsilon)^{1/2}$ versus photon energy $h\upsilon$ is plotted and the linear graph between $(\alpha h\upsilon)^{1/2}$ and $h\upsilon$ confirms the indirect nature of the transitions. The optical energy gap 'Eg' has been determined from the intercepts of extrapolations ($(\alpha h\upsilon)^{1/2} \rightarrow 0$ with the photon energy axis (i.e., Tauc extrapolation) as in figure 5.6(a). Variation of optical bandgap with respect to the film thickness is studied for $Ge_{27}Ga_9Se_{64}$ thin films and is shown

in figure 5.6(b). Optical bandgap decreases with increasing film thickness and it becomes constant at higher thickness.

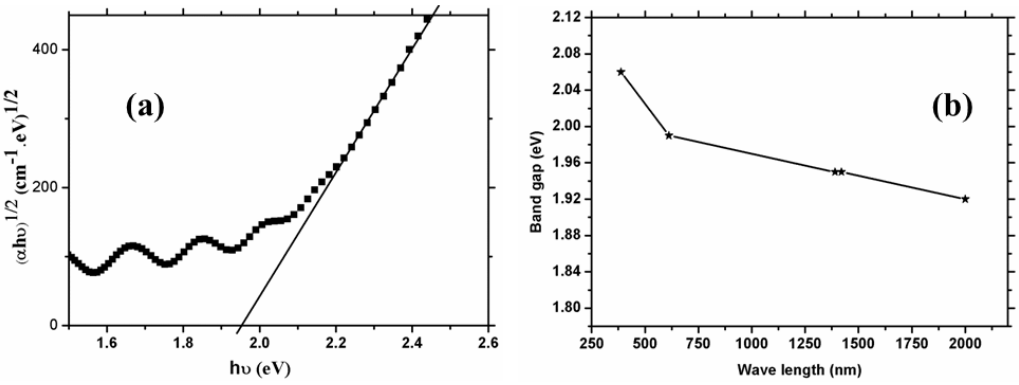

Figure 5.6: *(a) Plot of* $(\alpha h\upsilon)^{1/2}$ *versus photon energy* $h\upsilon$ *for* $Ge_{27}Ga_9Se_{64}$ *thin film of thickness 1390nm. (b) Variation of optical bandgap with respect to the film thickness for* $Ge_{27}Ga_9Se_{64}$ *thin films. Optical bandgap decreases with increasing film thickness and it becomes constant at higher thickness.*

Thin films of all compositions of chalcogenide glasses were thermally coated and the thickness of the films was controlled to around 1340nm with the help of a shutter and quartz crystal based digital thickness monitor. The extinction coefficient (k) which is known as the imaginary part of the complex refractive index ($n^* = n - ik$) is a measure of the fraction of light lost due to scattering. 'k' is estimated from the values of α and λ using the formula $k = {\alpha\lambda}/{4\pi}$.

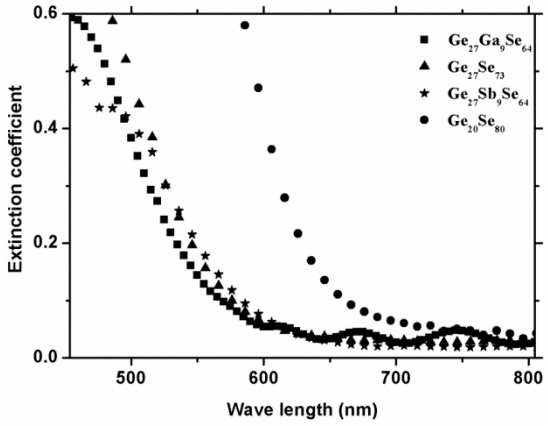

Figure 5.7: *The extinction coefficient 'k' against the wavelength* λ *for all compositions of chalcogenide glass films.*

Figure 5.7 illustrates the dependence of 'k' on the wavelength for different compositions of thin films. The value of 'k' decreases with the increase in wavelength. This indicates a reduction in the fraction of light scattered and an increase in the transmission with increasing wavelength. The loss is higher for $Ge_{20}Se_{80}$ thin film and it may be due to the presence of crystalline nature which is confirmed in XRD and Raman spectra. The presence of microcrystals in the amorphous glass matrix will act as a scattering centre and it will enhance the optical loss.

Figure 5.8 illustrates the dependence of the refractive index 'n' obtained by using Swanepoel method, on the wavelength for different compositions of chalcogenide glass thin films. The calculated values of 'n' are fitted to a two term Cauchy dispersion relation[18]

$$n = A + \frac{B}{\lambda^2} \tag{5.1}$$

and extrapolated to all wavelengths.

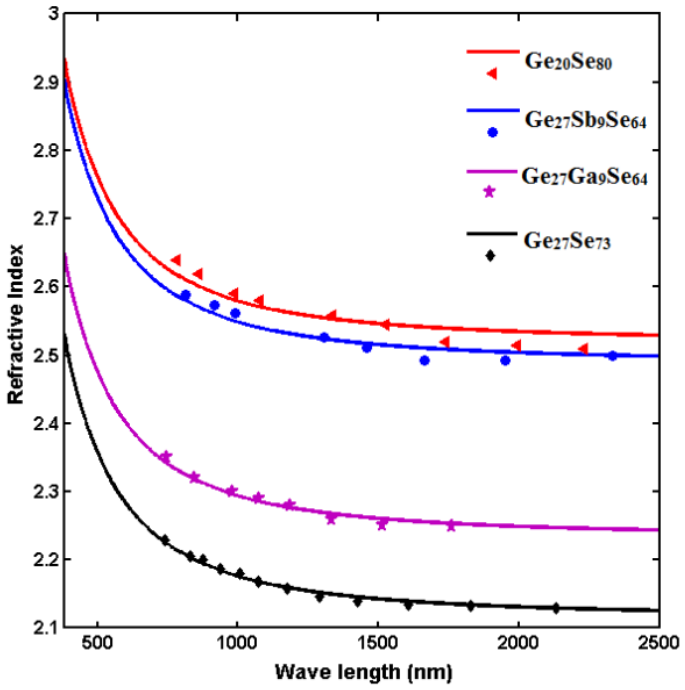

Figure 5.8: *Refractive index dispersion spectra for different compositions of chalcogenide glasses. The solid curves show the theoretical fit using Cauchy dispersion relation.*

It shows that the refractive index varies with the composition as $Ge_{20}Se_{80}$ > $Ge_{27}Sb_9Se_{64}$ > $Ge_{27}Ga_9Se_{64}$ > $Ge_{27}Se_{73}$. Thin film of composition

$Ge_{20}Se_{80}$ shows highest refractive index 2.57 for 1.06μm, which is slightly greater than the reported[19] value 2.49. This may be due to the deficiency of 'Ge' than the nominal composition which is observed from EDS spectra. The values of refractive indices for different compositions at 1.06μm with film thicknesses are shown in table 5.2.

Composition	Thickness d (nm)	Bandgap Eg (eV)	Refractive index at 1.06μm
$Ge_{27}Ga_9Se_{64}$	1390	1.95	2.29
$Ge_{27}Se_{73}$	1342	1.89	2.16
$Ge_{27}Sb_9Se_{64}$	1365	1.87	2.54
$Ge_{20}Se_{80}$	1395	1.76	2.57

Table 5.2: *Thickness (d), Bandgap (Eg), Refractive index at 1.06μm*

From the table it is clear that the addition of 'Ga' and 'Sb' leads to an increase in the values of refractive indices. Increase in refractive index with addition of 'Sb' in $Ge_{(25-x)}Sb_xSe_{75}$ thin films is reported by Shaaban[20] et al.

The optical energy gap 'Eg' for all compositions of thin films has been determined from the intercepts of extrapolations $(\alpha h\upsilon)^{1/2} \rightarrow 0$ with the photon energy axis (i.e., Tauc extrapolation) and is shown in figure 5.9.

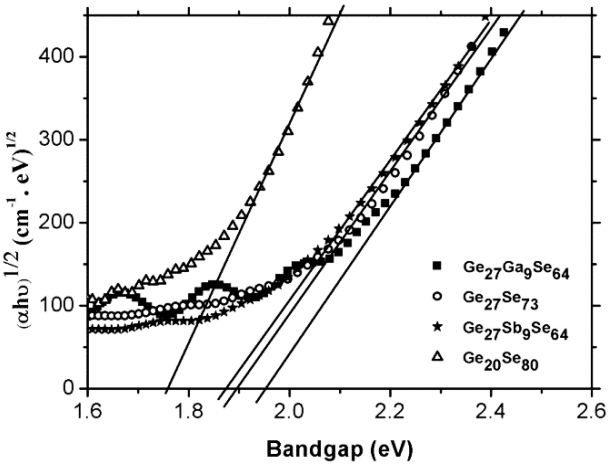

Figure 5.9: *The dependence of* $(\alpha h\upsilon)^{1/2}$ *on the photon energy* $h\upsilon$ *for the different compositions of chalcogenide glass films from which optical bandgap is estimated.*

The real (ε_r) and imaginary (ε_i) part of complex dielectric constant ($\varepsilon = \varepsilon_r + \varepsilon_i$) are calculated for all compositions of thin films. 'ε_r' is a measure of polarizability of a material and 'ε_i' indicates the energy loss, i.e. the energy lost in aligning the dipoles. The loss tangent, $\tan\delta = \frac{\varepsilon_i}{\varepsilon_r}$ measures the inherent dissipation of energy of a dielectric material. 'ε_r' and 'ε_i' have been calculated[21] and their values are given in table 5.3.

Composition	**Static Refractive index (n_0)**	**Re. part of dielectric constant (ε_r)**	**Im. part of dielectric constant (ε_i)**	**tanδ**	**E_d (eV)**	**E_0 (eV)**
$Ge_{27}Ga_9Se_{64}$	2.23	5.23	0.108	0.0207	16.72	4.18
$Ge_{27}Se_{73}$	2.13	4.70	0.103	0.0218	14.12	3.95
$Ge_{27}Sb_9Se_{64}$	2.50	6.46	0.168	0.026	20.12	3.82
$Ge_{20}Se_{80}$	2.50	6.61	0.068	0.0103	19.75	3.76

Table 5.3: *Static refractive index (n_0), real (ε_r) and imaginary (ε_i) part of complex dielectric constant (at 1.06μm), the loss tangent '**tanδ**' (at 1.06μm), dispersion energy (E_d), effective oscillator energy (E_0) for different compositions of thin films.*

The spectral dependence of the refractive index been fitted to the single oscillator, i.e. Wemple–DiDomenico[22] model (discussed in chapter 2) suggests a relation between refractive index and single oscillator strength, below the fundamental absorption edge. Plotting $(n^2-1)^{-1}$ versus $(h\upsilon)^2$ yields a straight line as shown in figure 5.10. The straight line fit provides the values of oscillator energy (E_0), which is the mean transition energy and the oscillator strength (E_d), which is a measure of the interband optical transitions. E_0 and E_d can be determined from the intercept, E_0/E_d, and the slope, $(E_0E_d)^{-1}$. The values of static refractive index n_0 has been calculated for all compositions from WDD dispersion parameters E_0 and E_d by using the formula

$$n_0 = \left(1 + {}^{E_d}/_{E_0}\right)^{1/2} \tag{5.2}$$

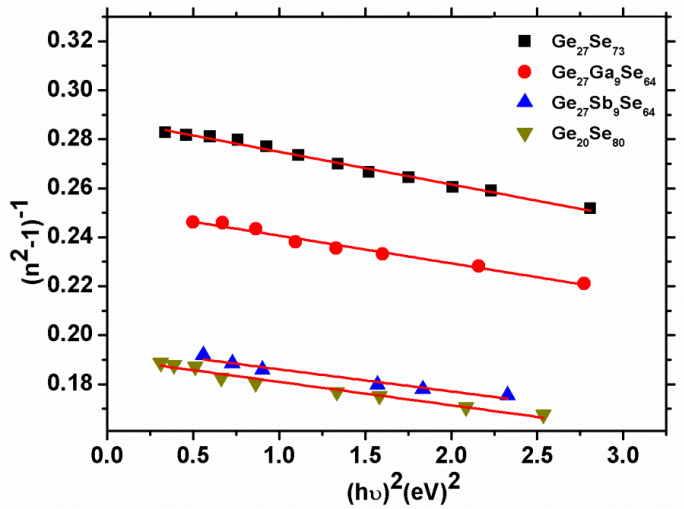

Figure 5.10: *Plot of the refractive index factor* $(n^2-1)^{-1}$ *versus* $(h\upsilon)^2$ *for different compositions of thin films.*

5.4 Studies on solution-derived thin films

Chalcogenide thin films obtained using thermal evaporation show a variety of inhomogeneities, mainly compositional drift which are caused by differential volatility of the glass constituents, leading to possible preferential condensation. Spin-coating of dissolved chalcogenide glasses is an effective technique for the fabrication[23] of thin films used in solution processes. Since there are no sudden temperature changes involved in solution processing and film preparation, different thermal expansion properties of substrate and film material, which have to be considered for conventional deposition techniques, are usually not issues.

Coating is done in the dry, atmosphere to prevent reaction with moisture from the air. A few drops of the solution are deposited onto a silica glass substrate which is then spun at 1000rpm. Spin-coated films are dried by thermal treatment in two steps, a soft-bake at lower temperatures that removes most of the solvent, and a hard-bake closer to the glass transition temperature of the bulk glass to remove residual solvent and reaction products, and to densify the glass. Figure 5.11 shows the photograph of thermal evaporated and spin coated thin films. '(a)' symbolizes the thermal evaporated thin film on silica microslide and '(b)' stands for spin coated thin film on 1cmx1cm silica slide.

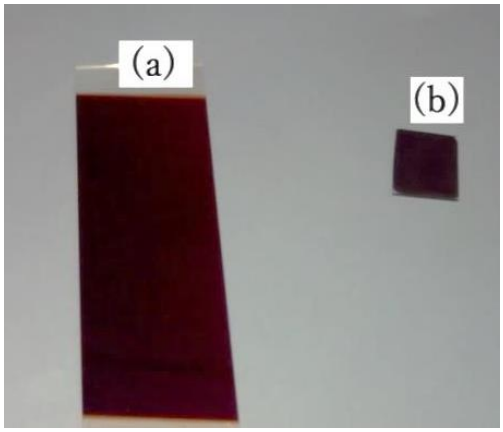

Figure 5.11: *(a) Photograph of thermally coated $Ge_{27}Sb_9Se_{64}$ thin film. (b) Photograph of spin coated thin film of $Ge_{27}Sb_9Se_{64}$/ethanolamine nanocolloidal solution after baking.*

Thin films of $Ge_{27}Sb_9Se_{64}$ glass were prepared from ethanolamine based nanocolloid using spin coating technique. Nanocolloidal solutions of concentration 0.05g/ml (G1) were prepared by dissolving finely grounded $Ge_{27}Sb_9Se_{64}$ glass in ethanol amine (Sigma Aldrich, 99.9%) as discussed in section of chapter 4.5. Ethanolamine is a viscous liquid having viscosity 19.4 centipoise (cP) which allows the fabrication of thick films via spin coating. Films are deposited by spin-coating onto glass microscope slides at 1000rpm for 30 seconds. Immediately after spin-coating, the films are transferred to an oven and heated at 90°C for one hour, and then at 160°C for 1 hour under vacuum, to remove residual solvent. This two-step heat treatment[24] procedure helps to stabilize the film at the initial step and in the second step by reducing the pressure, the boiling point of the solvent is lowered, allowing more efficient solvent removal. The presence of large amounts of solvent in the film above its boiling point can lead to bubbles[25], cracking or pin-hole formation. The use of the two-step procedure allows sufficient slow evaporation of the solvent at low temperature to prevent the formation of bubbles. The boiling point of ethanolamine is 170°C and the glass transition temperature of $Ge_{27}Sb_9Se_{64}$ glass obtained from DSC analysis (discussed in chapter 3) is 262°C. Therefore, 1 hour heating at 160°C in vacuum will not change the glass structure.

5.4.1 Structural characterization

X-ray diffraction studies

XRD technique is employed to analyze the thin film structure after baking. Figure 5.12 shows the XRD spectrum of spin coated thin film of $Ge_{27}Sb_9Se_{64}$/ethanolamine nanocolloidal solution after baking. No sharp structural peaks have been observed in the XRD traces of the thin film and this confirmed that no structural change has occurred after baking.

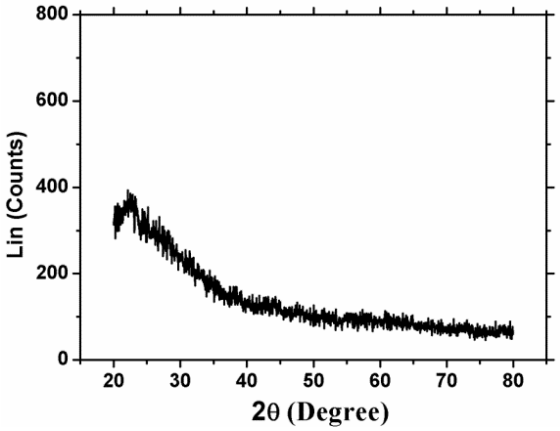

Figure 5.12: *XRD spectrum of spin coated thin film of $Ge_{27}Sb_9Se_{64}$/ethanolamine after baking shows no sharp structural peaks, confirming the absence of structural change after baking.*

FTIR Analysis

Using attenuated total internal reflection (ATR) Fourier-transform infrared spectroscopy (JASCO FT-IR-5300 Spectrometer), the amount of unevaporated solvent in the films was monitored. Important solvent signatures[26, 27] are observed in the ATR spectra as shown in figure 5.13. The broad absorption band from 2200-3500cm^{-1} corresponds to the various N-H bond stretches. Aliphatic C-H stretch is observed at 2800-3000cm^{-1}. The scissor bending vibration for N-H bond is observed around 1575cm^{-1}, while the C-H scissor bend is observed as the weak absorption peaks from 1465 and 1380cm^{-1}. C-N stretching vibration is located around 1070cm^{-1} and 1650cm^{-1}. Occurrence of different absorption peaks mentioned above confirms the existence of unevaporated solvent in the film matrix.

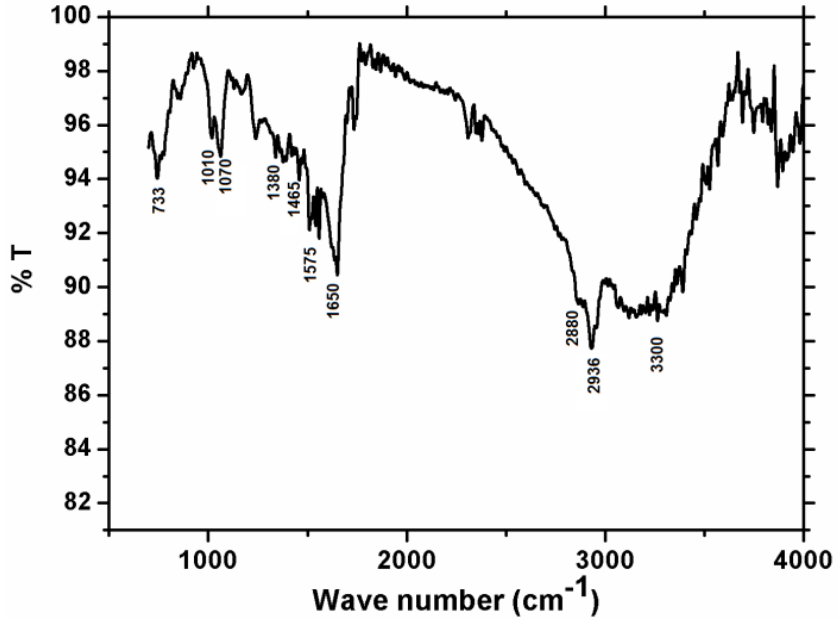

Figure 5.13: *ATR spectrum of spin coated thin film of $Ge_{27}Sb_9Se_{64}$/ethanolamine nanocolloidal solution after baking.*

Raman Analysis

In order to evaluate the variation of bonding structure of the spin coated thin film samples, Micro-Raman analysis has been employed with 785nm excitation. Figure 5.14 shows the Raman spectra of the spin coated thin film of $Ge_{27}Sb_9Se_{64}$/ethanolamine nanocolloidal solution on a 1cmx1cm silica glass substrate after baking. From the figure, it is clear that the structure of the film is similar to that of the bulk glass. The main band of the film centered around 198cm^{-1} is significantly broader than that of the bulk glass. This is attributed to the overlap of different bands corresponding to $GeSe_4$ units linked by Se-Se bridges. The band at 198cm^{-1}, which corresponds to the symmetric stretching of corner-shared (CS) $GeSe_4$ tetrahedra, merges with the shoulder band at 214cm^{-1} corresponding to the breathing mode of edge-shared (ES) Se atoms connected between two neighboring $GeSe_4$ tetrahedra. The high-intensity band centred around 257cm^{-1} is characteristic of pure Se and is related to Se-Se stretching in Se chains and rings[10,11,12]. Raman band assignments for all compositions are summarized in Table 3.1 of chapter 3.

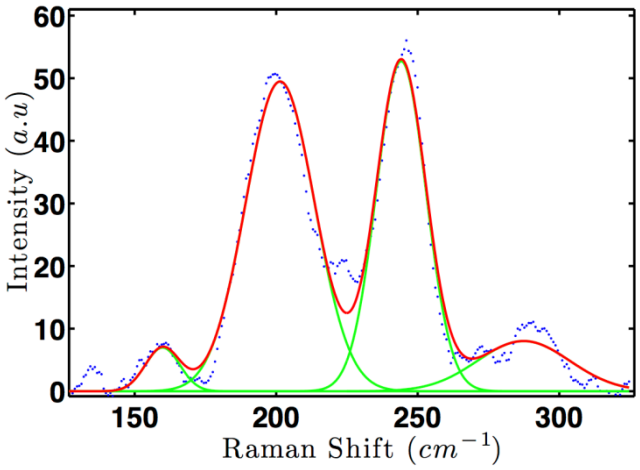

Figure 5.14: *Raman spectrum of spin coated $Ge_{27}Sb_9Se_{64}$/ethanolamine thin film on a 1cmx1cm silica glass substrate after baking shows similar bands as in the case of bulk glasses.*

5.4.2 Compositional analysis

EDS Analysis

The EDS composition of the films derived in this manner are shown in the Table 5.4 below. The composition of the spin-coated films shows some variation compared to the bulk glass composition. Atomic percentage of 'Sb' is found to be decreased after dissolution with respect to the bulk glass composition. 'Carbon' and 'oxygen' observed in the EDS spectra indicates the presence of traces of solvent in the thin film.

Nominal Composition	Element	Atomic %
$Ge_{27}Sb_9Se_{64}$	Ge	29.74
	Sb	4.02
	Se	64.10
	C	1.1
	O	1.04

Table 5.4: *Variation of atomic percentage of components obtained from EDS analysis with respect to the nominal composition in spin coated $Ge_{27}Sb_9Se_{64}$ of thin film*

5.4.3 Optical characterization

UV-VIS- NIR Spectroscopy

Optical characterization of spin coated thin films was carried out using UV-Vis-NIR spectroscopy, at normal incidence of light. From the UV-Vis absorption, it is observed that the thin film is not transparent in the visible region and is featured with an extended band tail upto IR region. The optical energy gap 'Eg' has been determined by plotting 'Tauc extrapolation' as discussed in chapter 2. Figure 5.15 shows optical Tauc plot of spin coated $Ge_{27}Sb_9Se_{64}$/ethanolamine thin film. Optical absorption edge is found to be blue shifted from that of the bulk $Ge_{27}Sb_9Se_{64}$ glass. The bandgap obtained for spin coated $Ge_{27}Sb_9Se_{64}$ thin film is 1.64 eV while the bandgap of bulk glass is 1.59 eV.

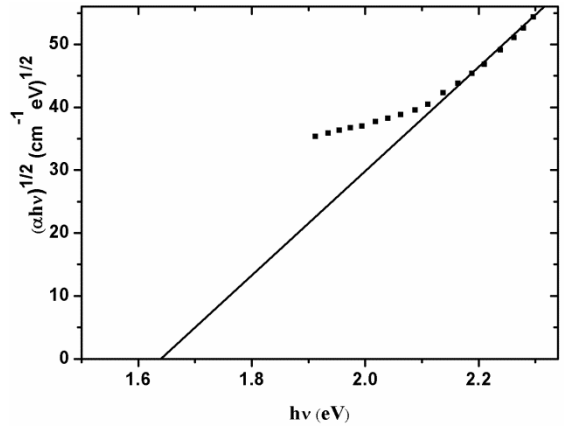

Figure 5.15: *Tauc plot of spin coated $Ge_{27}Sb_9Se_{64}$/ethanolamine thin film after baking.*

The study on spin coated thin films reveals that the solution derived $Ge_{27}Sb_9Se_{64}$ thin films retain most of their inherent properties while a detailed investigation and optimization on spin coating condition, baking atmosphere and time etc. are needed for the production of films with good optical quality.

5.5 Waveguide fabrication by capillary force lithography

Direct patterning of waveguides in a single step is possible by using techniques like screen-printing[28], ink-jet printing[29], micro-stamping (micro-contact printing)[30], capillary force lithography[31] etc. The first two methods give devices with relatively large geometries. In micro-stamping, a piece of

elastomeric patterned material (stamp) like Poly(dimethylsiloxane) (PDMS), is coated with an 'ink' solution. This is then carefully transferred to the substrate.

In the case of capillary force lithography (CFL) technique[25] the stamp is placed on the surface of a thin film and the film is then heat treated in order to allow the film to expand. As it expands, capillary force causes the material to fill into cavities in the pattern of the stamp as shown in figure 5.16. The film is then cooled and allowed to re-solidify and then the stamp is peeled off. The resultant thin film retains the negative imprint of the stamp pattern on the film.

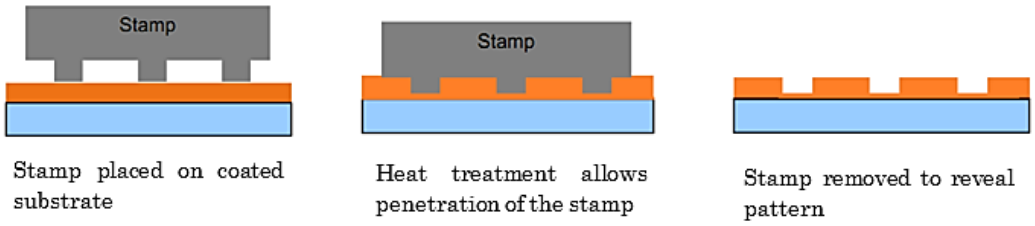

Figure 5.16: *Schematic of capillary force lithography [25]*

In the present studies, we have used the pattern of compact disk (CD) as 'master'. PDMS stamp is prepared by mixing PDMS elastomer base with curing agent cross-linker at 10:1 ratio and poured over the patterned surface of CD after removing the metallic film over it. It is allowed to polymerize by heating it at 70°C for 30 minutes and then the stamp is peeled off from the CD master. Figure 5.17 shows the photograph of PDMS stamp and figure 5.18 (a) shows the SEM image of the patterned surface of PDMS stamp taken using JEOL Model JSM-6390LV and figure 5.18 (b) is the corresponding FESEM image taken using ZEISS Ultra-55. Figure shows repeated lines of around 550nm width spaced around 760nm.

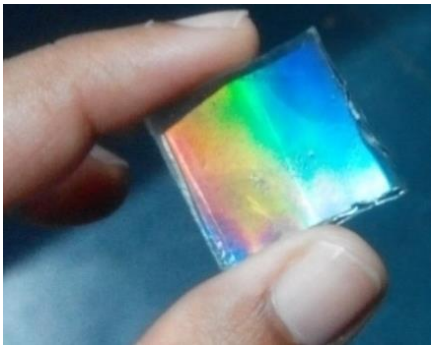

Figure 5.17: *Photograph of PDMS stamp polymerized over compact disk (CD).*

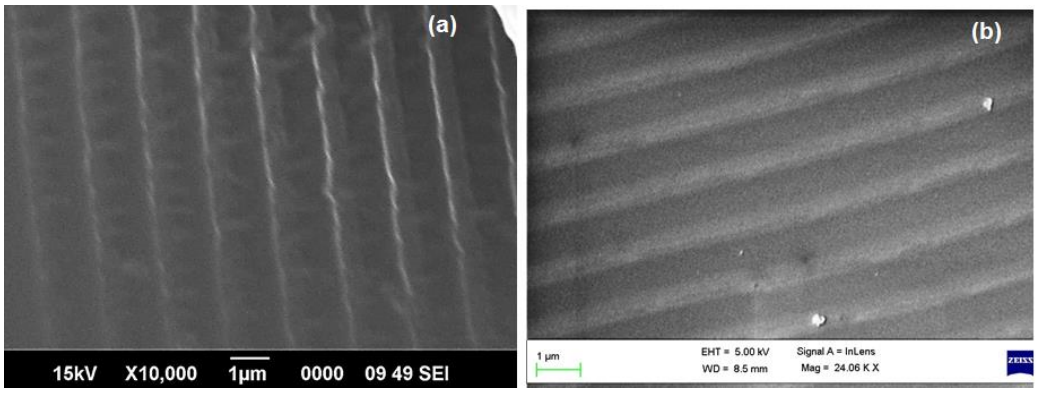

Figure 5.18: *: (a) The SEM image of the patterned surface of PDMS stamp taken using JEOL Model JSM 6390LV and (b) corresponding FESEM image taken using ZEISS Ultra-55.*

CFL patterns were fabricated on thermally evaporated $Ge_{27}Sb_9Se_{64}$ thin films by placing a small section of PDMS stamp on the thin film and heat treated for 30 minutes at glass transition temperature, 260°C for $Ge_{27}Sb_9Se_{64}$ glass. The PDMS mask was peeled off from the thin film surface after the film was cooled to room temperature and the resulting grating pattern effect was clearly visible on the sample surface.

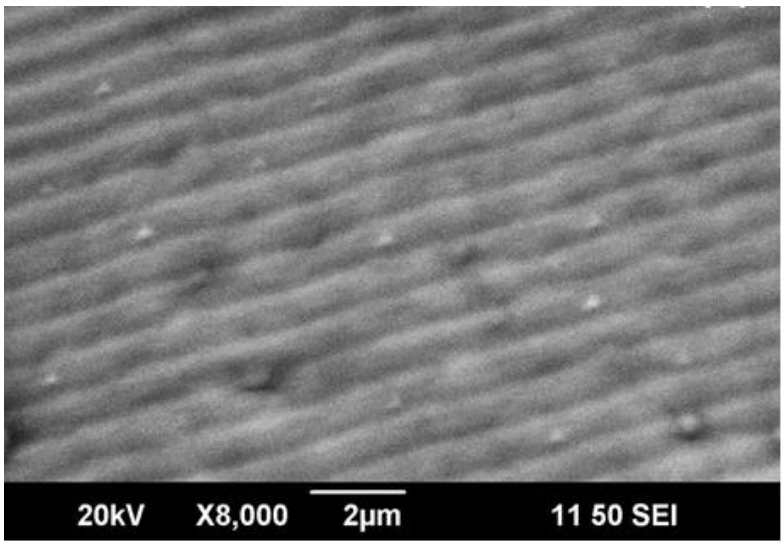

Figure 5.19: *(a) SEM image of patterned surface of $Ge_{27}Sb_9Se_{64}$ thin film*

CFL technique allows the easy fabrication of waveguide arrays on chalcogenide glass thin films. But to guide the IR waves through these

structures, the dimension of the waveguides should be large enough, ie in micrometers.

5.6 Summary of findings

- Chalcogenide glass thin films of compositions $Ge_{20}Se_{80}$, $Ge_{27}Se_{73}$, $Ge_{27}Sb_9Se_{64}$ and $Ge_{27}Ga_9Se_{64}$ have been prepared by thermal evaporation technique and its structural, compositional and optical characterization were carried out.
- X-ray diffraction studies were conducted on the thermally coated thin film samples and no prominent peaks were observed in the spectrum of $Ge_{27}Se_{73}$, $Ge_{27}Sb_9Se_{64}$ and $Ge_{27}Ga_9Se_{64}$ thin films which reveals the amorphous nature of the samples. However XRD pattern of $Ge_{20}Se_{80}$ glass film shows prominent peaks indicating the presence of crystalline trigonal phase of selenium.
- Structural characterization using Raman analysis predicts the bonding arrangement in $Ge_{27}Se_{73}$, $Ge_{27}Sb_9Se_{64}$ and $Ge_{27}Ga_9Se_{64}$ thin films as corner shared (CS) and edge shared (ES) $GeSe_4$ units interconnected with a comparable concentration of Se–Se bonds. The Raman spectrum of $Ge_{20}Se_{80}$ thin film shows no 'CS' and 'ES' vibrational band while a characteristic stretching band of trigonal selenium is observed.
- Compositional analysis of all thin film samples were carried out using EDS which reveals a large variation compared to the expected composition of $Ge_{20}Se_{80}$ film.
- Optical characterization of all compositions of thin films was carried out using UV-Vis-NIR spectroscopy. Various optical parameters are calculated for different compositions of thin films using Swanepoel method and there exists a compositional variation. The refractive index calculated by this way is fitted to a two term Cauchy dispersion relation and extrapolated to lower wavelength.
- Thin films of $Ge_{27}Sb_9Se_{64}$ glass were prepared from ethanolamine based nanocolloid using spin coating technique and its structural, compositional and optical characterization were carried out.
- X-ray diffraction studies were conducted on the spin coated thin film samples and no sharp structural peaks were observed which confirms that no structural change has occurred after baking.
- Compositional analysis of spin coated thin film samples carried out using EDS indicates a compositional variation. Atomic percentage of 'Sb' is found to be decreased in the solution processed film compared to

the bulk glass composition and a signature of unevaporated solvent traces are observed. FTIR studies confirmed the presence of residual solvent in the spin coated film.

- Structural characterization of the spin coated thin film using Raman analysis confirms that the film structure is similar to that of the bulk glass. The main bands of the film are significantly broader than that of the bulk glass and are attributed to the overlapping of different bands.
- Optical characterization on spin coated thin films was carried out using UV-Vis-NIR (JASCO V-570) spectroscopy. The thin film is not transparent in visible region and is featured with an extended band tail upto IR region
- The grating like pattern in the compact disc is successfully transferred to thermal evaporated $Ge_{27}Sb_9Se_{64}$ glass thin film by CFL technique, which opens the opportunity of fabrication of waveguide arrays for IR based sensor.

5.7 References

[1]Youden, K. E., T. Grevatt, R. W. Eason, H. N. Rutt, R. S. Deol, and G. Wylangowski. "Pulsed laser deposition of Ga-La-S chalcogenide glass thin film optical waveguides." *Applied physics letters* 63, no. 12 (1993): 1601-1603.

[2]Fedus, Kamil, G. Boudebs, Quentin Coulombier, Johann Troles, and X. H. Zhang. "Nonlinear characterization of GeS_2–Sb_2S_3–CsI glass system." *Journal of Applied Physics* 107, no. 2 (2010): 023108-023108.

[3]Troles, J., F. Smektala, G. Boudebs, A. Monteil, B. Bureau, and J. Lucas. "Chalcogenide glasses as solid state optical limiters at 1.064μm." *Optical materials* 25, no. 2 (2004): 231-237.

[4]Ogusu, Kazuhiko, Jun Yamasaki, Shinpei Maeda, Michihiko Kitao, and Makoto Minakata. "Linear and nonlinear optical properties of Ag-As-Se chalcogenide glasses for all-optical switching." *Optics letters* 29, no. 3 (2004): 265-267.

[5]Elliott, Stephen Richard, and S. R. Elliott. *Physics of amorphous materials*. Vol. 2. Essex: Longman Scientific & Technical, 1990.

[6]Chern, Geeng-Chuan, and I. Lauks. "Spin-coated amorphous chalcogenide films." *Journal of Applied Physics* 53, no. 10 (1982): 6979-6982.

[7]Tsay, Candice, Yunlai Zha, and Craig B. Arnold. "Solution-processed chalcogenide glass for integrated single-mode mid-infrared waveguides." *Optics express* 18, no. 25 (2010): 26744-26753.

[8]Unger, P., P. Cherin, and W. C. Cooper. "The physics of selenium and tellurium." *Pergamon Press, Oxford* (1969): 223.

[9]Seddon, A. B. "Chalcogenide glasses: a review of their preparation, properties and applications." *Journal of Non-Crystalline Solids* 184 (1995): 44-50.

[10]Jackson, Koblar, Arlin Briley, Shau Grossman, Dirk V. Porezag, and Mark R. Pederson. "Raman-active modes of a-$GeSe_2$ and a-GeS_2: A first-principles study." *Physical Review B* 60, no. 22 (1999): R14985.

[11]Wang, Yong, Osamu Matsuda, Koichi Inoue, Osamu Yamamuro, Takasuke Matsuo, and Kazuo Murase."A Raman scattering investigation of the structure of glassy and liquid Ge_xSe_{1-x}." *Journal of non-crystalline solids* 232 (1998): 702-707.

[12]Wang, Y., and K. Murase. "Floppy modes and relaxation in Ge_xSe_{1-x} glasses." *Journal of non-crystalline solids* 326 (2003): 379-384.

[13]Sugai, S. "Stochastic random network model in Ge and Si chalcogenide glasses." *Physical Review B* 35, no. 3 (1987): 1345.

[14]Ma, Yurong, Limin Qi, Wei Shen, and Jiming Ma. "Selective synthesis of single-crystalline selenium nanobelts and nanowires in micellar solutions of nonionic surfactants." *Langmuir* 21, no. 14 (2005): 6161-6164.

[15]Song, Ji-Ming, Jian-Hua Zhu, and Shu-Hong Yu. "Crystallization and shape evolution of single crystalline selenium nanorods at liquid-liquid interface: From monodisperse amorphous Se nanospheres toward Se nanorods." *The Journal of Physical Chemistry B* 110, no. 47 (2006): 23790-23795.

[16]Lucovsky, G., A. Mooradian, W. Taylor, G. B. Wright, and R. C. Keezer. "Identification of the fundamental vibrational modes of trigonal, α-monoclinic and amorphous selenium." *Solid State Communications* 5, no. 2 (1967): 113-117.

[17]R. Swanepoel,"Determination of the thickness and optical constants of amorphous silicon", *Journal of Physics E: Scientific Instruments* 16 (1983): 1214-1222.

[18]Paul, William. "Optical properties of semiconductors, a semiconductor monograph: TS Moss: General editor CA Hogarth. Butterworths Scientific Publications, London, and Academic Press, New York, 1959. 279 pp., 74 figs., 50s." (1959): 345-346.

[19]Boudebs, G., S. Cherukulappurath, M. Guignard, J. Troles, F. Smektala, and F. Sanchez. "Linear optical characterization of chalcogenide glasses." *Optics communications* 230, no. 4 (2004): 331-336.

[20]Shaaban, E. R., M. A. Kaid, and A. Adel. "Effect of compositional variations on the optical properties of Sb-Ge-Se thin films." *Journal of Physics D: Applied Physics* 41, no. 12 (2008): 125301.

[21]Rajesh, K. R., and C. S. Menon. "Estimation of the refractive index and dielectric constants of magnesium phthalocyanine thin films from its optical studies." *Materials letters* 53, no. 4 (2002): 329-332.

[22]Wemple, S. H., and M. DiDomenico Jr. "Behavior of the electronic dielectric constant in covalent and ionic materials." *Physical Review B* 3, no. 4 (1971): 1338.

[23]Zha, Yunlai, Maike Waldmann, and Craig B. Arnold. "A review on solution processing of chalcogenide glasses for optical components." *Optical Materials Express* 3, no. 9 (2013): 1259-1272.

[24]Waldmann, Maike, J. David Musgraves, Kathleen Richardson, and Craig B. Arnold. "Structural properties of solution processed $Ge_{23}Sb_7S_{70}$ glass materials." *Journal of Materials Chemistry* 22, no. 34 (2012): 17848-17852.

[25]Nathan A. Carlie, "A solution based approach to the fabrication of novel chalcogenide glass materials and structures", PhD thesis, Graduate school of Clemson university (2010)

[26]Chern, G. C., I. Lauks, and A. R. McGhie. "Spin coated amorphous chalcogenide films: Thermal properties." *Journal of applied physics* 54, no. 8 (1983): 4596-4601.

[27]Chern, G. C., and I. Lauks. "Spin coated amorphous chalcogenide films: Structural characterization." *Journal of Applied Physics* 54, no. 5 (1983): 2701-2705.

[28] Shaheen, Sean E., Rachel Radspinner, Nasser Peyghambarian, and Ghassan E. Jabbour. "Fabrication of bulk heterojunction plastic solar cells by screen printing." *Applied Physics Letters* 79, no. 18 (2001): 2996-2998.

[29]Yu, Xinhong, Zhe Wang, and Yanchun Han. "Microlenses fabricated by discontinuous dewetting and soft lithography." *Microelectronic Engineering* 85, no. 9 (2008): 1878-1881.

[30]Nagata, Hajime, Song Won Ko, Eunki Hong, Clive A. Randall, Susan Trolier-McKinstry, Pascal Pinceloup, Daniel Skamser, Michael Randall, and Azizuddin Tajuddin. "Microcontact printed $BaTiO_3$ and $LaNiO_3$ thin films for capacitors."*Journal of the American Ceramic Society* 89, no. 9 (2006): 2816-2821.

[31]Suh Kahp Y., Yun S. Kim, and Hong H. Lee. "Capillary force lithography."*Advanced Materials* 13, no. 18 (2001): 1386-1389.

Chapter 6

Fabrication and characterization of silver island structures

In this chapter silver island films of different morphology prepared both by dry process and wet process on silica and chalcogenide glass substrate are described. The dry process includes thermal evaporation technique by Oblique Angle Deposition (OAD) and the wet process implicates the preparation of colloids of silver nanoparticles by wet chemical methods so that island films could be coated by employing different techniques such as spin coating, drop-casting etc. Analysis on the size and morphology of silver nanoparticles were carried out using different techniques. The preparation and characterization of metal films pave the way to the development of more sensitive and efficient IR based sensor.

6.1 Introduction

As discussed in chapter 1, metal island films on the top of the chalcogenide glass film not only benefit for bio-functionalization of the core layer but also help to enhance the sensitivity by surface enhanced infrared absorption (SEIRA). Most Bio-functionalization is realized with the help of self-assembled monolayers (SAM) of anchor molecules on the surface of the metal island films.

SEIRA spectroscopy implicates the enhancement of the infrared band intensities for molecules that are either adsorbed on or in close proximity to metal surfaces island structures and is classified as a type of surface-enhanced vibrational spectroscopy similar to the well-established Surface-Enhanced Raman Spectroscopy (SERS) technique[1,2,3]. Though the enhancement predicted for SEIRA by the 'local enhanced electric field mechanism' can be as

large as 10^3; in practice, enhancements achieved are in the range[4] of 10 to 100. Surface plasmon (SP) absorption is found to be the process behind occurrence of SEIRA even though the process is not well understood. Depending on the metal structure morphologies[5], plasmon resonance frequency of metallic nanoparticles can be tuned in the infrared domain. Thus, SEIRA studies on metal nanostructures with various morphologies such as thin films[6,7,8] nanorods[9,10], nanoshells[11] etc. have been reported. Since infrared signatures of organic species and biomolecules are found to be in the mid-infrared domain, SEIRA can be used to improve the infrared detection limits of molecules. As compared to traditional infrared analysis, SEIRA provides improved sensitivity and allows for the quantitative and qualitative determination of chemical species in the picogram to microgram range.

SEIRA enhancements have predominately been observed for molecules that are physically in contact with a thin metallic film, typically silver or gold, composed of island-like structures. These metallic island films are traditionally fabricated using physical vapour deposition methods with deposition occurring either at normal incidence with thickness <15nm resulting in anisotropic metallic particles with their long axes lying along the surface of the substrate or oblique angle deposition. Metallic films providing the best SEIRA enhancements consist of discontinuous particles with oblate (ellipsoidal) geometries having aspect ratios (η) of 2 to 3 as in the case of SERS[12,13]. In addition to traditional vapour-deposited metal island films, many different types of nanostructures, such as nanowires, nanorods, and nanobundles, prepared by wet chemical methods have been used for vibrational surface enhancement[14,15].

6.2 Scope of the chapter

As discussed earlier 'metal island structures' on the top of the chalcogenide glass film benefit for bio-functionalization and it also help to enhance the sensitivity by surface enhanced infrared absorption (SEIRA). The enhancement in IR absorption depends upon the morphology and size of silver island structure. Therefore the preparation and detailed characterization on the size and morphology of metal island structures pave the way to the development of more sensitive and efficient IR based sensor.

6.3 Ag nanostructures by dry process

Oblique Angle Deposition

Oblique Angle Deposition (OAD) is a type of physical vapour deposition that involves tilting the substrate in the polar direction[16] in such a way that the vapour from the source impinges upon the substrate at incidence angles greater than 75°. As a result of shadowing effects, the incident flux of material arriving at the surface preferentially grows on top of surface features with large height[17] and this preferential growth dynamics gives rise to the formation of isolated columnar structures. In addition, the instrumentation required to carry out the OAD process can be any standard thermal evaporation system designed with a unique holder capable of rotation in the polar direction. Figure 6.1 (a) shows the schematic of traditional thermal evaporation process via normal incidence and 6.1 (b) represents the OAD method.

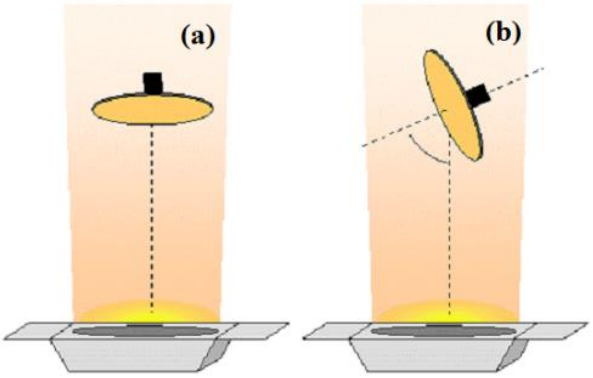

Figure 6.1: *The schematic of traditional thermal evaporation process (a) via normal incidence and (b) represents the OAD method.*

OAD is a flexible nanofabrication technique in which one can easily tune the size, density, shape and arrangement of the nanostructure arrays. Schematic view of growth of nanostructures via OAD method taken from[18] is shown in figure 6.2. The vapours come at an angle 'α' with the normal to the substrate plane. Initially random distribution of nuclei on substrate surface occurs and then they grow into columns, as seen in figure 6.2(b), and develop shadows. Since the columns and therefore the shadows have a size distribution, some nuclei will screen neighbouring nuclei from incoming vapour flux and suppress their growth (figure 6.2 (c)). Within sufficient time,

smaller nuclei and columns can become completely shadowed and stop growing as shown in figure 6.2 (d).

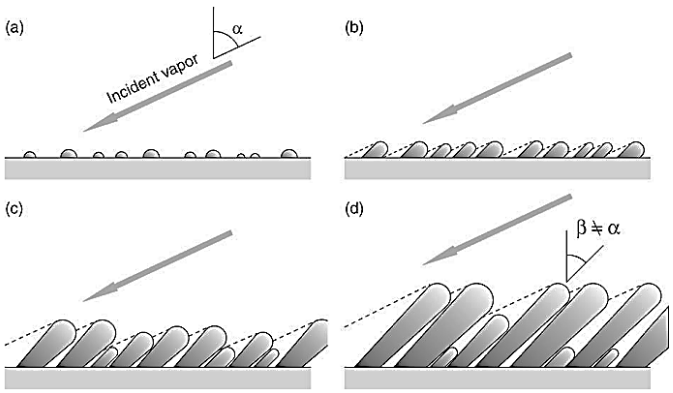

Figure 6.2: *Schematic view of OAD growth[18]: (a) random distribution of nuclei on substrate surface; (b) formation of columnar structures and shadows across substrate; (c) further development by partially shadowing smaller neighbours and suppressing their growth; (d) columns grow at an inclined angle. Some columns have become fully extinct and further growth is restricted to the top of columns.*

The Ag nanostructures were fabricated by the OAD method using thermal evaporation technique. Films were coated on both silica substrates and $Ge_{27}Sb_9Se_{64}$ glass thin film. The silica glass substrates show poor adhesion to silver such that the film peels off from the substrate even at very low mechanical impact while $Ge_{27}Sb_9Se_{64}$ film shows good adhesion for Ag. To improve adhesion between the silica glass substrate and film, glass surface has to be treated prior to a coating process[19]. The silica substrates were treated by immersing it in piranha solution which is the mixture of 30% H_2O_2 and concentrated H_2SO_4 in 1:3 ratio for 1hr to derive a hydroxyl surface[20,21,22] and rinsed with deionized water prior to use. Since piranha solutions are highly caustic and energetic, extreme caution must be taken during handling.

$Ge_{27}Sb_9Se_{64}$ glass thin film was prepared by thermal evaporation technique as discussed in chapter 5. Cross sectional SEM image of $Ge_{27}Sb_9Se_{64}$ glass thin film used for the deposition of silver nanostructure via OAD technique is taken for the evaluation of film thickness. FESEM image were taken using ULTRA 55, GEMINI technology and is shown in figure 6.3. More close-up view given in inset indicates almost uniform thickness of around 2.6μm throughout the film. Both silica and chalcogenide glass film surfaces were subjected to plasma cleaning for 5 minutes prior to Ag coating.

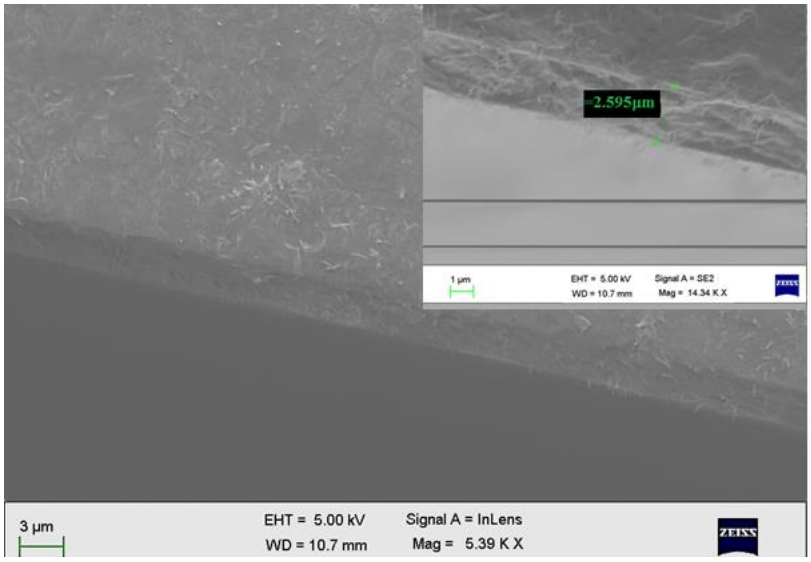

Figure 6.3: *Cross sectional SEM image $Ge_{27}Sb_9Se_{64}$ glass thin film used for the deposition of OAD silver nanostructures; inset shows close-up view indicating thickness of around 2.6µm.*

The nanostructured Ag films were deposited by OAD method by applying a current of 10A in a closed chamber at around 3×10^{-5}mbarr pressure to reduce contamination. The Ag metal piece of 99% purity were taken in a molybdenum boat and the coating has been carried out through resistive heating. The substrates were tilted at two oblique angles 70°, and 80° with no substrate rotation.

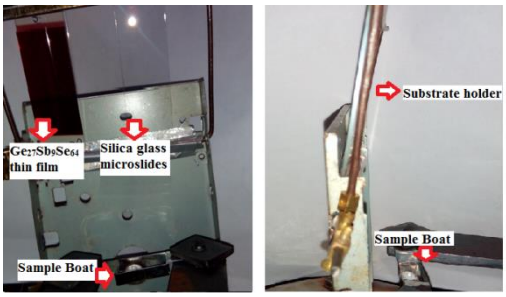

Figure 6.4: *The front view and side view of OAD substrate holder containing chalcogenide glass thin film as well as silica glass substrate.*

Figure 6.4 shows the front view and side view of OAD substrate holder containing chalcogenide glass thin film as well as silica glass substrate. The Ag nanostructures deposited onto the silica substrates resulted in films that were semi-transparent.

The Ag nanostructures deposited on silica substrate by OAD method for 5 minutes of deposition time show the initial nucleation stage. The distance from the source to the center of the substrates was around 30cm. The morphology of the Ag nanostructures were characterized using JEOL Model JSM- 6390LV SEM and the images of two oblique angles70° and 80° are displayed in figure 6.5 (a) & (b) respectively.

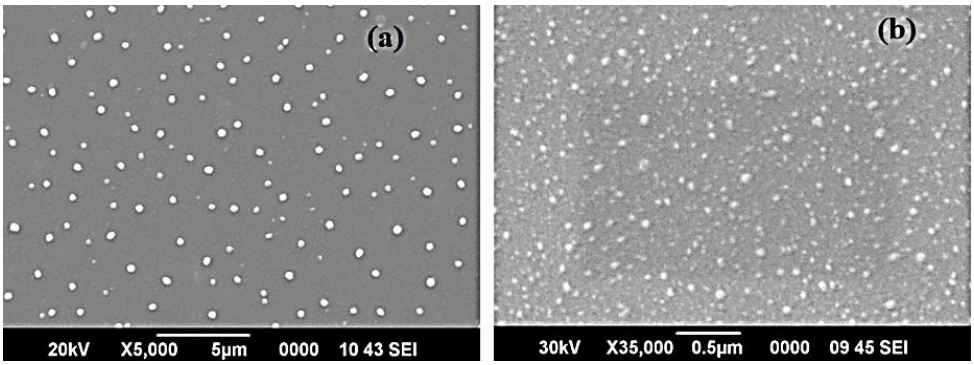

Figure 6.5: *SEM image of OAD nanostructures of Ag on silica substrate showing initial stage of nucleation (a) substrate were tilted at 70° (b) tilting angle is 80°.*

70° tilted substrate shows lesser density of nucleation. The size distribution predicted from the SEM image given in figure 6.6 (a) shows large sized particles with an average size of 309nm and 165nm full width at half maximum (FWHM). SEM image of 80° tilted substrate show denser distribution of nanostructures. The average size calculated by ploting distribution curve (figure 6.6(b)) is 38nm with FWHM of 21nm.

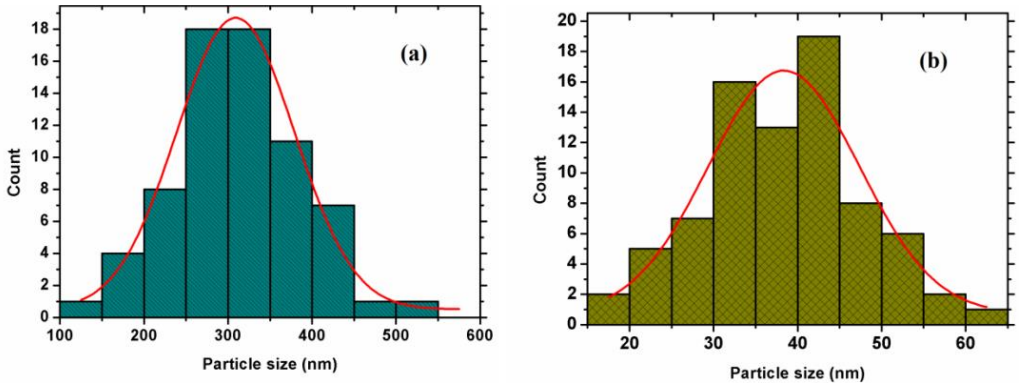

Figure 6.6: *(a) The size distribution curve of OAD nanostructures of Ag on 70° tilted silica substrate given in figure 6.5 (a) shows an average size of 309nm and 165nm FWHM (b) size distribution curve of 80° OAD nanostructures given in figure 6.5 (b) shows 38nm average size and 21nm FWHM.*

Figure 6.7 shows UV/Vis/NIR absorption spectra of 70° as well as 80° tilted silica glass plate with Ag nanostructures for 5 minute deposition time. A broad and intense absorption feature corresponding to surface plasmon resonance (SPR) appears at visible wavelength region. The absorption peaks are located at around 535nm and 430nm wavelengths and the FWHM calculated are 395nm and 355nm for 70° and 80° tilted substrates respectively.

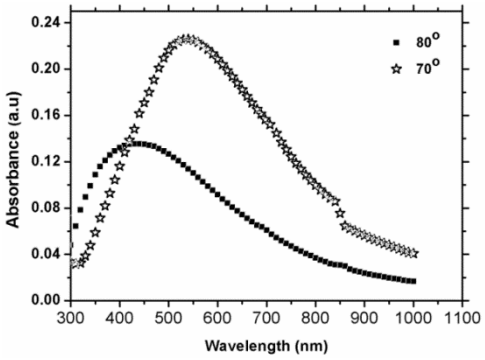

Figure 6.7: *UV/Vis/NIR absorption spectra of 70° as well as 80° tilted silica substrate with Ag nanostructures given in figure 6.5. The SPR peaks are located at around 535nm and 430nm wavelengths and the FWHM calculated are 395nm and 355nm for 70° and 80° tilted substrates respectively.*

More intense distribution of large nanostructures were obtained in 80° tilted substrate for 5 minutes of deposition time by reducing the distance from the source to the center of the substrates to 15cm. The morphology of the Ag nanostructures were characterized using FESEM and the images of 80° tilted silica substrate is given in 6.8 (a) and figure 6.8 (b) shows its magnified view. FESEM image of the Ag nanostructures coated on $Ge_{27}Sb_9Se_{64}$ glass film substrate is displayed in figure 6.8 (c) and its magnified image is shown in figure 6.8 (d). From the figure it is clear that the Ag film coated on both silica as well as $Ge_{27}Sb_9Se_{64}$ glass film substrate are not continuous and are composed of nano-sized islands which are the essential condition for the occurence of SPR and thereby SEIRA.

The size distribution calculated from the FESEM image is shown in figure 6.9. (a) shows the distribution curve for Ag nanostructre coated on silica substrate and (b) is for chalcogenide glass film substrate. Average size of almost equal values, 49nm and 51nm is obtained for silica and chalcogenide glass film substrates respectively. A narrow FWHM, 28nm is observed for silica substrate while for chalcogenide glass film substrates the FWHM is around 45nm.

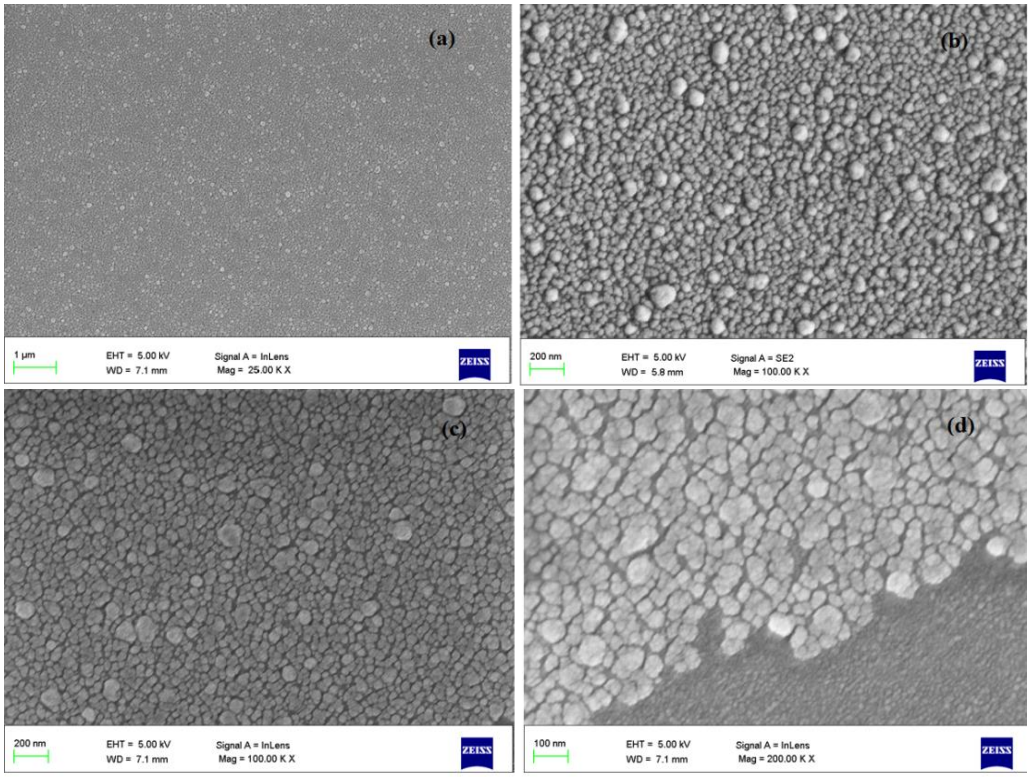

Figure 6.8: *SEM image of OAD nanostructures of Ag with substrate tilting angle 80°, deposition time 5 minutes and source to substrate distance 15cm (a); on silica glass plate; (b) magnified view of (a) ; (c) on chalcogenide glass film substrate; (d) magnified view of (c)*

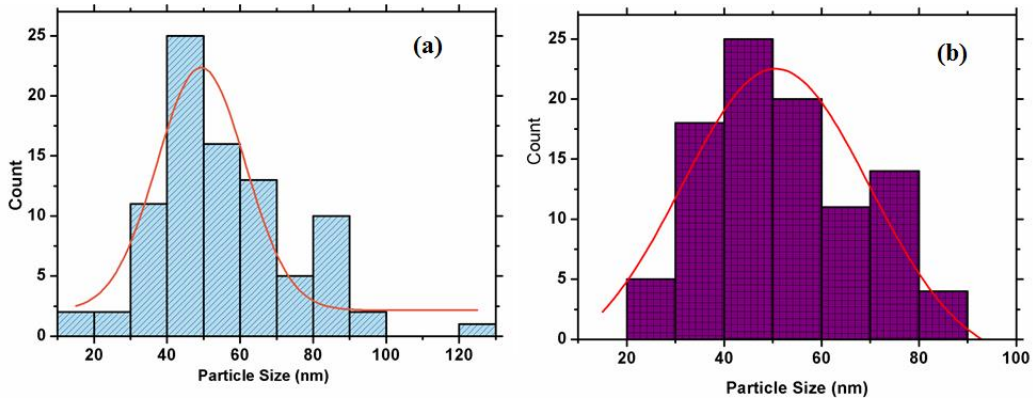

Figure 6.9: *(a) The size distribution curve of 80° OAD nanostructures on silica glass plate given in figure 6.8 (b) shows an average size of 49nm and 28nm FWHM (b) size distribution curve of 80° OAD nanostructures on chalcogenide glass film substrate shows 51nm average size and 45nm FWHM.*

Figure 6.10 shows UV/Vis/NIR absorption spectra of Ag nanostructures on 80° tilted silica glass plate as well as chalcogenide glass film substrate for 5 min deposition time. A broad and intense absorption feature corresponding to surface plasmon resonance (SPR) appears at visible wavelength region with an extended tail towards NIR region. The absorption peak maximum is located at around 750nm and this indicates the columnar growth of nanostructures grown out of the substrate with varying length, diameter, and shape. Broad, intense absorbance feature in visible wavelengths greater than 400nm and which continues into the NIR spectral region is observed for Ag columnar structures by Leverette[23] et al.

UV/Vis/NIR absorption spectrum of 80° tilted chalcogenide glass film substrate with Ag nanostructures shows no sharp SPR peak. Figure 6.10 (b) shows the absorption spectrum of $Ge_{27}Sb_9Se_{64}$ glass film with and without Ag nanostructures indicates an increase in the absorbance in the presence of Ag nanostructures. This confirms that the SPR peaks merges with the interference fringes observed in the band tail of absorption spectra of chalcogenide glass thin film.

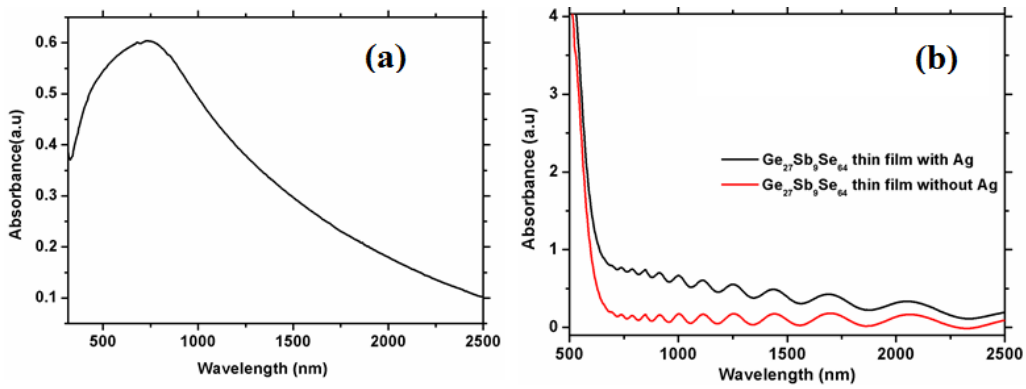

Figure 6.10: *(a) UV/Vis/NIR absorption spectra of 80° tilted silica glass substrate with Ag nanostructures given in figure 6.8 (a); (b) UV/Vis/NIR absorption spectra of 80° tilted $Ge_{27}Sb_9Se_{64}$ glass film substrate with Ag nanostructures given in figure 6.8 (c).*

More dense and smooth distribution of nanostructures were obtained in 70° tilted substrate for 5 minutes of deposition time with source to substrate distance 15cm and is shown in figure 6.11 (a). Figure 6.11 (b) shows the size distribution which indicates an average size of 31nm and FWHM 19nm.

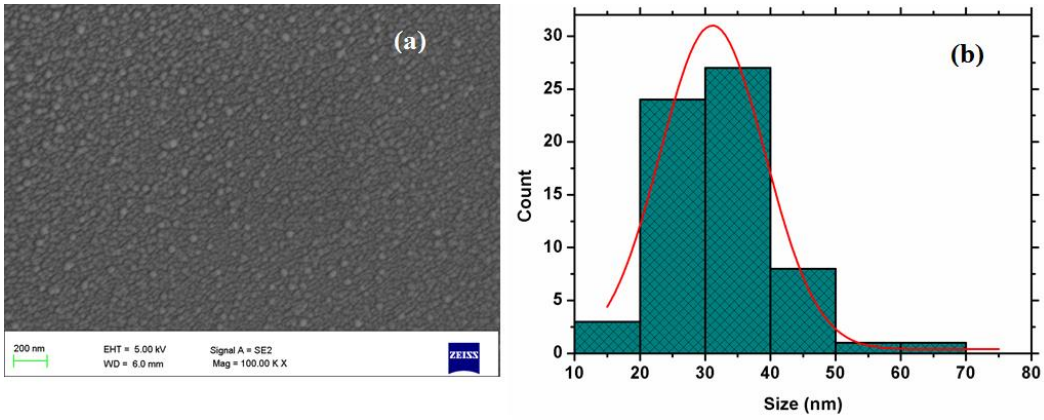

Figure 6.11: *(a) FESEM image of 70° tilted silica glass substrate with Ag nanostructures; (b) size distribution curve of 70° tilted substrate given in figure 6.11 (a)*

UV/Vis/NIR absorption spectrum of 70° tilted silica substrate with Ag nanostructures is given in figure 6.12 shows sharp SPR peak located at a wavelength around 320nm with 40nm FWHM.

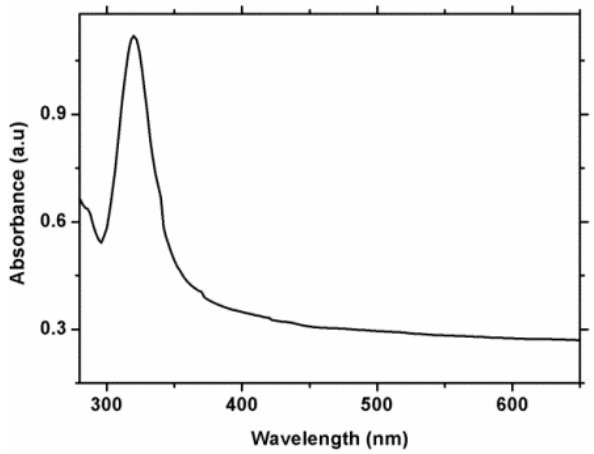

Figure 6.12: *UV/Vis/NIR absorption spectrum of 70° tilted silica substrate with Ag nanostructures given in figure 6.11(a). Here bare silica substrate as been used as reference.*

6.4 Ag nanostructures by wet chemical method

Ag island films can be prepared by coating Ag colloids on the required substrates prepared by chemical reduction method. The preparation of

chemically reduced Ag colloids in suspension is a widely used method for Surface Enhanced Raman Scattering (SERS) experiments[24]. Wet chemically prepared metal colloids have been employed in recent SEIRA experiments[25] and show good enhancement in IR absorption of antigen antibody binding event. Ag salt, generally silver nitrate is reduced by a chemical reducing agent and produce colloidal Ag suspensions integrated by nanoparticles with variable size depending on the method. Trisodiumcitrate[26,27] and sodiumborohydride[25] are the most commonly used reducing agents. The process of citrate reduction of silver is by adding the reducing agent to the silver nitrate solution followed by giving vigorous stirring and refluxing. For the sodium borohydride reduced silver colloid, a solution of sodium borohydride is mixed with a solution of silver nitrate with intensive stirring in an ice-cold bath. Comparing with other techniques, chemical reduction method helps rapid preparation of the colloidal suspension and has the advantage of the feasibility together with the higher stability of the suspended nanoparticles. The disadvantages of these colloids are the existence of impurities resulting from the oxidation residual species and the counter ions of the employed salts. The use of hydroxylamine hydrochloride as a reducing agent has the advantages of an easier preparation and the opportunity to carry out the reduction at room temperature[28,29].

6.4.1 Preparation of Hydroxylamine reduced Ag Colloid

The Ag colloids were prepared by the reduction of silver nitrate by the method described by Leopold and Lendl[22]. 10ml of sodium hydroxide/hydroxylamine hydrochloride solution mixture was added rapidly to 90 mL of silver nitrate aqueous solution of varying molarity. In all cases, the concentration of sodium hydroxide/hydroxylamine hydrochloride was calculated to be $3x10^{-2}$M/$1.5x10^{-2}$M in the finally obtained reaction mixture. After vigorous stirring, a milky gray colored homogeneous mixture was obtained. Various molar concentrations of silver nitrate taken and their assigned sample code are given in table 6.1. Sample 'A01' is prepared at 0^{o}C using ice bath at the time of mixing and stirring.

Sample code	Concentration of silver nitrate x10^{-3} M	SPR peak nm
A1	1.11	440
A2	0.96	433
A3	0.82	432
A4	0.63	420
A5	0.05	broad
A01	1.11 ice bath	418

Table 6.1: *Molar concentrations of silver nitrate taken and their assigned sample code.*

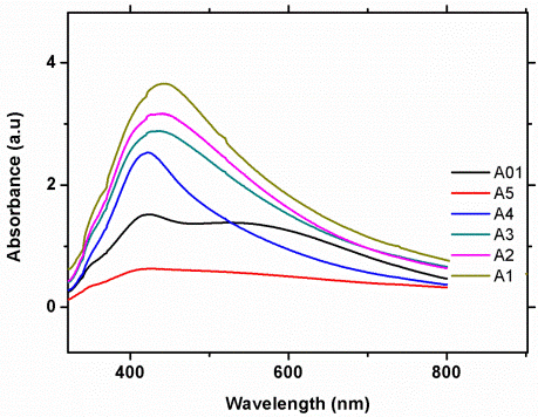

Figure 6.13: *UV/Vis/NIR absorption spectrum of different Ag colloids prepared by varying the $AgNO_3$ molar concentration.*

Figure 6.13 shows the UV-Vis absorption spectra of different Ag colloids prepared by varying the $AgNO_3$ molar concentration. The figure indicates a blue shift in the SPR absorption peak (given in table 6.1) with respect to the decrease in $AgNO_3$ molar concentration. Sample 'A01' shows very broad SPR absorption with a peak at 418nm indicating the possibility of 2 size distributions.

The colloids prepared in this way are less stable because of the formation of nitrogen oxides as residual oxidation products. These oxides react with water and leads to a gradual decrease in pH with time. Therefore, aqueous NaOH was added to the final solution to maintain the pH at 7. Figure 6.14 shows the UV-Vis absorption spectra of A3 before adding final NaOH solution which displays suppression of SPR peak located around 438nm due to ageing indicating instability of colloids.

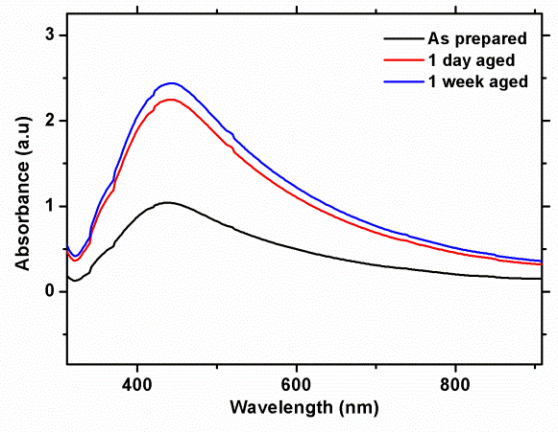

Figure 6.14: *UV/Vis/NIR absorption spectrum of A3 colloids shows suppression of SPR peak located at 438nm due to ageing.*

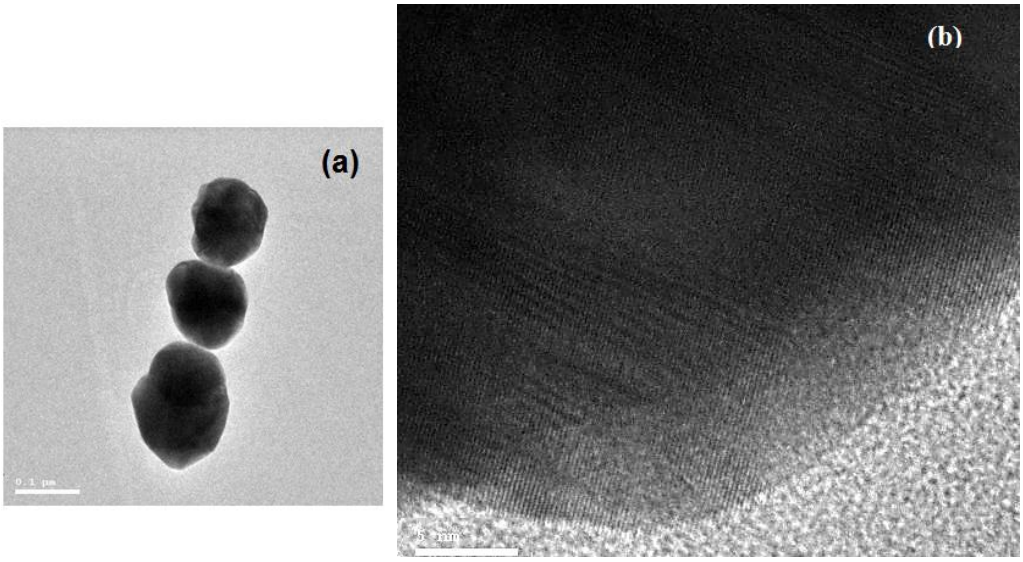

Figure 6.15: *(a) TEM image of 'A1' shows large particles (b) The lattice planes of silver*

TEM analysis were carried out for 'A1' and 'A01' samples in order to evaluate the size of the nanoparticles prepared. Figure 6.15 (a) shows the TEM image of 'A1' which displays large particles with size varying from 110nm to 140nm and (b) shows the lattice planes of silver. The same sample is prepared again in such a way that the sodium hydroxide/hydroxylamine hydrochloride mixture is added and stirred with silver nitrate aqueous solution placed in ice bath. Dynamic light scattering (DLS) at 532nm using Horiba SZ-100 nanoparticle size analyzer carried out for 'A1' and 'A01'

samples shows average size of 118nm with 31.5nm standard deviation for 'A1' sample. 'A01' shows two size distributions of sizes around 125nm and 7nm and this confirms the results obtained from UV-Vis spectra. The distributions curves obtained from DLS for 'A1' and 'A01' are shown in figure 6.16 (a) and (b) respectively.

TEM analysis for 'A01' is taken after centrifuging it using Eltek research centrifuge at 3000 rpm and for 15 min in order to remove the large particles which are settled down after centrifugation. The TEM image which is present in figure 6.17, shows small particles with average size around 5nm.

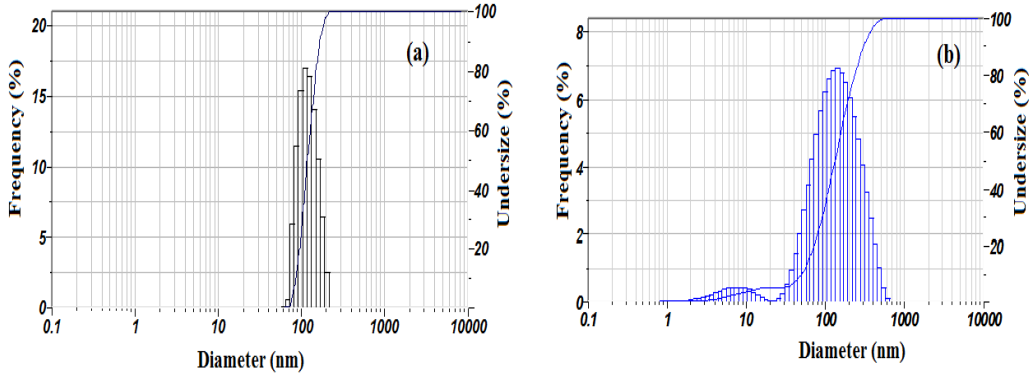

Figure 6.16: (*a) The distributions curve obtained from DLS for 'A1'. (b) DLS distribution curve for 'A01' showing two size distributions.*

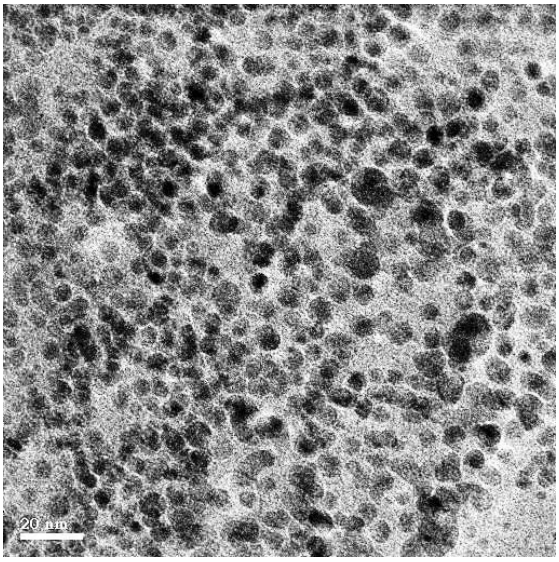

Figure 6.17: *Ag nanoparticles prepared using ice bath shows small particles with average size around 5nm.*

6.4.2 Studies on purchased Ag nanowires

Metallic nanostructures of different morphologies such as nanoparticles, films, nanowires and patterned structures etc. exhibits surface plasmons (SPs). Confinement of electrons in nanoparticles leads to localized SPs, while other large dimensional structures (compared with light wavelength) hold extended SPs that propagate along the interface between the metal and the dielectric medium. The surface Plasmon absorption is strongly affected by the metal particle shape or geometry in such a way that the restoring force on the surface electrons is related to the charge accumulated at the particle surface, which inturn is influenced by the particle size and geometry[30]. The shape effects are more noticeable in the case of the nanowires or nanorods[31,32]. A metal nanorod shows both longitudinal plasmons, electron oscillations along the rod axis as well as transverse plasmons, oscillations perpendicular to rod axis as shown in figure 6.18. The charge accumulation is maximum for transverse plasmons and minimum for longitudinal plasmons. Since the restoring force is proportional to this charge accumulation, longitudinal plasmon resonance frequency is smaller (i.e. larger resonant wavelengths) than transverse plasmon resonance frequency. The resonant frequency of transverse plasmons falls at visible region while the resonance of longitudinal plasmons moves towards larger wavelengths as the nanorod aspect ratio increases.

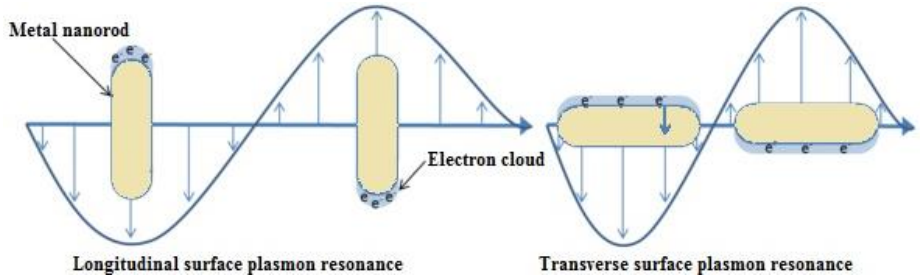

Figure 6.18: *Schematic showing longitudinal and transverse SPRs of nanorods*

Ag nanowires with 60nm diameter and 10µm length, dispersed in isopropyl alcohol with 0.785g/ml density were purchased from Sigma-Aldrich. This liquid is diluted to 0.0373g/ml by adding isopropyl alcohol since it is too thick to transmit light during UV-Vis analysis. The surface plasmon resonance peak of Ag nanowire, dispersed in isopropanol is observed from UV-Vis analysis at 383nm and it is shown in figure 6.19. In this case the contributions of longitudinal plasmons are negligible since it cannot be considered as a 'rod' because of its very long length i.e 10µm.

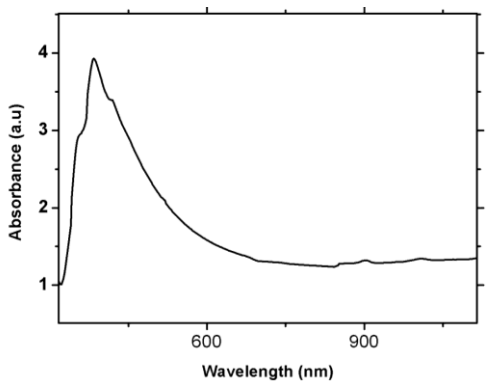

Figure 6.19: *UV/Vis/NIR absorption spectrum of Ag nanowires dispersed in isopropyl alcohol shows SPR peak at 383nm.*

Figure 6.20 (a) & (b) shows the TEM image of Ag nanowire and (c) shows the lattice planes of silver.

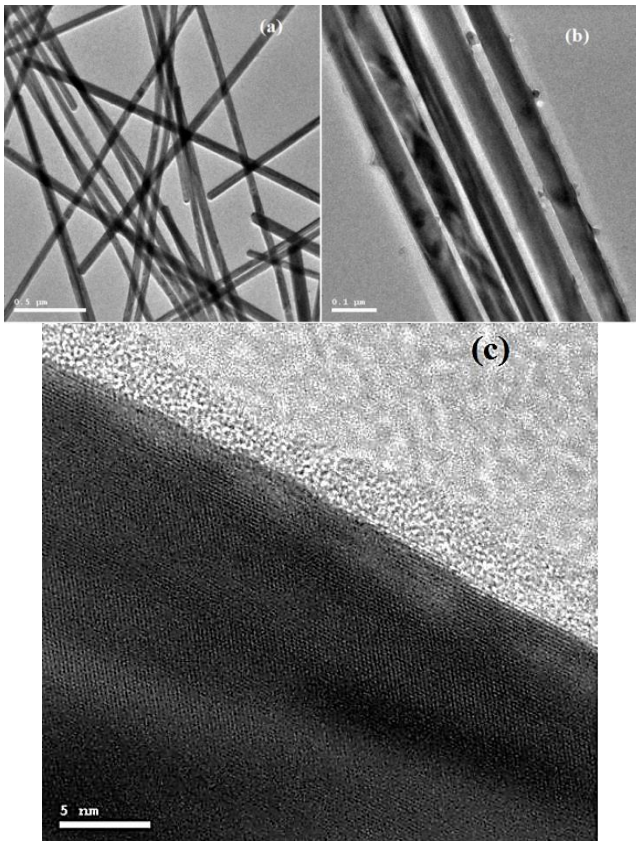

Figure 6.20: *(a) & (b) TEM image of Ag nanowires dispersed in isopropyl alcohol. (c) The lattice planes of silver.*

6.5 Summary of findings

- Silver island films of different morphology have been prepared both by dry process and wet process on silica and chalcogenide glass substrate.
- Silver island films prepared by OAD deposition technique results in the formation of silver nanostructures on the substrate for which average size can be tuned by changing the polar angle.
- The Ag colloids were prepared by the reduction of silver nitrate by the method described by Leopold and Lendl and are characterized by using UV-Vis, DLS and TEM. SPR absorption changes with respect to the molar concentration of $AgNO_3$ added.
- The sample prepared in ice bath shows very large SPR absorption peak with two peaks merged together indicating the possibility of 2 size distributions. DLS and TEM analysis confirmed the same.
- Ag nanowires dispersed in isopropyl alcohol were purchased from Sigma-Aldrich and are characterized by using UV-Vis and TEM.

6.6 References

[1]Osawa M, "Surface enhanced Infrared Absorption Spectroscopy in Handbook of Vibrational Spectroscopy M, Chalmers JM and Griffiths P R. Eds." *Chichester: Wiley* 1, no. 785 (2002): 2.

[2]Griffiths Peter R., and J. A. de Haseth. "Fourier Transform Infrared Spectroscopy." *New York: John Vlfiley & Sons* (1986).

[3]Hartstein A., J. R. Kirtley, and J. C. Tsang. "Enhancement of the infrared absorption from molecular monolayers with thin metal overlayers." *Physical Review Letters* 45, no. 3 (1980): 201.

[4]Aroca Ricardo F., Daniel J. Ross, and Concepción Domingo. "Surface-enhanced infrared spectroscopy." *Applied spectroscopy* 58 (2004): 324A-338A.

[5]Lal Surbhi, Stephan Link, and Naomi J. Halas. "Nano-optics from sensing to waveguiding." *Nature photonics* 1, no. 11 (2007): 641-648.

[6]Seki H., M. Takada, T. Tanabe, T. Wadayama, and A. Hatta. "Infrared absorption study of CO chemisorption on copper island films." *Surface science*506, no. 1 (2002): 23-32.

[7]Suzuki Y., Y. Ojima, Y. Fukui, H. Fazyia, and K. Sagisaka. "Post-annealing temperature dependence of infrared absorption enhancement of polymer on evaporated silver films." *Thin Solid Films* 515, no. 5 (2007): 3073-3078.

[8]Kamata Toshihide, Akira Kato, Junzo Umemura, and Toru Takenaka. "Intensity enhancement of infrared attenuated total reflection spectra of stearic acid Langmuir-Blodgett monolayers with evaporated silver island films."*Langmuir* 3, no. 6 (1987): 1150-1154.

[9]Neubrech Frank, Annemarie Pucci, Thomas Walter Cornelius, Shafqat Karim, Aitzol García-Etxarri, and Javier Aizpurua. "Resonant plasmonic and vibrational coupling in a tailored nanoantenna for infrared detection." *Physical review letters* 101, no. 15 (2008): 157403.

[10]Pucci A., F. Neubrech, D. Weber, S. Hong, T. Toury, and M. Lamy De La Chapelle. "Surface enhanced infrared spectroscopy using gold nanoantennas."*physica status solidi (b)* 247, no. 8 (2010): 2071-2074.

[11]Kundu Janardan, Fei Le, Peter Nordlander, and Naomi J. Halas. "Surface enhanced infrared absorption (SEIRA) spectroscopy on nanoshell aggregate substrates." *Chemical Physics Letters* 452, no. 1 (2008): 115-119.

[12]Schatz G. C., and R. P. Van-Duyne. "Electromagnetic enhancement of surface-enhanced raman spectroscopy." *Chalmers JM, Griffiths P. Handbook of vibrational spectroscopy. New York: Wiley* (2002).

[13]Gersten Joel I., and Abraham Nitzan. "Photophysics and photochemistry near surfaces and small particles." *Surface Science* 158, no. 1 (1985): 165-189.

[14]S. B. Chaney S. Shanmukh, R. A. Dluhy, and Y.-P. Zhao, Appl. Phys.Lett. 87, 031908 (2005).

[15]Huang Bei-Bei, Jin-Yi Wang, Sheng-Juan Huo, and Wen-Bin Cai. "Facile fabrication of silver nanoparticles on silicon for surface-enhanced infrared and Raman analysis." *Surface and Interface Analysis* 40, no. 2 (2008): 81-84.

[16]Abelmann Leon, and Cock Lodder. "Oblique evaporation and surface diffusion." *Thin solid films* 305, no. 1 (1997): 1-21.

[17]Karabacak T., G-C. Wang, and T-M. Lu. "Quasi-periodic nanostructures grown by oblique angle deposition." *Journal of applied physics* 94, no. 12 (2003): 7723-7728.

[18]Taschuk Michael T., Matthew M. Hawkeye, and Michael J. Brett. "Glancing angle deposition." *Handbook of Deposition Technologies for Films and Coatings*(2010): 621-678.

[19]Chitvoranund N., S. Jiemsirilers, and D. P. Kashima. "Effects of surface treatments on adhesion of silver film on glass substrate fabricated by electroless plating." *Journal of the Australian Ceramic Society* 49, no. 1 (2013): 62-69.

[20]Huo Sheng-Juan, Xiao-Kang Xue, Qiao-Xia Li, Su-Fan Xu, and Wen-Bin Cai. "Seeded-growth approach to fabrication of silver nanoparticle films on silicon for electrochemical ATR surface-enhanced IR absorption spectroscopy." *The Journal of Physical Chemistry B* 110, no. 51 (2006): 25721-25728.

[21]Huo Sheng-Juan, Qiao-Xia Li, Yan-Gang Yan, Yi Chen, Wen-Bin Cai, Qun-Jie Xu, and Masatoshi Osawa. "Tunable surface-enhanced infrared absorption on Au nanofilms on Si fabricated by self-assembly and growth of colloidal particles." *The Journal of Physical Chemistry B* 109, no. 33 (2005): 15985-15991.

[22]Yan Yan-Gang, Qiao-Xia Li, Sheng-Juan Huo, Min Ma, Wen-Bin Cai, and Masatoshi Osawa. "Ubiquitous strategy for probing ATR surface-enhanced infrared absorption at platinum group metal-electrolyte interfaces." *The Journal of Physical Chemistry B* 109, no. 16 (2005): 7900-7906.

[23]Leverette C. L., S. A. Jacobs, S. Shanmukh, S. B. Chaney, R. A. Dluhy, and Y-P. Zhao. "Aligned silver nanorod arrays as substrates for surface-enhanced infrared absorption spectroscopy." *Applied spectroscopy* 60, no. 8 (2006): 906-913.

[24]Creighton J. Alan, Christopher G. Blatchford, and M. Grant Albrecht. "Plasma resonance enhancement of Raman scattering by pyridine adsorbed on silver or gold sol particles of size comparable to the excitation wavelength." *Journal of the Chemical Society, Faraday Transactions 2: Molecular and Chemical Physics* 75 (1979): 790-798.

[25]Enders Dominik, Swen Rupp, Alexander Küller, and Annemarie Pucci. "Surface enhanced infrared absorption on Au nanoparticle films deposited on SiO_2/Si for optical biosensing: Detection of the antibody–antigen reaction."*Surface science* 600, no. 23 (2006): L305-L308.

[26]Lee P. C., and D. Meisel. "Adsorption and surface-enhanced Raman of dyes on silver and gold sols." *The Journal of Physical Chemistry* 86, no. 17 (1982): 3391-3395.

[27]Rivas L., S. Sanchez-Cortes, J. V. Garcia-Ramos, and G. Morcillo. "Growth of silver colloidal particles obtained by citrate reduction to increase the Raman enhancement factor." *Langmuir* 17, no. 3 (2001): 574-577.

[28]Leopold Nicolae, and Bernhard Lendl. "A new method for fast preparation of highly surface-enhanced Raman scattering (SERS) active silver colloids at room temperature by reduction of silver nitrate with hydroxylamine hydrochloride." *The Journal of Physical Chemistry B* 107, no. 24 (2003): 5723-5727.

[29]Canamares M. V., J. V. Garcia-Ramos, J. D. Gomez-Varga, C. Domingo, and S. Sanchez-Cortes. "Comparative study of the morphology, aggregation, adherence to glass, and surface-enhanced Raman scattering activity of silver nanoparticles prepared by chemical reduction of Ag+ using citrate and hydroxylamine." *Langmuir* 21, no. 18 (2005): 8546-8553.

[30]Zeng Shuwen, Ken-Tye Yong, Indrajit Roy, Xuan-Quyen Dinh, Xia Yu, and Feng Luan. "A review on functionalized gold nanoparticles for biosensing applications." *Plasmonics* 6, no. 3 (2011): 491-506.

[31]Burda Clemens, Xiaobo Chen, Radha Narayanan, and Mostafa A. El-Sayed. "Chemistry and properties of nanocrystals of different shapes." *Chemical reviews* 105, no. 4 (2005): 1025-1102.

[32]Link Stephan, and Mostafa A. El-Sayed. "Spectral properties and relaxation dynamics of surface plasmon electronic oscillations in gold and silver nanodots and nanorods." *The Journal of Physical Chemistry B* 103, no. 40 (1999): 8410-8426.

Chapter 7

Binding Of Anchor Molecules: Surface Enhanced Infrared Absorption Studies

This chapter discusses in detail the binding and characterisation of anchor molecules on the surface of silver island films with different host substrates. Self-assembled monolayer (SAM) of hexadecane-thiol (HDT) is fabricated on silver island surface of different morphology since thiol group shows good affinity to gold or silver enabling easier binding. The SAM layer acts as a handle on the film surface to which biological functional molecules can be attached. The binding of HDT on silver surface is confirmed from IR spectra. Enhancement of IR absorption of HDT molecule with the increase of Ag content is observed. Variation of enhancement in IR absorption with respect to host substrate is also observed. Feasibility of microcontact printing on the fabrication of silver patterns and anchor layer altogether is checked.

7.1 Introduction

As discussed in chapter 6, molecules that are either adsorbed on or in close proximity to the surface of metal island structures gives an enhanced infrared absorption[1,2] which is termed as surface enhanced infrared absorption spectroscopy (SEIRA). Both physisorbed and chemisorbed molecules show SEIRA, while chemisorbed molecules exhibit larger enhancement than physisorbed molecules. This is because chemisorption arises from strong bonding between adsorbates and adsorbents whereas in physisorption the binding happens by weak forces like electrostatic force etc. Therefore in order to observe SEIRA spectra of biological molecules like DNA, proteins, antibodies etc, these molecules should be adsorbed on the metal surface. The process of binding biological functional groups on metal surfaces is called bio-functionalization of metal. Since molecules without polar groups consequently, have no possibility of being chemisorbed to the metallic surface, bio-

functionalization is realized with the help of anchor molecules[3]. Anchor molecules firmly attach and form a self-assembled monolayer (SAM) on the surface of metal island film and will act as a handle on the film surface to which biological functional molecules can be attached. Anchor molecules should have functional groups that can react and bind with biological functional molecules (DNA, antibody, etc.). The motivation behind the fabrication of self-assembled monolayer of anchor layer on the surface of metal island structures is to extend the possibility of SEIRA technique towards the enhancement of infrared absorption spectra for molecules that show weak IR absorption.

Some organic compounds like 'thiols' can easily be chemisorbed on metal surfaces and are commonly used for the fabrication of anchor layers. Studies on SEIRA active surfaces fabricated by coating the metal island structures with SAMs of different 'thiols' have been reported for many metal-substrate systems including gold-silicon[4,5], gold-germanium system[6], gold-chalcogenide glass system[7] etc. During the adsorption process of a SAM, the molecules are arranged parallel next to each other on the surface of the metal. A thiol molecule consists of three parts: 1) a sulphur containing headgroup which forms a strong covalent bond with the metal surface, 2) a hydrocarbon chain of different length which helps the formation and stabilization of SAM through van der Waals interactions, and 3) a terminal group, which can have different functionalities. By changing the functionalities of terminal group, it is possible to vary the physical and chemical properties of the SAM layer[8, 9, 10]. For example, occurrence of $-CH_3$ and $-CF_3$ as terminal groups turn the SAM surface hydrophobic, metallophobic and highly anti-adherent[11]. On the other hand the presence of -COOH, $-NH_2$ or -OH groups yield hydrophilic surfaces having good protein and metal ion binding properties[12,13] and -SH terminated thiols, which is known as dithiols also show good binding with metallic ions and nanoparticles[14,15]. Therefore SAMs of 'thiols' having terminal functional groups that can react and bind with biological functional molecules (DNA, antibody, etc.) can be utilized for bio-functionalization of metal island structures.

7.2 Scope of the chapter

If the 'SAM modified chalcogenide glass substrates' succeed in bio-functionalization of metallic structures, their infrared spectra would benefit from enhancement of IR signature peaks. Since metals like silver or gold shows good adhesiveness to chalcogenide glass compounds and thiols show

strong affinity to silver or gold, the realization of 'SAM modified chalcogenide glass substrates' is effortlessly possible. In this chapter SAM layer of hexadecane-thiol (HDT) is fabricated on different silver island structures created on silica as well as chalcogenide glass thin film substrates. The binding of HDT on the surface of silver island films is characterized using IR spectra analysis.

7.3 Alkanethiol

Alkanethiols also known as mercaptans, which are organic compounds containing one or more thiol (-SH) functional groups i.e, comparing with alcohols, the oxygen atom is replaced by sulphur. alkanethiols are named as from the corresponding 'alkane' and the ending 'thiol' (e.g ethanethiol, propanethiol etc.). Linear alkanethiol with long chain, like hexa-decanethiol ($C_{16}H_{33}SH$) or octa-decanethiol ($C_{18}H_{37}SH$) are commonly used for the fabrication of self-assembled monolayers (SAM). The -SH group present in the thiol form a strong bond with the metal surface. Figure 7.1 shows the molecular structure of hexadecanethiol

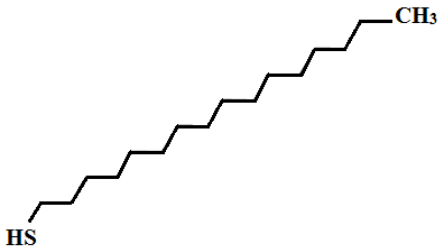

Figure 7.1: *The molecular structure of hexadecanethiol*

As mentioned earlier, self-assembling occurs in such a way that the molecules are arranged parallel to each other on the metal surface. The van der Waals interaction between the adjacent alkyl chains results in a standing up geometry in which the molecules are being tilted with respect to the surface normal[1617] as shown in figure 7.2 (a) and (b). As the length of the alkane chain increases the adsorbate-adsorbate interaction also will rise[18].

Alkanethiol based SAMs are well-suited as anchor layer because

- Easiness of their fabrication. Facilities like, ultrahigh vacuum or other specialized equipments are not required.

- Ability of SAM formation on objects of different shapes or sizes, for example thin films, nanowires, colloids, and other nanostructures.
- The surface of a SAM is very inert and therefore the multilayer adsorption is not possible.
- Fabrication of SAMs on the metal surface will act as a protective coating which will keep the metal from any other adverse chemical reactions like corrosion etc.
- By replacing the terminal $-CH_3$ in alkanethiol with appropriate functional group that can react and bind with biological functional molecules, the bio-functionalization of the surface can be realized.

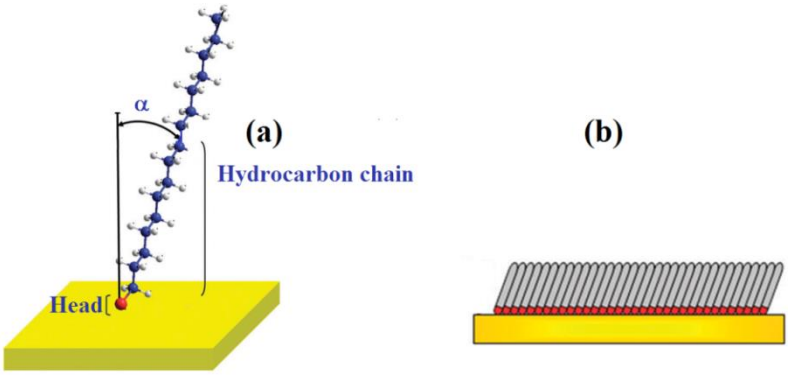

Figure 7.2: *(a) Schematic of HDT molecule adsorbed on metal surface. (b) self-assembled monolayer formed by thiol molecules shows standing up geometry.*

7.4 Preparation and characterization of SAM on OAD film

The HDT molecules are capable to chemisorb and make a self-assembled monolayer on silver surface. HDT (1-hexadecanethiol) purchased from Sigma Aldrich was stored in a refrigerator to slow down deterioration. This chemical is solid when cold, and is liquid at room temperature. For SAM fabrication HDT is dissolved in ethanol by mixing 0.04ml of molten HDT with 10ml ethanol and after thorough shaking 10ml more ethanol is added. This HDT/ethanol solution is prepared just before use. SAM layer is fabricated on silver island structures, deposited on silica as well as thermal evaporated $Ge_{27}Sb_9Se_{64}$ glass film substrate by oblique angle deposition (OAD). The thickness of $Ge_{27}Sb_9Se_{64}$ film used in this study was 2.6μm. The silver deposition was carried out for 5 minutes at a substrate tilting angle of 80° and source to substrate distance 15cm. 6μl of the solution is pipetted using a micropipette and drop casted on the OAD deposited silver island film surface

and allowed to dry in air. The substrates were then rinsed with the solvent ethanol to remove any physisorbed molecules and dried again.

The dimension[19] of HDT molecules are around 2.4nm and therefore the characterization of SAM using SEM is difficult. The SEIRA spectra of HDT self-assembled samples were recorded with a JASCO FT-IR-5300 Spectrometer in transmission mode, using a DTGS detector. The background spectrum of atmosphere was used as a reference. A baseline correction with silica substrate was carried out for $Ge_{27}Sb_9Se_{64}$ glass film to eliminate the absorption of the silica.

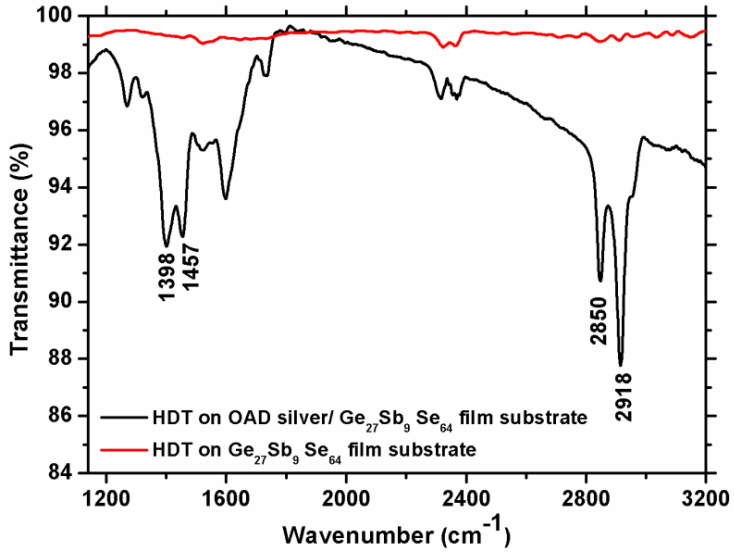

Figure 7.3: The infrared transmission spectrum of HDT molecules, adsorbed on OAD deposited silver on $Ge_{27}Sb_9Se_{64}$ glass film substrate. The IR transmission spectrum of HDT molecules coated on $Ge_{27}Sb_9Se_{64}$ glass film in the absence of silver structures is shown as red continuous line.

Figure 7.3 shows the infrared transmission spectrum of HDT molecules, adsorbed on OAD deposited silver on mid-IR transparent $Ge_{27}Sb_9Se_{64}$ glass film substrate. The IR transmission spectrum of HDT molecules coated on $Ge_{27}Sb_9Se_{64}$ glass film in the absence of silver structures shows no IR absorption because of low HDT content in the film while the presence of silver island structures enhances the IR absorption. The IR spectra of n-alkanethiols are similar to that of n-alkanes because of their structural similarity.

	Vibration assignment	Band position (cm^{-1})	Strength
CH_3	antisymmetric stretch	2952-2972	vs
	symmetric stretch	2862-2882	vs
	antisymmetric bending	1440-1470	m
	$C(CH_3)$ symmetric bending	1370-1380	ms
CH_2	antisymmetric stretch	2916-2936	
	symmetric stretch	2843-2863	vs
	scissor	1445-1475	vs
			ms
	$-(CH_2)n-$ in phase, twist	1295-1305	
	$-(CH_2)n-$ in phase, rock	720-726	
	C-C skeletal stretch	1120-1180	-
			m
	R-SH (liquid)	2560-2590	(doublet)
S-H	S-H stretch	650-660	w
C-S	C-S stretch		w

Table 7.1: *The details of different vibrational modes of alkanethiols; vs - very strong, ms - medium strong, m - medium, w - weak*

The details of different vibrational modes[20] of alkanethiols are given in table 7.1. The absorption features observed at 2918cm^{-1} and 2850cm^{-1} correspond to the vibrational antisymmetric and symmetric stretching modes of $-CH_2$ respectively[21,22]. Vibrational band corresponding to the symmetric stretching of $-CH_3$ located around 2862-2882cm^{-1}, is merged with the symmetric stretching band of $-CH_2$. Figure 7.4 shows a close-up view of these absorption features, which indicates an additional shoulder at 2955cm^{-1} corresponding to the antisymmetric stretching vibration of $-CH_3$. The absorption features corresponding to antisymmetric bending of $-CH_3$ and scissoring of $-CH_2$ are merged together and are observed at 1457cm^{-1}. Symmetric bending vibration of $-C(CH_3)$ is also observed at 1398cm^{-1}. Thiol molecules are bound to the silver surface through the Ag-S bond. The absorption band at 2560-2590cm^{-1} corresponding to S-H stretching present in liquid form of HDT is absent and it is attributed to the cleavage of S-H bond

for forming Ag-S bond. This phenomenon proved the 'SAM formation' on Ag surface through the Ag-S bond[23].

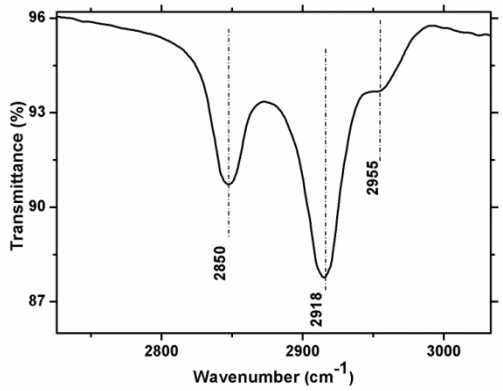

Figure 7.4: *A close-up view of vibrational antisymmetric and symmetric stretching features indicates an additional shoulder at 2955cm^{-1} corresponding to antisymmetric stretching vibration of -CH$_3$.*

The IR transmission spectrum of HDT molecules adsorbed on OAD deposited silver on silica glass substrate is also taken. All coating parameters, such as the deposition angle, time and source to substrate distance were kept constant. Figure 7.5 (a) shows the IR transmission spectrum of OAD deposited silver on silica substrate and (b) shows its close-up view. Since silica substrate shows high IR absorption, the absorption features of HDT layer is merged with the substrate absorption. Vibrational antisymmetric and symmetric stretching modes of HDT molecules are more visible in the close-up view while all other IR absorption signatures, which are located in the low energy region, are absent.

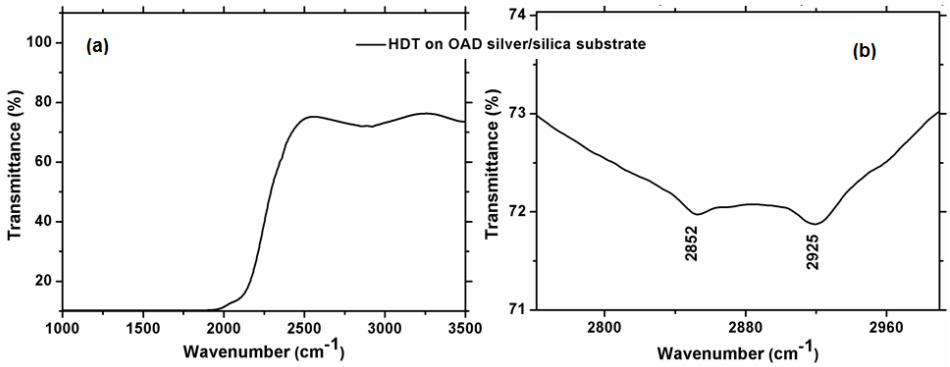

Figure 7.5: (a) *The IR transmission spectrum of OAD deposited silver on silica substrate and (b) its close-up view.*

7.5 Fabrication and characterization of SAM on wet chemically prepared silver nanostructures

SAMs of thiols can be realized on colloidal metal nanostructures, where the metal colloids are prepared by reduction of metal ions as discussed in chapter 6. Aqueous metal colloids are one of the most common media employed in Surface Enhance Raman Scattering (SERS) because of the very low Raman scattering cross-sections of water. But the straightforward application of aqueous metal colloids in SEIRA studies is challenging, because of the extremely high IR absorption of water which masks IR signatures of adsorbate molecules. However, SEIRA enhancement using colloidal silver and gold casted thick aggregated films of colloidal particles has been reported[24,25].

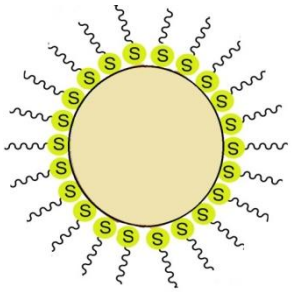

Figure 7.6: *Schematic of self-assembled monolayer formed by thiol molecules on the surface of metal particle.*

The Ag colloids were prepared by the reduction of silver nitrate by the method described by Leopold and Lendl[26] as discussed in chapter 6. A mixture of sodium hydroxide ($3x10^{-2}$M)/hydroxylamine hydrochloride ($1.5x10^{-2}$M) is prepared and 10ml of which is added rapidly to 90 mL of $1.11x10^{-3}$M silver nitrate aqueous solution. Large sized particles of above 100nm are obtained. Details about preparation and characterization of colloidal silver particles are described in chapter 6. Freshly prepared silver colloids were pre-concentrated tenfold, using an Eltek research centrifuge at 3000 rpm centrifuge for 15 min followed by the removal of excess supernatant. The pre-concentrated silver colloid and HDT solution prepared in ethanol were mixed in three different volume ratios; 50% of silver colloid and 50% of HDT solution (50-50), 25% of silver colloid and 75% of HDT solution (25-75), and 10% of silver colloid and 90% of HDT solution (10-90). As was in previous case, 6μl of each sample is pipetted using a micropipette and drop casted directly on thermal evaporated $Ge_{27}Sb_9Se_{64}$ glass film substrates followed by drying at ambient conditions.

The SEIRA spectra of samples were recorded in transmission mode as discussed above. Figure 7.7 shows the variation of vibrational antisymmetric and symmetric stretching absorption features of $-CH_2$ and $-CH_3$ groups in infrared transmission spectrum for different samples. Absence of absorption band at 2560-2590cm^{-1} corresponding to S-H stretching confirmed the formation of SAM layer. Vibrational antisymmetric stretching modes of $-CH_2$ is observed at 2920cm^{-1} and the absorption observed at 2858cm^{-1} corresponds to symmetric mode of $-CH_2$ and $-CH_3$. A small shoulder corresponding to antisymmetric stretching vibration of $-CH_3$ at 2952cm^{-1} is also observed. Absence of absorption band at 2560-2590cm^{-1} corresponding to S-H stretching confirmed the formation of SAM.

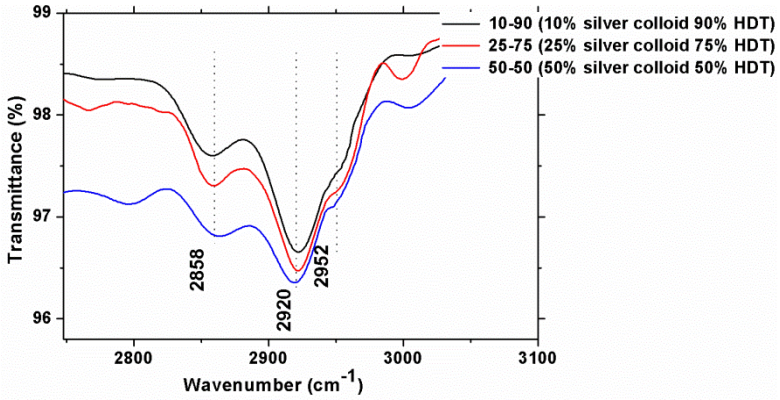

Figure 7.7: *The infrared transmission spectrum of HDT molecules, adsorbed on wet chemically prepared silver particles on $Ge_{27}Sb_9Se_{64}$ glass film substrate. FWHM for each IR absorption peak is found to be decreased with the increase of percentage of silver colloid.*

From the figure, it is found that all IR absorption features enhance with Ag content. Thin film sample which is prepared with 50% of silver colloid and 50% of HDT solution (50-50) shows maximum enhancement in IR absorption.

7.6 Fabrication and characterization of SAM on silver nanowires

SAMs of HDT were fabricated on Ag nanowires. Ag nanowires were purchased from Sigma-Aldrich and have a dimension of 60nm diameter and 10μm length, dispersed in isopropyl alcohol with 0.785g/ml density. Details about characterization of Ag nanowires suspension are described in chapter 6.

The purchased liquid is diluted to 0.0373g/ml by adding isopropyl alcohol and mixed with HDT solution where the HDT solution is prepared by dissolving 0.04ml of molten HDT in 10ml of isopropyl alcohol and after thorough shaking 10ml more isopropyl alcohol is added. This HDT/isopropyl alcohol solution is prepared right before use. The Ag nanowire suspension and HDT solution were mixed in three different volume ratios as was in previous case; 50% of silver colloid and 50% of HDT solution (50-50), 25% of silver colloid and 75% of HDT solution (25-75), and 10% of silver colloid and 90% of HDT solution (10-90). 6µl of the samples are drop casted on the thermally evaporated $Ge_{27}Sb_9Se_{64}$ glass film substrates followed by drying at ambient conditions.

The SEIRA spectra of samples were recorded in transmission mode and the variation of vibrational antisymmetric and symmetric stretching absorption features of $-CH_2$ and $-CH_3$ groups are shown in figure 7.8. Enhancement in all IR absorption features with Ag content is observed as before, in the case of wet chemically prepared Ag particles. The maximum enhancement in IR absorption is obtained for sample having 50% of silver colloid and 50% of HDT solution (50-50). From figure 7.8, it is found that all IR absorption features are shifted to lower energy side than it is observed in the case of SAM on wet chemically prepared Ag particles. These shifts in IR absorption of the SAM are attributed to structural variation of SAM which considerably affects symmetric and asymmetric stretching vibration, and absorption intensity of C-H bonding[27].

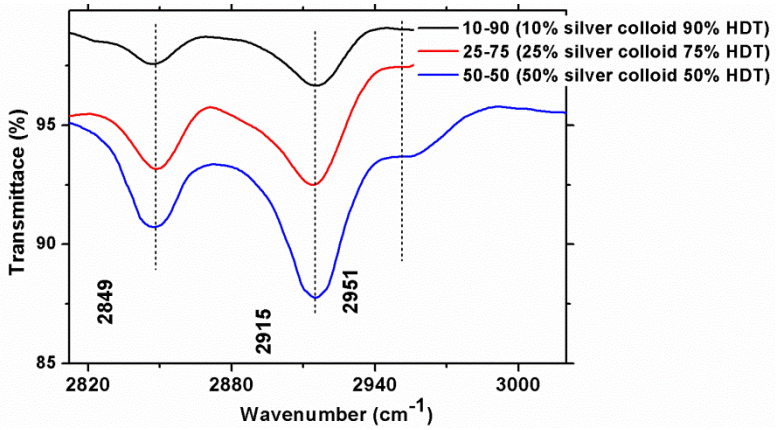

Figure 7.8: *The infrared transmission spectrum of HDT molecules, adsorbed on silver nanowires on $Ge_{27}Sb_9Se_{64}$ glass film substrate.*

Bulk $Ge_{27}Sb_9Se_{64}$ glass plates were also used as SEIRA substrates by slicing $Ge_{27}Sb_9Se_{64}$ glass rod into thin pieces with 1mm thickness. These pieces were then polished using cerium oxide powder for obtaining smooth and clear

surface. Figure 7.9(a) shows the photograph of $Ge_{27}Sb_9Se_{64}$ glass plate used as SEIRA substrate. Three different volume ratios of Ag nanowire and HDT solution mixture were prepared; 50% of silver colloid and 50% of HDT solution (50-50), 25% of silver colloid and 75% of HDT solution (25-75), and 10% of silver colloid and 90% of HDT solution (10-90). 6µl of the sample is drop casted on the $Ge_{27}Sb_9Se_{64}$ glass plates followed by drying at ambient conditions.

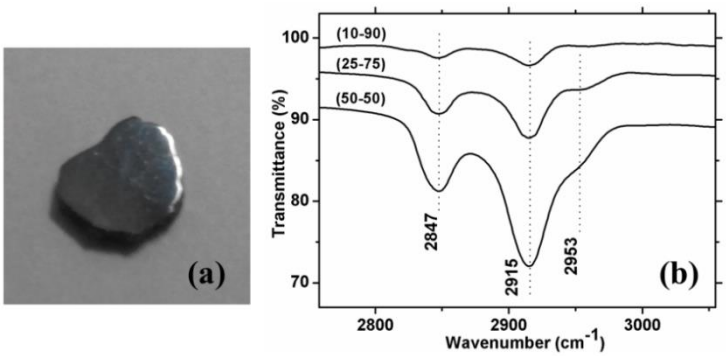

Figure 7.9: *(a) Photograph of $Ge_{27}Sb_9Se_{64}$ glass plate used as SEIRA substrate (b) the infrared transmission spectrum of HDT molecules, adsorbed on silver nanowires on $Ge_{27}Sb_9Se_{64}$ glass plate.*

The SEIRA spectra of samples were recorded in a transmission mode where the background spectrum of atmosphere was used as a reference. Figure 7.9 (b) shows the variation of vibrational antisymmetric and symmetric stretching absorption features of $-CH_2$ and $-CH_3$ groups. The absorption features are more clear when bulk chalcogenide glass was used as SEIRA substrate. Enhancement in all IR absorption features with Ag content is observed where the maximum enhancement in IR absorption is obtained for sample having 50% of silver colloid and 50% of HDT solution (50-50). It is found that irrespective to substrate used, the FWHM of IR absorption peaks for all samples containing Ag nano wire decrease with the increase of Ag content.

Solution processed $Ge_{27}Sb_9Se_{64}$ glass films which are derived by spin coating $Ge_{27}Sb_9Se_{64}$/ethanolamine solution on silica substrate are also employed as SEIRA substrates. The details about the fabrication and characterization of solution processed films are discussed in chapter 5. The recorded IR transmission spectra after background and baseline correction using silica substrate are shown in figure 7.10 where (a) shows the IR spectra of 50% Ag nanowire and 50% HDT solution mixture drop casted on solution processed $Ge_{27}Sb_9Se_{64}$ film and (b) indicates the IR spectra of 50% wet chemically prepared Ag particles and 50% HDT solution mixture drop casted

on solution processed $Ge_{27}Sb_9Se_{64}$ film. The vibrational antisymmetric and symmetric stretching absorption features of -CH_2 and -CH_3 groups are not clearly visible from the figure but the spectra show large distortion and impurity absorption features.

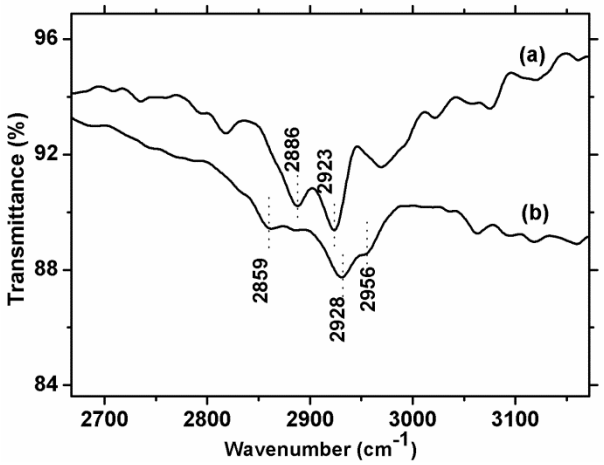

Figure 7.10: *(a) IR spectra of 50% Ag nanowire and 50% HDT solution mixture drop casted on solution processed $Ge_{27}Sb_9Se_{64}$ film (b) IR spectra of 50% wet chemically prepared Ag particles and 50% HDT solution mixture drop casted on solution processed $Ge_{27}Sb_9Se_{64}$ film.*

The IR enhancement in absorption is found to vary with respect to the substrate used. IR spectra of different volume percentages of Ag nanowire and HDT solution mixture drop casted on silica substrate also show HDT signature peaks as shown in figure 7.5(b) but the enhancement is very less. As a measure of IR absorption, the area under the IR absorption feature of HDT for different volume percentage of Ag nanowire is calculated in 'OriginPro 8'. The area swept by absorption feature located at 2916-2936cm^{-1}, which arised due to antisymmetric stretching vibration of CH_2 was calculated for different substrates having different percentage of Ag nanowire. Area is calculated by plotting a baseline having constant Y- value which is the maximum value (P_{max}) at the intercept region of symmetric (S) and antisymmetric (A) vibrational feature as shown in figure 7.11 (a), where area of the shaded portion is calculated. Figure 7.11 (b) shows the variation of area swept by antisymmetric stretching vibration of CH_2 of HDT with respect to the change in volume percentage of Ag nanowire for different substrates.

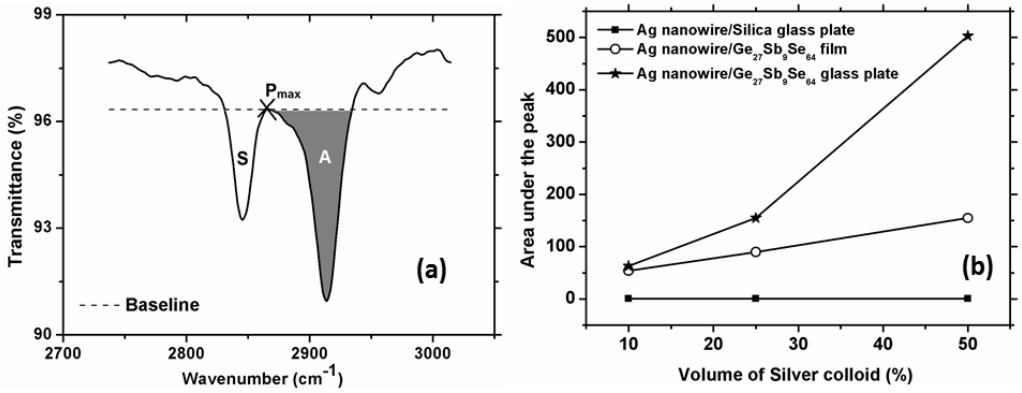

Figure 7.11: *(a) Schematic of area calculation; S- CH_2 symmetric stretching, A- CH_2 antisymmetric stretching, P_{max}- the maximum value at the intercept region of S & A, dotted line is the baseline ($x = P_{max}$). Area of the shaded portion is calculated. (b) variation of area swept by 'A' of HDT with respect to the change in volume percentage of Ag nanowire for different substrates.*

From figure 7.11 (b) it is clear that among various substrates, $Ge_{27}Sb_9Se_{64}$ glass plate shows maximum enhancement in IR absorption. Silica substrate shows minimum enhancement because the substrate itself shows intense absorption in IR region. In the case of $Ge_{27}Sb_9Se_{64}$ thin film substrates, the enhancement is not as high as $Ge_{27}Sb_9Se_{64}$ glass plate. This may be because the spectra measurement was in transmission mode where the HDT attached silver contained $Ge_{27}Sb_9Se_{64}$ thin film coated on silica substrate was kept normal to the incident beam. Even though the baseline correction using silica was carried out, the thickness variation of silica glass substrate (average 1mm thickness) may cause variation in enhancement. This can be overcome by avoiding the effect of supporting substrate silica i.e, by coupling IR waves from one end of the thin film with suitable cladding layer as shown in figure 7.12. Here the enhancement is achieved by means of evanescent waves.

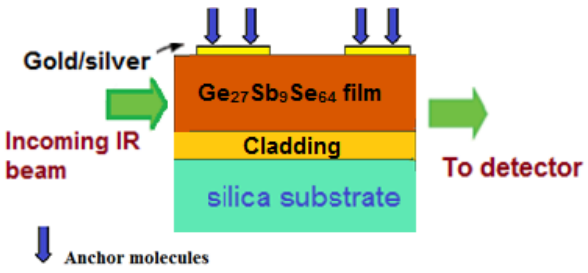

Figure 7.12: *Schematic of evanescent wave based SEIRA.*

The change in composition and thereby the dielectric function of $Ge_{27}Sb_9Se_{64}$ bulk glass after thermal coating may also be the reason for less enhancement in the case of $Ge_{27}Sb_9Se_{64}$ thermal coated substrate. Effective medium theories (EMT) can be employed to model SEIRA enhancement, which use the effective optical property of the heterogeneous system consisting of the organic coating/analyte, the metal film and the host substrate[28,29,30]. The effective property such as conductivity or dielectric function represents an average for entire system i.e, the organic coating/analyte, the metal films and the substrate. Finding the dielectric function for the surface-enhanced sample involves finding the effective dielectric function of the sample comprising host substrate, metal structures and analyte. The main formalisms for effective medium calculations are the Maxwell–Garnet and the Bruggeman methods. According to Maxwell–Garnet model[31]

$$\bar{\varepsilon} = \varepsilon_h \left(\frac{3+2\sum_i f_i \alpha_i}{3-\sum_i f_i \alpha_i} \right) \tag{7.1}$$

where '$\bar{\varepsilon}$' is the average dielectric function, 'ε_h' is the dielectric function of host material in which the particles are embedded, 'f' represents the volume fraction of the inclusions, 'α_i' is the polarizability of the inclusions and 'i' is the index over different metal particles. This is valid only for a low filling fraction ($f \ll 1$) and for the effective dimension. The condition $f \ll 1$ may not be fulfilled for dense metal film and for such films dipole-dipole interaction between the metal particles occurs, and the frequency of the particles are influenced by oscillating dipoles of the neighboring particles. Maxwell-Garnett model cannot be used for such systems where the Bruggeman method is used[32]. This can be expressed in general as

$$\bar{\varepsilon} = \varepsilon_h \left(\frac{3(1-f)+f\alpha'}{3(1-f)-2f\alpha'} \right) \tag{7.2}$$

where α' is the polarizability of the inclusions.

7.7 Microcontact printing

Presence of self-assembled monolayers of anchor molecules over the surface of Ag film protects the surface from other chemical reactions. By utilizing this advantage we can pattern island structures on a continuous silver film by microcontact printing. So island film preparation and anchor layer fabrication can be done altogether by microcontact printing. The procedure of microcontact printing is shown in figure 7.13.

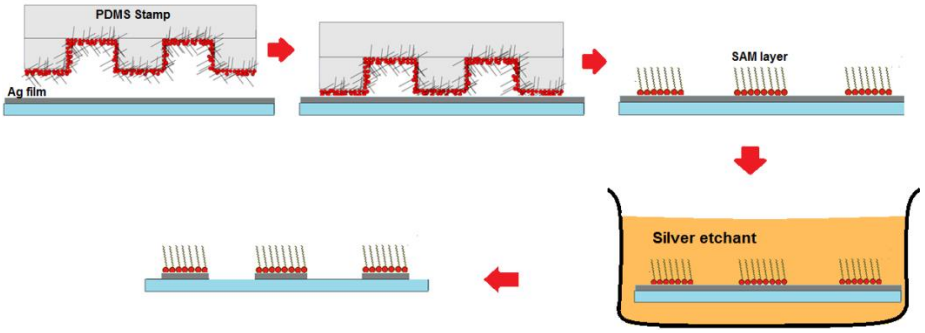

Figure 7.13: *Schematic of the procedure of microcontact printing.*

As discussed in chapter 5, PDMS stamp or mould was prepared by polymerizing it on the patterned surface of compact disc (CD) master. For printing this pattern on the surface of silver film, an ink solution is coated on the patterned surface of PDMS mould. HDT solution prepared in isopropyl alcohol is used as ink. After inking, the stamp is transferred to the surface of the silver film, where the patterned surface of the stamp is allowed to be in contact with the silver surface for 10 to 30 seconds. Then the HDT molecules self-assemble onto the metal, leaving a pattern representative of the stamp. After printing, the samples were immersed in silver etchant. Unprotected silver surface will be etched out while area with self-assembled monolayer (SAM) of HDT will be protected from etchant solution. After etching, sample retains the required pattern. Silver etchant is an aqueous solution of 0.025M sodium thiosulphate ($Na_2S_2O_3$), 0.0025M potassium hexacyanoferrate(III) ($K_3Fe(CN)_6$) and 0.00025M potassium hexacyanoferrate(II) trihydrate ($K_4Fe(CN)_6 \cdot 3H_2O$). This solution is yellow in colour and degrades over time by turning from yellow to light blue. This solution is stored in a refrigerator to prolong its life.

Using microcontact printing, silver film surface is patterned by taking compact disc pattern as master. Silver film is coated on silica substrate in direct deposition arrangement, using thermal evaporation technique. The thickness of the silver film is monitored as 200nm using digital thickness monitor. PDMS stamp is prepared by mixing PDMS elastomer base with curing agent cross-linker at 10:2 ratio and poured over the patterned surface of CD after removing the metallic film over it. It is allowed to polymerize by heating it at 70°C for 45 minutes. Then the stamp is peeled off from the CD master. For printing CD pattern on the surface of silver film, HDT/isopropyl alcohol ink solution is prepared by mixing 0.04ml of molten HDT with 10ml isopropyl alcohol and after thorough shaking 10ml more isopropyl alcohol is added. Since PDMS surface is highly

hydrophobic, in order to wet PDMS surface it is plasma treated for 3minutes. HDT/isopropyl alcohol ink solution is dropped on the patterned surface of PDMS mould and allowed to dry. After drying, the patterned surface of the stamp is allowed to be in contact with the silver surface for 30 seconds. The HDT molecules bind with silver surface by mere contact of inked PDMS with Ag surface. The PDMS stamp is then removed and the patterned silver film is immersed in silver etchant solution.

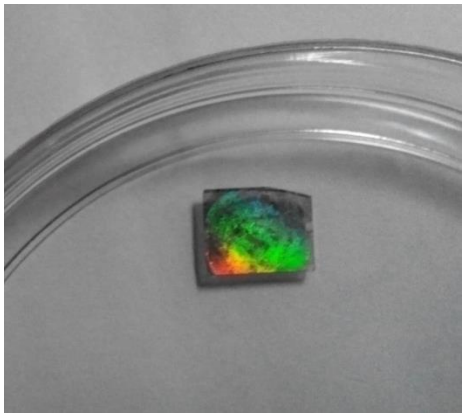

Figure 7.14: *The photograph of patterned silver surface which shows reflecting colours as was observed in CD master.*

Figure 7.14 indicates the photograph of patterned silver on silica substrate which shows reflecting coloures as was observed in CD master. The IR spectra of the patterned silver on silica substrate shows no significant peaks of HDT molecules but broad absorption of silica substrate.

7.8 Summary of findings

- SAM layer of HDT is fabricated on silver island structures, deposited on silica as well as thermally evaporated $Ge_{27}Sb_9Se_{64}$ glass film substrate by oblique angle deposition (OAD). SAM formation on Ag surface is confirmed from IR spectra. The IR absorption of HDT molecules are found to be enhanced with the presence of Ag island structures.
- SAM layer of HDT molecules are fabricated on wet chemically prepared silver nanostructures on $Ge_{27}Sb_9Se_{64}$ glass film substrate and are characterized. The IR absorption of HDT molecules are found to be enhanced with the increase of Ag content.

- Fabrication and characterization of HDT-SAM on purchased Ag nanowire on $Ge_{27}Sb_9Se_{64}$ glass film, $Ge_{27}Sb_9Se_{64}$ bulk glass plate and silica substrate are carried out. Enhancement in IR absorption with the increase in Ag content is observed. SAM contained Ag nanowire on $Ge_{27}Sb_9Se_{64}$ bulk glass plate shows maximum enhancement.
- Anchor layer fabrication and patterning of silver film were carried out altogether by using microcontact printing. CD pattern is achieved on silver film which is coated on silica substrate.

7.9 References

[1]Osawa M, "Surface enhanced Infrared Absorption Spectroscopy in Handbook of Vibrational Spectroscopy M, Chalmers JM and Griffiths P R. Eds." *Chichester: Wiley* 1, no. 785 (2002): 2.

[2]Hartstein A., J. R. Kirtley, and J. C. Tsang. "Enhancement of the infrared absorption from molecular monolayers with thin metal overlayers." *Physical Review Letters* 45, no. 3 (1980): 201.

[3]Reimhult Erik, and Fredrik Höök. "Design of Surface Modifications for Nanoscale Sensor Applications." *Sensors* 15, no. 1 (2015): 1635-1675.

[4]Seelenbinder, John A., and Chris W. Brown. "Comparison of organic self-assembled monolayers as modified substrates for surface-enhanced infrared absorption spectroscopy." *Applied spectroscopy* 56, no. 3 (2002): 295-299.

[5]Seelenbinder, John A., Chris W. Brown, and Daniel W. Urish. "Self-assembled monolayers of thiophenol on gold as a novel substrate for surface-enhanced infrared absorption." *Applied Spectroscopy* 54, no. 3 (2000): 366-370.

[6]Domingo, C., J. V. García-Ramos, S. Sanchez-Cortes, and J. A. Aznarez. "Surface-enhanced infrared absorption of DMIP on gold–germanium substrates coated by self-assembled monolayers." *Journal of molecular structure* 661 (2003): 419-427.

[7]Verger F, Pain T, Nazabal V, Boussard-Plédel C, Bureau B, Colas F, Rinnert E, Boukermab K, Compèreb C, Guilloux-Viry M, Deputier S, Perrinc A, Guind J P, " Surface enhanced infrared absorption (SEIRA) spectroscopy using gold nanoparticles on As_2S_3 glass", *Sensors and Actuators B: Chemical* 175, (2012): 142–148.

[8]Gates Byron D., Qiaobing Xu, Michael Stewart, Declan Ryan, C. Grant Willson, and George M. Whitesides. "New approaches to nanofabrication: molding, printing, and other techniques." *Chemical reviews* 105, no. 4 (2005): 1171-1196.

[9]Nuzzo Ralph G., and David L. Allara. "Adsorption of bifunctional organic disulfides on gold surfaces." *Journal of the American Chemical Society* 105, no. 13 (1983): 4481-4483.

[10]Allara David L., and Ralph G. Nuzzo. "Spontaneously organized molecular assemblies. 1. Formation, dynamics, and physical properties of n-alkanoic acids adsorbed from solution on an oxidized aluminum surface." *Langmuir* 1, no. 1 (1985): 45-52.

[11]Schilardi Patricia L., Patricio Dip, Paula C. dos Santos Claro, Guillermo A. Benítez, Mariano H. Fonticelli, Omar Azzaroni, and Roberto C. Salvarezza. "Electrochemical Deposition onto Self-Assembled Monolayers: New Insights into Micro-and Nanofabrication." *Chemistry-A European Journal* 12, no. 1 (2006): 38-49.

[12]Burshtain Doron, and Daniel Mandler. "The effect of surface attachment on ligand binding: studying the association of Mg^{2+}, Ca^{2+} and Sr^{2+} by 1-thioglycerol and 1,4-dithiothreitol monolayers." *Physical Chemistry Chemical Physics* 8, no. 1 (2006): 158-164.

[13]Love J. Christopher, Lara A. Estroff, Jennah K. Kriebel, Ralph G. Nuzzo, and George M. Whitesides. "Self-assembled monolayers of thiolates on metals as a form of nanotechnology." *Chemical reviews* 105, no. 4 (2005): 1103-1170.

[14]Wilbur James L., and George M. Whitesides. "Self-assembly and self-assembled monolayers in micro-and nanofabrication." In *Nanotechnology*, pp. 331-369. Springer New York, 1999.

[15]Schreiber Frank. "Structure and growth of self-assembling monolayers."*Progress in surface science* 65, no. 5 (2000): 151-257.

[16]Ulman, Abraham. "Formation and structure of self-assembled monolayers."*Chemical reviews* 96, no. 4 (1996): 1533-1554.

[17]Schreiber Frank. "Self-assembled monolayers: from'simple'model systems to biofunctionalized interfaces." *Journal of Physics: Condensed Matter* 16, no. 28 (2004): R881.

[18]Vericat C., M. E. Vela, G. Benitez, P. Carro, and R. C. Salvarezza. "Self-assembled monolayers of thiols and dithiols on gold: new challenges for a well-known system." *Chemical Society Reviews* 39, no. 5 (2010): 1805-1834.

[19]Ito Eisuke, Takayuki Arai, Masahiko Hara, and Jaegeun Noh. "Surface Potential Change Depending on Molecular Orientation of Hexadecanethiol Self-Assembled Monolayers on Au (111)." *Bulletin of the Korean Chemical Society*30, no. 6 (2009): 1309-1312.

[20]Dominik Enders "Surface Enhanced Infrared Absorption on Au Nanoparticle Films for Optical Biosensing", natural science Ph.D thesis.

[21]Kim Chan-Kyu, Gregory M. Marshall, Matthieu Martin, Michel Bisson-Viens, Zbigniew Wasilewski, and Jan J. Dubowski. "Formation dynamics of hexadecanethiol self-assembled monolayers on (001) GaAs observed with photoluminescence and Fourier transform infrared spectroscopies." *Journal of Applied Physics* 106, no. 8 (2009): 083518. infrared spectroscopies, J. Appl. Phys. 106 (2009) 083518.

[22]Marshall Gregory M., Farid Bensebaa, and Jan J. Dubowski. "Observation of surface enhanced IR absorption coefficient in alkanethiol based self-assembled monolayers on GaAs (001)." *Journal of Applied Physics* 105, no. 9 (2009): 094310.

[23]Aryal Santosh, B. K. C. Remant, N. Dharmaraj, Narayan Bhattarai, Chi Hun Kim, and Hak Yong Kim. "Spectroscopic identification of S-Au interaction in cysteine capped gold nanoparticles." *Spectrochimica Acta Part A: Molecular and Biomolecular Spectroscopy* 63, no. 1 (2006): 160-163.

[24]Enders Dominik, Swen Rupp, Alexander Küller, and Annemarie Pucci. "Surface enhanced infrared absorption on Au nanoparticle films deposited on SiO_2/Si for optical biosensing: Detection of the antibody–antigen reaction."*Surface science* 600, no. 23 (2006): L305-L308.

[25]Kamnev Alexander A., Lev A. Dykman, Petros A. Tarantilis, and Moschos G. Polissiou. "Spectroimmunochemistry using colloidal gold bioconjugates."*Bioscience reports* 22, no. 5-6 (2002): 541-547.

[26]Leopold Nicolae, and Bernhard Lendl. "A new method for fast preparation of highly surface-enhanced Raman scattering (SERS) active silver colloids at room temperature by reduction of silver nitrate with hydroxylamine hydrochloride." *The Journal of Physical Chemistry B* 107, no. 24 (2003): 5723-5727.

[27]Nguyen Kien Cuong. "Quantitative analysis of COOH-terminated alkanethiol SAMs on gold nanoparticle surfaces." *Advances in Natural Sciences: Nanoscience and Nanotechnology* 3, no. 4 (2012): 045008.

[28]Osawa Masatoshi, Ken-Ichi Ataka, Katsumasa Yoshii, and Yuji Nishikawa. "Surface-enhanced infrared spectroscopy: the origin of the absorption enhancement and band selection rule in the infrared spectra of molecules adsorbed on fine metal particles." *Applied spectroscopy* 47, no. 9 (1993): 1497-1502.

[29]Albrecht M. Grant, and J. Alan Creighton. "Anomalously intense Raman spectra of pyridine at a silver electrode." *Journal of the American Chemical Society* 99, no. 15 (1977): 5215-5217.

[30]Johnson Eric, and Ricardo Aroca. "Surface-enhanced infrared spectroscopy of monolayers." *The Journal of Physical Chemistry* 99, no. 23 (1995): 9325-9330.

[31]Norrman S., T. Andersson, C. G. Granqvist, and O. Hunderi. "Optical properties of discontinuous gold films." *Physical Review B* 18, no. 2 (1978): 674.

[32]Fujiwara H., Joohyun Koh, P. I. Rovira, and R. W. Collins. "Assessment of effective-medium theories in the analysis of nucleation and microscopic surface roughness evolution for semiconductor thin films." *Physical Review B*61, no. 16 (2000): 10832.

Chapter 8

Conclusion and future research prospects

This chapter deals with the main conclusions of the work presented in this thesis. A brief sketch of future research prospects is also mentioned in this chapter.

This work is focused on the design and step by step fabrication and characterization of a prototype infrared (IR) sensor with chalcogenide glass (ChGs) as the sensor platform.

8.1 Major conclusions

- Four different compositions of Germanium based selenide glasses $Ge_{20}Se_{80}$, $Ge_{27}Se_{73}$, $Ge_{27}Sb_9Se_{64}$ and $Ge_{27}Ga_9Se_{64}$ were prepared by melt quenching method and their physical, structural, thermal and optical characterization were conducted. A composition dependent variation is observed in bulk glass properties. The details of bulk glass preparation, characterization and observations with valid arguments are discussed in chapter 3. For the realization of an IR based sensor, the bulk chalcogenide glass should be converted to thin film form. Therefore solution processed and thermal evaporated thin films of different compositions of chalcogenide glass were prepared.
- Solution processing of above four chalcogenide glass compositions and a detailed structural, compositional and optical evaluation of the processed colloidal solution were presented in chapter 4. The formation of nanoclusters after dissolution and the dependence of cluster size with concentration were confirmed from different analysis. Various characterizations carried out on nanocolloids confirmed a concentration dependent variation in linear and nonlinear optical properties of all

compositions of nanocolloids. Photo irradiation experiments were carried out using pulsed and continuous lasers of different wavelengths and variations in its structural and optical properties were studied using different techniques.

- A detailed discussion on fabrication and structural and optical characterizations of all selected thin films compositions of chalcogenide glasses are given in chapter 5. Solution derived thin films of $Ge_{27}Sb_9Se_{64}$ glass were fabricated and characterized. Even though the structural, compositional and optical analysis on solution derived thin films of $Ge_{27}Sb_9Se_{64}$ glass requires some improvement, solution processing pave way to a new technology for the development of waveguide structures. Array of ridge waveguides were fabricated on thermally evaporated $Ge_{27}Sb_9Se_{64}$ glass thin films by capillary force lithography (CFL) technique which opens up the opportunity for the fabrication of waveguide arrays in IR based sensor.
- Since 'metal island structures' on the top of the chalcogenide glass film benefit for bio-functionalization of the core layer and also help to enhance the sensitivity by surface enhanced infrared absorption (SEIRA), silver island films of different morphology were prepared and characterized. Silver island films prepared by oblique angle deposition technique results in the formation of silver nanostructures on the substrate for which average size can be tuned by changing the polar angle. Silver nanostructures were also prepared by wet chemical methods. Analysis on the size and morphology of wet chemically prepared silver nanoparticles were carried out using different techniques.
- Self-assembled monolayers (SAM) of anchor molecules on the surface of silver island films on different substrates were prepared and characterized. The binding of anchor molecules is confirmed from IR spectra. SAM layer fabricated on the surface of Ag island structures with different morphology shows enhancement in IR absorption and the enhancement is found to be increased with the increase in Ag content. SEIRA studies using chalcogenide glass as host substrate reveal that they are promising host material. Microcontact printing is employed for the fabrication of silver patterns and anchor layer and it was found to be an effective technique to pattern the silver surface.

In a nutshell, this research work confirms that the selected glasses are promising materials for IR based sensing because of their favorable properties like high IR transparency, high refractive index, processibility into thin film form, chemical compatibility for adhesion of silver nanoparticles and thin

films etc. The presence of silver island structures shows enhanced infrared absorption and helps for bio-functionalization. For realizing the final goal- a prototype IR based sensor, binding of biological functional molecules on the top of anchor layer should be achieved.

8.2 Future research prospects

Sensing scheme based on infrared spectroscopy is a forthcoming technology because of its simplicity, reliability, and fast response, cost-effective and non-destructive nature etc. Use of metallic nanoparticles in association with a good IR transparent sensing substrate, enhances the sensitivity. The present work evidences that

- Chalcogenide glasses are promising materials for IR based sensing applications.
- Metals like silver shows a good adsorption to chalcogenide glass substrates.
- Fabrication of self-assembled monolayer of anchor molecules on silver is quiet easy.
- The presence of silver island structures shows enhanced infrared absorption and helps in IR based sensing.

The immediate future work for the realization of a prototype IR based sensor is that

- Binding of biological functional molecules like DNA, antibody, etc. on the top of anchor layer. For that, anchor layer should be modified in such a way that it possess functional groups that can react with biological functional molecules (DNA, antibody, etc.).

The work can be extended with

- A detailed study on solution processed film fabrication i.e., optimization of spin coating condition, baking parameters etc. in order to prepare a solvent free thin film that can be effectively utilized as a promising sensing substrate. Solution processing enables large area deposition and other patterning techniques such as mold casting, ink jet printing etc. Therefore investigations on different compositions of solution processed thin films open a new set of opportunities for the fabrication of chalcogenide glass waveguide structures.

- Waveguide array fabrication with suitable cladding and core materials as shown in figure 8.1 and optimization of different parameters like width, thickness, length etc. in order to guide IR waves through these structures.

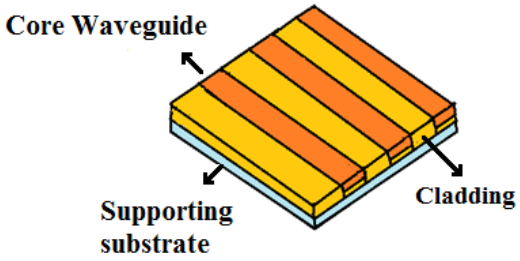

Figure 8.2.1: *Schematic of waveguide array with cladding and guiding core.*

Fabrication of grooves on the top of the polished surface of the bulk glass plate by using high power laser and spin coating high refractive index chalcogenide glass solution on the top of the grooved surface gives new set of wave guide arrays for IR based sensors.

- Optimization of different parameters of metal island structures such as, size, shape, density etc. in order to obtain maximum SEIRA effect for different chemical species adsorbed on the metal surface.
- SEIRA study using different metals on thiols containing deuterium-carbon (C-D) bonds instead of C-H bonds to isolate the 'absorption signatures' of ascorbates from other organic moieties.
- Finally integration of the designed sensor unit with suitable miniaturized IR source and detector in order to achieve a 'sensor-on-a-chip' all-integrated microphotonic technology.

Appendix

APPLIED PHYSICS LETTERS **102**, 031115 (2013)

Impact of intermediate localized states on nonlinear optical absorption of Ga-Ge-Se nanocolloidal solutions

Indu Sebastian,[a] S. Divya, V. P. N. Nampoori, P. Radhakrishnan, and Sheenu Thomas
International School of Photonics, Cochin University of Science and Technology. Cochin, Kerala, India

(Received 20 August 2012; accepted 11 January 2013; published online 25 January 2013)

We present the linear and nonlinear optical studies on nanocolloidal solutions of $Ga_9Ge_{27}Se_{64}$ glass with varying concentrations. Optical bandgap of the material is found to vary with respect to the concentration of the solute in the solution. An intermediate peak in the band tail of the absorption spectra is observed due to the presence of energy band in the forbidden gap. The existence of fluorescence emission confirms the above argument. Nonlinear absorption is studied using open aperture Z-scan technique. The mechanism behind nonlinear absorption is predicted as two photon as well as two step photon absorption. Nonlinearity increases with decrease in optical bandgap which in turn depends on the concentration of the nanocolloidal solutions. © *2013 American Institute of Physics*. [http://dx.doi.org/10.1063/1.4789436]

Chalcogenide glasses are special amorphous semiconductors with high infrared transparency, low phonon energy, low glass transition temperature, high optical nonlinearity, and are good hosts for rare earths. In general, chalcogenide glasses present the highest third order nonlinear optical properties among the different families of glasses. The large optical nonlinearity is mainly due to the presence of the localized states in the gap, as well as the high lone pair electron concentration.[1,2] This high concentration of readily polarizable lone pair electrons (two in each chalcogen atom) leads to a large linear and nonlinear dielectric susceptibility. Materials with large n_2 and β are desirable for devices like all-optical switches and intensity stabilizers respectively.[3]

Studies on nonlinear refractive indices and nonlinear absorption coefficients of chalcogenide bulk glasses with different compositions and thin films deposited using physical vapour deposition (PVD) techniques such as thermal evaporation, sputtering, or pulsed laser deposition are available in literature.[4–7] The PVD techniques are generally limited to two-dimensional surfaces, and require high vacuum. Thermal evaporation method gives films with different stoichiometry from that of parent glass due to differential volatility in multi-component materials. Chalcogenide glasses when dissolved in organic solvents allow new and simple deposition routes such as spin coating technique.[8,9] Dissolution of chalcogenide glasses is a low cost process and it results in the formation of clusters with dimensions of several nanometers which retains the bulk glass stoichiometry. Bandgap of these nanoclusters varies with the size, which in turn depends upon the concentration of the solution.[8]

The nonlinear optical studies on various nanocolloidal solutions are being carried out in our laboratory for the past few years.[10] In this paper, we focus on the synthesis and third order nonlinear optical characterization of nanocolloidal solutions of Ga-Ge-Se glass system using the Z-scan technique. We have correlated the nonlinear optical properties and the band structures by analysing the optical absorption and fluorescence spectra. We have also evaluated their potentialities for optical limiting application. Nanocolloidal solutions of suitable solute concentration predict their application as optical limiters for protecting sensitive devices from intense optical radiations.

Chalcogenide glass solutions exhibit reverse saturable absorption (RSA), in which the excited state absorption cross section is higher than the ground state absorption cross section. The origin of the high third order non-linearity predicted from Z-scan calculation is attributed to resonant two photon absorption (TPA) as well as cascaded two photon absorption, which is confirmed by the bandgap analysis. In the present study, we have undertaken studies on $Ga_9Ge_{27}Se_{64}$ glass which were prepared by conventional melt quenching method. High purity materials were used for the glass preparation. The samples were prepared by melting appropriate weight percentage of elemental form of Se, Ge, Ga (Sigma Aldrich, 5N purity) in an evacuated fused quartz ampoule at 1000 °C for 24 h for thorough mixing and homogenization of the melt and then rapidly quenched in ice cold water. X-ray diffraction (XRD) (Bruker AXS D8 Advance X-ray Diffractometer) studies on bulk glass confirmed the absence of long range order. Energy dispersive X-ray spectroscopy (JEOL Model JED-2300) revealed that the bulk glass formed has the same expected composition. Nanocolloidal chalcogenide glass solutions of three different concentrations, C1 = 1.45 mg/ml, C2 = 0.72 mg/ml, and C3 = 0.54 mg/ml were prepared by dissolving it in n-butyl amine. Optical absorption measurements of both bulk and solutions were carried out using a JascoV-570 UV/VIS/IR spectrophotometer. The fluorescence studies were done using flourimeter (Varian). Nonlinear absorption coefficient (ß) and optical limiting threshold of the three C1, C2, and C3 concentrations were calculated using open aperture Z-scan technique comprising of Nd-YAG laser (532 nm, 7 ns, 10 Hz). 1 ml of sample C3 was exposed to laser radiation at 400 MW/cm^2 for 45 min. Scanning electron microscope (SEM) (JEOL Model JSM-6390LV) images and XRD analysis of spin coated C3 and laser exposed C3 were taken to check for any structural change after laser exposure.

The absorption spectra and the bandgaps calculated for different concentrations are presented in Figures 1(a) and 1(b).

[a]Electronic mail: indusebastian@gmail.com.

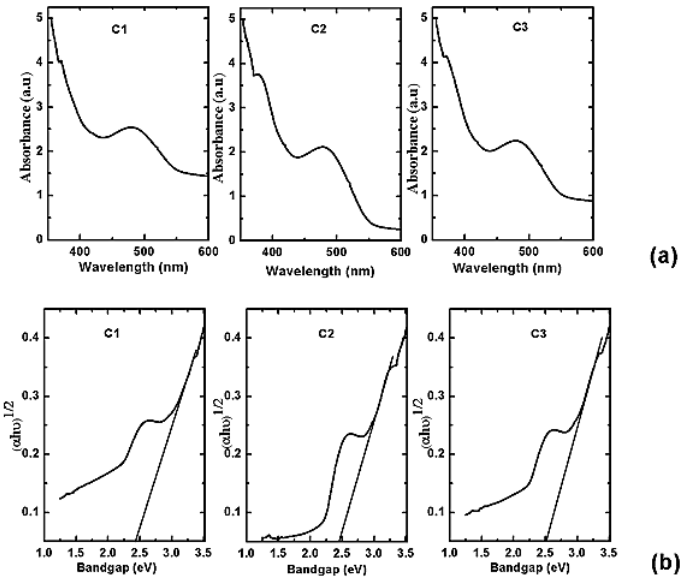

FIG. 1. (a) As concentration increases, absorption corresponding to different indirect transitions shifts to lower energy side. The absorption peak near 480 nm is due to the occurrence of intermediate energy states in the bandgap. (b) Variation of bandgaps with concentration. Bandgap is enhanced with decrease in solute concentration. The broadening in the band tail is expected as due to the presence of high density localized states in the forbidden energy gap.

The absorption edge of the chalcogenide bulk glass is located in the near IR range, whereas for solutions it is located in the visible range. The present system of Ga-Ge-Se colloids obeys indirect transition and the relation between the optical gap, optical absorption coefficient α, and the energy $h\nu$ of the incident photon is given by[11]

$$\alpha h\nu = B(h\nu - Eg)^2. \quad (1)$$

B, the slope of the Tauc edge is known as band tail parameter. To evaluate bandgaps, the variation of $(\alpha h\nu)^{1/2}$ versus photon energy $h\nu$ is plotted and the optical energy gap Eg has been determined from the intercepts of extrapolations to zero with the photon energy axis $(\alpha h\nu)^{1/2} \rightarrow 0$ (i.e., Tauc extrapolation) as in Figure 1(b). As the solute concentration in the nanocolloids decreases, a blue shift in the band edge is found because of decreasing cluster size. The dependence of the bandgap with cluster size was reported by Kohoutek *et al.*[8] The bandgaps obtained for C1, C2, and C3 samples are 2.4 eV, 2.47 eV, and 2.52 eV, respectively.

The absorption spectra and hence the bandgap of the nanocolloidal solutions observed were not sharp. The band broadening and occurrence of peak (around 480 nm) in the band tail are explained using the model proposed by Davis and Mott.[12] According to them, the geometrical disorder such as lack of long range order, forms a range of localized states at the band edges while neutral band dangling bonds give rise to a well separated narrow band of localized states at the centre of the gap where Fermi energy (E_F) lies. The defects states due to charge dangling[13] bonds (proportional to the D+ and D− centres and appears as two narrow bands) are located in the forbidden gap around the E_F level. A schematic representation of density of states corresponding to this model is presented in Figure 2.

The excitation and emission spectra of nanocolloidal solution of concentration C3 are given in Figure 3. The excitation spectrum consists of a broad peak around 480 nm and the emission peak is at about 580 nm. The existence of fluorescence emission and a peak in the absorption spectrum for 480 nm implies the presence of intermediate energy band in the forbidden energy gap.[14]

The nonlinear optical characterization of the samples was carried out using the *Z*-scan technique at 532 nm. The samples to be investigated were translated through the focal point of a lens of focal length 20 cm. The beam waist radius ω_0 was estimated to be 35.4 μm. The Rayleigh length $Z_0 = \pi\omega_0^2/\lambda$ was calculated to be 7.4 mm. The samples were taken in 1 mm cuvette which is much lesser than Z_0; therefore, the essential prerequisite for z-scan experiment is satisfied.[14]

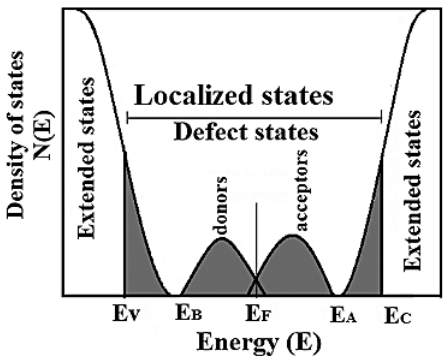

FIG. 2. Schematic density of states for amorphous semiconductors.

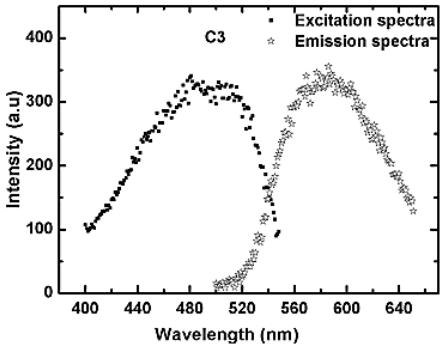

FIG. 3. Excitation and emission spectra of sample C3. The excitation spectrum which consists of abroad peak around 480 nm shows the presence of localized states.

The open-aperture curve exhibits a normalized transmittance valley at the focal point, indicating the presence of RSA in the nanocolloidal solutions.

The normalized transmittance for TPA in the open-aperture condition is given by[14]

$$T(z,\ s=1)=\frac{1}{\sqrt{\pi}q_0(z,0)}\int_{-\infty}^{\infty}\ln\left[1+q_0(z,0)e^{-\tau^2}\right]d\tau, \quad (2)$$

where

$$q_0(z,0)=\beta I_0 L_{eff}/(1+Z^2/Z_0^2). \quad (3)$$

Here, I_0 is the laser intensity in the focal plane, ß is the nonlinear optical absorption coefficient, L_{eff} is the effective thickness with linear absorption coefficient α.

L_{eff} is given by

$$L_{eff}=(1-e^{-\alpha l})/\alpha. \quad (4)$$

The open aperture Z scan plot for different concentrations is depicted in Figure 4. The fits of Eq. (2) to experimental data are shown as solid curves. From the fit, we can confirm that the basic mechanism involved in the nonlinear absorption of nanocolloidal solutions of $Ga_9Ge_{27}Se_{64}$ glass is TPA process because the photon energy of the 532 nm laser is within the range $E_g < 2h\upsilon < 2E_g$, where $h\upsilon = 2.33$ eV.[14] Since the energy

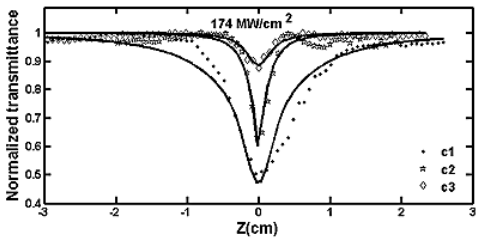

FIG. 4. Normalized transmittance as a function of the position for different concentrations in the open aperture scheme at 532 nm with a laser power of 174 MW/cm^2. The solid line shows the theoretical fit.

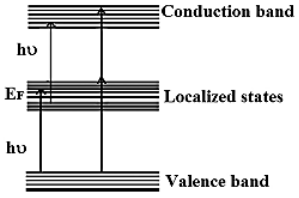

FIG. 5. Schematic of two step photon absorption as well as resonant two photon absorption in nanocolloids.

corresponding to 532 nm ($h\nu = 2.33$ eV) lies in "band tail peak," absorption of "$h\nu$" might have resulted to the excitation of the carriers to the localized state in the gap. From this energy level, the carriers can go to the conduction band by absorbing another photon. Instead of a virtual state, these localized energy bands may act as a resonant intermediate level which leads to a two-step cascade photon[15] absorption. Probability for resonant two photon absorption; that is, simultaneous absorption of two photons is also there. Schematic representation of two step photon absorption as well as resonant two photon absorption in nanocolloidal solution is given in Figure 5.

The nonlinear absorption coefficient (ß) calculated from the above fits shows a dependence on the size and concentration of the nano clusters.

Nonlinear absorption of chalcogenide glass colloids is found to increase with decrease in optical bandgaps as reported.[10] The optical bandgap of the material could be tuned by varying the chalcogenide glass concentration in butyl amine. Therefore, for greater nonlinearity, large cluster size is required.

The measured values of optical bandgap for various concentrations and nonlinear absorption coefficient at wavelength of 532 nm for input laser power density of 174 MW/cm^2, are given in the Table I. The experimental data show that ß value increases with decreasing bandgap. This is due to the increased optical nonlinear interaction between the radiations and the sample which increases with cluster size resulting from high concentration. Thus, cluster size has a significant effect on limiting performance. With a small increase in the bandgap, a significant increase in the nonlinear absorption is observed. This can be explained as due to the fact that with the increase in solute concentration, the number of particles in the solvent increases which results to a rise in the multiple scattering from the nanoclusters, than with solutions with less solute contents. This rise in multiple scattering leads to a large effective interaction length which in turn results to an enhancement in nonlinear absorption.

TABLE I. Variation of nonlinear absorption coefficient with concentration at 174 MW/cm^2.

Sample	Optical bandgap (E_g) (eV)	Nonlinear absorption coefficient (ß) (cm/GW)	Optical limiting threshold (MW/cm^2)
c1	2.40	91.1	60
c2	2.47	79.6	150
c3	2.52	23.3	160

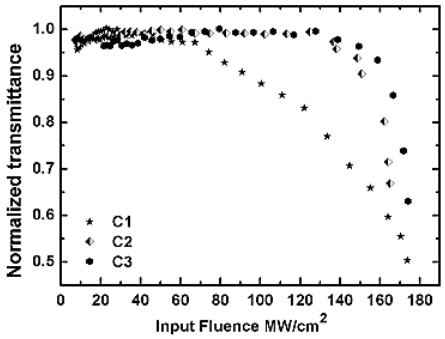

FIG. 6. Optical limiting response of C1, C2, and C3 at 532 nm at an input power density of 174 MW/cm^2. The optical limiting threshold is found to decrease with concentration.

Figure 6 illustrates the optical limiting response of samples at an input laser intensity of 174 MW/cm^2. The optical limiting threshold is seen to decrease with increase in cluster size. The optical limiting threshold (onset optical limiting) is the corresponding fluence value at which the deviation from linearity in the normalized transmittance is observed. The limiting threshold obtained from Figure 6 is given in the Table I.

Figures 7(a) and 7(b) show X-ray diffraction graph of spin coated C3 and laser exposed C3 nanocolloids, respectively. Lack of any sharp peak in the XRD pattern of the sample after laser exposure elucidates that the tendency to crystallize after laser exposure is less. The SEM images of unexposed and laser exposed C3 displayed in Figures 8(a) and 8(b), respectively, show some agglomeration but no structural change is observed after laser irradiation. The average cluster size measured from the SEM image is around 100 nm. But, the actual cluster size of the solute in solution will be much less than the grain size of the spin coated thin films used for SEM analysis as reported by Kohoutek *et al.*[8] using dynamic light scattering method. The increase in the cluster size in the thin films compared to that in solution is due to the agglomeration of chalcogenide clusters during solvent evaporation from the film structure at the time of spin coating.

To conclude, $Ge_{27}Ga_9Se_{64}$ glass and its nanocolloidal solutions of different concentrations were synthesized. Linear and nonlinear optical properties were studied using optical absorption, fluorescence spectroscopy, and open aperture z-scan technique. Structural characterizations were done using XRD and SEM. The energy level of the dispersed chalcogenide nanoclusters was found to be broad and was tunable with concentration. Nonlinear optical response studies using nano second laser show RSA explained through two step photon absorption. The energy gaps increase with decrease in concentration. The existence of peak in the band tail and broad absorption is due to localized defect state absorption. Fluorescence spectra from the intermediate state confirm this result. The nonlinear absorption in the nano colloidal solution can be attributed to the phenomenon of two photon absorption combined with two step cascade photon absorption. The localized state located in the forbidden energy gap acts as an intermediate state, from whereon the second photon gets excited. The measured ß values were found to enhance with decrease in optical energy gap. The optical limiting threshold calculated for each concentration reveals that the solution with high solute concentration is better optical limiters. Analysis using XRD and SEM reveals

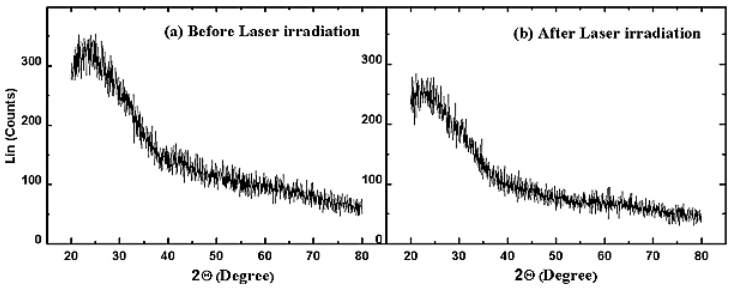

FIG. 7. (a) and (b) XRD of spin coated nanocolloidal solution "C3" before and after laser exposure showing tendency for crystallization after laser exposure is less.

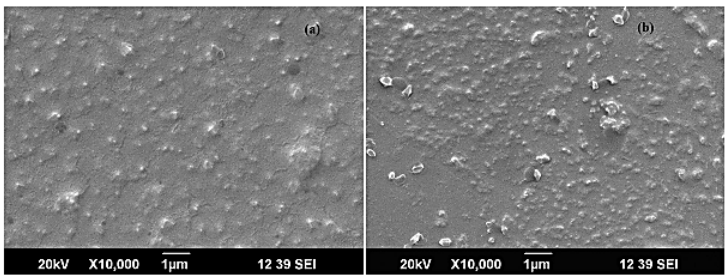

FIG. 8. (a) and (b) SEM image of unexposed and laser exposed nanocolloid.

that there is no structural change after high power laser exposure. The studies show that these materials are promising candidates for optoelectronic devices.

Authors wish to acknowledge KSCSTE for the financial help through research project and SAIF-STIC for SEM and XRD analysis.

[1]V. Babin, M. Popescu, M. Ciobanu, N. D. Nicolae, C. Talianu, and G. Ciuciu, J. Mater. Sci.: Mater. Electron. **17**, 307–314 (2006).
[2]C. Quémard, F. Smektala, V. Couderc, A. Barthélémy, and J. Lucas, J. Phys. Chem. Solids **62**, 1435–1440 (2001).
[3]T. Kamiya and M. Tsuchiya, Jpn. J. Appl. Phys., Part 1 **44**, 5875 (2005).
[4]K. Fedus, G. Boudeds, Q. Coulombier, J. Troles, and X. H. Zhang, J. Appl. Phys. **107**, 023108 (2010).
[5]K. Ogusu, J. Yamasaki, and S. Maeda, Opt. Lett. **29**, 265 (2004).
[6]J. Troles, F. Smektala, G. Boudebs, A. Monteil, B. Bureau, and J. Lucas, Opt. Mater. **25**, 231–237 (2004).
[7]A. Zakery and S. R. Elliott, *Optical Nonlinearities in Chalcogenide Glasses and Their Applications* (Springer-Verlag, Berlin, 2007).
[8]T. Kohoutek, T. Wagner, and M. Frumar, J. Appl. Phys. **103**, 063511 (2008).
[9]S. Song, N. Carlie, J. Boudies, L. Petit, K. Richardson, and C. B. Arnold, J. Non-Cryst. Solids **355**, 2272–2278 (2009).
[10]R. Tintu, V. P. N. Nampoori, P. Radhakrishnan, and S. Thomas, J. Appl. Phys. **108**, 073525 (2010).
[11]D. L. Wood and J. Tauc, J. Phys. Rev. B **5**, 3144 (1972).
[12]E. A. Davis and N. F. Mott, Philos. Mag. **22**, 903–927 (1970).
[13]R. A. Street and N. F. Mott, Phys. Rev. Lett. **35**, 1293–1296 (1975).
[14]M. Sheik-Bahae, A. A. Said, T. H. Wei, D. J. Hagan, and E. W. Van Stryland, IEEE J. Quantum Electron. **26**, 760–769 (1990).
[15]K. Tanaka, J. Mater. Sci. **16**, 633–643 (2005).

JOURNAL OF APPLIED PHYSICS **114**, 053102 (2013)

Concentration tuned bandgap and corresponding nonlinear refractive index dispersion in Ga-Ge-Se nanocolloids

Indu Sebastian,[a] S. Mathew, V. P. N. Nampoori, P. Radhakrishnan, and Sheenu Thomas
International School of Photonics, Cochin University of Science and Technology, Cochin, Kerala, India

(Received 18 April 2013; accepted 15 July 2013; published online 1 August 2013)

Solution-processing of chalcogenide glass materials has attracted attention for the fabrication of photonic devices. We have carried out linear and nonlinear optical studies on $Ga_9Ge_{27}Se_{64}$ nanocolloidal solutions with varying concentrations and witnessed the opportunity for engineering the optical properties of the material by simply changing the concentration of solute in the solvent. An enhancement of bandgap, deterioration, and blue shift in the band tail states with decrease in concentration were observed from the absorption spectra. Open and closed aperture Z-scan studies reveal tunability of nonlinear absorption coefficient (β) and nonlinear refractive index (n_2). As the bandgap approaches the one photon absorption edge, the material shows very large negative nonlinear refraction and also "two step photon absorption" due to the presence of intermediate tail states. The radial phase shift ($\Delta\varphi_0$) induced after travelling through the nanocolloidal solution with respect to bandgap is plotted and we predict that the variation of $\Delta\varphi_0$ is governed by a quadratic polynomial of Eg. © *2013 AIP Publishing LLC*. [http://dx.doi.org/10.1063/1.4817176]

I. INTRODUCTION

Since Photonics is growing towards miniaturized optical functionality, aiming to integrate multiple components onto the same chip—the relevance of researches on nanostructured chalcogenides are now gaining attention among photonic society. Nanophotonic devices typically make use of a high refractive index contrast in order to achieve tight optical confinement, allowing wavelength-scale resonators and waveguide bends.

Chalcogenide glasses are known to manifest a variety of photoinduced phenomena[1,2] due to the flexibility of its atomic structure and presence of defect states. It is known that the localized states[3,4] in the band edge and in the bandgap are responsible for many optical and electrical properties in the noncrystalline semiconductors. Hence engineering the defect state-density and energy helps to tune both linear and nonlinear optical properties in chalcogenide glasses. Chalcogenide glasses when dissolved in organic solvents allow new and simple deposition routes such as spin coating technique.[5,6] Dissolution of chalcogenide glasses is a low cost process and it results in the formation of clusters with dimensions of several nanometers which retain the bulk glass stoichiometry. Bandgap of these nanoclusters varies with the size, which in turn depends on the concentration of the solution.[7] So far, there have been reports on device application of solution processing of inverse opal photonic crystal,[8] integrated single-mode mid-infrared waveguides,[9] etc. The determination of optical nonlinearities is of great relevance to the practical application in optical limiting devices, all optical switching elements (AOS), optic fibers, waveguides, etc. as it provides awareness about different nonlinear optical phenomena such as intensity dependent absorption, intensity dependent refractive index, self-focusing damage, etc. Material with large nonlinear refractive index (n_2) and low nonlinear absorption coefficient (β) is desirable in various device engineering such as optical switches, etc.[10,11] The major limitation of chalcogenide glass as an optical switch is the existence of band tail states which leads to two step photon absorption[12] resulting in the enhancement of β.

Here, we present third order nonlinear optical characterization of nanocolloidal solutions of Ga-Ge-Se glass system using the Z-scan technique at 532 nm. We observed a varying negative nonlinear refraction and nonlinear absorption with respect to the change in concentration of nanoclusters, which is explained in terms of the impact of bandgap resonant effects and variation in the intermediate defect states, respectively. These phenomena will help to tune the optical property of the nanoclusters to our desire.

II. EXPERIMENTAL

In the present work, we have undertaken studies on $Ga_9Ge_{27}Se_{64}$ glass which were prepared by conventional melt quenching method. High purity materials were used for the glass preparation. The samples were prepared by melting appropriate weight percentage of elemental form of Se, Ge, Ga (Sigma Aldrich, 5N purity) in an evacuated fused quartz ampoule at 1000 °C for 24 h for thorough mixing and homogenization of the melt and then rapidly quenched in ice cold water. X-ray diffraction (XRD) (Bruker AXS D8 Advance X-ray Diffractometer) studies confirmed its amorphous nature. Energy dispersive X-ray spectroscopy (JEOL Model JED-2300) revealed that the bulk glass formed has the same expected composition. Nanocolloidal chalcogenide glass solutions of five different concentrations, C1 = 0.30 mg/ml, C2 = 0.25 mg/ml, C3 = 0.2 mg/ml, C4 = 0.11 mg/ml, and C5 = 0.096 mg/ml were prepared by dissolving it in n-butyl amine. Optical absorption measurements of both bulk and

[a]Electronic mail: indusebastian@gmail.com

solutions were carried out using a JascoV-570 UV/VIS/IR spectrophotometer. Nonlinear absorption and refraction studies of above concentrations were carried out using open and closed aperture Z-scan technique employing an Nd-YAG Laser (532 nm, 7 ns, 10 Hz).

III. RESULTS AND DISCUSSIONS

Figure 1(a) shows absorption spectrum of bulk glass and Figure 1(b) is the corresponding spectra of nanocolloidal solutions of different concentrations. The absorption edge of bulk glass extends up to near infrared region and is not transparent to visible wave lengths, whereas in nanocolloidal solutions a concentration dependent shift for band edge in visible region is observed. As the concentration of bulk glass in the solution decreases, it is observed that the band edge is blue shifted in the visible region of electromagnetic spectrum. There exists a peak, centred about 480 nm in the band tail of all samples including the bulk due the presence of defect states in the bandgap. These defects are responsible for various desirable (photo-induced phenomena,[1] nonlinear absorption applicable for optical limiters,[13] etc.) and undesirable (nonlinear two-step absorption[12] in optical switches, etc.) optical phenomena in chalcogenide glasses. From the absorption spectra (Figure 1(b)), it is clear that there exists a concentration dependent blue shift and diminishment in the density of defect states while varying the samples from bulk to nanocolloids with least concentration. Figure 2 shows the photograph of c1, c2, c3, c4, and c5 nanocolloidal solutions in decreasing order of their concentrations. A corresponding blue shifted and faded luminescence from the intermediate defect states is obvious in this photograph.

The defects in chalcogenide glasses arise due to the unique property of chalcogens such that the presence of lone pair (LP) states which lies in between the bonding states (σ) and antibonding states (σ^*). In solid, these atomic energy states become broad and form energy band. Since the "σ" energy band in chalcogen lies far below, the lone pair energy band acts as valance band. In Ge atom, the fourfold coordination undergoes sp^3 hybridization and split into occupied "bonding (σ)" and "unoccupied antibonding" (σ^*) bands. If we alloy these two to a vitreous compound, the coordination environment will be adjusted to satisfy valance requirement of each atom and results in the formation of an inorganic Se-Se, Ge-Se polymer network. The LP band of Se fall near the gap of Ge, therefore, the presence of excessive Se-Se bonds leads to the delocalization of LP band thus the resultant bandgap in chalcogenide glass becomes narrower which is clear from bulk glass absorption spectrum. The situation is demonstrated in Figure 3. The presence of Gallium (Ga) in this material result in further broadening of valence band tail since the LP electrons adjacent to the electropositive atoms will have higher energy than that of electronegative atom.[3] When the particle size decreases, both the conduction and valence bands shifts away from each other and results in the increase the bandgap. As the solute concentration in the solvent decreases, size of the nanoclusters also decreases as reported by Kohoutek *et al.*[5] and it leads to a blue shift in the band edge. This "size effect" affects the fluorescence emission such that the emission wavelength also is blue shifted and it is clear from the photograph (Figure 2). During dissolution, the continuous network of bulk glass solute is fragmented[14] and therefore the number of Se-Se bonds gets decreased. This leads to the localization of the LP band in the gap and its density diminishes with the decrease in the cluster size and this explains the reduction in defect state density with the decrease in cluster size.

The nonlinear optical characterization of the samples was carried out using the Z-scan technique at 532 nm. Figure 4(a) gives the open aperture z-scan traces of nanocolloids of different concentrations at a typical fluence of 320 MW/cm^2. The open-aperture Z-scan curve exhibits a normalized transmittance valley, indicating reverse saturable absorption in the colloids. The data were analysed using the procedure described by Bahae *et al.*[15] The nonlinear absorption coefficient is obtained by fitting the experimental z-scan plot to

$$T(z,\ s=1) = \frac{1}{\sqrt{\pi}q_0(z,0)}\int_{-\infty}^{\infty} ln[1+q_0(z,0)e^{-\tau^2}]d\tau, \quad (1)$$

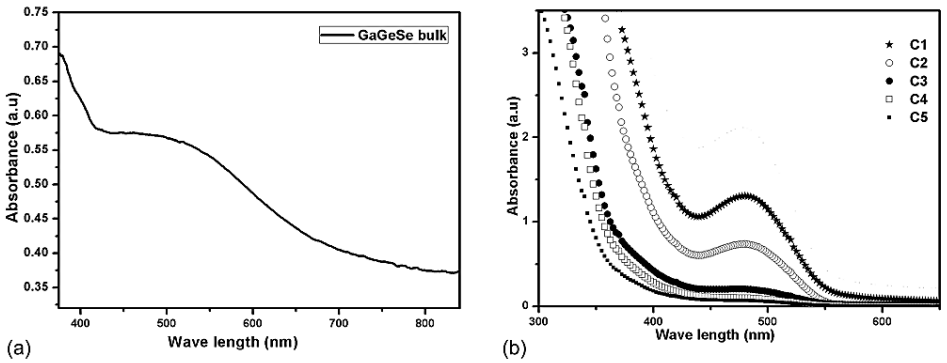

FIG. 1. Absorption spectra of bulk glass showing band edge extends up to NIR region. (b) Absorption spectra of nanocolloidal solutions of various concentrations.

FIG. 2. Photograph of C1, C2, C3, C4, and C5 nanocolloids showing quantum size effect.

where

$$q_0(z,0) = \frac{\beta\, I_0\, L_{eff}}{(1+\frac{z^2}{z_0^2})}. \quad (2)$$

Here I_0 is the laser intensity in the focal plane, ß is the nonlinear optical absorption coefficient, L_{eff} is the effective thickness with linear absorption coefficient α.

L_{eff} is given by

$$L_{eff} = \frac{(1-e^{-\alpha l})}{\alpha}. \quad (3)$$

Figure 4(b) gives the closed-aperture z-scan traces of nanocolloids of different concentrations at a fluence of 320 MW/cm^2. The closed-aperture curve exhibited a peak to-valley shape, indicating a negative nonlinear refractive index n_2. For samples with refractive and absorptive nonlinearities, closed-aperture measurements contain contributions from intensity-dependent changes in the transmission.[15] By dividing the normalized closed-aperture transmittance by the corresponding normalized open-aperture data, we could get the phase distortion created due to the change in refractive index only; this result is shown in Fig. 4(b). It is observed that the peak-valley of the closed-aperture z-scan satisfied the condition $\Delta z \sim 1.7 z_0$, therefore, satisfying the existence of cubic nonlinearity.[15] The value of $\Delta\varphi_0$, the phase shift, due to change in refractive index could be obtained from the theoretical fit to

$$T(z,\Delta\varphi_0) = 1 - \frac{4\Delta\varphi_0 x}{(x^2+9)(x^2+1)}. \quad (4)$$

From the open aperture Z-scan studies, it is noticeable that the nonlinear absorption decreases and finally vanishes as the concentration decreases to C4 and C5. The band tail states resulting from the localized defects, lead to a two-step photon absorption which is responsible for the high β value at high concentrations.[13] From Figures 1(a) and 1(b), it is clear that as the concentration decreases the density of these defect states diminishes and the absorption shifted to shorter wavelength due to size effect. Therefore, for very low concentrations (C4 and C5), the density of defect states are very less and they are lying above the photon energy of pump laser ($h\upsilon = 2.33$ eV), so that it will not act as the intermediate step in two step photon absorption.

The nonlinear refractive index n_2, real (Re $\chi 3$) and imaginary (Im $\chi 3$) part of the third order nonlinear susceptibility are presented by

$$n_2 = \frac{cn_0\lambda\Delta\varphi_0}{80\pi^2 I_0 L_{eff}}\ (\text{esu}), \quad (5)$$

where n_0 is linear refractive index (here $n_0 = 2.53$), and c is velocity of light in vacuum,

$$Re\chi^3 = \frac{n_0 n_2}{3\pi}\ (\text{esu}), \quad (6)$$

$$Im\chi^3 = \frac{n_0^2 c^2 \beta}{240\pi^2\omega}\ (\text{esu}). \quad (7)$$

Figure 5 demonstrates the variation of radial phase shift ($\Delta\varphi_0$) at the exit surface of the sample, after travelling a path of 1 mm through the nanocolloids with respect to the change in bandgaps. From the figure, it is obvious that the variation of $\Delta\varphi_0$ with Eg is not a linear one. Theoretical fit performed

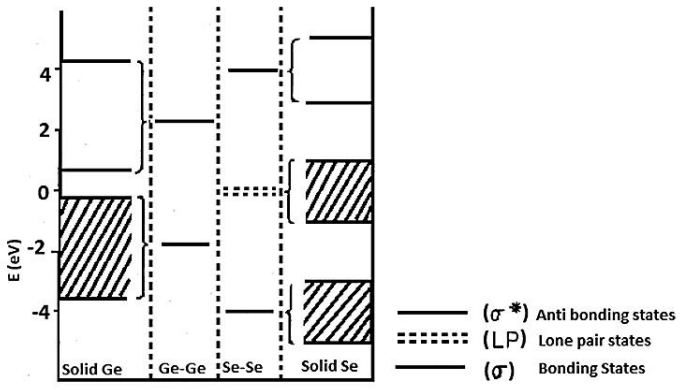

FIG. 3. Molecular energy states of Ge-Ge and Se-Se bonds and corresponding broadened energy bands in their solid form.

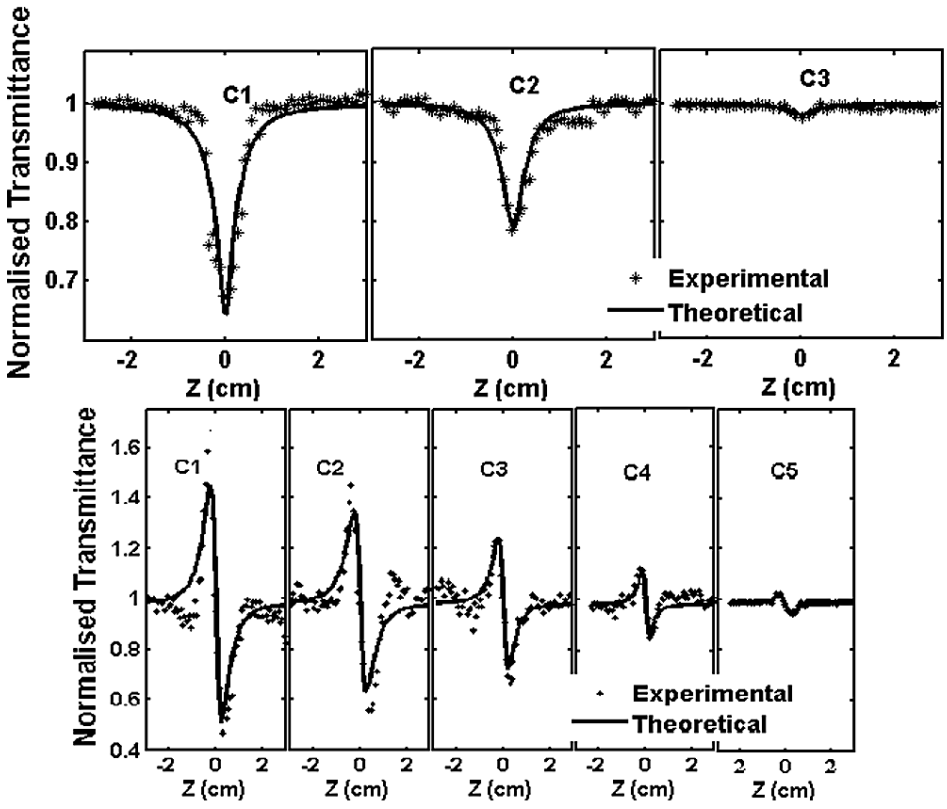

FIG. 4. (a) Nonlinear absorption of C1, C2, and C3 nanocolloids. Samples C4 and C5 show little nonlinear absorption and are not included. (b) Closed aperture Z-scan trace of C1, C2, C3, C4, and C5 concentrations at an aperture size S = 0.3 shows a bandgap dependent reduction in negative nonlinear refraction.

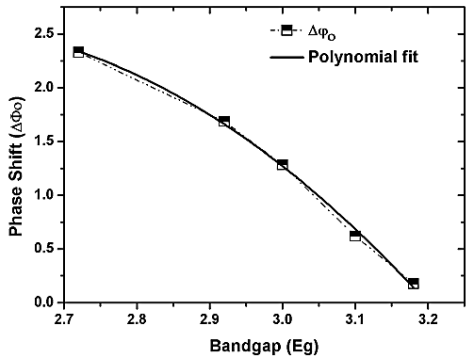

FIG. 5. Variation of radial phase shift ($\Delta\varphi_0$) with respect to the change in bandgaps. Solid curve shows quadratic polynomial fit.

on the data reveals that the relation between $\Delta\varphi_0$ and Eg is governed by a quadratic polynomial given by

$$\Delta\varphi_0 = -12.59221 + 10.8963Eg - 2.17566Eg^2. \quad (8)$$

Table I shows the variation of nonlinear absorption coefficient (β), nonlinear refractive index n_2, nonlinear susceptibility (χ^3) and figure merit (FOM $= |\frac{\gamma}{\beta\chi}|$, where γ is nonlinear refractive index in m^2/W) with respect to the bandgap of different nanocolloids. In semiconductors, the sign and magnitude of nonlinear refraction is determined by bandgap (Eg) as well as the energy of laser photon ($h\upsilon$) such that by exciting optical materials at frequencies much less than the gap, a considerably smaller, but faster, positive nonlinear refractive index n_2 (magnitude of this positive n_2 increases with "$h\upsilon$" upto Two Photon Absorption (TPA) edge (Eg/2) where $\frac{h\upsilon}{Eg} = 0.5$ and then it starts to decrease.) due to bound electronic effects is observed.[16] At frequencies ($\frac{h\upsilon}{Eg} \approx 0.7$), substantially above TPA edge n_2 is negative[17] whose magnitude increases as it approaches to one photon absorption edge Eg due to TPA generated free carrier

TABLE I. Variation of nonlinear optical coefficients with respect to bandgap.

Concentration	Bandgap (eV)	Nonlinear absorption coefficient β (cm/GW)	Nonlinear refractive index $n_2\ 10^{-10}$ (esu)	Imaginary part of nonlinear susceptibility Im $\chi^3 \times 10^{-10}$ esu	Real part of nonlinear susceptibility Re$\chi^3 \times 10^{-10}$ esu	Nonlinear Susceptibility $(\chi^3) \times 10^{-10}$ esu	Figure of merit (FOM) $\lvert \frac{\gamma}{\beta\lambda} \rvert$
C5	3.18	…	−0.25	…	−0.07	0.07	…
C4	3.10	…	−1.2	…	−0.30	0.30	…
C3	3.0	1.7	−2.0	0.017	−0.55	0.55	3.8
C2	2.92	26	−2.9	0.18	−0.77	0.80	0.34
C1	2.72	40	−4.0	0.28	−1.07	1.10	0.3

refraction and other bandgap resonant effects such as ac stark effect.[10] In chalcogenide nanocolloids, at 532 nm ($h\upsilon = 2.33$ eV) bandgap resonant effects (since $\frac{h\upsilon}{E_g} > 0.7$ for all concentrations) in combination with defect state assisted thermal nonlinearity leads to self-defocusing and therefore we get negative nonlinear refractive index n_2. From the table it is clear that as the bandgap approaches to the one photon absorption edge ($h\upsilon = 2.33$ eV) the negative nonlinear refractivity increases sharply as reported. The first two nanocolloids with highest bandgap in Table I (C4 and C5) show little nonlinear absorption since their defect states are very less and are lying above the photon energy ($h\upsilon = 2.33$ eV) of laser. Nonlinear susceptibility (χ^3) increases with concentration and is shown in Table I. Figure of merit (FOM) displayed in table shows very large value for C4 and C5 since nonlinear absorption ($\beta \sim 0$) is absent.

IV. CONCLUSION

Linear and nonlinear optical studies on Ga-Ge-Se nanocolloids of varying concentration were carried out. The studies reveal large negative nonlinear refraction near the one photon absorption edge due to bandgap resonant effects as well as defect state assisted thermal nonlinearity. Nonlinear absorption is found to be decreased and finally vanished as decreasing the concentration of nanocolloids due to the detraction of defect states in the bandgap at low concentrations. A bandgap dependent variation in phase shift ($\Delta\varphi_0$) is observed and fitted using a quadratic polynomial. That is by varying the concentration of solute in the solvent we can tune the bandgap, density, and energy of midgap defect states and thereby nonlinear optical properties of nanocolloids. Since defect states have inevitable participation in designing the linear and nonlinear optical properties in chalcogenide glasses, by tuning the bandgap and defects, we can control and engineer linear and nonlinear optical devices with desirable potentials by doping or materialising chalcogenide nanoclusters in appropriate matrix.

ACKNOWLEDGMENTS

Authors wish to acknowledge KSCSTE, Government of Kerala and DST for financial help through research project and SAIF-STIC for different analysis.

[1]K. Shimakawa, A. Kolobov, and S. R. Elliott, Adv. Phys. **44**, 475–488 (1995).
[2]K. S. Sangunni, J. Indian Inst. Sci. **91**, 2 (2011).
[3]M. Kastner, Phys. Rev. Lett. **28**(6), 355 (1972).
[4]S. C. Agarwal, Phys. Rev. B **7**, 685 (1973).
[5]T. Kohoutek, T. Wagner, and M. Frumar, J. Appl. Phys. **103**, 063511 (2008).
[6]S. Song, N. Carlie, J. Boudies, L. Petit, K. Richardson, and C. B. Arnold, J. Non-Cryst. Solids **355**, 2272–2278 (2009).
[7]R. Tintu, V. P. N. Nampoori, P. Radhakrishnan, and S. Thomas, J. Appl. Phys. **108**, 073525 (2010).
[8]T. Kohoutek, J. Orava, T. Sawada, and H. Fudouzi, J. Colloid Interface Sci. **353**, 454–458 (2011).
[9]C. Tsay, Y. Zha, and C. B. Arnold, Opt. Express **18**(25), 26744 (2010).
[10]M. Sheik-Bahae, D. C. Hutchings, D. J. Hagan, and E. W. Van Stryland, IEEE J. Quantum Electron. **27**(6), 1296 (1991).
[11]A. Zakery and S. R. Elliott, J. Noncryst. Solids **330**, 1–12 (2003) .
[12]K. Tanaka, J. Mater. Sci.: Mater. Electron. **16**, 633–643 (2005).
[13]I. Sebastian, S. Divya, V. P. N. Nampoori, P. Radhakrishnan, and S. Thomas, Appl. Phys. Lett. **102**, 031115 (2013).
[14]G. C. Chern and I. Lauks, J. Appl. Phys. **54**(5), 2701 (1983).
[15]M. Sheik-Bahae, A. A. Said, T. H. Wei, D. J. Hagan, and E. W. Van Stryland, IEEE J. Quantum Electron. **26**, 760–769 (1990).
[16]R. Adair, L. L. Chase, and S. A. Payne, Phys. Rev. B **39**, 3337–3349 (1989).
[17]M. Sheik-Bahae, D. J. Hagan, and E. W. Van Stryland, Phys. Rev. Lett. **65**(1), 96 (1990).

J Mater Sci (2014) 49:3732–3735
DOI 10.1007/s10853-014-8084-8

Experimental verification of localized defect states in Ga-Ge-Se nano colloidal solutions

Indu Sebastian · V. P. N. Nampoori · P. Radhakrishnan · Sheenu Thomas

Received: 16 July 2013 / Accepted: 24 January 2014 / Published online: 7 February 2014

Abstract Linear optical studies on $Ga_9Ge_{27}Se_{64}$ nanocolloidal solutions were carried out. Evidence for the existence of defect states in these nanoclusters are obtained from absorption spectra, and its occurrence is emphasized by analyzing the fluorescence and thermal diffusivity studies. An intermediate peak in the band tail of the absorption spectrum is observed at high concentration, and it is interpreted as the absorption due to localized defect states. Fluorescence emission corresponding to this peak confirms the same. The thermal diffusivity studies show that nanocolloidal solutions with less solute concentration have high thermal diffusivity. This indicates the existence of high defect states density which increases with the increase in cluster size, leads to scattering of phonons from the defect centers and in turn results in lowering of thermal diffusivity.

Introduction

Chalcogenide glass nanocolloidal solutions prepared [1–3] by dissolving in organic solvents allow new and simple deposition routes such as spin coating technique, spray coating, etc. The dissolution process is cost effective, and it results in the formation of clusters with dimensions of several nanometers which retains the bulk glass stoichiometry. Band gap of these nanoclusters varies with the size, which in turn depends upon the concentration of solute in the solution [4]. So far, there have been reports on device application of solution processing as inverse opal photonic crystal [5], integrated single-mode mid-infrared waveguides [6], etc.

Chalcogenide glasses are known to have a variety of photoinduced phenomena [7, 8] due to the flexibility of its atomic structure and presence of defect states. It is known that the intermediate localized states [9, 10] in the band gap are responsible for many optical and electrical properties in the noncrystalline semiconductors. The Mott Davis Street (MDS) [11, 12] model or charged dangling bond model for chalcogenide glass satisfactorily explains the continuous wave photoluminescence (PL), which accounts for most of the PL quantum efficiency. A photoinduced electron (e^-) or hole (h^+) is trapped by an isolated charged defect

$$D^+ + e^- \rightarrow D^0$$

$$D^- + h^+ \rightarrow D^0$$

and then a hole or electron recombines with the D^0:

$$D^0 + e^- \rightarrow D^- + h\nu_{PL}$$

$$D^0 + h^+ \rightarrow D^+ + h\nu_{PL},$$

where h is the Plank's constant, υ_{PL} is the frequency of the emitted radiation, D stands for the chalcogen dangling bond, and the superscripts stand for the charge state. According to Davis and Mott [13], the geometrical disorder, such as lack of long range order, forms a range of localized states at the band edges, while neutral band dangling bonds give rise to a well separated narrow band of localized states at the center of the gap where Fermi energy (E_F) lies. The defects states due to charge dangling[7] bonds (proportional to the D^+ and D^- centers and appears as two narrow bands) are located in the forbidden gap around the E_F level.

I. Sebastian (✉) · V. P. N. Nampoori · P. Radhakrishnan · S. Thomas
International School of Photonics, Cochin University of Science and Technology, Cochin, Kerala, India
e-mail: indusebastian@gmail.com

J Mater Sci (2014) 49:3732–3735

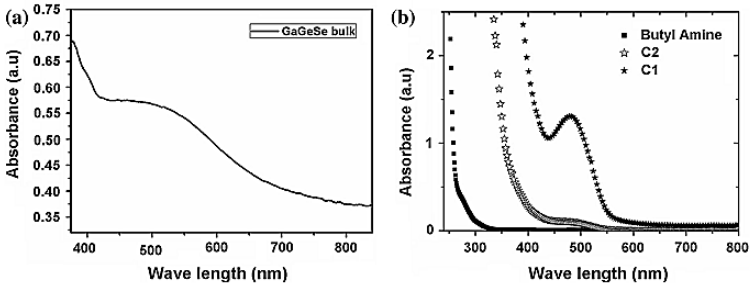

Fig. 1 **a** Absorption spectra of bulk $Ga_9Ge_{27}Se_{64}$ glass show a broad absorption hump in the band tail. **b** Absorption spectra of nanocolloidal solutions C1, C2, and solvent butyl amine

In this work, we present the experimental evidence for the existence of localized defect states in the bandgap of nano Ga-Ge-Se glass structures. As the material is transformed from bulk to nano regime, a well-separated absorption peak centered on 480 nm in the absorption spectra is witnessed. It is observed that the localized states get diminished as the cluster size decreases.

In the present work, we have carried out studies on $Ga_9Ge_{27}Se_{64}$ glass prepared by conventional melt quenching method. The bulk sample was prepared by melting appropriate weight percentage of elemental form of Se, Ge, Ga (Sigma Aldrich, 5 N purity) in an evacuated fused quartz ampoule at 1,000°C for 24 h for thorough mixing and homogenization of the melt and then rapidly quenched into ice cold water. X-ray diffraction (XRD) (Bruker AXS D8 advance XRD) studies were conducted and its amorphous nature were confirmed. Energy dispersive X-ray spectroscopy (JEOL Model JED-2300) conducted on bulk glass reveals that it has the same expected composition. Nanocolloidal chalcogenide glass solution of two different concentrations C1 = 0.30 and C2 = 0.096 mg/ml was prepared by dissolving it in *n*-butyl amine. Optical absorption studies of the solutions were carried out by using a JascoV-570 UV/VIS/IR spectrophotometer, and the fluorescence studies were done using Cary Eclipse fluorimeter (Varian). The heat diffusivity studies in nanocolloids at 532 nm were conducted using Dual mode-matched thermal lens method.

Results and discussions

Absorption spectra of bulk $Ga_9Ge_{27}Se_{64}$ glass is given in Fig. 1a. Bulk glass absorption shows a broad hump extending from visible to near infrared region, which has resulted from defects. Figure 1b shows absorption of C1, C2, and the solvent butyl amine. From the figure, it is clear that the solvent butyl amine has no absorption in the visible region and as the solute concentration in the solvent increases the absorption edge is red shifted. A broad absorption peak, but sharper than bulk glass, around 480 nm is observed in both C1 and C2. This is due to the absorption due to localized defect states which is located in the bandgap region [14]. As the solute concentration in the solvent increases, the size of the nano clusters also increases [1], and it leads to increase in the defect states density compared to the samples with less concentration. Thermal lens analysis which is presented in following section emphasizes this prediction.

Emission spectra of sample C1 for different excitation wavelengths are presented in Fig. 2a given below. As the excitation wavelength shifts from shorter to longer wavelength, the fluorescence emission peak also shifts toward longer wavelength region. A maximum fluorescence emission peak is observed at 580 nm with 480 nm excitation. For a wavelength higher than 480 nm excitation, the emission intensity decreases but the peak intensity is scattered around 580 nm. The most intense fluorescence emission is observed at 480 nm excitation. Intermediate absorption peak in the forbidden energy gap and the corresponding fluorescence emission in C1 emphasizes the existence of localized energy band in the nanoclusters with an increase in density of states up to a level corresponding to 480 nm (2.58 eV).

Figure 2b shows fluorescence emission spectra of the sample at C2 concentration for different wavelengths of excitation. From the absorption spectrum of C2, it is clear that the absorption by localized defect states (around 480 nm) in the band gap is very less. Fluorescence studies on C2 reveal that a comparably less intensity fluorescence emission is observed for low wave length excitation which starts from UV side. This is due to the absorption of defect states (located in the band tail leading to a spread in band tail) originating from the lattice disorder, which is the signature of amorphous materials, which in turn depends upon the thermal history of the sample.

Fluorescence spectra for C1 are broader than C2, and it is explained as follows. Absorption spectrum of bulk glass is very broad due to the delocalization [15] of defect (originating from the Se dangling bonds) states which

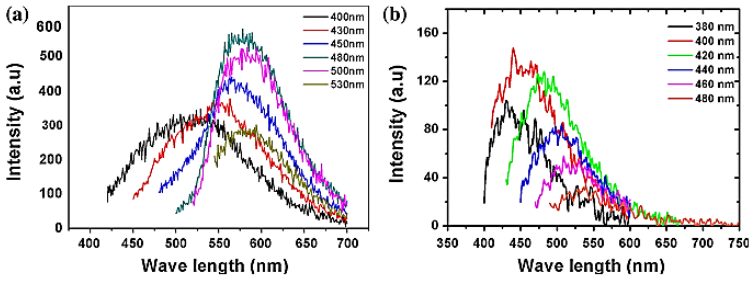

Fig. 2 **a** Emission spectra of C1 corresponding to different excitation wavelengths show a maximum emission with 480 nm excitation. **b** Fluorescence emissions from C2 at different excitation wave lengths show a maximum emission with 500 nm excitation

extends up to infrared region. But in the nanocolloidal solutions, the defect states are localized in the bandgap and show specific absorption peak in the absorption spectra as observed in C1. The localization of defect states occurs due to the fragmentation of solute bulk glass during dissolution [16], and the fragments have a lesser number of Se bonds. Obviously, as the concentration of solute glass in the solvent decreases, the density of localized defect states will also decrease as observed in the absorption spectra of C2. Since C1 has a broad and well-defined defect state absorption which covers a range of wavelengths, fluorescence emission spectra are also broad for C1, and it embraces most of the visible region. For shorter wavelength excitation, the energy of excited carriers has been quenched and transited to the lower lying defect states by nonradiative transitions and the corresponding emission spectra are less intense and wide-ranging. As the excitation wavelength increases to the wavelength at which maximum defect states occur (i.e., around 480 nm), the fluorescence width decreases and becomes almost constant. In the case of C2, the intermediate defect state absorption is comparatively less and, therefore, the fluorescence emission is not as broad and intense as C1.

Dual mode-matched thermal lens method has been used to study the heat diffusivity in nanocolloids at 532 nm. Figure 3 represents decay curve for $Ga_9Ge_{27}Se_{64}$ nanocolloid at concentration C2. Thermal diffusivity of a material depends on its thermal conductivity which is governed by phonon mean free path which inturn depends upon the network structure. Table 1 shows thermal diffusivity variation of nanocolloidal solution with different concentration. Thermal diffusivity of $Ga_9Ge_{27}Se_{64}$ nanocolloidal solution decreases with increase in solute concentrations. It is clear from the absorption spectra that as the solute concentration in the solvent increases the defect density also increases. Since the presence of defect states leads to scattering of thermal waves [17], nanocolloidal solutions with large cluster size offer more resistance to thermal wave propagation and results in a lower thermal diffusivity. Thus, the thermal diffusivity studies confirm the predictions based on absorption spectra analysis.

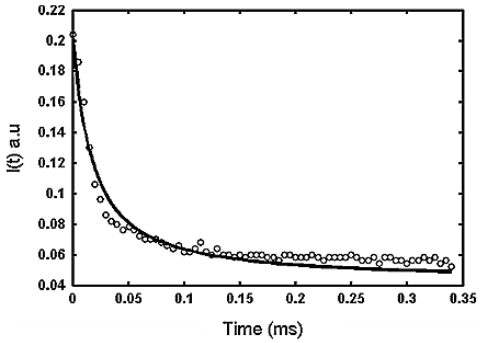

Fig. 3 Decay curve for GaGeSe nanocolloid for concentration C1

Table 1 Variation of thermal diffusivity with respect to concentration

Samples	Thermal diffusivity (cm^2/s)
C1	4.5×10^{-4}
C2	24.9×10^{-4}

Conclusions

Chalcogenide glass of composition $Ga_9Ge_{27}Se_{64}$ is prepared. Signature of defect states as a broad absorption, which extends from visible to near infrared region is observed in bulk glass. The prepared bulk glass is converted to its nano form by dissolving appropriate weight of it in butyl amine solvent. The defect state absorption in nano clusters is observed as a sharp peak around 480 nm in the absorption spectra. Fluorescence emission for every wavelength in the band tail peak is observed, and it is maximum at 480 nm excitation. These results emphasize the occurrence of defect states with varying density of states with a maximum energy corresponding to 480 nm. As the concentration of solute glass decreases, the defect state absorption diminishes and shows a fluorescence blue

shift. Thermal lens analysis shows a higher thermal diffusivity for sample with less defect state density, which is attributed to the low levels of scattering of thermal waves from defect centers.

Acknowledgements Authors wish to acknowledge KSCSTE Government of Kerala, DST and UGC for financial help and SAIF-STIC for different analysis.

References

1. Kohoutek T, Wagner T, Frumar M (2008) J Appl Phys 103:063511
2. Song Shanshan, Carlie Nathan, Boudies Julie, Petit Laeticia, Richardson Kathleen, Arnold Craig B (2009) J Non-cryst Solids 355:2272–2278
3. Waldmann Maike, David Musgraves J, Kathleen Richardson, Arnold CB (2012) Structural properties of solution processed Ge23Sb7S70 glass materials. J Mater Chem 22:17848
4. Tintu R, Nampoori VPN, Radhakrishnan P, Thomas S (2010) J Appl Phys 108:073525
5. Kohoutek T, Orava J, Sawada T, Fudouzi H (2011) J Colloid Interface Sci 353:454–458
6. Tsay C, Zha Y, Arnold CB (2010) Solution-processed chalcogenide glass for integrated single-mode mid-infrared waveguides. Opt Express 18(25):26745
7. Shimakawa K, Kolobov A, Elliott SR (1995) Photoinduced effects and metastability in amorphous semiconductors and insulators. Adv Phys 44:475–488
8. Sangunni KS (2011) J Indian Inst Sci 91:2
9. Narc Kastner Bonding Bands (1972) "Lone-Pair Bands, and Impurity States in Chalcogenide Semiconductors", Phys Rev Lett 28:6
10. Agarwal SC (1973) Nature of localized states in amorphous semiconductors—a study by electron spin resonance. Phys Rev B 7:685
11. Street RA, Mott NF (1975) Phys Rev Lett 35:1293
12. Street RA (1976) Adv Phys 25:397
13. Davis EA, Mott NF (1970) Phill Mag 22:903–927
14. Sebastian Indu, Divya S, Nampoori VPN, Radhakrishnan P, Sheenu Thomas (2013) Appl Phys Lett 102:031115
15. Narc Kastner, Bonding Bands (1972) "Lone-Pair Bands, and Impurity States in Chalcogenide Semiconductors", Phys Rev Lett 28:6
16. Sebastian Indu, Mathew S, Nampoori VPN, Radhakrishnan P, Thomas Sheenu (2013) Concentration tuned bandgap and corresponding nonlinear refractive index dispersion in Ga-Ge-Se nanocolloids. J Appl Phys 114:053102. doi:10.1063/1.4817176
17. Manikandan N, Paulraj M, Asokan S (2009) J Non-cryst Solids 355:58–60